

University of Eastern Piedmont
“Amedeo Avogadro”

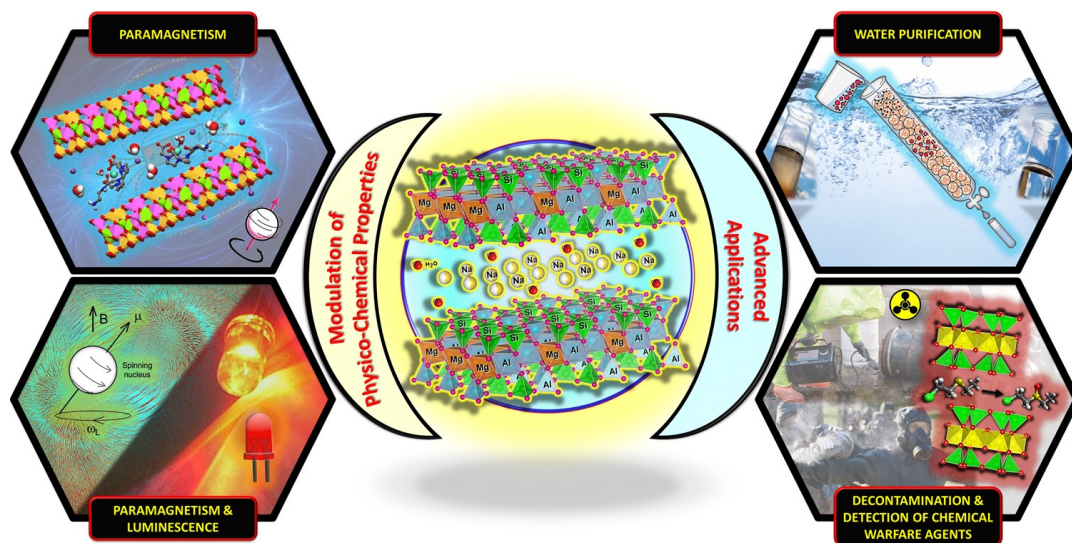
Department of Sciences and Technological Innovation

Ph.D. Program in “Chemistry & Biology”

Cycle XXXII, a.y. 2016-2019

curriculum: “Chemical Methodologies for New Molecules and Nanomaterials” (SSD: CHIM/02-03)

Improving the Multifunctional Properties of Clay Materials through combination of Lanthanides and Synthetic Saponites: From Environmental to Nanotechnology Applications



Stefano Marchesi

Supervised by: Prof. Chiara Bisio and Dr. Fabio Carniato

Ph.D. Program Co-Ordinator: Prof. Luigi Panza

University of Eastern Piedmont
“Amedeo Avogadro”

Department of Sciences and Technological Innovation

Ph.D. Program in “Chemistry & Biology”

Cycle XXXII, a.y. 2016-2019

curriculum: “Chemical Methodologies for New Molecules and
Nanomaterials” (SSD: CHIM/02-03)

**IMPROVING THE MULTIFUNCTIONAL
PROPERTIES OF CLAY MATERIALS
THROUGH COMBINATION OF
LANTHANIDES AND SYNTHETIC
SAPONITES:
FROM ENVIRONMENTAL TO
NANOTECHNOLOGY APPLICATIONS**

Stefano Marchesi



Supervised by: Prof. Chiara Bisio and Dr. Fabio Carniato



Ph.D. Program Co-Ordinator: Prof. Luigi Panza



UNIVERSITÀ DEL PIEMONTE ORIENTALE

DOTTORATO DI RICERCA
IN CHEMISTRY & BIOLOGY

Via Duomo, 6
13100 – Vercelli (ITALY)

DECLARATION AND AUTHORISATION TO ANTIPLAGIARISM DETECTION

The undersigned **STEFANO MARCHESI** student of the Chemistry & Biology
Ph.D. course (**XXXII – 32°** Cycle)

Declares:

- to be aware that the University has adopted a web-based service to detect plagiarism through a software system called “Turnit.in”,
- his/~~her~~ Ph.D. thesis was submitted to Turnit.in scan and reasonably it resulted an original document, which correctly cites the literature;

Acknowledges:

- his/~~her~~ Ph.D. thesis can be verified by his/~~her~~ Ph.D. tutor and/~~or~~ Ph.D. Coordinator in order to confirm its originality.

Date: **15/11/2019**

Signature:

Table of Contents

<i>Title Page</i>	I
<i>Plagiarism Declaration</i>	III
<i>Table of Contents</i>	V
<i>List of Abbreviations</i>	IX

Chapter 1 **01**

“Introduction: Clay Materials”

1.1	Phyllosilicates	02
1.2	Natural clays	07
1.3	Synthetic clays: Saponite	10
1.4	Synthetic methods for the preparation of saponites	16
1.5	Applications of synthetic saponites	19
1.6	Notes and References	23

Chapter 2 **27**

“Outline”

Chapter 3 **33**

“Synthetic Saponite Clays as Promising Solids for Lanthanide Ions Recovery”

3.1	Introduction	34
3.2	Experimental Approach	37
3.2.1	Materials	37

3.2.2	Simulated aqueous solutions	38
3.3	Results and Discussion	39
3.3.1	Characterization of saponite materials	39
3.3.2	Uptake and recovery tests of lanthanide ions from aqueous solutions	42
3.4	Conclusions	57
3.5	Notes and References	58

Chapter 4 **63**

“Solution and Solid-State NMR Study of Synthetic Saponite Materials Intercalated with Lanthanide Chelates”

4.1	Introduction	64
4.2	Experimental Approach	68
4.2.1	Saponite clay	68
4.2.2	Gd ³⁺ /Y ³⁺ -complexes	69
4.2.3	Intercalated materials	77
4.3	Results and Discussion	79
4.3.1	Characterization of GdL1/SAP and GdL2/SAP materials	79
4.3.2	Characterization of GdL0/SAP and YL0/SAP materials	92
4.4	Conclusions	104
4.5	Notes and References	106

Chapter 5 **111**

“Inclusion of Paramagnetic and Luminescent Lanthanide Ions in the Framework of Synthetic Saponite Clays”

5.1	Introduction	112
5.2	Experimental Approach	114
5.2.1	Materials	114
5.3	Results and Discussion	118
5.3.1	Characterization of GdEuSAP material	118
5.3.2	Luminescence enhancement of GdEuSAP by intercalation of Phen	129
5.4	Conclusions	135

5.5	Notes and References	138
-----	----------------------	-----

Chapter 6	143
------------------	------------

“Bifunctional Eu^(III) and Nb^(V)-containing Saponites for Optical Detection and Catalytic Abatement of Chemical Warfare Agents”

6.1	Introduction	144
6.2	Experimental Approach	149
6.2.1	Materials	149
6.3	Results and Discussion	153
6.3.1	Characterization of Eu ^(III) /Nb ^(V) -containing saponite materials	153
6.3.2	Catalytic oxidative abatement tests	159
6.3.3	Optical detection tests	165
6.4	Conclusions	168
6.5	Notes and References	169

Chapter 7	175
------------------	------------

“Conclusions”

Chapter 8	183
------------------	------------

“Experimental Techniques”

8.1	Analytical Methods	183
8.2	Tables	190
8.3	Notes and References	194

Curriculum Vitae et Studiorum & List of Publications	197
---	------------

Acknowledgements	203
-------------------------	------------

List of Abbreviations

Frequently Used Materials

- Gd^{3+} , Eu^{3+} , Nb^{5+} , La^{3+} , Lu^{3+} : gadolinium, europium, niobium, lanthanum and lutetium ions
- *f*-block: lanthanide element
- Ln^{3+} : trivalent lanthanide ion
- SAP: saponite
- DOTA: 1,4,7,10-tetraazacyclododecane-1,4,7,10-tetraacetic acid
- AAZTA: 6-amino-6-methylperhydro-1,4-diazepine-*N,N',N'',N'''*-tetraacetic acid
- TETA: 1,4,8,11-tetraazacyclotetradecane
- EDTA: ethylenediaminetetraacetic acid
- Phen: 1,10-phenantroline
- CEES (or 2-CEES): (2-chloroethyl)ethyl sulphide
- CEESO: (2-chloroethyl)ethyl sulfoxide
- CEESO₂: (2-chloroethyl)ethyl sulfone

Frequently Used Experimental Techniques

- ICP-MS: inductively coupled plasma mass spectrometry
- ICP-AES: inductively coupled plasma mass spectrometry
- XRPD: X-ray powder diffraction
- HPLC-MS ESI^{+/·}: High-Performance Liquid Chromatography-Mass Spectrometry equipped with an Electrospray Ion Source
- HRTEM: high-resolution transmission electron microscopy
- SEM: scanning electron microscopy
- NMR: nuclear magnetic resonance
- ssNMR: solid-state nuclear magnetic resonance
- UV-Vis-NIR: ultraviolet-visible-near infrared spectrophotometry
- FTIR: Fourier transform infrared spectroscopy
- TGA: thermogravimetric analyses
- DLS: dynamic light scattering

- PL: (photoluminescence) spectrofluorimetry

Other

- *O*-layer/sheet: Octahedral-layer/sheet
- *T*-layer/sheet: Tetrahedral-layer/sheet
- *T-O*, *T-O-T* (*vide supra*)
- CEC: cation-exchange capacity
- MRI: magnetic resonance imaging
- CA: contrast agent
- REE: rare-earth elements
- LLE: liquid-liquid extraction
- LSE: liquid-solid extraction
- MMET: metal-to-metal energy transfer
- FRET: Förster resonance energy transfer
- LMET: ligand-to-metal energy transfer
- NMRD: nuclear magnetic relaxation dispersion profiles
- CWA: chemical warfare agent

“One, remember to look up at the stars and not down at your feet. Two, never give up work. Work gives you meaning and purpose and life is empty without it. Three, if you are lucky enough to find love, remember it is there and don’t throw it away.”

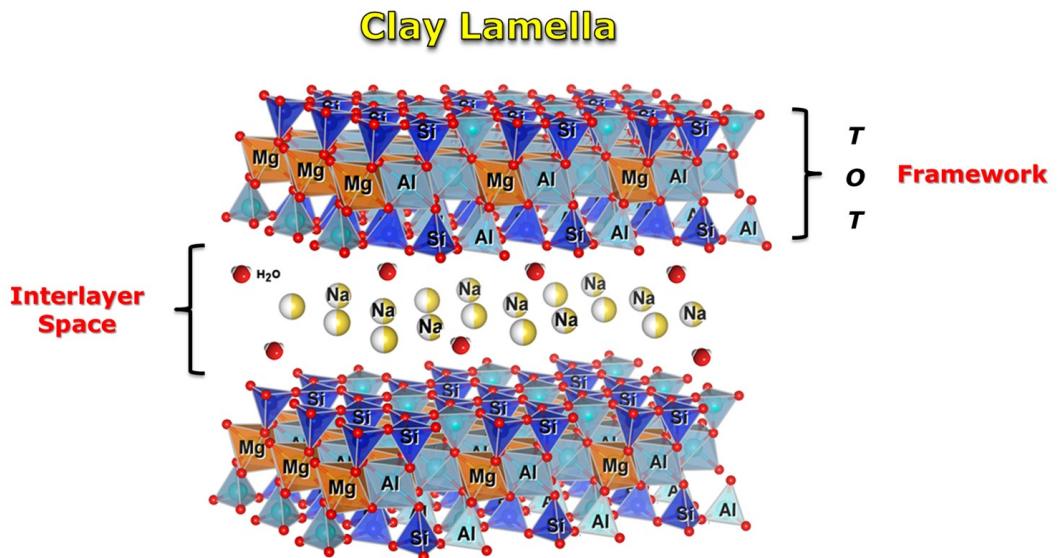
- Stephen Hawking

1

“Introduction: Clay Materials”

In this chapter, a general introduction to clays materials was given, clarifying the differences between natural and synthetic ones especially with reference to a specific kind of synthetic clays called saponites (see Figure below).

The literature data demonstrate the growing interest in the synthetic saponites, due to their peculiar physico-chemical properties, which proved to be excellent versatile materials for the preparation of novel advanced layered materials.



1.1 Phyllosilicates

The **silicates**¹ represent a large family of minerals mainly consisting of oxygen and silicon atoms, distinguished according to the complexity of the bonds between the individual tetrahedral units of $[\text{SiO}_4]^{-4}$ and the number of vertices in common between them. The silicates in which the $[\text{SiO}_4]^{-4}$ tetrahedra are organized in bidimensional-*like* (2D) layers linked together by sharing three vertices along a plane, thus forming sheets of tetrahedral structures, are classified as **phyllosilicates** (also called **sheet silicates**).¹ In each layer, the tetrahedral units present a central silicon atom that coordinates four oxygen atoms, thus constituting a lattice with a general composition of $[\text{Si}_2\text{O}_5]^{-2}$. Six member rings of $[\text{SiO}_4]^{-4}$ tetrahedral units interconnected together through common vertices to form hexagonal rings that extend outward in infinite sheets (Figure 1A); three out of the four oxygens from each tetrahedra are shared with other tetrahedral units. The terminal/apical oxygen atoms of a layer interact with the other cations of the adjacent layer, thus forming octahedral layers. These are arranged in such a way that three vertices lie in a plane while the other three are in another one parallel to it. The remaining free vertices are normally occupied by an additional hydroxyl/ OH^- ions located at the centre of the hexagonal ring as shown in Figure 1B, in which the triangles become the faces of the octahedral groups that can bind to the tetrahedral layers.

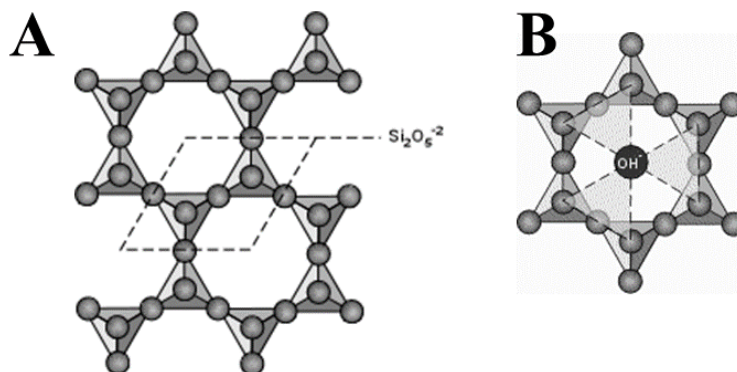


Figure 1. (A) Schematic representation of a Si-O-Si plane of phyllosilicates. (B) Schematic view of a OH^- ion with respect to the lattice of phyllosilicates.

The phyllosilicates are constituted by a lamellar structure and each single lamella (or tectoid) is formed by the overlapping of single layers joined by covalent forces, which stabilize the entire inorganic framework. These layers (or sheets) can contain chemical elements in tetrahedral (*T*) and/or octahedral (*O*) coordination (Figure 2A). The phyllosilicates are categorized according to the number of layers that form the structure of the lamella. Phyllosilicates of 1:1 type are constituted by one *T*-layer joined to one *O*-layer (*T-O* structure), while 2:1 type are formed by one *O*-sheet sandwiched by two *T*-sheets (*T-O-T* structure). The space between each 1:1 or 2:1 sandwich is called interlayer or interlamellar region: this zone is populated by positively-charged ions (*i.e.* Al^{3+} , Na^+ , Mg^{2+} ...), which neutralize the residual negative charges of the inorganic Si-O lattice (Figure 2B).

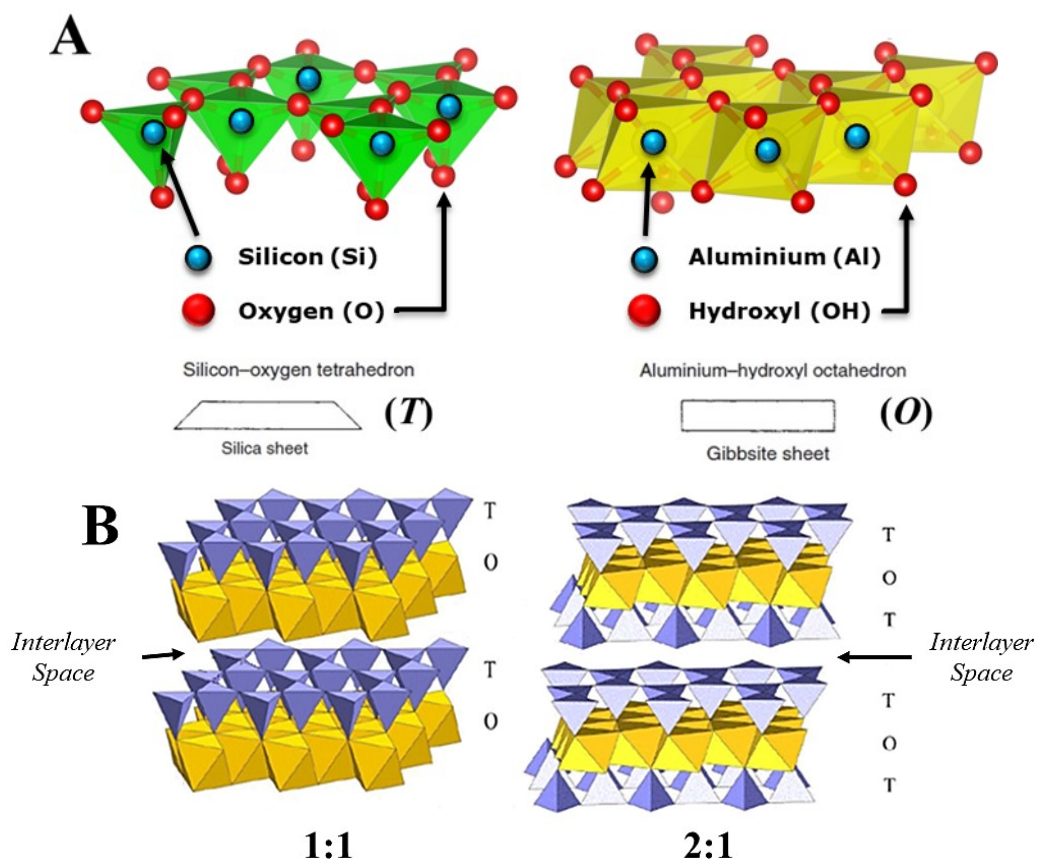


Figure 2. (A) Tetrahedral (*T*) and octahedral (*O*) basic units constituting the phyllosilicates. (B) Structure of 1:1 (*T-O*) and 2:1 (*T-O-T*) type phyllosilicates.

According to the number of layers which constitute the lamella structure (1:1 or 2:1 type), on the net charge value of the structural formula and on the cations present inside the interlayer space, phyllosilicates are further distinguished in two three main sub-classes (Figure 3 and 4): 1) kaolinite-serpentine (1:1), 2) talc-pyrophyllite, smectite, vermiculite, chlorite and mica (2:1), and 3) interstratified clays like sepiolite and palygorskite (2:1 inverted ribbons).¹ The chemical composition of the main phyllosilicates is reported in Figure 4.

Natural phyllosilicates are commonly generated by the chemical action of atmospheric agents on siliceous minerals based on hydrated alumino-silicates (also called **clays**),¹ which are commonly found on the Earth's surface. Indeed, clay minerals (Figure 5), also defined as a class of hydrated phyllosilicates making up fine-grained fraction of soils,¹ are one of the primary products of chemical weathering and one of the most abundant constituents of sedimentary rocks. Besides from some compounds of the groups of chlorite and mica and of the sub-group of serpentine, most of the phyllosilicates are constituted by clays.

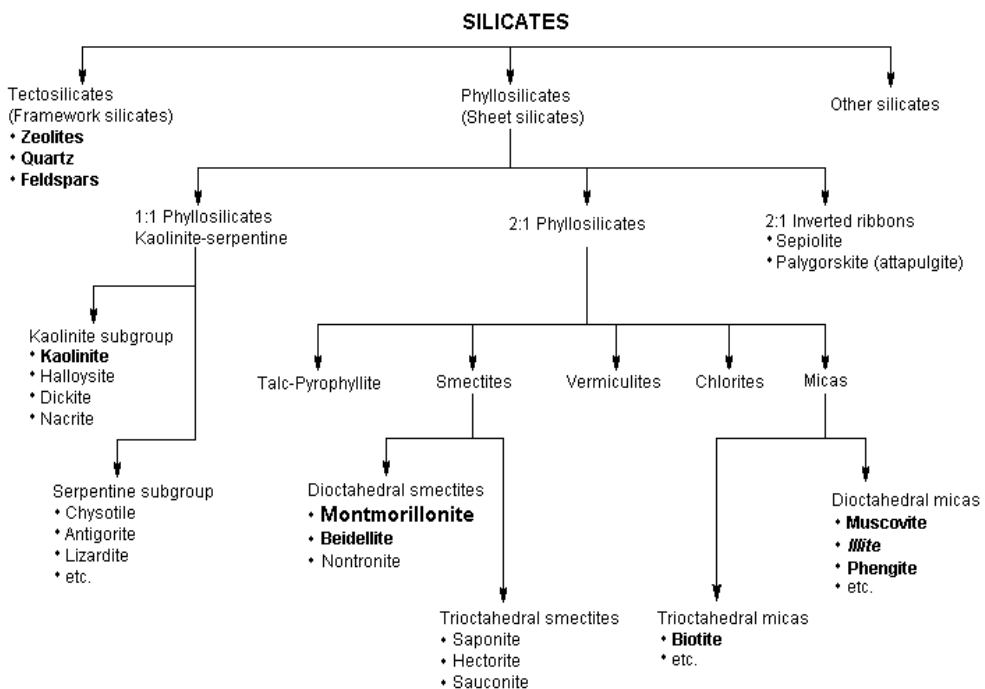


Figure 3. Family of silicates.

Layer type	Interlayer material ^a	Group	Octahedral character	Species
1:1	None or H ₂ O only (x 0)	Kaolin-serpentine	Trioctahedral	Lizardite, berthierine, amesite, cronstedtite, nepouite, kellyite, fraipontite, brindleyite
			Diocahedral Di-trioctahedral	Kaolinite, dickite, nacrite, halloysite (planar) Odinite
2:1	None (x 0)	Pyrophyllite-Talc	Trioctahedral	Talc, willemsite, kerolite, pimelite
			Diocahedral	Pyrophyllite, ferripyrophyllite
	Hydrated exchangeable cations (x 0.2-0.6)	Smectite	Trioctahedral	Saponite, hectorite, sauconite, stevensite, swinefordite
			Diocahedral	Montmorillonite, beidellite, nontronite, volkonskoite
	Hydrated exchangeable cations (x 0.6-0.9)	Vermiculite	Trioctahedral	Trioctahedral vermiculite
			Diocahedral	Diocahedral vermiculite
	Non-hydrated monovalent cations (x 0.6-1.0)	True (flexible) mica	Trioctahedral	Biotite, phlogopite, lepidolite, etc.
			Diocahedral	Muscovite, illite, glauconite, celadonite, paragonite, etc.
	Non-hydrated divalent cations (x 1.8-2.0)	Brittle mica	Trioctahedral	Clintonite, kinoshitalite, bityite, anandite
			Diocahedral	Margarite
	Hydroxide sheet (x = variable)	Chlorite	Trioctahedral	Clinochlore, chamosite, pennantite, nimite, baileychlore
			Diocahedral	Donbassite
2:1	Regularly interstratified (x = variable)	Variable	Trioctahedral	Cookeite, sudoite
			Diocahedral	Corrensite, aliettite, hydrobiotite, kulkeite Rectorite, tosudite

Mineral name	Formula
kaolinite	$Al_2Si_4O_{10}(OH)_2$
chrysotile	$Mg_3Si_2O_5(OH)_4$
pyrophyllite	$Al_2Si_4O_{10}(OH)_2$
talc	$Mg_3Si_2O_5(OH)_4$
montmorillonite	$M_{x/n}^{n+} [Al_{4-x}Mg_x] [Si_8] O_{20} (OH)_4 \cdot nH_2O$
beidellite	$M_{x/n}^{n+} [Al_4] [Si_{8-x}Al_x] O_{20} (OH)_4 \cdot nH_2O$
nontronite	$M_{x/n}^{n+} [Fe_4] [Si_{8-x}Al_x] O_{20} (OH)_4 \cdot nH_2O$
saponite	$M_{x/n}^{n+} [Mg_6] [Si_{8-x}Al_x] O_{20} (OH)_4 \cdot nH_2O$
(F-)hectorite	$M_{x/n}^{n+} [Mg_{6-x}Li_x] [Si_8] O_{20} (OH,F)_4 \cdot nH_2O$
stevensite	$M_{x/n}^{n+} [Mg_{6-x}Vacancy_x] [Si_8] O_{20} (OH)_4 \cdot nH_2O$
vermiculite	$[Mg,Ca]_{x/2}^{2+} [Al_{4-x}Mg_x] [Si_8] O_{20} (OH)_4 \cdot 8H_2O$
vermiculite	$[Mg,Ca]_{x/2}^{2+} [Mg_6] [Si_{8-x}Al_x] O_{20} (OH)_4 \cdot nH_2O$
paragonite	$Na_2 [Al] [Si_6Al_2] O_{20} (OH)_4$
phlogopite	$K_2 [Mg,Fe]_6 [Si_6Al_2] O_{20} (OH,F)_4$
clinocllore	$[(Al_xMg_{6-x})(OH)_6] [Mg_6] [Si_{8-x}Al_x] O_{20} (OH)_4$
thuringite	$[(Fe^{3+}_xFe^{2+}_{6-x})(OH)_6] [Fe^{2+}_{6-y}Mg_y] [Si_{8-x}Al_x] O_{20} (OH)_4$

Figure 4. (A) Classification of phyllosilicates; the x parameter represents the net charge of the material, obtainable from the structural formula. (B) Chemical composition of the main phyllosilicates.

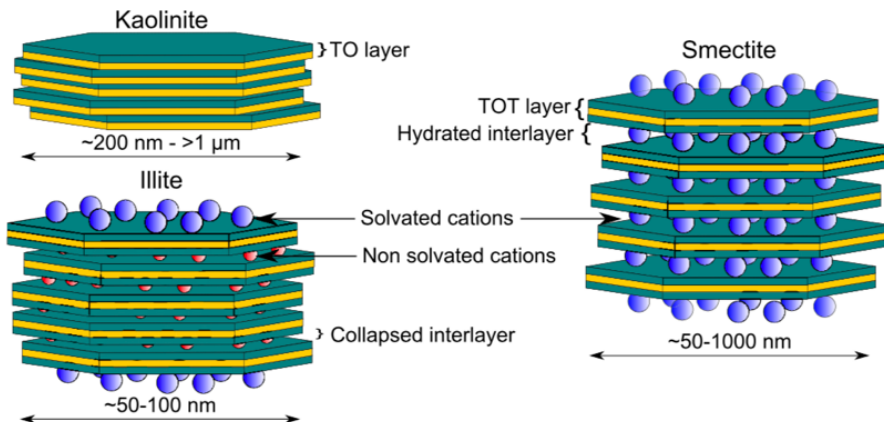


Figure 5. Representation of $T-O$ and $T-O-T$ type clay mineral particles.

The *O*-sheet possesses a remarkable compositional variability since the cation(s) present in it can be replaced by others (a process named “vicariance”), creating a charge imbalance. The base structure of the phyllosilicates is formed by three octahedrons for the *O*-sheet. The layer is called *di-octahedral* if two of the three octahedrons are occupied by a cation and the third is unoccupied, while if all three octahedrons are filled by a cation the layer is classified as *tri-octahedral*.¹ In the case of a di-octahedral sheet silicates, a trivalent ion (*i.e.* Al^{3+} , Fe^{3+} ...) is present only in two of the three octahedrons, and in the structure of the lamella an octahedron is linked to only one other octahedron (each O^{2-} or OH^- ion is surrounded by three divalent cations). In the tri-octahedral sheet silicates, instead, an octahedron is joined to other two and compensates the positive charge of a divalent cation present in it (*i.e.* Mg^{2+} , Fe^{2+} ...) (each O^{2-} or OH^- ion is surrounded by two trivalent cations). (Figure 6).

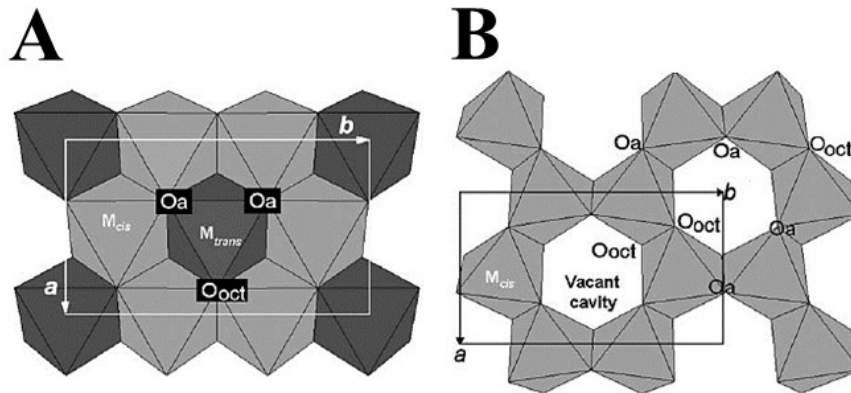


Figure 6. Tri-octahedral (A) and di-octahedral (B) structure of the *O*-sheet.

The phyllosilicates have been used since the prehistoric era due to their wide diffusion and great diversity in nature.^{2,3} The intrinsic properties of the di- and tri-octahedral phyllosilicates (Figure 3 and 4), such as the high specific surface area, the cation-exchange capacity and the hydration degree, have made these materials suitable for a large number of applications: for example, in building materials, in the industrial and pharmaceutical field, as catalysts, ion exchangers or decolouring agents...⁴⁻⁸ Because of their particle size, commonly in the order of tens to hundreds

of nanometres, phyllosilicates are considered excellent nanomaterials, for example as nanoreactors for the synthesis of nanoparticles and for functional nanodevices.⁹ The variability of chemical species that can be hosted in the interlayer space has allowed to develop a wide range of new advanced lamellar systems.¹⁰⁻¹⁷ Because of these reasons, in recent years the employment of natural and synthetic clays on the nanoscience and nanotechnology fields has attracted a considerable interest in the scientific community.

1.2 Natural clays

Over the years, natural clays have been employed in several industrial applications, for paper, plastics, rubber, building and electrical industry, paints, cosmetics, coating, foundries, ceramic... In Figure 7 are shown most of the uses of two natural clays, kaolin and bentonite (*n.b.* the latter is a fine powder/solid mixture consisted of *ca.* 90 % of montmorillonite).

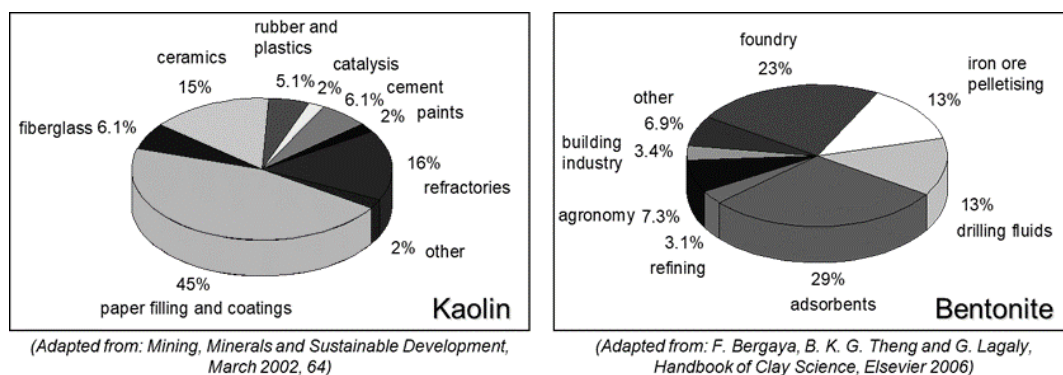


Figure 7. Industrial applications of some of most used natural clays (kaolin and bentonite).

In 2001-2019 range, more than 116.000 papers have been published worldwide about the clays, and of these more than 5.000 papers are dealing with the application of clay materials in the catalysis field. Moreover, more than 500 patents have been

reported in the last two decades for the applications of natural clays as catalysts (Figure 8).

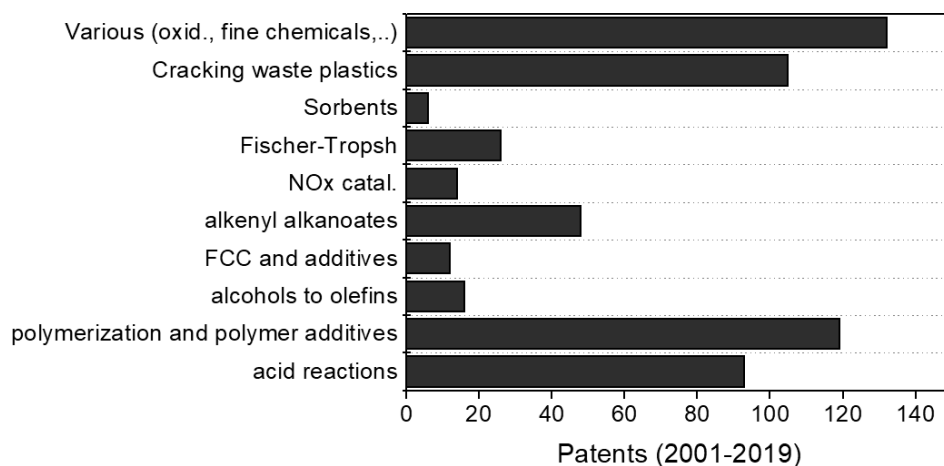


Figure 8. Patents (from 2001 to 2019) related to the uses of natural clays in the catalysis.

Despite the high abundance on the Earth's crust, the naturally occurring clay minerals have significant disadvantages compared to their synthetic counterparts, such as *i*) non-controllable variability of the chemical compositional (they are, in fact, a physical mixture of variable amounts of iron, magnesium, alkali metals, alkaline earths and other cations), *ii*) variable colour and textural properties (*i.e.* specific surface area, pore volume, pore distribution and particle aggregation), *iii*) presence of crystallographic defects and, depending on the genesis process and the area of origin, *iv*) different kinds of impurities and contaminants present in the deposits (*i.e.* grit and amorphous clays, carbonates, other silicates, organic material and various oxides), which require long, expensive and complex procedure for their elimination (Figure 9). All these disadvantages limit the use of natural clays in those systems where the purity and control of the properties are fundamental.

The preparation of clays through synthetic procedure, on the other hand, allows to obtain pure phyllosilicate phases and to control the final properties from a physico-chemical point of view, leading to final solids with *i*) more controlled chemical composition, morphology, shape and particle size, *ii*) high aspect ratio, *iii*) controlled

surface chemistry and *iv*) well-defined ratio of the constituent elements (*i.e.* isomorphous substitutions content) and type of ions introduced in the framework or into the interlamellar space.³⁸ The knowledges acquired from the synthetic methodologies applied over the years has allowed to have a more detailed understanding of the formation of these minerals, especially regarding the modification of their composition and properties (Figure 9).

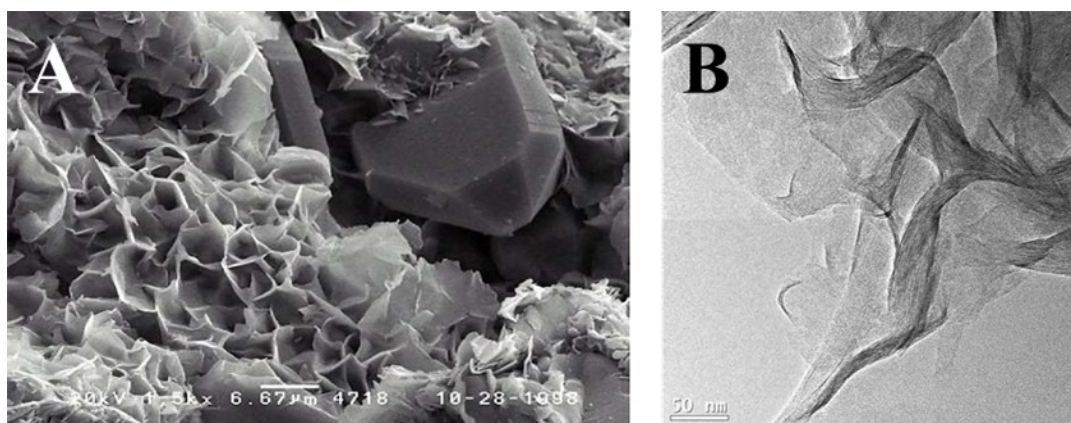


Figure 9. Examples of electron microscope micrographs of natural³⁸ (A) and synthetic (B) clays.

The synthetic phyllosilicates, in particular a specific type of clay of the family of smectites named **saponite**,⁵⁰ have been proved to be incredible versatile materials, and through the chemical functionalization and modulation of their structure at three different domain levels (morphology and particle size, interlayer/interlamellar space and inorganic lattice) it is possible to obtain several interesting novel advanced layered materials. Indeed, thanks to their greater homogeneity and well-defined physico-chemical properties, the synthetic saponite clays have obtained greater interest compared to natural solids, both in academic and industrial fields, particularly in the optimization of materials for catalytic, industrial, optoelectronic, biological and nanotechnological applications.^{28-31,50}

1.3 Synthetic clays: Saponite

Saponite clays¹ are a class of hydrated aluminosilicates of the family of phyllosilicate smectites, essentially made of aluminium, magnesium, silicon and oxygen elements. The general formula of the saponite is:



where M is the exchange cation with n charge residing in the interlayer, x is the aluminium fraction present in the structure and m is the total number of water molecules.¹⁸

The saponite has a 2:1 T-O-T tri-octahedral structure that repeats along the xy plane. The two T -sheets are mainly constituted by silicon in tetrahedral coordination with oxygen, while the O -sheet is formed by magnesium in octahedral coordination with oxygen and hydroxyls. Each tetrahedron has a brute formula $[\text{SiO}_4]^{-4}$ and connects with the other three tetrahedra through the three coplanar vertices in which the oxygen is positioned; in the planar plane the tetrahedrons are arranged forming a hexagonal ring. The fourth oxygen, called apical because it is placed perpendicularly to the plane of the other three oxygens, connects with the overlying layer, the octahedral one. The O -sheet consists of octahedrons with vertices occupied by four hydroxyls, two oxygens and a central Mg^{2+} ion. The octahedrons are joined along an edge and rest on the same plane with a triangular face. On this plane, three octahedra are arranged to form a face-centred hexagon, with six hydroxyls at the vertices and a hydroxyl at the centre of the ring. The O -sheet is connected to the T -sheet by covalent bonds between the apical oxygens of T -layer and the hydroxyls in the O -layer, both arranged in hexagon structures. A second T -sheet binds to the O -sheet on the opposite side and in a parallel manner to the first, forming the final T - O - T lamellar structure along the z -axis (Figure 10).

The isomorphic substitution of Si with Al ($\text{Al} \rightarrow \text{Si}$) in the T -sheet generates a charge imbalance in the inorganic structure, due to a non-compensation of the

negative charge located on the oxygen of the tetrahedron (silicon is Si^{4+} while aluminium is Al^{3+}).

The total negative charge can vary between 0.2-0.6 charge units per structural formula and is compensated by positive ions called exchange cations. Given the tendency of the lamella to pack, these cations (*i.e.* Na^+ , K^+ , Ca^{2+} ...) are in the interlayer space between the lamella. This region presents a general thickness that can vary between 0.10-10 nm depending on the charge of the lamella and chemical species present in it. Each lamella is linked to the others by weak ionic bonds, since the charges are distributed along the entire lamella.

The *O*-sheet, on the other hand, normally does not possess vicariances, even though aluminium can replace magnesium thus generating a charge imbalance (as in montmorillonite clay). The characteristics of the *O*-sheet influences the structural parameters, as the parameter *b* of the crystalline cell.

The elemental cell of saponite belongs to the monoclinic system, where the cell parameters are $a \sim 0.53$ nm, $b \sim 0.92$ nm e $c \sim 1.5$ nm, while the angle β is between $97-100^\circ$.¹⁹ The value of *b* for saponite is typical of disorderly-packed lamellar systems.²⁰ The *T* and *O* layers extend along the *xy* plane and are described by the cell parameters *a*, *b* and *c*₀ (lamella thickness). The *T-O-T* sheets are stacked along the *z* axis with a repetition period *c*: this is given by the sum of the thicknesses of the three layers ($c_0 \sim 0.9$ nm)²¹ and of the interlamellar space. The values of *a* and *b* are almost constant because they are related to the tri-octahedral nature of the structure; the size of the octahedron varies according to the ionic radius of the coordinated element. The parameter that varies considerably is the repetition period *c*, which is dependent on *i*) the number of layers and on *ii*) the presence of cations and water molecules in the interlamellar space (Figure 11).

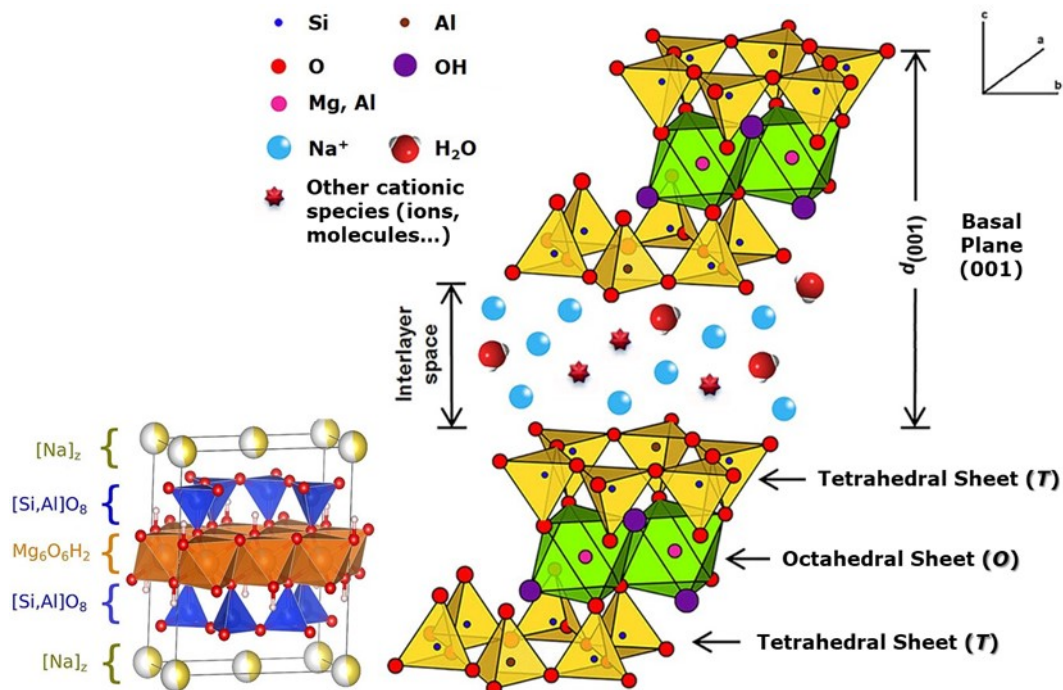
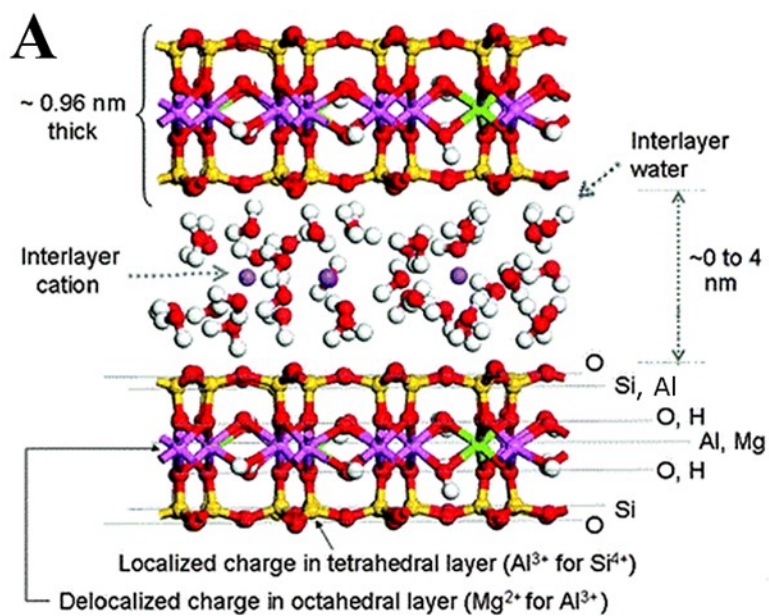


Figure 10. Schematic views of the structure of saponite.



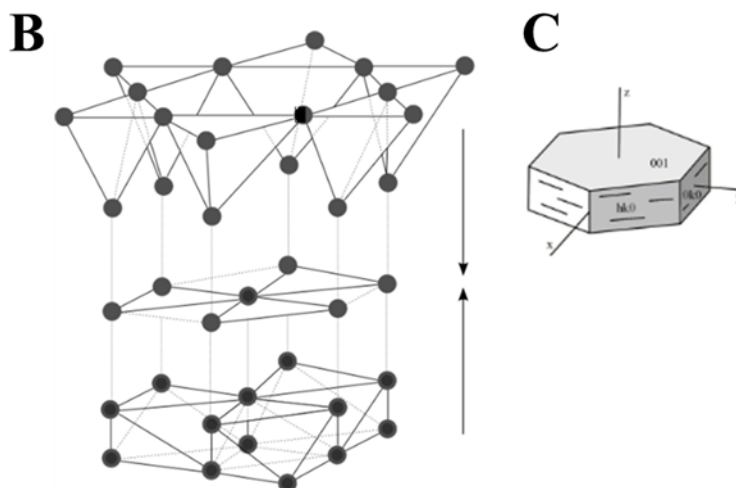


Figure 11. A) Scheme of the saponite lamella with estimated thickness of *T-O-T* structure and interlayer space. B) Illustration of the contact plane between *T* and *O*-sheets of the lamella. C) Crystallographic reflexes associated with saponite lamella.

Saponite clays (and smectites in general) show different levels of spatial organization (“multi-scale structure”). The *T-O-T* basic unit repeats laterally in the *xy* plane up to a hundred of nanometres, thus forming the primary superstructure called lamella. The lamellae are joined by ionic bonds through the exchange cations in the interlayer space, and tend to be stacked on top of each other. The lack of spatial organization of lamellae is called *turbostratic stacking*: the absence of a constraint on the rotation of one layer with respect to another causes the lamellae to be arranged randomly, assuming different orientations with respect to the under- and overlying sheets (*open house of cards* structure) (Figure 12).²⁰

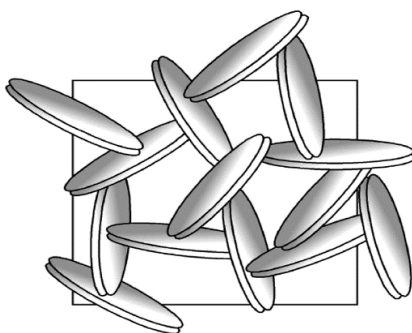


Figure 12. *Open house of cards* spatial organisation of saponite lamellae.

The physico-chemical properties of saponites are attributed to *i*) morphology and chemical composition of lamellae, *ii*) electrostatic charge of lamellae and *iii*) high thermal stability of the structure. Together, these features confer interesting characteristics to these kinds of clays, especially in terms of high chemical versatility.⁵⁰

The lamellar structure allows to include chemical species with different dimensions (charge to radius ratio) and properties. Saponites lamellae can undergo swelling or can be broken down into single units, thus obtaining greater interlamellar space. Natural saponites have specific surface areas between 30-160 m²/g, while those of synthetic origin present greater values, in the order of 300-400 m²/g.²² Several procedures can be adopted to modulate the surface properties such as the specific area and acidity of saponites (*i.e.* treatment with low concentrated acid solutions to increase the surface acidity).^{16,23}

The electrostatic charge of lamellae allows the introduction of positively charged ions and molecules (*i.e.* inorganic cations, organic species, polymers...) in the interlamellar region (intercalation process). The total amount of intercalated cations defined the cation-exchange capacity (CEC) of the saponite, expressed in milliequivalents (meq) of cations per 100 g of clay material. The CEC is related to the amount of Al → Si substitutions that generate charge imbalances, offset by exchange cations. These substitutions are also responsible for the surface acidity of saponite, in terms of concentration and strength. The acid sites possess variable nature and acidic strength. When the compensation of the negative charge of the structure is carried out by a proton, the site generally has a Brønsted-type acidity: the acid sites are formed by labile protons that are present in the structure in form of hydroxyls bound to tetrahedral aluminium (Figure 13). Theoretically, the number of Brønsted acid sites is equal to the number of aluminium present in the *T*-sheet but, in reality, not all exchange cations can be replaced by protons, so the value represents an approximation.²⁴ Furthermore, the same structural hydroxyls can be considered as Brønsted-type acids. Besides this, another kind of acid sites (Lewis-type) can be

generated by extra-framework aluminium, which can be present in defective zones of the structure, and by exchange cations positioned near the tetrahedral aluminium. The presence of bivalent cations, such as structural magnesium placed in defective sites, can also act as a Lewis acid site.²⁵

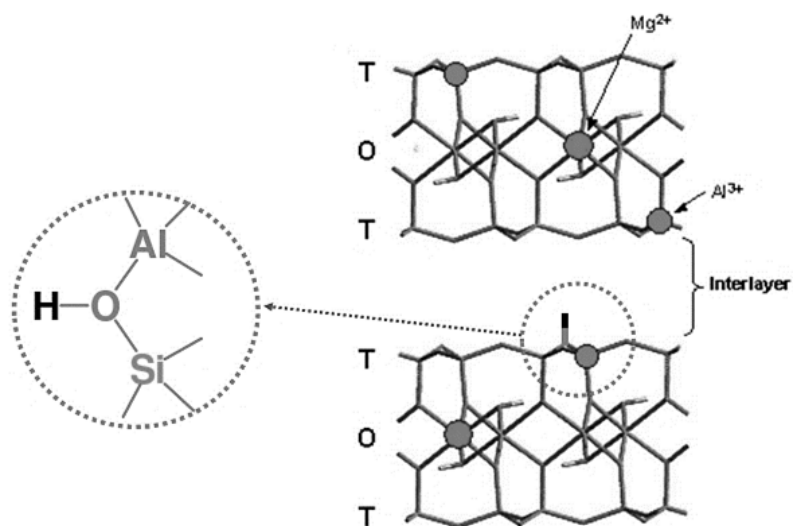


Figure 13. Representation of a Brønsted acid site (Si-O(H)-Al) in the saponite.

The high thermal stability of saponite is another important feature, in addition to the surface acidity, which has allowed its use in several scientific fields, especially for catalysis.²⁶ Saponite does not undergo significant structural changes up to *ca.* 550 °C: at lower temperatures there is the gradual loss of water adsorbed on the surface and located in the interlamellar layer, while at higher temperatures the dehydroxylation of the octahedral layer and the collapse of the structure begins. Vogel *et al.*²⁷ have correlated the thermal stability of saponite with the nature of the octahedral cation. Indeed, the thermal stability of the clay increases in the sequence Zn²⁺ (400 °C) → Co²⁺ (600 °C) → Mg²⁺ (700 °C) → Ni²⁺ (800 °C). The size of the octahedral cation causes a rotation of the tetrahedral layer to adapt to the extensions of the two layers. Relatively small cations, such as Ni²⁺, cause a rotation of about 9° and an increase in the ionic radius minimizes the rotation angle. Vogel *et al.*²⁷ has shown that an octahedral cation with a relatively small ionic radius, which is

associated with a high rotation angle for the *T*-sheet, favours the thermal stability of saponite clays.

1.4 Synthetic methods for the preparation of saponites

Different synthetic procedures employed for the preparation of saponites have been explored in the literature in the last two decades. The synthetic methods developed over the years tried to simulate the natural processes (*genesis*) involved in the formation of the clay minerals, as a result of the gradual chemical weathering of silicates rocks and by some natural-occurring hydrothermal processes over long periods of time.¹ The synthetic procedures have been optimized in order to obtain clay materials, with more defined physico-chemical properties than natural counterparts, in shorter time by modulating *ad-hoc* several parameters such as temperature, pressure and composition of the synthesis gel.^{1,50}

The synthetic saponites have been synthesized through different methodologies: *i*) “classical” hydrothermal conditions, performed at relatively high temperatures and in sophisticated apparatus (autoclave); *ii*) microwave-assisted hydrothermal procedures, carried out at lower temperatures and reduced preparation times compared to classical methods; *iii*) Sol-Gel procedures, executed under varying mild experimental conditions (generally at low temperature and ambient pressure); *iv*) other processes (*i.e.* conversion from starting natural clays at mild temperature, with clays obtained through microbe-induced mechanism, and by using the sonication process to speed up the synthesis) (Figure 14).^{17,19,26,32,50}

Authors	Starting materials	Conditions	Products
Farmer et al. (1991, 1994)	Si(O ₂ H ₂) ₄ , AlCl ₃ , FeCl ₂ , CaCO ₃ , hydrazine	296 K, 12 weeks; 362 K, 8 weeks	Feldspathoids, nontronite, saponite
Klopprogge et al. (1993a,b, 1994a)	NH ₄ OH, amorphous silica, aluminiumtriisopropylate, and magnesium-acetate-tetrahydrate	Autogenous water pressure, 398–553 K, 72 h	NH ₄ -saponite
Klopprogge et al. (1994b)	Amorphous silica, aluminiumtriisopropylate, and magnesium-acetate-tetrahydrate containing Na ⁺ , K ⁺ , Rb ⁺ , Ca ²⁺ , Ba ²⁺ , or Ce ⁴⁺ as interlayer cations	Autogenous water pressure, 473 K, 72 h	Mg-saponite
Vogels et al. (1997)	SiO ₂ , altriiso-propoxide, Mg(NO ₃) ₂ , Mg(OH) ₂ , Al(NO ₃) ₃ , NH ₄ OH, NH ₄ F	Autogenous water pressure, 473 K, 16 h	NH ₄ -saponite
Kawi and Yao (1999)	NaOH, NaHCO ₃ , Na silicate, AlCl ₃ ·6H ₂ O, MgCl ₂ ·6H ₂ O and NiCl ₂ ·6H ₂ O	558 K, 48 h	[Mg _x Ni _y]-saponite
Vogels et al. (2005)	Na ₂ SiO ₃ , GaCl ₃ , NaOH, aerosil, borax, Mg(NO ₃) ₂ ·6H ₂ O, Zn(NO ₃) ₂ ·4H ₂ O, NaNO ₃	0.1 MPa, 363 K, 20 h	B-saponite, Ga-saponite
Yao et al. (2005)	NaOH, NaHCO ₃ , Na ₂ SiO ₃ , AlCl ₃ ·6H ₂ O, MgCl ₂ ·6H ₂ O	0.1–3.5 MPa, microwave radiation for 2 h, 448 K, 72 h	Saponite
Higashi et al. (2007)	NaOH/LiOH, silicic acid, MnCO ₃ , Al(NO ₃) ₃ ·9H ₂ O		Mn-saponite, Mn-hectorite, Mn-stevensite
Bisio et al. (2008)	Amorphous silica, aluminium isopropoxide, NaOH, magnesium acetate tetrahydrate	513 K, pH 4–5, 72 h	Saponite
Vicente et al. (2010)	Mg(CH ₃ COO) ₂ ·4H ₂ O, Al(CH ₃) ₂ , NH ₃ , NH ₄ F	393 K, pH 7, microwave radiation for 6 h	Saponite
Xue and Pinnavaia (2010)	Bis(triethoxysilyl)methane (BTESM), water glass (27 wt.% silica, 14 wt.% NaOH), Al(NO ₃) ₃ ·9H ₂ O, Mg(NO ₃) ₂ ·6H ₂ O, NaOH, urea	363 K, 24 h	Organic-inorganic hybrid saponite

Figure 14. Some of the experimental conditions adopted for the synthesis of saponites.

The **hydrothermal methods** are the most and well explored procedures adopted for the preparation of synthetic saponites, because the basic formation mechanism is like the one exploited in the nature. The typical procedures require temperature ranging from 150 to 450 °C, synthesis gel with acid or basic pH (range 1-10) and a gel aging from 1 h to several days/months. The gel phases can also contain different sources of the main composing elements (*i.e.* amorphous silica, TEOS, Al₂O₃, Al(OH)₃, NaAlO₃, NaOH, Mg(CH₃COO)₂, H₂O...), with or without so-called “mineralizing agents” (F⁻, OH⁻...). The process typically exploited the autogenous pressure of water up to 1500 bars which lead to the formation of the clay crystal structure. This process requires dedicated and relatively expensive equipment (autoclave systems), and this could be a limit to the use of saponites at industrial level. However, the hydrothermal conditions have the potential to be allow the scale-up of the synthesis, thus producing high amount of desired clays. Bisio *et al.*³⁴, together with Klopprogge *et al.*^{22,35} showed that the dilution of the synthesis gel led to substantial modification of the surface and structural properties of the saponite clay. In this way, it is possible to easily modify the morphological and structural features of saponites directly in the synthesis phase, obtaining final materials with particle size varying from nano- to micrometres and different cation-exchange

capacity (Figure 15).^{28-31,24,44} Another important aspect in the synthesis is the inclusion of the aluminium ion: the poor control of tetrahedral substitutions by aluminium in the synthesis gel can lead to saponites with magnesium and aluminium ions in the interlamellar layer, as reported by Kloprogge *et al.*³⁶ Kawi *et al.*³⁷ prepared saponites through hydrothermal methods by varying the content of magnesium and nickel in the octahedral layer. Kloprogge *et al.*²² synthesized saponite with NH_4^+ as an exchange cation, under mild temperature. Vogel *et al.*³³ shown that the formation of NH_4^+ -saponite is favoured both by a high $\text{NH}_4^+/\text{Al}^{3+}$ molar ratio and by the presence of fluorine ions.

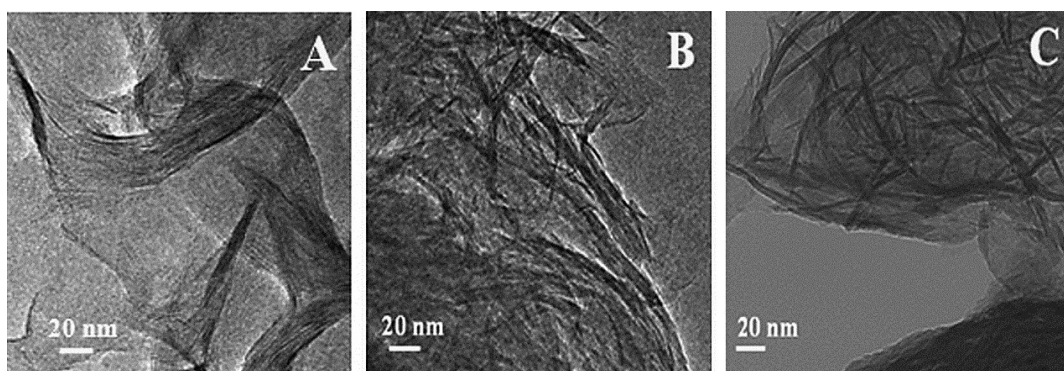


Figure 15. HRTEM micrographs of saponites prepared with different $\text{H}_2\text{O}/\text{Si}$ molar ratio: Na-SAP-20 (A), Na-SAP-110 (B) and Na-SAP-150 (C).³⁴

The hydrothermal process has been also modified to be like **Sol-Gel** methods, by exploiting lower temperature and pressure, in order to reduce the preparation times and the associated costs. A synthetic procedure to obtain different isomorphous substitutions (*i.e.* B^{3+} and Ga^{3+}) at lower temperature (*ca.* 100 °C) and pressures (0.1 MPa) compared to hydrothermal route was developed by Vogel *et al.*²⁷ Sol-Gel conditions have also been used by Pinnavaia *et al.*³⁸ and Prikhod'ko *et al.*³⁹ obtaining saponites in 24-72 h and 90 °C. Higashi *et al.*⁴⁰ synthesized Zn-smectites and Mn-saponites from an unconventional mixture of reagents.

Another route explored with the aim to obtain synthetic saponites in relatively shorter times is the **microwave-assisted hydrothermal methodology**, well studied

by Yao *et al.*,⁴² Vogel *et al.*³³ and Vincente *et al.*⁴³ These procedures, carried out in microwave synthesis reactor, are influenced by several parameters such as heating time, presence of fluorine ions and the initial pH of the synthesis gel. Vincente *et al.*⁴³, for example, managed to synthesize several saponites with higher crystallinity and CEC values than those prepared with the conventional hydrothermal route, under mild conditions (90-120 °C, neutral pH and in 6-12 h).

Taking advantage of the high chemical versatility of the synthetic saponites, the materials can be further modified by introduction of functional guest molecules into the structure. In this manner, porosity, acidity and other physical and chemical properties can be easily tuned. Several types of saponite-based hybrids or composites materials have been successfully prepared by the intercalation in the interlamellar region of organic and inorganic positively-charged ions, molecules and polymers.^{1,50} Covalent grafting of a moiety of organic molecules onto the surface of saponite clays also proved to be feasible. For examples, Xue and Pinnavaia⁴¹ developed a method to prepare an organic-inorganic (hybrid) saponite in which the organic moieties are covalently linked to the tetrahedral layer, maintaining at the same time the 2:1 *T-O-T* lamellar structure.

In conclusion, the ability to easily modulate the final physico-chemical properties of synthesized saponite clays through the chemical functionalization and modulation of their morphology and particle size, interlayer space and inorganic lattice, responds to the need to obtain new advanced layered materials suitable for several applications spanning from nanotechnology to biomedical fields.⁵⁰

1.5 Applications of synthetic saponites

In the last decades, synthetic smectites clays, in particular saponites, have attracted growing interest in the scientific community and they are considered for a large number of applications especially in relation to their peculiar chemical-physical properties (*i.e.* high specific surface area and acidity, controlled chemical

compositions and high thermal stability),^{30,31} low costs and high chemical versatility, thus leading to novel functionalized materials with extremely fine-tuned properties.

The classic uses of clays range from agriculture to surface coatings, for environmental purposes (*i.e.* adsorbents, ion exchangers, water decontamination...),⁴⁹ removal and recovery of metals and hazardous compounds and for the photocatalytic decomposition of organic molecules. More modern applications range from catalysis (*i.e.* as heterogeneous catalysts for preparation of organo-modified clays,⁴⁴ as nanoadditives and for polymeric nanocomposites with improved mechanical properties), optoelectronics, in pharmaceutical industry (*i.e.* excipients, drugs delivery, sun cream formulations...),²⁸ for chemical sensors, for high porosity siliceous systems and in the field of nanocomposite polymers (Figure 16).⁵⁰

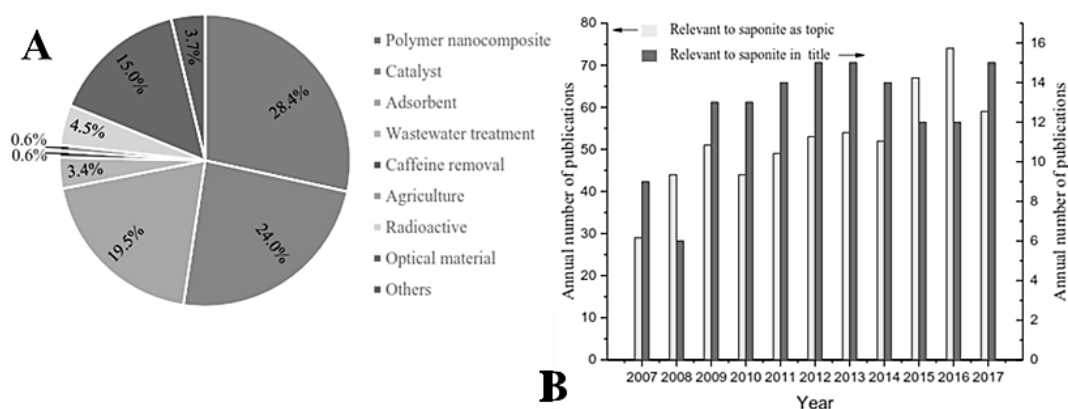


Figure 16. Uses and applications of saponite-based materials (A) and annual number of peer-reviewed papers published (B) relevant to saponite (2007-2017).⁵⁰

Great attention has been paid to the development of hybrid photophysical luminescent materials based on synthetic clays. They present several advantages: *i*) easily modulation of fluorescent/dye compounds loading, which represents a critical parameter in order to reduce the formation of harmful aggregates for optical performance; *ii*) protection of the molecules hosted in the interlamellar space, limiting the diffusion of oxygen and thus improving their thermal and chemical stability compared to the pure compound. Clay materials have been also used as

active layers for the development of novel electroluminescent light emitting diodes (LEDs) devices (Figure 17A).^{45,46}

Synthetic saponites have been successfully exploited as additives for the stabilization of quasi-solid electrolytes employ in the organic-based photovoltaic devices such as dye-sensitized solar cells (DSSCs), obtaining interesting results in terms of sunlight conversion efficiency and stability.⁴⁷

Acid smectites are often used as catalysts for dimerization reactions and hydrocarbon polymerization, esterification, (de)hydration, disproportionation, hydrolysis, oxidation, acylation and alkylation processes. The use of clay materials made these processes environmentally friendly, because they can be performed in mild conditions. These solids present a high surface area and acidity, and for this reason the acid activation has been considered as an alternative and competitive method for the preparation of porous silicas with a high specific surface area.²⁸

Synthetic saponites have been also employed for environmental remediation, particularly for the decontamination of hazardous materials as chemical warfare agents (CWAs). The development of adequate techniques for the destruction of CWAs with environmentally safe methods is attracting more and more attention. While conventional abatement methods have a strong environmental impact and are associated with high energy consumption and disposal costs, lamellar materials are considered cheap and reliable alternative. Advantages such as high strength, excellent chemical versatility and very low production costs make these catalysts really promising for the oxidative degradation of CWAs. In the last years, Carniato *et al.*⁴⁸ have developed heterogeneous niobium-loaded saponite catalysts capable of triggering selective oxidation reactions and transforming highly toxic CWAs into nonnoxious products with reduced environmental impact (Figure 17B).

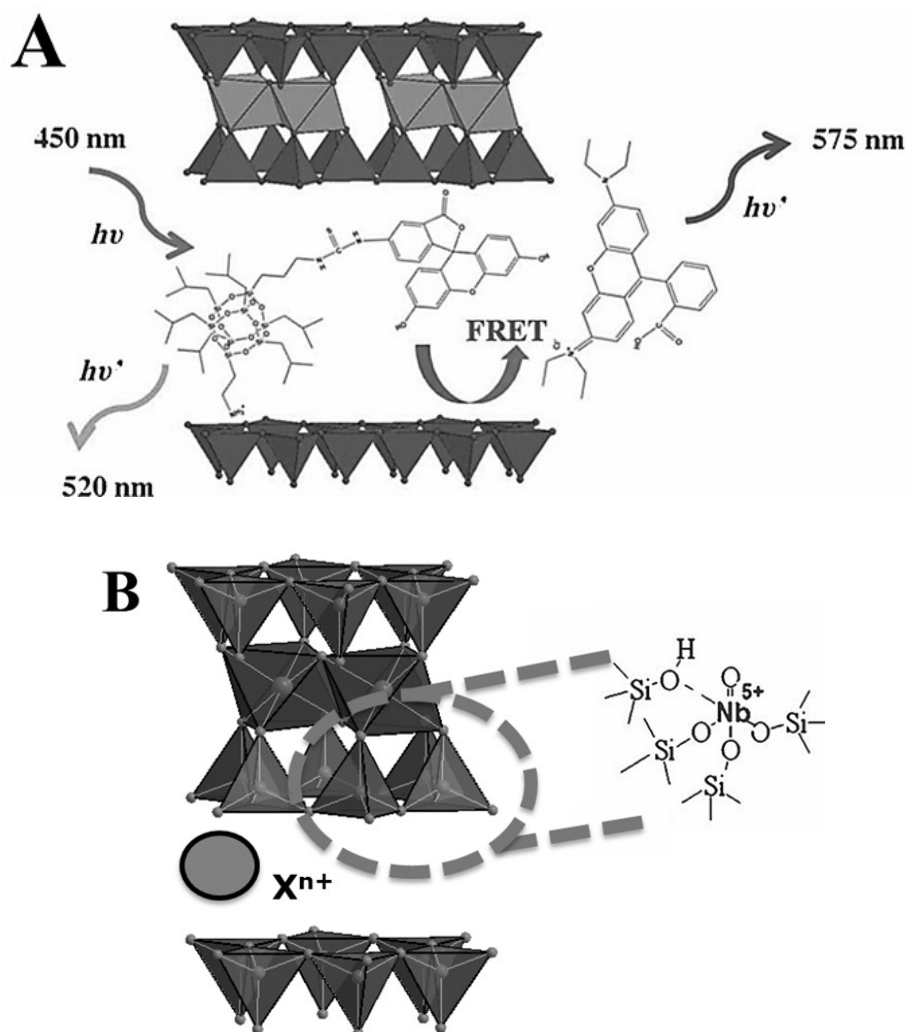


Figure 17. A) Schematic representation of the Förster resonance energy transfer (FRET) process inside an optical-functionalized saponite clays.^{46,47} B) Schematic view of the structure of a niobium-containing saponite used for the decontamination of CWAs.⁴⁸

Thanks to their excellent chemical versatility, it is expected that the development of advanced layered materials based on the combination of synthetic saponites and different compounds (*i.e.* metal complexes, ions, organic molecules...) will continue to grow in the future.⁵⁰

1.6 Notes and References

- 1 F. Bergaya, B. K. G. Theng and G. Lagaly, *Handbook of Clay Science (Developments in Clay Science, 1)*, 2006, Elsevier Science, D.A.C. Manning, **ISBN: 9780080441832**; B) C. Tournassat, Carl I. Steefel, Ian C. Bourg and Faqza Bergaya, *Handbook of Clay Science (Developments in Clay Science, 6)*, 2015, Elsevier Science, D.A.C. Manning, **ISBN: 9780081000274**.
- 2 A) A. Vaccari, *Catalyst Today*, 1998, **41**, 53-71; B) M. Carretero and G. Lagaly, *Appl. Clay Sci.*, 2007, **15**, 61-97.
- 3 J. Konta, *Appl. Clay Sci.*, 1995, **10**, 275-335.
- 4 H. Murray, *Appl. Clay Sci.*, 2000, **17**, 207-221.
- 5 Z. Ding, J. Klopogge, R. Frost, G. Lu and H. Zhu, *J. Porous Mat.*, 2001, **8**, 273-293.
- 6 S. Babel and T. Kurniawan, *J. Hazard Mat.*, 2003, **97**, 219-243.
- 7 J.-H. Choy, S.-J. Choi, J.-M. Oh and T. Park, *Appl. Clay Sci.*, 2007, **36**, 122-132.
- 8 C. Zhou, D. Tong, M. Bao, Z. Du, Z. Ge and X. Li, *Catalysis*, 2006, **6**.
- 9 C. Zhou, X. Li, Z. Ge, Q. Li and D. Tong, *Catal. Today*, 2004, **93**, 607-613.
- 10 S. Yariv and H. Cross, *Organo-clay complexes and interactions*, New York: Marcel Dekker Inc., 2002, **ISBN: 0824705866**.
- 11 D. Tong, H. Xia and C. Zhou, *Journal of Catalysis*, 2009, **17**.
- 12 S. Adoor, M. Sairam, L. Manjeshwar, K. Raju and T. Aminabhavi, *J. Membr. Sci.*, 2006, **285**, 182.
- 13 Y. Kim, J. Lee, C. Rhee, H. Kim and H. Chang, *J. Power Sources*, 2006, **162**, 180-185.
- 14 R. Lin, B. Chen, G. Chen, J. Wu, H. Chiu and S. Suen, *J. Membr. Sci.*, 2009, **326**, 117-129.
- 15 A) J. Villaluenga, M. Khayet, M. Lopez-Manchado, J. Valentin, B. Seoane and J. Mengual, *European Polymer Journal*, 2007, **3**, 1132-1175; B) T. T. Selvan and S. C. Prasanna, *International Journal of Mechanical and Production Engineering Research and Development*, 2018.
- 16 T. L. Bergaya, *Handbook of Clay Science*, 2006, Elsevier, **ISBN: 978-0080993645**.
- 17 J. Klopogge, S. Komarneni and J. E. Amonette, *Clay Miner.*, 1999, **47**, 529-554.
- 18 G. Brindley and G. Brown, *Mineralogical Society*, 1980.
- 19 V. C. Farmer, W. McHardy, F. Elsass and M. Robert, *Clay Miner.*, 1994, **42**, 180-186.
- 20 H. Suquet, J. T. Iiyama and H. Kodama, *Clay Miner.*, 1977, **25**, 231-242.
- 21 O. Prieto, M. Vicente and M. Banarez-Munoz, *J. Porous Mat.*, 1999, **6**, 335-344.
- 22 J. Klopogge, J. Breukelaar and J. B. Jansen, *Clay Miner.*, 1993, **41**, 423-430.
- 23 S. Branner, E. Emmett and E. Teller, *J. Am. Chem. Soc.*, 1938, **60**, 309.

- 24 M. Zanjanchi and M. Mohammadi, *Journal of Sciences Islamic: Republic of Iran*, 2001, **7**.
- 25 J. Lercher, C. Gründling and G. Eder-Mirth, *Catal. Today*, 1996, **27**, 353-376.
- 26 A) D. Zhang, C. Zhou, C. Lin, D. Tong and W. Yu, *Appl. Clay Sci.*, 2010, **50**, 1-11; B) S.M. Lee and D. Tiwari, *Appl. Clay Sci.*, 2012, **59**, 84-102; C) M. Jaber, S. Komarneni and C.-H. Zhou, *Handbook of Clay Science (Chapter 7.2 - Synthesis of Clay Minerals)*, 2013, **5**, 223-241.
- 27 A) R. Vogels, J. Klopogge and J. Geus, *Micropor. Mesopor. Mat.*, 2005, **77**, 159-165; B) R. Vogels, J. Klopogge and J. Geus, *Am. Mineral.*, 2005, **90**, 931-944.
- 28 C. Bisio, G. Gatti, E. Boccaleri, L. Marchese, L. Bertinetti and S. Coluccia, *Langmuir*, 2008, **24**, 2808-2819.
- 29 C. Bisio, G. Gatti, E. Boccaleri, L. Marchese, G.B. Superti, H.O. Pastore and M. Thommes, *Micropor. Mesopor. Mat.*, 2008, **107**, 90-101.
- 30 F. Carniato, C. Bisio, G. Gatti, S. Roncoroni, S. Recchia and L. Marchese, *Catal. Lett.*, 2009, **131**, 42-48.
- 31 D. Costenaro, G. Gatti, F. Carniato, G. Paul, C. Bisio and L. Marchese, *Micropor. Mesopor. Mat.*, 2012, **162**, 159-167.
- 32 P. Andrieux and S. Petit, *Appl. Clay Sci.*, 2010, **48**, 5-17.
- 33 R. Vogels, J. Breukelaar, J. Klopogge, J. Jansen and J. Geus, *Clay Min.*, 1997, **45**, 1-7.
- 34 C. Bisio, G. Gatti, E. Boccaleri, G. Superti, H. Pastore and M. Thommes, *Micropor. Mesopor. Mat.*, 2008, **107**, 90-101.
- 35 J. Klopogge, L. Hickey and R. Frost, *Journal of Materials Science Letters*, 1999, **18**, 1921-1923.
- 36 J. Klopogge, J. Breukelaar, A. Wilson, J. Geus and J. Jansen, *Clay Miner.*, 1994, **42**, 18-22.
- 37 S. Kawi and Z. Yao, *Micropor. Mesopor. Mat.*, 1999, **33**, 49-59.
- 38 T. Pinnavaia and S. Xue, *Micropor. Mesopor. Mat.*, 2008, **107**, 134-140.
- 39 R. V. Prikhod'ko, M. V. Sychev, I. M. Astrelin, K. Erdmann, E. J. M. Hensen and R. A. van Santen, *Inorganic Synthesis and Industrial Inorganic Chemistry*, 2003, **76**, 700-705.
- 40 A) S. Higashi, H. Miki and S. Komarneni, *Appl. Clay Sci.*, 2007, **38**, 104-112; B) S. Higashi, K. Miki and S. Komarneni, *Clay Miner.*, 2002, **50**, 299-305.
- 41 S. Xue and T. Pinnavaia, *Appl. Clay Sci.*, 2010, **48**, 60-66.
- 42 M. Yao, Z. Liu, K. Wang, M. Zhu and H. Sun, *Spectrosc. Spectral Anal.*, 2005, **25**, 870-873.
- 43 I. Vicente, P. Salagre, Y. Cesteros, F. Medina and J. Sueiras, *Appl. Clay Sci.*, 2010, **48**, 26-31.
- 44 C. Bisio, F. Carniato, G. Paul, G. Gatti, E. Boccaleri and L. Marchese, *Langmuir*, 2011, **27**, 7250-7257.

- 45** F. Olivero, F. Carniato, C. Bisio and L. Marchese, *J. Mater. Chem.*, 2012, **22**, 25254-25261.
- 46** F. Olivero, F. Carniato, C. Bisio and L. Marchese, *Chem. Asian J.*, 2014, **9**, 158-165.
- 47** D. Costenaro, C. Bisio, F. Carniato, G. Gatti, F. Oswald, T. B. Meyer and L. Marchese, *Solar Energy Materials & Solar Cells*, 2013, **117**, 9-14.
- 48** F. Carniato, C. Bisio, R. Psaro, L. Marchese and M. Guidotti, *Angew. Chem. Int. Ed.*, 2014, **53**, 10095-10098.
- 49** L. M. Whittaker, L. N. Lammers, S. Carrero, B. Gilbert and J. F. Banfield, *PNAS*, 2019, **116**, 22052-22057.
- 50** C. H. Zhou, Q. Zhou, Q. Q. Wu, S. Petit, X. C. Jiang, S. T. Xia, C. S. Li and Q. H. Yu, *Appl. Clay Sci.*, 2019, **168**, 136-154.

2

Outline

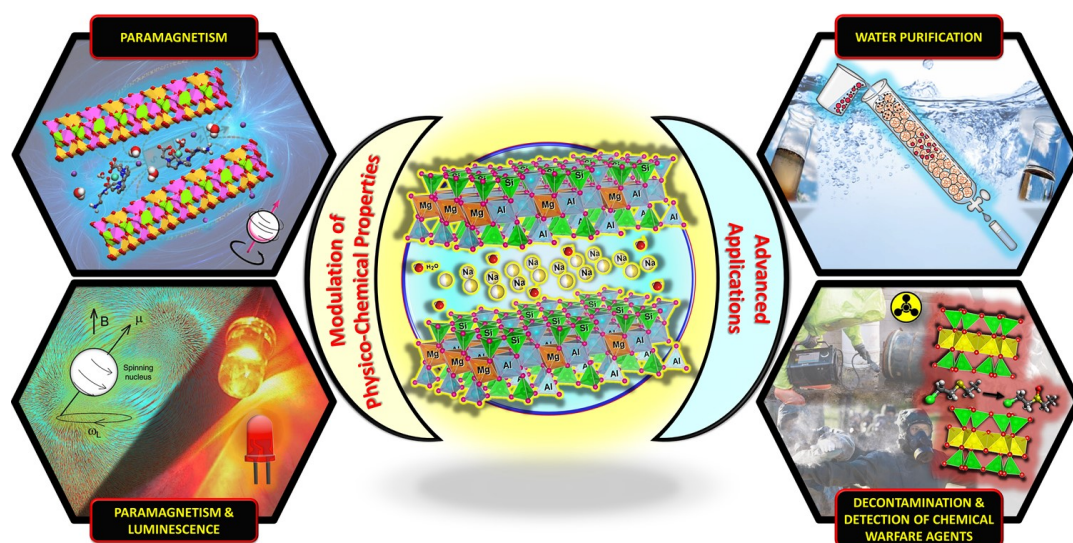


Figure 1.

The Ph.D. Thesis' work is related to the development of novel nanostructured multifunctional layered materials based on synthetic saponite clays containing lanthanides (gadolinium and europium) and catalytic transition metals (niobium) centres. These novel materials were designed with the idea of being applied in different scientific fields, from environmental to catalysis and in the nanotechnology. Proper modifications of the characteristic features of the saponite at three different domain levels (morphology and particle size, composition of the interlayer space and inorganic framework), made it possible to easily integrate in the clay the metal

elements selected, in form of complexes or ions, leading to the preparation of interesting functionalized layered solids (Figure 1). The properties of these novel lamellar materials were exploited in different advanced applications (Figure 1). The samples were prepared by applying or modifying existing hydrothermal protocols or by defining brand-new synthetic procedures. The materials were deeply characterized by means of a multi-technique approach, aiming to determine their final physico-chemical properties, especially considering their future applications.

In the first part the research work, two synthetic Na⁺-exchanged saponite clays were employed as cheap and efficient solid sorbents for the extraction of lanthanides with different ionic radius (La³⁺, Gd³⁺ and Lu³⁺) from aqueous solutions, exploiting an ion-exchange process. The saponite samples were synthesized by simple hydrothermal approach and they were characterized by different particle size and cation exchange capacity. A relationship between the uptake capability and the physico-chemical properties of the saponite clays was observed. The materials showed good sorption capacity with an effective extraction of the lanthanides after few hours in pure water and in simulated freshwater/seawater solutions. The solids were tested in the presence of an equimolar mixture of lanthanum, gadolinium and lutetium and a marked selectivity for the latter, which presents the lowest ionic radius, was observed compared to the other ions.

Then, three paramagnetic cationic Gd³⁺-chelates and one diamagnetic with Y³⁺, with different molecular geometries and properties based on three macrocycle derivatives, were intercalated in the interlayer space of a nanosized saponite clay by cation-exchange process. The materials were designed in order to increase the knowledge on the chemistry of the interlayer space of the clays (*i.e.* accessibility of exchanges sites...) and for potential applications in diagnostic (MRI) and theranostics, as catch-and-release systems for the purification of surface waters and for the study of the diffusion phenomena of liquids inside layered systems.

Structural, morphological and thermal analyses indicated that complexes are firmly confined in the interlamellar region of the hybrid materials. ^1H -NMR relaxometric and solid-state NMR investigations provided interesting insights on the chemical nature and accessibility of exchange sites to water molecules, on the molecular dynamics of water inside the saponite gallery and on the molecular organization of the intercalated metal chelates. The confined complexes are defined by an anisotropic and markedly slowed molecular motion that increase the longitudinal relaxivity at high magnetic fields. The effective exchange rate of the water bound/interacting to gadolinium slows down, suggesting a decrease of water diffusion along the interlayer due to strong host-guest interactions between the complexes/water and the layered structure. The chelates are also positioned near the tetrahedral layers of saponite, with a parallel organization to the lamellae. This behaviour explains the remarkable stability observed in aqueous media with varying complexity (*i.e.* human serum...).

Subsequently, in order to overcome the limitations observed for the development of previous intercalated clays (associated to the long preparation times and relatively high costs of the complexes), two different lanthanides gadolinium and europium, as ions, were directly inserted in the tetrahedral in-framework positions of synthetic saponites, through an innovative *one-pot* hydrothermal procedure. The presence of the two lanthanides confer to the final materials paramagnetic and luminescent properties, which can be exploited synergistically for *i*) several applications in optoelectronic and diagnostic fields and *ii*) in order to have a more comprehensive view of the chemical environment surrounding the lanthanides itself.

Structural, morphological and ^{27}Al solid-state NMR analyses confirm the inclusion of the metals in the tetrahedral layers, thus they are more accessible to water molecules inside the interlayer space. Photophysical analyses, performed at solid state and in aqueous suspensions, provided insights on chemical/geometrical nature of the environment around the metal centres. The gadolinium to europium

energy transfer observed also increased luminescence of the europium sites. The emission of the europium was further photosensitized by Förster resonance energy transfer process through coordination of an antenna ligand (1,10-phenantroline), introduced in the interlayer space. $^1\text{H-NMR}$ relaxometric analyses in aqueous phase indicated that the inner-sphere water molecules exchange quickly with the intra-interlayer water molecules, then diffuse through the lamellae channel and slowly exchange with the bulk water outside the lamellae. Therefore, the diffusion is the rate-limiting step of the overall relaxation effect. The structure of the materials proved to be robust even in harsh conditions (*i.e.* EDTA solution).

In the last section, starting from a previous work concerning the application of niobium-containing saponites for the decontamination of blistering chemical warfare agents, two novel bifunctional niobium & europium-containing synthetic saponites were developed. The luminescence properties of europium were exploited for the optical detection of the blistering agent simulant of mustard gas named (2-chloroethyl)ethyl sulphide (CEES), while the niobium centres (in addition to the surface acidity of the clays) were employed for the catalytic oxidative abatement of the organic compound. The tests were performed in simple conditions, in water medium at neutral pH, room temperature and atmospheric pressure and with the aid of a mild oxidant (aq. hydrogen peroxide). The samples were prepared by 1) ion-exchange with europium ions of a niobium-saponite clay and 2) *one-pot* hydrothermal synthesis in which both europium and niobium were directly inserted in the tetrahedral in-framework positions of the saponite.

Information on coordination of Nb^{5+} centres, surface acidity and photophysical features were extrapolated from a multi-technique approach. The CEES abatement, tested in liquid-phase under batch conditions, was monitored with UV-Vis-NIR and $^1\text{H-NMR}$ techniques. The materials were able to decompose from 70 to 90% of CEES after 24 h. The presence of europium in the structure did not inhibit the catalytic performance of the catalysts. Optical detection tests showed that both

materials were able to rapidly and effectively detect the presence of CEES in water after few seconds, as showed by decrease of intensity of main emission band of europium, sensible to interaction with the simulant.

In conclusion, in this Ph.D. work novel lanthanide-*based* multifunctional layered clay materials were successfully designed and thoroughly characterized, with potential applications in diagnostic techniques (magnetic/optical imaging), luminescent devices (sensors for hazardous compounds as chemical warfare agents), catch-and-release systems for water purification (from metals as lanthanides) and, ultimately, to expand the overall knowledge on the properties of the layered systems.

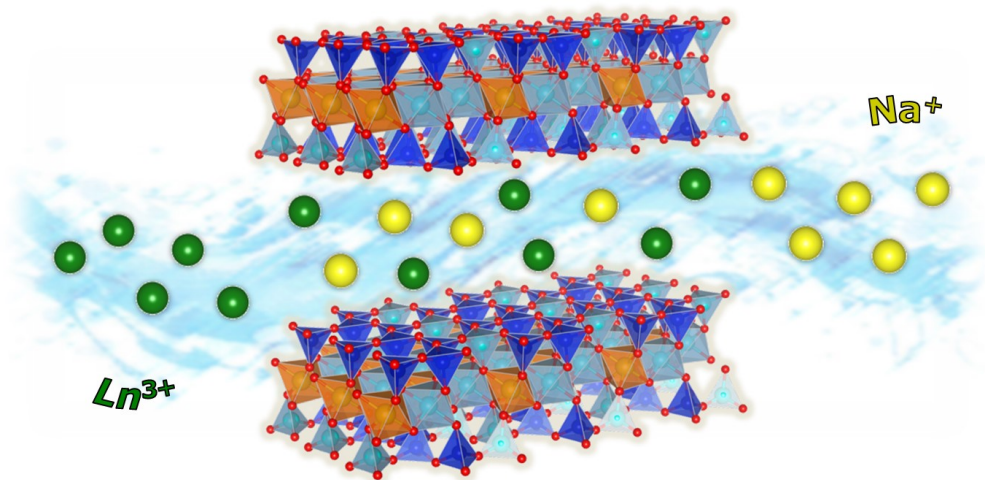
3

“Synthetic Saponite Clays as Promising Solids for Lanthanide Ions Recovery”

In this chapter, the use of synthetic saponite samples for the recovery of lanthanide ions, with different ionic radius (lanthanum, gadolinium and lutetium), from water solutions was explored, exploiting a simple cation exchange-based extraction process at room temperature and in static contact conditions between the solid sorbents and the ions.

The saponite clays, prepared through a simple and low-cost hydrothermal approach, were characterised by different particle size, specific surface area and cation-exchange capacity.

The metal uptake tests were performed over time in several aqueous solutions with varying complexity (pure water and simulated freshwater and seawater solutions), in the presence of fixed concentrations of the lanthanide selected or in a mixture of all the three metals (see Figure below). Preliminary studies related to the recovery of these ions from the clays were also explored.



3.1 Introduction

Lanthanides (Ln^{3+}), including scandium and yttrium, are commonly known as rare-earth elements (REEs) and make a unique contribution to various economically relevant important worldwide technologies owing to their unique electronic, magnetic, optical and catalytic properties.¹ Over the last decades, REEs have found a practical key role in a very broad range of different scientific and technological fields, in particular for the development of energy-efficient devices (*i.e.* phosphors for light-emitting diodes, LEDs, and luminescent sensors, novel batteries, solar panels, lasers and superconductors)^{2,3} as well as in biomedical applications (*i.e.* magnetic resonance (MRI) and optical imaging).⁴⁻⁶

REEs have therefore acquired an ever-increasing strategic importance at worldwide level: however, their availability on the planet is often inhomogeneous, since they are located in specific areas of the world, with low concentrations in the mineral ores.⁷ Moreover, REEs have no established biological role and their accumulation in the environment could be a critical problem to be assessed in the future. Some evidences have already put emphasis on REEs s emerging contaminants able to diffuse into the environment through waste water from health-care facilities, uncontrolled leachate solution from electronic waste or industrial effluents.⁸ For example, non-negligible levels of gadolinium ions (Gd^{3+}) have been found in surface, sewage and ground water of the urban area of Berlin⁹ and in the San Francisco Bay⁹ due to anthropogenic use. For these reasons, both the European Union and the United Nations Environment Program (UNEP) classify REEs as *critical raw materials* for the current and future worldwide economies.^{10,11}

Currently, most of the available REEs is supplied by primary mining, while their recovery is still very limited.⁷ Recycling processes for REEs from aqueous solutions are generally based on liquid-liquid (LLE) or liquid-solid (LSE) extractions,¹² the former being the most commonly used method, thanks to its good general selectivity and separation performance.⁷ Different types of ligands, functionalized with

carboxylic or sulfoxide groups, quaternary ammonium salts with chelating agents like ethylenediaminetetraacetic acid (EDTA) or amide/amine species are also used in combination with the chosen solvent for the recovery of REEs with LLE treatments, especially from electronic waste materials.¹³⁻¹⁸ However, LLE methods normally require multiple sequential extraction steps in continuous or in batch systems to attain the necessary purity, and generally they need large amounts of harmful and expensive extractants.¹⁹ Nevertheless, current solvent extraction methods are still insufficient to meet the current and, especially, future economic expectations and environmental guidelines associated with the recovery of REEs from conventional aqueous waste flows.

Liquid-solid (LSE) extraction process can be thus considered a valid alternative to LLE methods.²⁰ Indeed, some solid sorbents have been selected for their high chemical affinity towards *f*-block species or for their different capture mechanisms (*i.e.* ion-exchange, adsorption, complexation), which could lead to lower extraction time as well as reduced maintenance and operating costs.²¹ A wide range of solid sorbents have been proposed in the literature, such as porous silicas,²² carbon materials,²³ metal oxides²⁴ and metal-organic frameworks (MOFs).²⁵

A common strategy adopted to further improve the extraction process with these solid sorbents is the addition of chelating agents, which can selectively capture specific lanthanides.²⁶ Functionalized mesoporous silica-based materials proved to be quite promising for the selective capture and removal of heavy metals, due to their high surface areas and abundant presence of silanol groups on the surfaces, resulting in greater enhanced adsorption capacities over non-modified systems.²⁷ Mesoporous nanoparticles based on MCM-41 modified with maleic anhydride and KIT-6 silica with diglycolylamide (DGA), 3,6-dioxaoctanodioic acid and diamide phthalate (1,2-PA), for example, have been employed in this field.^{14,15,28-31} MCM-41 was functionalized with maleic anhydride, in order to improve the regeneration stability of the silica matrix, and showed good selective bonding characteristics towards several lanthanide elements, especially Eu^{3+} and Gd^{3+} . KIT-6 mesoporous silica

functionalized with DGA and derivatives exhibited remarkable sequestration performance of lanthanides from aqueous solutions. Chitosan-silica hybrid materials functionalized with chelating agents, such as diethylenetriaminepentaacetic acid (DTPA) and EDTA,³² and magnetic iron-nanoparticles coated with a silica shell and loaded with DTPA (dMNP-DTPA)³³ were also tested in the capture of lanthanides from water. Chitosan-silica materials showed better uptake performance for lighter metals, while dMNP-DTPA nanoparticles proves to be more selective towards heavier elements.

Natural clays have been used effectively as economic adsorbents for some metals and pollutants, due to their high abundance in natural environments. These solids generally feature an ion-exchange process for the recovery of metal ions. In particular, Ln^{3+} ions undergo hydrolysis on the interlayer surface of clays,^{34,35} thus achieving a good capture performance if compared to porous-like sorbents.³⁶⁻³⁸ Several examples on the use of clay minerals for the recovery of both lanthanides and actinides ions from the nuclear waste were discussed in the literature.^{34,35} For example, natural smectites and bentonites, due to their large cation exchange capacity, were tested for the ionic exchange of radionuclides (*i.e.* neptunium) solution with interlayer cations.³⁵

However, natural clays also present impurities and, generally, show less controlled or tuneable physico-chemical properties with respect to their synthetic counterparts,^{36,37} which can affect the capture process. In recent years, synthetic clays have been chosen for a large number of applications as a result of their unique physico-chemical properties, such as high chemical versatility and thermal stability, controlled chemical composition, particles size, adjustable aggregation and textural features, large availability and very low production costs.^{39,40}

In the light of these considerations, two different synthetic cationic saponite samples were examined in this chapter as solid sorbents for the ionic extraction of three lanthanides with similar ionic charge, but different radius (lanthanum/ La^{3+} , Gd^{3+} and lutetium/ Lu^{3+}). It is worth noting that most chemists include lanthanum in

the lanthanide series because, although it does not fill the $4f$ subshell, its properties are very similar to those of the Ln^{3+} . Clays differ in terms of particle size and cation-exchange capacity (CEC). The uptake of Ln^{3+} was tested in pure water as well as in simulated freshwater and seawater solutions, at different concentrations of lanthanide ions. In addition, the exchange capability of the solids was evaluated in the simultaneous presence of an equimolar mixture of La^{3+} , Gd^{3+} and Lu^{3+} ions, aiming to investigate the selectivity properties of the saponite clays for lanthanide ions with different ionic radius. Such studies on the recovery of Ln^{3+} ions from saponite clays showed encouraging results. The study provides a basis for the development of novel synthetic solid sorbents based on lamellar materials for the extraction of ubiquitous dispersed lanthanide pollutants from environmentally-relevant aqueous media.

3.2 Experimental Approach

3.2.1 Materials

Two synthetic saponite clays with different particles size and cation-exchange capacity were prepared through a simple and cheap hydrothermal method, previously optimized in our laboratories, by using two different H_2O/Si molar ratio in the synthesis gel: 20 (SAP-20) and 110 (SAP-110).⁴¹ Both samples underwent an ion-exchange step in saturated sodium chloride (NaCl) solution in order to replace the cations located in the interlayer space (*i.e.* Al^{3+} , Mg^{2+} , H^+) with Na^+ ions. This process was chosen to ensure a chemical uniformity of the exchange sites in the final saponite clays.

- **Synthesis of SAP-20 and Na-SAP-20 clays:** SAP-20 was synthesized following the hydrothermal procedure reported in the literature by Costenaro *et al.*⁴¹ A gel with $[SiO_2:MgO:Al_2O_3:Na_2O:H_2O]$ 1:0.835:0.056:0.056:20 molar composition was prepared. In detail, 11.91 g (0.19 mol) of amorphous silica (SiO_2 fumed,

99.8%) were gradually dispersed in a solution prepared by dissolving 0.93 g (0.02 mol) of sodium hydroxide (NaOH) in 58.20 g (3.23 mol) of ultrapure water (equal to 5/6 of the total water content). The obtained gel was then mixed accurately. After 1 h, 37.78 g (0.18 mol) of magnesium acetate tetrahydrate ($\text{Mg}(\text{CH}_3\text{COO})_2 \cdot 4\text{H}_2\text{O}$, 99%) and 4.71 g (0.02 mol) of aluminium isopropoxide ($\text{Al}[\text{OCH}(\text{CH}_3)_2]_3$, $\geq 98\%$) were added to the reaction mixture, along with the remaining ultrapure water (16.36 g, 0.91 mol). After 2 h, the gel, with a pH between 8-9, was introduced into a Teflon cup (125 mL capacity) of an autoclave (Anton Paar 4748) and heated in an oven for 72 h at 240 °C. The water amount used to prepare saponite gel was chosen in relation to the quantity of silicon within the gel: a $\text{H}_2\text{O}/\text{Si}$ molar ratio of 20 was here used. After the hydrothermal treatment, the product was filtered, washed with hot water up to neutral pH and dried in an oven overnight at 100 °C. The so-produced material called SAP-20 (10.80 g of white powder) was submitted to cation-exchange procedure (in order to ensure a chemical uniformity of the exchange sites): 2.50 g of SAP-20 were dispersed in 250 mL of saturated NaCl solution for 36 h at 25°C in order to replace all cations of the interlayer space (*i.e.* Al^{3+} , Mg^{2+} , H^+) with Na^+ ions. Then, the solid (named Na-SAP-20) was filtered, washed with hot ultrapure water until the complete elimination of chlorides (confirmed by AgNO_3 spot test) and dried in an oven overnight at 100 °C.

- **Synthesis of SAP-110 and Na-SAP-110 clays:** SAP-110 was prepared by adopting the same procedure used for the synthesis of SAP-20, but with a different $\text{H}_2\text{O}/\text{Si}$ molar ratio (= 110).⁴¹

3.2.2 Simulated aqueous solutions

- **Preparation of Simulated Seawater Solution:** 23.926 g of NaCl (409.392 mM), 4.008 g of sodium sulphate (Na_2SO_4 ; 28.217 mM), 0.677 g of potassium chloride (KCl; 9.081 mM), 0.196 g of sodium hydrogen carbonate (NaHCO_3 ; 2.333 mM), 0.098 g of potassium bromide (KBr; 0.824 mM), 0.026 g of boric

acid (H_3BO_3 ; 0.420 mM) and 0.003 g of sodium fluoride (NaF ; 0.071 mM) were dissolved in 1 L of ultrapure water.⁴²⁻⁴⁴

- **Preparation of Simulated Freshwater Solution:** 0.375 g of magnesium sulphate heptahydrate ($\text{MgSO}_4 \cdot 7\text{H}_2\text{O}$; 3.043 mM), 0.048 g of NaHCO_3 (1.143 mM), 0.0075 g of calcium chloride dihydrate ($\text{CaCl}_2 \cdot 2\text{H}_2\text{O}$; 0.102 mM), 0.200 g of NaCl (6.844 mM), 0.015 g of KCl (0.402 mM) and 0.030 g of calcium sulphate dihydrate ($\text{CaSO}_4 \cdot 2\text{H}_2\text{O}$; 0.348 mM) were dissolved in 0.500 L of ultrapure water.⁴⁵

3.3 Results and Discussion

3.3.1 Characterization of saponite materials

The chemical composition of the clays determined by inductively coupled plasma atomic emission spectrometry (ICP-AES) analysis is significantly different. The amount of Na^+ ions in Na-SAP-20 and Na-SAP-110 is 0.5 mmol/g and 0.3 mmol/g, respectively. The aluminium loading, distributed in the tetrahedral and octahedral layers of Na-SAP-20 is 1.1 mmol/g in agreement with data reported in the literature for parent saponites.⁴¹ A significant increase of Al^{3+} concentration is observed moving from Na-SAP-20 to Na-SAP-110 (1.4 mmol/g). Such behaviour, already documented for the same materials previously and studied by ^{27}Al solid state NMR, is related to a different amount of tetrahedral and octahedral aluminium sites.⁴¹ For Na-SAP-110, a predominance of octahedral Al^{3+} sites was recorded. These results can explain the different cationic exchange capacity of the two clays.

The structural features of Na^+ -exchanged saponites named Na-SAP-20 and Na-SAP-110 were analysed by X-ray powder diffraction (XRPD), and both solids showed the typical signals of the pristine saponite clay (Figure 1).^{41,47} In particular, the position of the (060) plane at $60.5^\circ 2\theta$ is indicative of the presence of 2:1 T-O-T tri-octahedral layered structure.^{41,47} As previously observed,^{47,49} the basal reflection

(001) of Na-SAP-20 (Figure 1, *a*) is more intense and resolved than that of Na-SAP-110 (Figure 1, *b*), because of the higher structural order along the *c*-axis.

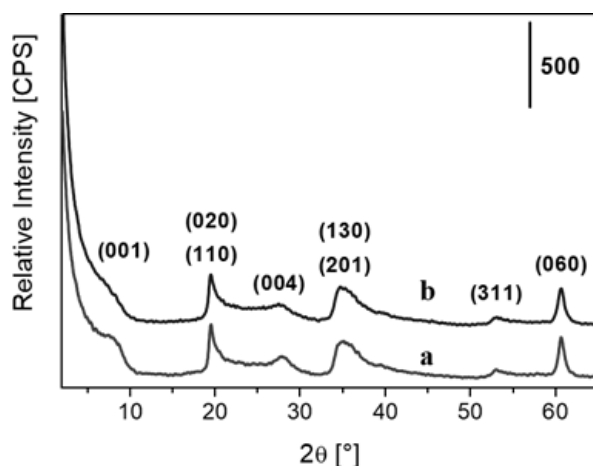


Figure 1. X-ray powder diffraction profiles of Na-SAP-20 (*a*) and Na-SAP-110 (*b*).

The morphological properties of Na-SAP samples were investigated by high-resolution transmission electron microscopy (HRTEM), which showed different levels of spatial organization of the lamellae, from single crystal structures with sheet-like morphology to aggregates, with formation of tactoids of different size (Figure 2). The dilution of the synthesis gel had an evident effect on the particles size: Na-SAP-110 showed lamellae with size of *ca.* 50 nm (Figure 2A), while Na-SAP-20 is characterized by particles with sub-micrometre size (Figure 2B).

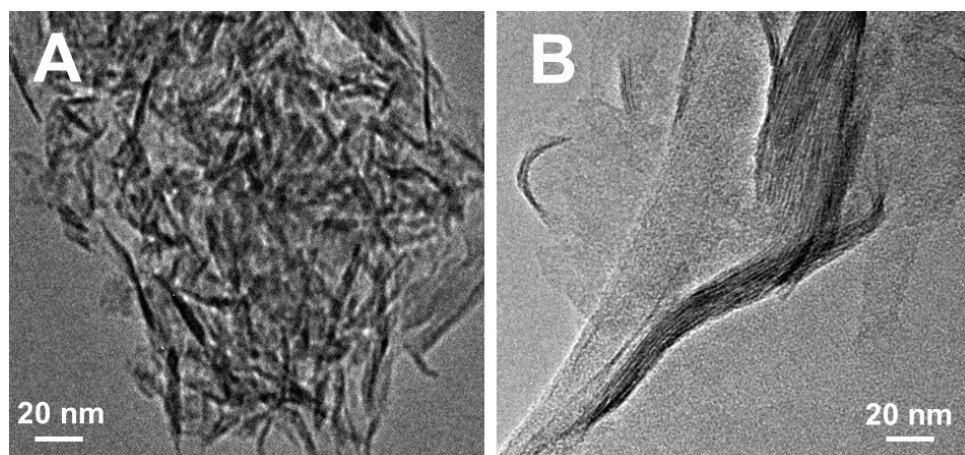


Figure 2. HRTEM micrographs of Na-SAP-110 (A) and Na-SAP-20 (B).

The textural features of Na-SAP samples were investigated by N₂ physisorption analysis at 77 K (Figure 3). The samples showed type IV isotherms (IUPAC classification), typical of micro- and meso-porosity, with H3 hysteresis loops, indicative of aggregates of lamellae that generate such mesoporosity.⁴¹ The specific surface area (SSA) was found to be 213 m²/g and 353 m²/g for Na-SAP-20 and Na-SAP-110, respectively, as estimated by the Brunauer-Emmett-Teller (BET) algorithm. These values are in line with those found for saponites previously published.⁴¹

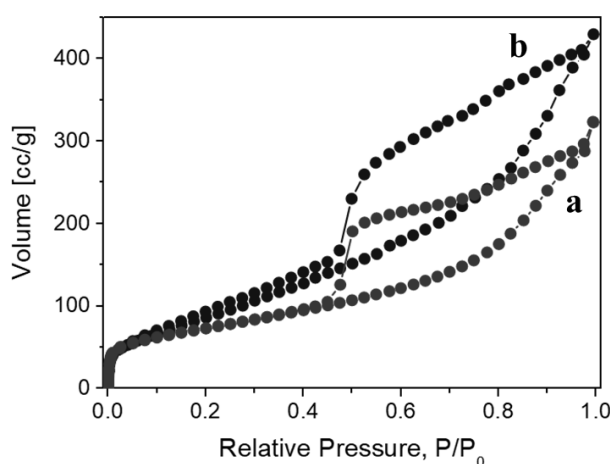


Figure 3. N₂ adsorption/desorption isotherms at 77K of Na-SAP-20 (a) and Na-SAP-110 (b).

The cationic exchange capacity (CEC) of saponite samples, evaluated through the classical UV-Vis-NIR method reported in literature,^{47,48} was estimated to be 87.9 ± 2.3 meq/100 g for Na-SAP-20 and 37.3 ± 1.8 meq/100 g for Na-SAP-110, with values in line with previous observations.⁴¹ The different CEC value is associated to the different amount of Al³⁺ in the tetrahedral layers.

3.3.2 Uptake and recovery tests of lanthanide ions from aqueous solutions

Lanthanum (La^{3+}), gadolinium (Gd^{3+}) and lutetium (Lu^{3+}) cations were selected as representative of the lanthanide series in order to evaluate the uptake performance of the saponite samples from environmentally-relevant aqueous solutions. The three elements were selected according to their different ionic radius, which decreases across the lanthanide series from La^{3+} (1.06 Å/106 pm) to Lu^{3+} (0.85 Å/86 pm). The metal uptake process for cationic clays is mainly based on the ionic exchange between the Na^+ ions in the interlayer space and the lanthanide ions dissolved in aqueous solution.^{49,50} An important ionic interaction between the negative tetrahedral sites of the lamellae (exchange sites) and the lanthanide cations takes place during the intercalation process. However, some adsorption processes (*i.e.* on the surface of lamellae) can also be involved in the capture of lanthanides from water. The exchange mechanism depends on several parameters, such as the cation-exchange capacity (CEC) of the clay, the particle size of solid and the charge/radius ratio of the metal ions.^{49,50}

The metal uptake experiments were carried out in three aqueous solutions with varying complexity, in pure water and simulated freshwater and seawater solutions (see *Paragraph 3.2.2* for preparation of the two simulated waters), with a fixed concentration of the lanthanide ion selected (individually or in a mixture of all the three elements). The tests were performed at room temperature (25 °C) and in static contact conditions between the solid clays and the metal ions (*n.b.*: no stirring). In detail, 15 mg of Na-SAP were added to 1 mL of aqueous solutions of chloride salts of lanthanides (Gd^{3+} , La^{3+} and Lu^{3+}) with different concentrations (10 mM and 0.1 mM), at pH 6.5. Under these pH conditions, more than 90% of lanthanide ions exists in solution as aquo-complexes.⁵⁰ The Gd^{3+} -uptake test was also performed for both Na-SAP-20 and Na-SAP-110 in simulated freshwater and seawater solution (10 mM). Selectivity tests were also carried out in pure water and simulated freshwater water solutions with a concentration of 3.33 mM of each lanthanide ions (Gd^{3+} , La^{3+}

and Lu^{3+}), for a total of 10 mM, at neutral pH. The experiments were carried at 25°C in a thermostatic sand bath, with the global system kept under static conditions. The uptake tests were monitored over the time until 5 h or 24 h, by analysing the amount of lanthanide ion remained in solution, after elimination of the powder by filtration. The amount of Ln^{3+} remained in solution during tests was quantified by ICP-AES analysis. The uptake efficiency for Na-SAP samples was identified by the mass weighted distribution coefficient (K_d) parameter.⁴⁶

Preliminary recovery tests of the lanthanides extracted by saponite solids were also explored. The solids were dispersed in a saturated NaCl solution and then sonicated in order to facilitate the release of the ions in water, trying to reconstitute the initial chemical composition of the interlayer space at the same time, thus regenerating the clay for subsequent extractions. In detail, Na-SAP-20 and Na-SAP-110 solids employed in the uptake tests of Gd^{3+} in pure water solution ($[\text{Gd}^{3+}] = 10$ mM) were dried and added to 1 mL of saturated NaCl at neutral pH and sonicated for 1 h. The amount of Gd^{3+} released in solution was determined by ICP-AES analysis.

In the first step, the uptake of lanthanides was evaluated in pure water solution at neutral pH and 25 °C with concentration of metal ions fixed at 10 and 0.1 mM. The uptake was monitored over time by measuring the metal concentration remaining in solution after clay filtration, by means of ICP-AES analysis. In addition, we extrapolated the mass-weighted distribution coefficient (K_d) for each test in order to further compare the uptake performance of the Na-SAP solids to other materials reported in the literature. This parameter is normally adopted to compare the metal sequestration performance of different systems.⁴⁶ The K_d parameter was calculated by the following equation (1):⁴⁶

$$K_d = \left(\frac{C_i - C_f}{C_f} \right) \cdot \left(\frac{V}{m} \right) \quad (1)$$

where C_i is the initial concentration (mM) of the lanthanide ion in the solution, C_f is the final concentration (mM) of ions left after the uptake, V is the volume of the solution (mL) and m is the mass (g) of solid sorbent used in the uptake tests.

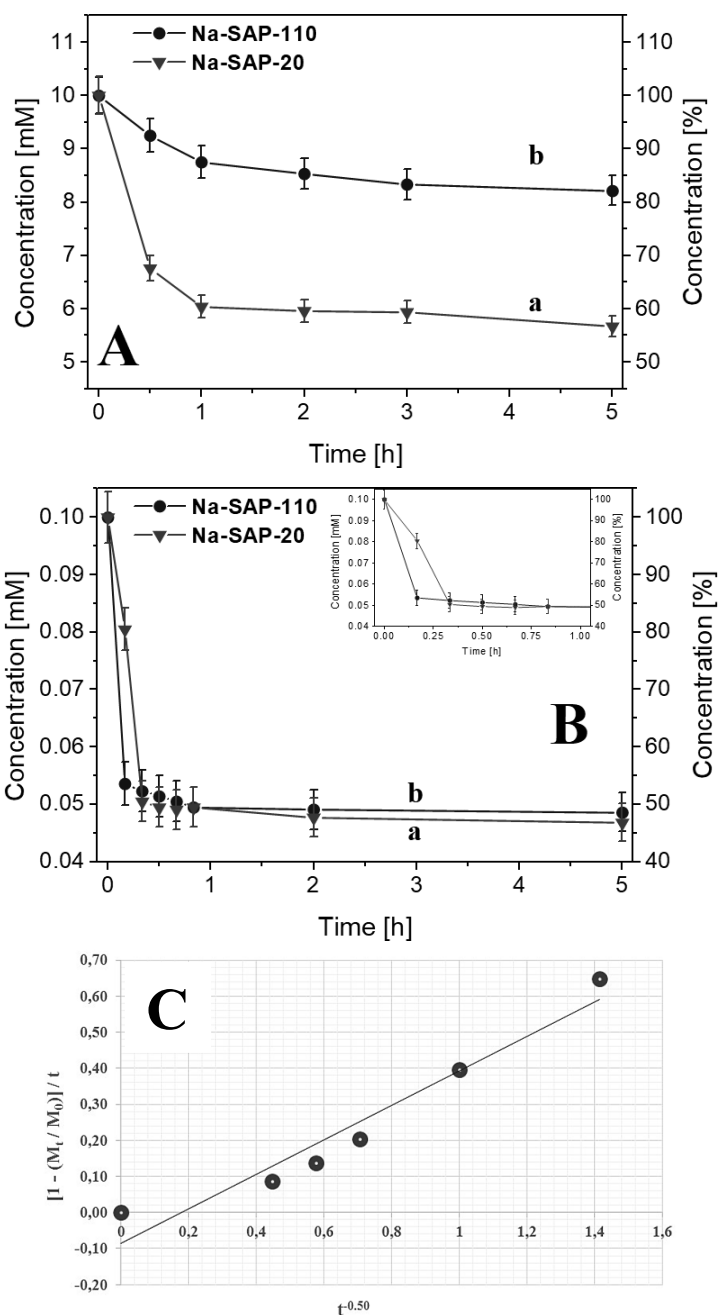
The first test was carried out in a pure water solution containing 10 mM of Gd^{3+} ions (Figure 4A). The correlation between the concentration of Gd^{3+} left in solution and the contact times is described by an exponential decay, with an evident reduction of the Gd^{3+} concentration in the first 30-60 min of time, especially for Na-SAP-20 (a), followed by a slight decrease from 1 to 5 h ('plateau-like' behaviour). At the end of the experiment, the Na-SAP-20 sample extracted 4.33 mM of Gd^{3+} , corresponding to 43.3% of the initial concentration. Interestingly, the amount of recovered metal ions corresponds to the complete cationic exchange capacity of the clay. The uptake of Na-SAP-110 (b) was lower than the previous sample and only 1.79 mM, corresponding to 17.9% of the initial concentration, were extracted. In this case too, however, 99.2% of the exchange sites of clay were involved in the exchange process. The difference observed is mainly due to the reduced CEC of Na-SAP-110 in comparison to Na-SAP-20 (Figure 4A and Table 1). The data were quantitatively analysed by a parabolic diffusion model that describes the diffusion-controlled event in clays (Figure 4C).⁵⁰ The model is described by the following equation:

$$\left(\frac{\left(1 - \frac{M_t}{M_0}\right)}{t} \right) - k^{t-0.5} + m \quad (2)$$

were M_0 and M_t are the amount of Gd^{3+} ions in the clays at time "0" and "t", respectively, k the rate constant and m a constant of which chemical significance is not clearly resolved.⁵⁰ The k values extrapolated by the data obtained for Na-SAP-20 and Na-SAP-110 were 0.48 and 0.11 s⁻¹, respectively.

The uptake was also performed in a diluted solution containing 0.1 mM of Gd^{3+} ions (Figure 4B). Both clays showed similar behaviour with a fast Gd^{3+} uptake during the first 30 min followed by a plateau after 1 h. The rate constant (k) calculated for both Na-SAP-20 and Na-SAP-110 was in this case 0.63 and 1.1 s⁻¹, respectively.

After 5 h, both solids extracted almost the same amount of Gd^{3+} , with values of 0.053 mM (53.0%) and 0.051 mM (51.0%), corresponding to 1.3% and 2.8% of the CEC for Na-SAP-20 (a) and Na-SAP-110 (b), respectively (Figure 4B and Table 1). These data suggest that the uptake significantly decreases in diluted solution for both saponites.



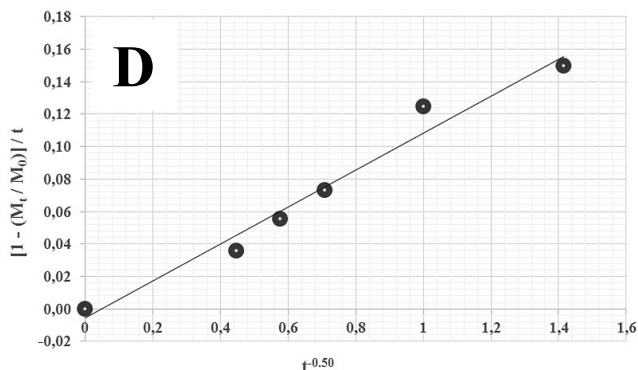


Figure 4. Molar and weight concentration (mM and wt.%) of Gd^{3+} in pure water solutions (10 mM (A) and 0.1 mM (B)) after uptake with Na-SAP-20 (*a*, -▼-) and Na-SAP-110 (*b*, -●-) samples, over the time (neutral pH and 25 °C). Plots of the kinetic parabolic model for the Gd^{3+} -uptake for Na-SAP-20 (C) and Na-SAP-110 (B) from aqueous solution (10 mM).

The uptake values for both Na^+ -exchanged saponites were also reported in terms of milligrams of metal ions extracted per gram of saponite used in the test in Table 1. In the experiment in the pure water solution at 10 mM of Gd^{3+} ions, after 5 h of contact Na-SAP-20 sample extracted 46.94 mg/g of gadolinium, while for Na-SAP-110 sample the value is 19.39 mg/g. The different amount captured between the clays is related to the higher CEC of Na-SAP-20 compared to Na-SAP-110. In the test at concentration of 0.1 mM of Gd^{3+} ions, instead, both clays removed almost the same amount of gadolinium (*ca.* 0.6 mg/g): these values, however, are much lower than the ones found in the tests performed at 10 mM. This behaviour, as suggested before, is attributed to the dilution of the aqueous solution which affects the uptake process. The amount of Gd^{3+} ions extracted by the sodium-exchanged saponite samples (considering the test at 10 mM) is consistent with the results described in literature for other solid sorbents.^{32,33}

Table 1. Gd³⁺ uptake data for Na-SAP-20 and Na-SAP-110 obtained from pure water solutions (10 mM and 0.1 mM of Gd³⁺ ions) after 5 h.

[Gd ³⁺] solution [mM]	Sample	Gd ³⁺ -uptake [%]	Gd ³⁺ -uptake [mg/g]
10 mM	Na-SAP-20	43.28 ± 3.41	46.94 ± 1.71
	Na-SAP-110	17.88 ± 3.53	19.39 ± 0.89
0.1 mM	Na-SAP-20	53.00 ± 4.01	0.56 ± 0.02
	Na-SAP-110	51.00 ± 2.04	0.54 ± 0.01

The K_d values were calculated from the data obtained after 5 h of contact time with a 10 mM solution of Gd³⁺ ions. The data obtained for Na-SAP-110 (1) and Na-SAP-20 (2) samples, reported in Figure 5A, were compared to similar cation-exchange solids like natural clays (kaolinite and montmorillonite, 4-5) and a reference synthetic zeolite (Zeolite A, 3) studied in the literature.^{46,51} The Na-SAP-110 sample showed the lowest K_d value, whereas Na-SAP-20 exhibited an uptake performance comparable to porous Zeolite A and slightly lower than kaolinite. Furthermore, both Na-SAP clays presented a better uptake compared to the classical liquid-liquid extractions (LLE), which normally employed different metal binding molecules such as 1,2-DOPA,¹⁸ TODOODA¹⁵ and TOFDGA¹⁵ (Figure 5B).

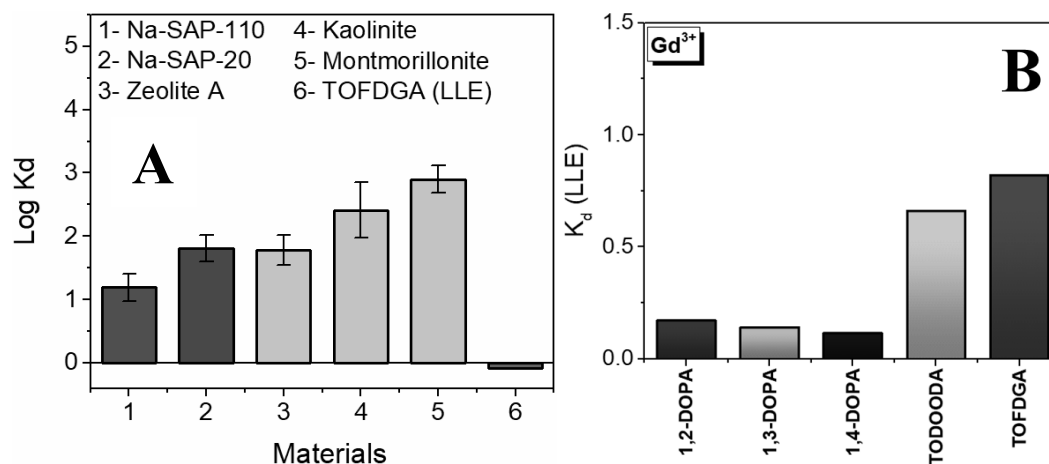


Figure 5. (A) Comparison of K_d values for Gd³⁺ (10 mM, 5 h) for Na-SAP-110 (1), Na-SAP-20 (2), Zeolite A (3), natural layered solids (kaolinite and montmorillonite)

(4, 5) and TOFDGA.^{15,46,51} (B) K_d values of some compounds employed in the liquid-liquid extraction of Gd^{3+} ions.^{15,18}

Preliminary studies on the recovery of Gd^{3+} ions from the saponite clays were also carried out. The experiments were performed on Na-SAP solids tested before in the pure water solution of Gd^{3+} at 10 mM (after 5 h of contact time). The solids, previously dried, were added to 1 mL of saturated solution of NaCl at neutral pH and sonicated for 1 h, in order to promote a “re-generation” of clays through a retro-exchange mechanism of Gd^{3+} with Na^+ . The amount of Gd^{3+} recovered from clays was determined by measuring the metal concentration in NaCl solution after clay centrifugation, by means of ICP-AES analysis. The Na-SAP-20 releases back in solution 1.38 mM of Gd^{3+} ions, that is 32.0% of the intercalated amount (4.3 mM), while for Na-SAP-110 the value was calculated to be 1.31 mM, corresponding to 73% of the total amount confined in the interlayer space (1.8 mM). The performance of Na-SAP-20 is very low if compared to Na-SAP-110 and LLE processes: this can be ascribed to the different charge density (higher for Na-SAP-20 → higher CEC).

Then, the Gd^{3+} uptake was evaluated in simulated freshwater and seawater solutions, containing several ions in different concentrations (Mg^{2+} , Ca^{2+} , Na^+ , K^+ , Cl^- , SO_4^{2-} , HCO_3^-) enriched by Gd^{3+} ions at concentration of 10 mM (Figure 6).

In the tests performed in the simulated freshwater solution (Figure 6A), the uptake kinetics for Na-SAP-20 and Na-SAP-110 appeared to be slightly slower than those observed in pure water solution (Figure 4A), with a decrease of the initial concentration of Gd^{3+} ions in the first 30 min, followed by a plateau from 5 to 24 h. After 5 h, Na-SAP-20 (a) extracted 4.88 mM of Gd^{3+} ions, corresponding to 48.8% of the initial concentration. Na-SAP-110 (b), instead, was able to extract 2.08 mM (20.8%) of Gd^{3+} . Both solids showed an uptake values (Table 2) comparable to those observed in pure water solution (Table 1), indicating that the presence of other cations in the simulated freshwater solution has a limited effect on the metal uptake. All the exchange sites were involved in the process for both clays.

Concerning the tests in simulated seawater solution (Figure 6B), Na-SAP-20 and Na-SAP-110 samples showed an exponential-like decay uptake kinetics, with a noticeable capture of Gd^{3+} ions in the first 30 min. After 5 h, Na-SAP-20 (a) extracted from the solution 21.1% of Gd^{3+} ions (Table 2), corresponding to 48.0% of the total exchange sites. These values are lower than those recorded in the tests in pure water and freshwater solutions (Figure 4B and 6A, Table 1 and 2). The marked reduction in the uptake performance for this sample, contrary to what was observed in simulated freshwater, is probably related to a major competition effect in the uptake of the Gd^{3+} ions by other cations present in the solution, which are in higher concentrations than those used for the preparation of the simulated freshwater. The Na-SAP-110 (b) sample extracted after 5 h an amount of Gd^{3+} equal to 17.2% (Table 2), rather similar to the value obtained over the Na-SAP-20 sample and in the tests in pure water and freshwater solutions (Figure 4B and 6A, Table 1 and 2).

In terms of uptake performance normalized to 1 g of material, after 5 h of contact in simulated freshwater solution, Na-SAP-20 sample extracted 49.48 mg/g of gadolinium while Na-SAP-110 removed from solution an amount of 21.07 mg/g of it (Table 2), similar to the values observed in pure water solution (Table 1). In the simulated seawater solution, instead, Na-SAP-20 extracted a lower amount of gadolinium than previous tests (only 22.12 mg/g), whereas for Na-SAP-110 sample the value calculated was close to the ones obtained in pure water and freshwater experiments (18.03 mg/g).

Na-SAP-20 tends to have a more ordered stacking of the sub-micrometre lamellae than Na-SAP-110, thanks to stronger interactions between lamellae due to a higher charge density. The two samples display different particles size, from sub-micro to nanometric dimensions for Na-SAP-20 and Na-SAP-110 respectively.^{39,41} Probably, these features affect the diffusion processes within the lamellae of Na-SAP-20, resulting in a marked competition between the mono- and di-valent ions, which are especially present in high concentration in the simulated seawater solution, and the Gd^{3+} ions.

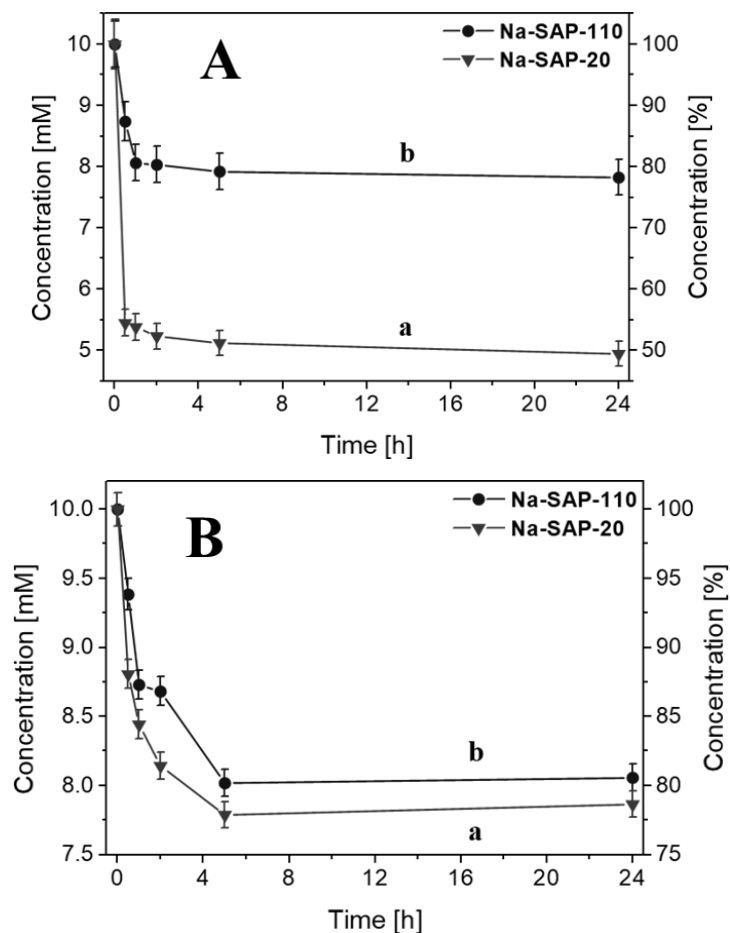


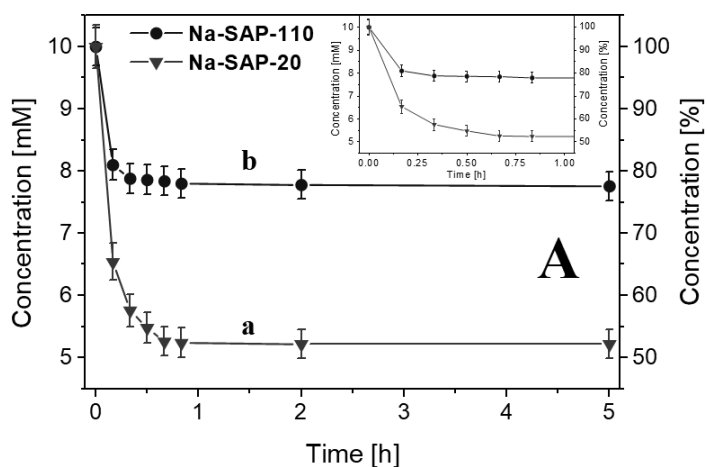
Figure 6. Molar and weight concentration (mM and wt.%) of Gd^{3+} in simulated freshwater (A) and seawater (B) solutions (10 mM) after uptake with Na-SAP-20 (a) and Na-SAP-110 (b) samples, over the time (neutral pH and 25 °C).

Table 2. Gd^{3+} uptake data for Na-SAP-20 and Na-SAP-110 obtained from simulated freshwater and seawater solutions (10 mM of Gd^{3+} ions) after 5 h.

[Gd^{3+}] simulated solution [mM]	Sample	Gd^{3+} -uptake [%]	Gd^{3+} -uptake [mg/g]
Freshwater [10 mM]	Na-SAP-20	48.77 ± 4.01	49.48 ± 1.98
	Na-SAP-110	20.77 ± 3.71	21.07 ± 0.99
Seawater [10 mM]	Na-SAP-20	21.10 ± 1.87	22.12 ± 1.96
	Na-SAP-110	17.20 ± 1.70	18.03 ± 1.78

The Ln^{3+} -uptake performance of Na-SAP solids were then tested in pure water solutions containing other two lanthanides, namely Lu^{3+} and La^{3+} (Figure 7). These two ions were selected because of their different ionic radius, corresponding to 175 pm for Lu^{3+} and 187 pm for La^{3+} , in order to investigate the effect of the ion size on the uptake capability of saponites.⁵² The tests were carried out in pure water solutions containing 10 mM of chosen lanthanide.

The uptake curves of both Na-SAP-20 and Na-SAP-110 for La^{3+} ions (Figure 7A) are similar to those obtained for Gd^{3+} , with a rapid removal in the first 30 min followed by a plateau from 1 h to 5 h. After 5 h, Na-SAP-20 (a) extracted 4.88 mM of La^{3+} (48.8%), whereas Na-SAP-110 (b) removed from the solution an amount equal to 2.02 mM (20.2%) (Table 3). The same behaviour was observed for the lanthanide with smaller ionic radius, Lu^{3+} (Figure 7B). After 5 h, Na-SAP-20 (a) and Na-SAP-110 (b) extracted 4.71 mM (47.1%) and 2.06 mM (20.6%) of Lu^{3+} , respectively (Table 3). Both experiments showed that all of the available sites for Na-SAP-20 and Na-SAP-110 samples took part in the exchange process.



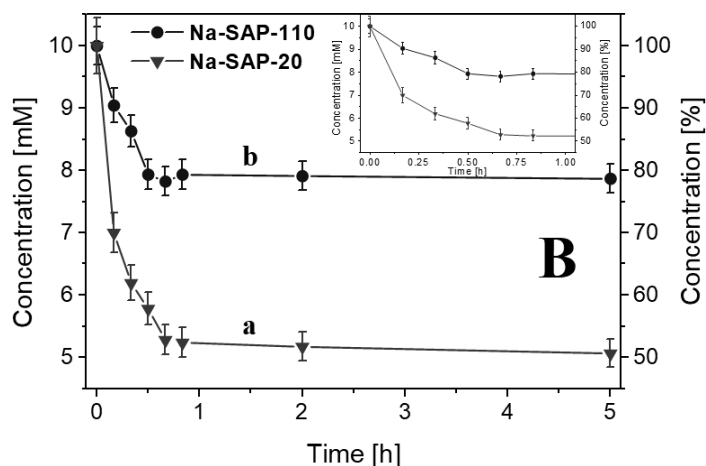


Figure 7. Molar and weight concentration (mM and wt.%) of La^{3+} (A) and Lu^{3+} (B) in pure water solutions (10 mM of each lanthanide) after uptake with Na-SAP-20 (a) and Na-SAP-110 (b) over the time (neutral pH and 25 °C).

Considering the amount in milligrams of metal removed from the solutions, saponite solids extracted, in general, more Lu^{3+} ions than Gd^{3+} and La^{3+} (see Tables 1 and 3). This behaviour is particularly evident for the Na-SAP-20 sample, which showed the capability of removing 54.89 mg/g of Lu^{3+} and 45.21 mg/g of La^{3+} as reported in Table 3, while extracting 46.94 mg/g of Gd^{3+} (Table 1). The Na-SAP-110 sample, instead, removed 23.98 mg/g of Lu^{3+} and 18.69 mg/g of La^{3+} (Table 3), while for Gd^{3+} ions the value is of 19.39 mg/g as reported in Table 1. Such results suggest a high capacity of saponite clays to capture lanthanides with smaller ionic radius, in analogy to what observed for other solids described in the literature.^{33,53}

Table 3. La^{3+} and Lu^{3+} uptake data for Na-SAP-20 and Na-SAP-110 obtained from pure water solutions (10 mM of lanthanide ions) after 5 h.

Lanthanide Ions	Sample	Ln^{3+} -uptake [%]	Ln^{3+} -uptake [mg/g]
La^{3+}	Na-SAP-20	48.82 ± 2.24	45.21 ± 1.12
	Na-SAP-110	20.18 ± 2.06	18.69 ± 0.45
Lu^{3+}	Na-SAP-20	47.06 ± 2.21	54.89 ± 1.31
	Na-SAP-110	20.56 ± 2.05	23.98 ± 0.55

The K_d values calculated for Na-SAP-20 and Na-SAP-110 in the uptake of La^{3+} (Figure 9A) and Lu^{3+} (Figure 9B), after 5 h, were compared to the values reported for classical LLE methods^{15,18} and for some natural clays.^{34,50,54} The synthetic saponites showed uptake performances markedly higher than those observed for classical LLE methods for La^{3+} (Figure 8A) and Lu^{3+} (Figure 8B).^{15,18} Na-SAP-20 and Na-SAP-110 samples showed uptake performances comparable to those of natural clays for both La^{3+} (Figure 9A) and Lu^{3+} (Figure 9B) elements.

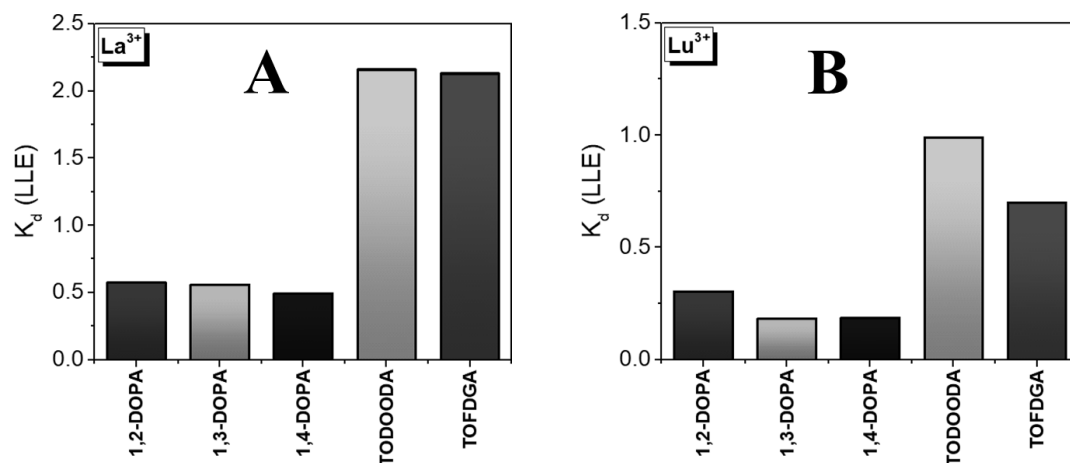


Figure 8. K_d values of some compounds employed in the liquid-liquid extraction methods of La^{3+} (A) and Lu^{3+} (B) ions.^{15,18}

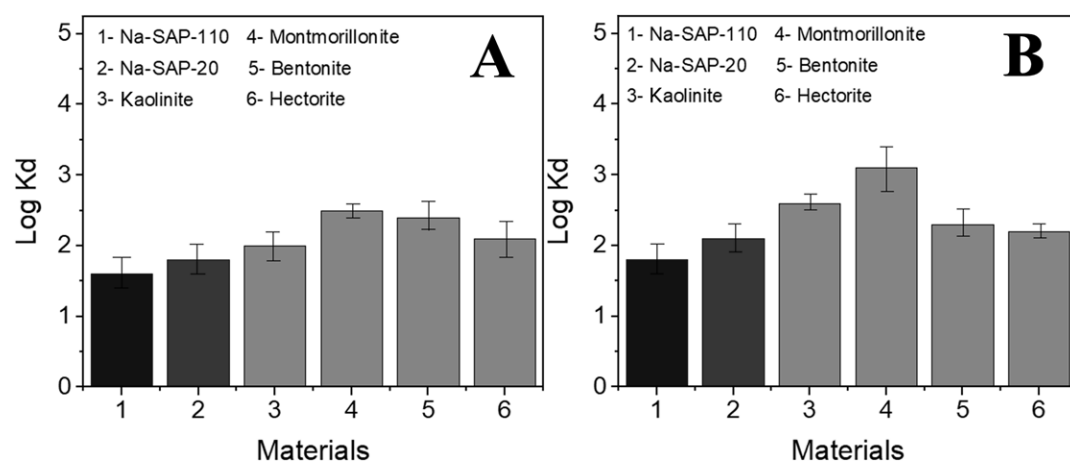
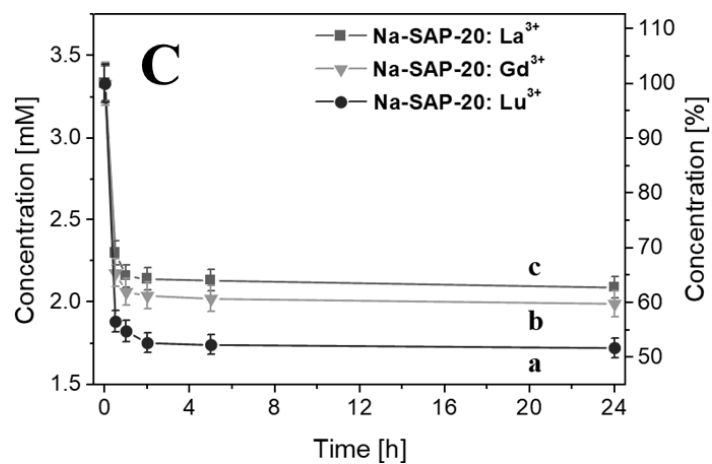
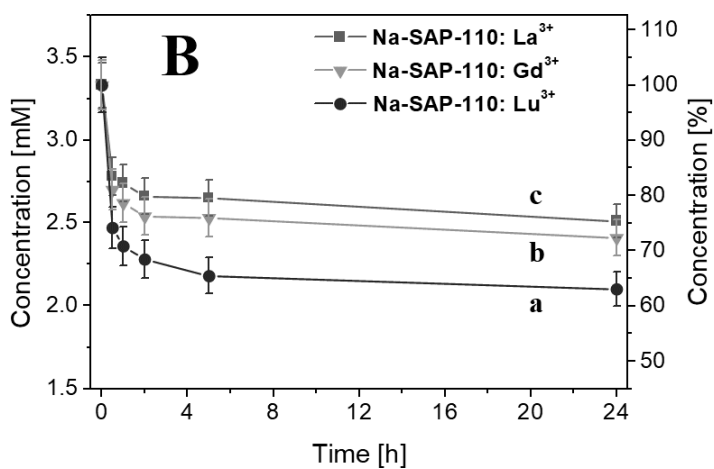
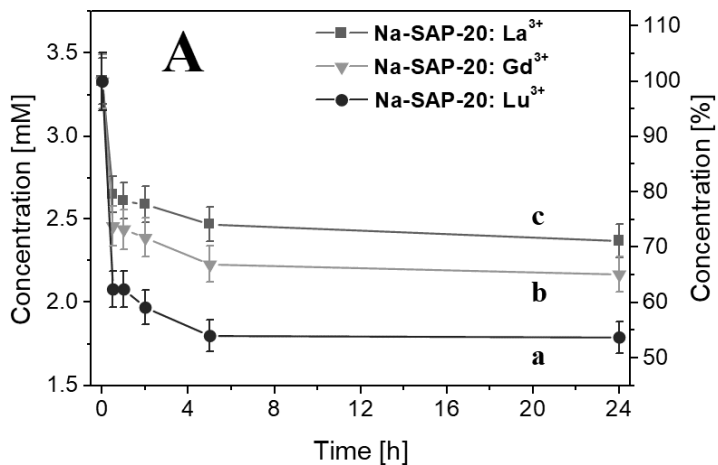


Figure 9. Comparison of K_d values for La^{3+} (A) and Lu^{3+} (B) for Na-SAP-110 (1), Na-SAP-20 (2) and different natural clays (3-6).^{34,50,54}

Finally, Na-SAP samples were tested in a pure water solution in the presence of an equimolar mixture of La^{3+} , Gd^{3+} , Lu^{3+} ions, each one in 3.33 mM concentration, corresponding to a total amount of lanthanide ions of *ca.* 10 mM. This allowed to evaluate the selectivity of saponite samples for ions featuring different ionic radii (Figure 10).^{32,33,53} The uptake selectivity tests for both Na-SAP-20 (Figure 10A) and Na-SAP-110 (Figure 10B) were carried out over 24 h. For both samples, the uptake kinetics appeared slower than the individual experiments performed in pure water solutions (Figure 4 and 7), in a similar manner to what it is observed in the tests in simulated freshwater (Figure 6A) and seawater (Figure 6B) solutions for Gd^{3+} ions, with a more marked shift of the plateau zone towards the 5 h range. This effect can be attributed to the co-presence of all the three lanthanides in competition with the same ion-exchange sites of saponite. Lutetium (*a*), having the smallest ionic radius, was the element mostly retained in both saponites, followed by gadolinium (*b*) and lanthanum (*c*) (Figure 10A and B, Table 4). Therefore, the amount of each element extracted by saponite was lower than the one observed in previous individual uptake tests (Tables 1 and 3). Indeed, in terms of uptake performance normalized to 1 g of material (Table 4), after 5 h of contact Na-SAP-20 sample extracted 7.96 mg/g of lanthanum, 11.49 mg/g of gadolinium and 17.84 mg/g of lutetium. On the other hand, Na-SAP-110 removed from aqueous solution a lower amount of each lanthanides (6.25 mg/g of lanthanum, 8.38 mg/g of gadolinium and 13.41 mg/g of lutetium).

A set of experiments was also carried out in simulated freshwater with an equimolar concentration of 3.33 mM of lanthanides (total amount of *ca.* 10 mM) (Figure 10C and D, Table 4), showing the same uptake behaviour previously observed in pure water solution (Figure 10A and B).



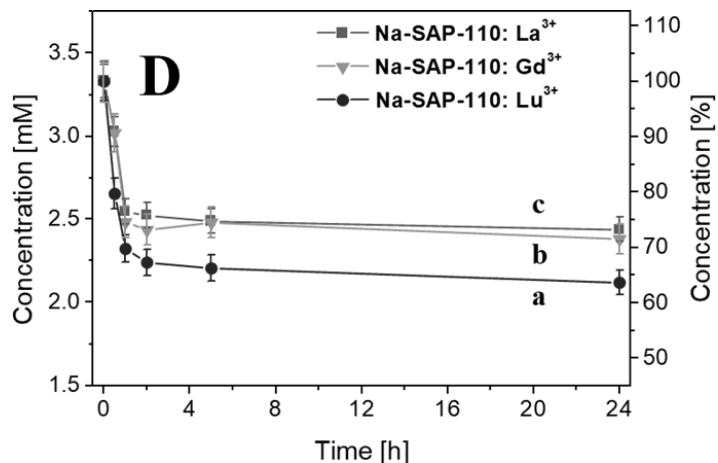


Figure 10. Molar and weight concentration (mM and wt.%) of Lu³⁺ (a), Gd³⁺ (b) and La³⁺ (c) in aqueous solutions (pure water (A-B) and simulated freshwater (C-D) solutions; 3.33 mM of each lanthanide ions, for a total amount of 10 mM) after uptake with Na-SAP-20 and Na-SAP-110, over the time (neutral pH and 25 °C).

Table 4. Selectivity of Na-SAP-20 and Na-SAP-110 for the removal of lanthanide ions obtained from aqueous solutions (pure water (A) and simulated freshwater (B)); 3.33 mM of each lanthanide ion, for a total amount of 10 mM) after 5 h.

Sample	Lanthanide Ions	<i>Ln</i> ³⁺ -uptake [%]	<i>Ln</i> ³⁺ -uptake [mg/g]
A) Pure Water			
Na-SAP-20	La ³⁺	25.82 ± 4.15	7.96 ± 0.42
	Gd ³⁺	32.92 ± 4.89	11.49 ± 0.61
	Lu ³⁺	45.92 ± 5.25	17.84 ± 0.98
Na-SAP-110	La ³⁺	20.28 ± 4.05	6.25 ± 0.33
	Gd ³⁺	23.99 ± 4.48	8.38 ± 0.46
	Lu ³⁺	34.53 ± 4.98	13.41 ± 0.75
B) Freshwater			
Na-SAP-20	La ³⁺	35.92 ± 3.15	11.08 ± 0.46
	Gd ³⁺	39.25 ± 3.89	13.70 ± 0.64
	Lu ³⁺	47.70 ± 3.51	18.53 ± 0.76
Na-SAP-110	La ³⁺	25.28 ± 3.00	7.79 ± 0.34
	Gd ³⁺	25.50 ± 3.78	8.90 ± 0.45
	Lu ³⁺	33.76 ± 3.50	13.11 ± 0.57

3.4 Conclusions

The uptake of lanthanide ions of different ionic radius (La^{3+} , Gd^{3+} and Lu^{3+}) from different environmentally relevant aqueous solutions (pure water and simulated freshwater and seawater solutions) has been evaluated by using two Na^+ -exchanged synthetic saponite clays. The clays, prepared through a classical hydrothermal synthesis with different $\text{H}_2\text{O}/\text{Si}$ molar ratio ('110' for Na-SAP-110 sample and '20' for Na-SAP-20 sample), differ in terms of cation-exchange capacity (87.9 ± 2.3 meq/100 g for Na-SAP-20, 37.3 ± 1.8 meq/100 g for Na-SAP-110), particles size (in the sub-micrometer region for Na-SAP-20, *ca.* 50 nm for Na-SAP-110) and textural properties. Both samples, exploiting a cation-exchange process for the extraction of the lanthanides from the aqueous solutions tested, showed a good uptake performance for the three metal ions analysed, comparable to the one currently observed for several natural clays employed in the industry and significantly higher respect to the conventional liquid-liquid extraction methods.

In the individual tests conducted in pure water at concentration of 10 mM of each lanthanide, Na-SAP-20 was able to remove larger amounts of lanthanide ions than Na-SAP-110, due to its higher cation-exchange capacity. In terms of mg of lanthanide ions extracted per gram of solid sorbent used, Na-SAP-20 was able to remove from aqueous solutions a general amount of 45-55 mg/g of lanthanides, whereas for Na-SAP-110 the values were in between 18-24 mg/g. A promising performance was also obtained in the uptake of Gd^{3+} under simulated freshwater and seawater conditions. In simulated freshwater, both clays demonstrated the same extraction behaviour observed in pure water. In simulated seawater, instead, Na-SAP-20 showed a reduced uptake due to its higher charge density, which led to a marked competition between the mono- and di-valent ions and the Gd^{3+} ions in the final extraction process. Both saponite clays showed a marked selectivity towards lanthanide ions with lower ionic radius, such as lutetium, both in pure water and simulated freshwater solutions. Finally, a set of preliminary metal recovery tests in

saturated NaCl solution showed promising results in terms of recovery of lanthanide ions from an aqueous medium and of regeneration of clays, especially for the Na-SAP-110 sample.

In the light of these results and considering the low costs associated with the preparation of this class of clays, synthetic saponite samples can be considered an attracting alternative to the solids reported so far in the literature for the recovery of pollutant lanthanide ions from different environmentally-relevant aqueous solutions.

3.5 Notes and References

- 1 V. Balzani, P. Ceroni and A. Juris, *Photochemistry and Photophysics: Concepts, Research, Applications*, 2014, Weinheim, Wiley-VCH Verlag GmbH & Co, **ISBN: 978-3-527-33479-7**.
- 2 S. Massari and M. Ruberti, *Res. Policy*, 2013, **38**, 36-43.
- 3 J.-C. G. Bünzli, *Coordin. Chem. Rev.*, 2015, **293-294**, 19-47.
- 4 A. F. Mingo, S. C. Serra, S. Baroni, C. Cabella, R. Napolitano, I. Hawala, I. M. Carnovale, L. Lattuada, F. Tedoldi and S. Aime, *Magn. Reson. Med.*, 2016, **78**, 1523-1532.
- 5 D. Parker, *Handbook on the Physics and Chemistry of Rare Earths*, 2016, **50**, 269-299, Amsterdam: Elsevier, edited by J.-C. G. Bünzli and V. K. Pecharsky, **ISBN: 978-0-444-63851-9**.
- 6 F. Carniato, L. Tei and M. Botta, *Eur. J. Inorg.*, 2018, **46**, 4936-4954.
- 7 A. Tsamis and M. Coyne, *Recovery of Rare Earths from Electronic Wastes: An Opportunity for High-Tech SMEs*, 2015, European Parliament, Directorate-General for Internal Policies of the Union.
- 8 A) H. Herrmann, J. Nolde, S. Berge and S. Heise, *Ecotoxicology and Environmental Safety*, 2016, **124**, 213-238; B) G. Klaver, M. Verheul, I. Bakker, E. Petelet-Giraud and P. Négrel, *Appl. Geochem.*, 2014, **47**, 186-197.
- 9 A) A. Knappe, P. Möller, P. Dulski and A. Pekdeger, *Chem. Erde-Geochem.*, 2005, **65**, 167-189; B) V. Hatje, K. W. Bruland and A. R. Flegal, *Environ. Sci. Technol.*, 2016, **50**, 4159-4168.
- 10 http://ec.europa.eu/growth/sectors/raw-materials/specific-interest/critical_en.
- 11 M. Sethurajan, E. D. van Hullebusch, D. Fontana, A. Akcil, H. Deveci, B. Batinic, J. P. Leal, T. A. Gasche, M. A. Kucuker, K. Kuchta, I. F. F. Neto, H. M. V. M. Soares and A. Chmielarz, *Crit. Rev. Env. Sci. Tec.*, 2019, 1-64.

- 12 A) L. Chen, Y. Wu, H. Dong, M. Meng, C. Li, Y. Yan, and J. Chen, *Sep. Purif. Technol.*, 2018, **197**, 70-85; B) N. N. Hidayah, and S. Z. Abidin, *Miner. Eng.*, 2017, **112**, 103-113.
- 13 A. Roca-Sabio, M. Mato-Iglesias, D. Esteban-Gòmez, E. Tòth, A. de Blas, C. Platas Iglesias and T. Rodríguez-Blas, *J. Am. Chem. Soc.*, 2009, **131**, 3331-3341.
- 14 L. Tei, Z. Baranyai, E. Breucher, C. Cassino, F. Demicheli, N. Masciocchi, G. B. Giovenzana and M. Botta, *Inorg. Chem.*, 2010, **49**, 616-625.
- 15 J. Florek, A. Mushtaq, D. Larivière, G. Cantin, F.-G. Fontaine and F. Kleitz, *RSC Adv.*, 2015, **5**, 103782-103789.
- 16 A. Leoncini, P. K. Mohapatra, A. Bhattacharyya, D. R. Raut, A. Sengupta, P. K. Verma, N. Tiwari, D. Bhattacharyya, S. Jha, A. M. Wouda, J. Huskens and W. Verboom, *Dalton Trans.*, 2016, **45**, 2476-2484.
- 17 P. Kishor, A. Sengupta, N. K. Gupta and S. Biswas, *Sep. Sci. Technol.*, 2017, **53**, 286-294.
- 18 Y. Hu, E. Drouin, D. Larivière, F. Kleitz and F.-G. Fontaine, *ACS Appl. Mater. Interfaces*, 2017, **9**, 38584-38593
- 19 P. Anastas and N. Eghbali, *Chem. Soc. Rev.*, 2010, **39**, 301-312.
- 20 E. P. Horwitz, R. Chiarizia, M. L. Dietz, H. Diamond and D. M. Nelson, *Anal. Chim. Acta*, 1993, **281**, 361-372.
- 21 E. Juère, J. Florek, D. Larivière, J. Kim and F. Kleitz, *New J. Chem.*, 2016, **40**, 4325-4334.
- 22 P. D. Hopkins, T. Mastren, J. Florek, R. Copping, M. Brugh, K. D. John, M. F. Nortier, E. R. Birnbaum, F. Kleitz and M. E. Fassbender, *Dalton Trans.*, 2018, **47**, 5189-5195.
- 23 M. Choi and J. Jang, *J. Colloid Interface Sci.*, 2008, **325**, 287-289.
- 24 E. P. Legaria, S. D. Topel, V. G. Kessler and G. A. Seisenbaeva, *Dalton Trans.*, 2015, **44**, 1273-1282.
- 25 X. Zhao, M. Wong, C. Mao, T. X. Trieu, J. Zhang, P. Feng and X. Bu, *J. Am. Chem. Soc.*, 2014, **136**, 12572-12575.
- 26 J. R. Kumar, J.-S. Kim, J.-Y. Lee and H.-S. Yoon, *Sep. Purif. Rev.*, 2011, **40**, 77-125.
- 27 I. Sierra and D. Perez-Quintanilla, *Chem. Soc. Rev.*, 2013, **42**, 3792-3807.
- 28 J. Florek, F. Chalifour, F. Bilodeau, D. Larivière and F. Kleitz, *Adv. Funct. Mater.*, 2014, **24**, 2668-2676.
- 29 X. Zheng, C. Wang, J. Dai, W. Shi and Y. Yan, *J. Mater. Chem. A*, 2015, **3**, 10327-10335.
- 30 A. S. Suneesh, K. V. Syamala, K. A. Venkatesan, M. P. Antony and P. R. Vasudeva Rao, *J. Colloid Interf. Sci.*, 2015, **438**, 55-60.
- 31 J. Florek, S. Giret, E. Juère, D. Larivière and F. Kleitz, *Dalton Trans.*, 2016, **45**, 14832-14854.

- 32 J. Roosen, J. Spoorenand and K. Binneman, *J. Mater. Chem. A*, 2014, **2**, 19415-19426.
- 33 A) H. Zhang, R. G. McDowell, L. R. Martin and Y. Qiang, *ACS Appl. Mater. Interfaces*, 2016, **8**, 9523-9531; B) L. M. Whittaker, L. N. Lammers, S. Carrero, B. Gilbert and J. F. Banfield, *PNAS*, 2019, **116**, 22052-22057.
- 34 A) P. Olivera Pastor, E. Rodriguez Castellon and A. Rodriguez, *Solv. Extr. Ion Exch.*, 1987, **5**, 1151-1169; B) P. Olivera Pastor, E. Rodriguez-Castellon and A. Rodriguez Garcia, *Clay Clay Miner.*, 1988, **36**, 68-72.
- 35 A) A. Alshameri, H. He, C. Xin, J. Zhu, W. Xinghu, R. Zhu and H. Wang, *Hydrometallurgy*, 2019, **185**, 149-161; B) D.R. Fröhlich, *Clay Clay Miner.*, 2015, **63**, 262-276.
- 36 E. Tertre, G. Berger, E. Simoni, S. Castet, E. Giffaut, M. Loubet and H. Catalette, *Geochim. Cosmochim. Ac.*, 2006, **70**, 4563-4578.
- 37 N. Finck, M. L. Schlegel and D. Bosbach, *Environ. Sci. Technol.*, 2009, **43**, 8807-8812.
- 38 E. Galunin, M. D. Alba, M. J. Santos, T. Abrao and M. Vidal, *J. Hazard. Mat.*, 2011, **186**, 1930-1941.
- 39 C. Bisio, G. Gatti, E. Boccaleri, L. Marchese, L. Bertinetti and S. Coluccia, *Langmuir*, 2008, **24**, 2808-2819.
- 40 S. Marchesi, F. Carniato, C. Bisio, L. Tei, L. Marchese and M. Botta, *Dalton Trans.*, 2018, **47**, 7896-7904.
- 41 D. Costenaro, G. Gatti, F. Carniato, G. Paul, C. Bisio and L. Marchese, *Microp. Mesop. Mat.*, 2012, **162**, 159-167.
- 42 D. R. Kester, I. W. Duedall, D. N. Connors, and R. M. Pytkowicz, *Preparation of Artificial Seawater I. Limnology and Oceanography*, 1967, **12**, 176-179.
- 43 G2MT Labs, *Preparation of Substitute Ocean Water* (retrieved 25 June 2019).
- 44 H. Wang, M. Gao, Y. Guo, Y. Yang and R. Hu, *Desalination*, 2016, **398**, 198-207.
- 45 S. Simpson and G. Batley, *Sediment quality assessment: A practical guide (2nd Ed.)*, 2016, CSIRO Publishing, **ISBN: 978-1-486-30384-7**.
- 46 A) C. E. Housecroft, and A. G. Sharpe, *Inorganic Chemistry (2nd Ed.)*, 2004, Prentice Hall., pp: 536, 649, 743, **ISBN: 978-0-130-39913-7**; B) C. E. Housecroft, and A. G. Sharpe, *Inorganic Chemistry (5nd Ed.)*, 2018, Pearson, **ISBN: 978-1-292-13414-7**.
- 47 O. Prieto, M. A. Vincente and M. A. Banares-Munoz, *J. Porous Mater.*, 1999, **6**, 335-344.
- 48 J. C. Dabrowiak, *Metals in Medicine (2nd Ed)*, 2017, John Wiley & Sons Ltd, **ISBN: 978-1-119-19130-8**.
- 49 C. Bisio, G. Gatti, E. Boccaleri, L. Marchese, G. B. Superti, H. O. Pastore and M. Thommes, *Microp. Mesop. Mat.*, 2008, **107**, 90-101.

- 50** A) J. Maza-Rodriguez, P. Olivera-Pastor, S. Bruque and A. Jimenez-Lopez, *Clay Miner.*, 1992, **27**, 81-89; B) P. Djurdjević, R. Jelić, L. Joksović, I. Lazarević and M. Jelikić-Stankov, *Acta Chim. Slov.*, 2010, **57**, 386-397; C) H. Zhang, D. Pan and X. Duan, *J. Phys. Chem. C*, 2009, **113**, 12140-12148; D) Z. Gu, A. C. Thomas, Z. P. Xu, J. H. Campbell and G. Q. Lu, *Chem. Mater.*, 2008, **20**, 3715-3722; E) M. K. Uddin, *Chem. Eng. J.*, 2017, **308**, 438-462.
- 51** J. Bronić and B. Subotić, *J. Radioan. Nucl. Ch. Ar.*, 1986, **100**, 91-101.
- 52** H. Royen and U. Fortkamp, *Report C 211 - Rare Earth Elements - Purification, Separation and Recycling*, 2016, IVL Swedish Environmental Research Institute Ltd., Sweden, **ISBN: 978-91-88319-12-8**.
- 53** G. E. Fryxell, W. Chouyyok, and R. D. Rutledge, *Inorg. Chem. Comm.*, 2011, **14**, 971-974.
- 54** S. Bruque, T. Mozas, and A. Rodriguez, *Clay Miner.*, 1980, **15**, 413-420.

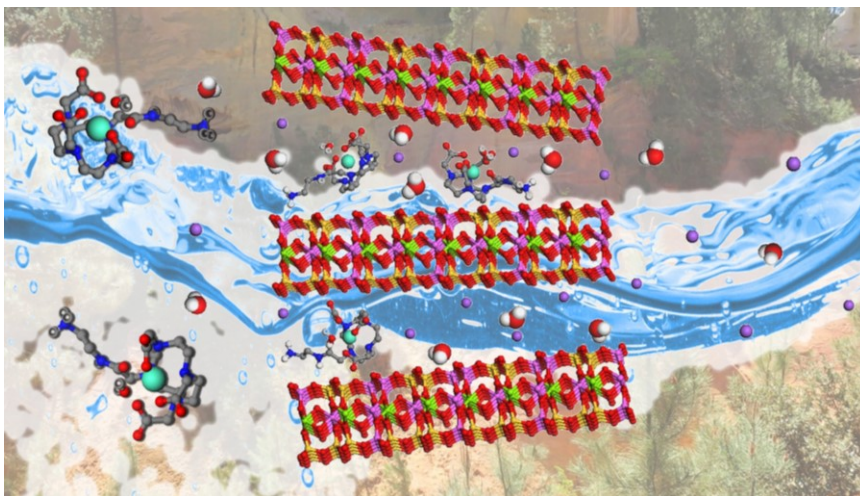
4

“Solution and Solid-State NMR Study of Synthetic Saponite Materials Intercalated with Lanthanide Chelates”

In this chapter, novel paramagnetic and diamagnetic synthetic saponite clays, bearing in the interlayer space positively charged gadolinium and yttrium complexes, were synthesized through hydrothermal approach followed by intercalation procedure (see Figure below).

A detailed characterization was performed to assess the physico-chemical properties of hybrid samples, especially to evaluate the stabilization degree of the metal complexes confined in the interlayer space of the host clay.

¹H-NMR relaxometric studies in aqueous solution and solid-state NMR experiments were carried out to evaluate the local chemical environment of the intercalated metal chelates and their interaction with the water molecules and the inorganic framework. The stability over time in different aqueous solutions was also evaluated by relaxometric techniques.



(Adapted from: "S. Marchesi et al., Dalton Trans., 2018, 47, 7896")

4.1 Introduction

Over the last decade, natural and synthetic clays have been the subject of considerable attention for a large number of different applications as a result of their unique physico-chemical properties, large availability, low costs and high chemical versatility.¹⁻³ In particular, synthetic clays, typically prepared by hydrothermal methods,¹ show more controlled chemical composition and particles size, aggregation and textural features than natural counterpart minerals. For these reasons, they proved to be excellent versatile materials and they are generally preferred for nanotechnology applications spanning from agriculture and surface coatings to environmental purposes, particularly as adsorbents, ion exchangers and water decontaminants.⁴⁻⁵ Among the family of smectite clays, synthetic saponite was largely studied because of its high specific surface area, acidic properties and thermal stability.¹ These properties make them of great interest for catalysis and polymer science applications. Over the last few years, saponite clays have been employed as heterogeneous catalysts for controlled oxidation reactions⁶⁻⁷ and as additives for the preparation of polymer nanocomposites especially based on polyolefines.^{8,9} More recently, clays have also been used for the immobilization of luminescent organic dyes with the aim of making the final composite materials suitable for optical and optoelectronic applications.¹⁰⁻¹² All these examples indicate the possibility of developing clays with innovative properties through the proper selection of the guest species with different functionalities (*i.e.* metal ions, organic surfactants or dyes).

Along this direction, the introduction of *f*-block elements (*i.e.* ions or related complexes) may lead to clays with additional optical and/or magnetic features. The combination of layered materials with *f*-block elements have been only marginally investigated and the studies in the literature are mainly related to the preparation of paramagnetic and luminescent systems.¹³⁻¹⁵ For instance, the intercalation of lanthanide chelates (based on europium, Eu^{3+} , and terbium, Tb^{3+}) in clay minerals was adopted to prepare luminescent hybrid materials with improved properties in

terms of high chemical stability and enhanced light-emission.¹⁶⁻¹⁷ Among these types of luminescent clays, some solids have found applications for the fingerprints detection,¹⁸ while others have been tested as chemical sensors for the selective identification of different organic species such as biothiols (*i.e.* glutathione)¹⁹ or cationic surfactants.²⁰

Unmodified aluminosilicates clays and zeolite when combined with gadolinium (Gd^{3+}) ions were also proposed as oral magnetic resonance imaging (MRI) contrast agents (CAs) for the gastrointestinal tract.²¹ For instance, Balkus and co-workers^{22,13} and Sur *et al.*²³ investigated the relaxation behaviour of aqueous suspensions of hectorite and zeolite NaY, after ion-exchange with Gd^{3+} , in view of their potential use as MRI probes. Despite the good stability of these materials, the risk associated to the release of toxic Gd^{3+} ions in physiological conditions is particularly relevant. This has been partly overcome in the case of zeolite materials, through the treatment of such solids with EDTA (ethylenediaminetetraacetic acid) and DTPA (diethylenetriaminepentaacetic acid) ligands, able to coordinate the metal ion within the supercages.²³ The result was an increase in the chemical stability of the final material. Therefore, the direct confinement of thermodynamically stable and kinetically inert $Ln(III)$ complexes in host materials would allow the safe use for final environmental and biological applications.

Following this approach, in this chapter different stable cationic Gd^{3+} -chelates were confined in the interlamellar region of nanosized saponite clays. The choice of the Gd^{3+} ion is motivated by its well-known excellent properties as relaxation agent, due to the high value of the magnetic moment combined with a particularly long value of the electronic relaxation times.²⁴ In principle, the introduction of Gd^{3+} cations in the layered host should enable to obtain relevant information on the chemical nature of the intercalation compound. Indeed, by measuring the relaxation rate of water protons, enhanced through short- and/or long range dipolar interactions with Gd^{3+} species in the interlayer space of saponite, additional information on the accessibility of the exchange sites of intercalated samples and diffusion of water

molecules can be derived.²⁵ Such information can be extended to the comprehension of other intercalated materials based on different *Ln(III)* compounds.

In the first part of this study we have selected two positively charged Gd^{3+} -complexes that differ in the coordination geometry and hydration state of the metal ion. The complexes are based on amino-functionalized derivatives of the macrocyclic DOTA (1,4,7,10-tetraazacyclododecane-1,4,7,10-tetraacetic acid; **GdL1**)^{26,27} and AAZTA (6-amino-6-methylperhydro-1,4-diazepine-*N,N',N'',N'''*-tetraacetic acid; **GdL2**)²⁸ (Figure 1). Both **GdL1** and **GdL2** show high thermodynamic stability and good kinetic inertness. The selection of these complexes was carried out in consideration of their following distinct characteristics: 1) although the complexes possess an overall charge “+1”, the charge distribution is different. In **GdL1** the positive charge is localized on the terminal amino group of the pendant arm, while the coordination cage is neutral. On the other hand, **GdL2** features a negatively charged coordination cage and two positive charges on the pendant polyamine moiety. Thus, it is important to highlight possible differences in the final intercalated materials. In addition, 2) **GdL1** and **GdL2** are expected to exhibit a remarkably different relaxometric behaviour, because characterized by a different number of inner-sphere water molecule(s) ($q = 1$ for **GdL1** and $q = 2$ for **GdL2**) with different water exchange rate. A detailed ¹H-NMR relaxometric study as a function of temperature and applied magnetic field strength was undertaken on the Gd^{3+} -complexes before and after intercalation into the clays. The structural and relaxometric properties of these novel paramagnetic materials, hereafter named **GdL1/SAP** and **GdL2/SAP**, were then thoroughly investigated.

Moreover, in order to have a more comprehensive evaluation of the molecular dynamics of water in the interlamellar region of saponite and to investigate in detail the structural/chemical interactions between complex/water molecules and layered framework, the molecular organization of second-sphere water molecules around paramagnetic centres and the structural defects of clay, a combined multi-technique

study by ^1H -NMR relaxometric and solid-state NMR (ssNMR) analyses was employed in the second part of this study.

For this purpose, chelates based on a novel TETA (1,4,8,11-tetraazacyclotetradecane)^{29,30} monoamide derivative coordinated to gadolinium and yttrium ion (GdL0 and YL0, respectively, Figure 1) were prepared, together with the respective intercalated saponites (called GdL0/SAP and YL0/SAP). These complexes have been selected because they present no water molecule(s) bound to the metal centre ($q = 0$): in this way, specific insights on the diffusion mechanisms of water molecules in the saponite gallery can be derived from the relaxometric analyses. Yttrium, instead, was chosen because it shares with Gd^{3+} similar ionic radius (Y^{3+} $r = 240$ pm, Gd^{3+} $r = 238$ pm) and coordination chemistry. Furthermore, ^{89}Y isotope is an NMR-active nucleus with diamagnetic properties and comparable low gyromagnetic ratio (γ) to gadolinium.

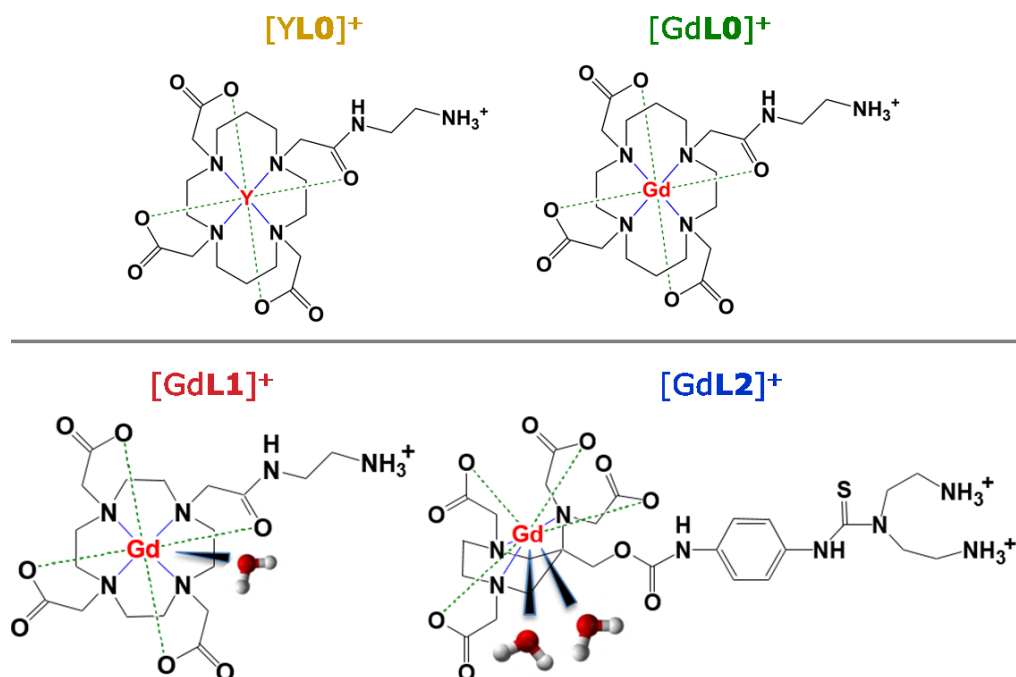


Figure 1. Chemical structure of YL0, GdL0, GdL1 and GdL2 chelates.

4.2 Experimental Approach

4.2.1 Saponite clay

- **Synthesis of SAP and Na-SAP clays:** Nanosized synthetic saponite with a cationic exchange capacity (CEC) of 37.3 ± 1.8 meq/100 g was synthesized following the hydrothermal procedure adopted in the literature by Costenaro *et al.*¹ A gel with the molar composition of [SiO₂:MgO:Al₂O₃:Na₂O:H₂O] 1:0.835:0.056:0.056:110 and H₂O/Si molar ratio of 110 was prepared. In detail, 3.97 g (0.06 mol) of amorphous silica (SiO₂ fumed, 99.8%) were gradually dispersed in a solution prepared by dissolving 0.31 g (0.007 mol) of sodium hydroxide (NaOH) in 109.00 g (6.05 mol) of ultrapure water (equal to 5/6 of the total water content). The obtained gel was then mixed accurately. After 1 h, 11.93 g (0.05 mol) of magnesium acetate tetrahydrate (Mg(CH₃COO)₂·4H₂O, 99%) and 1.75 g (0.007 mol) of aluminium isopropoxide (Al[OCH(CH₃)₂]₃, ≥ 98 %) were added to the reaction mixture, along with the remaining ultrapure water (22.00 g, 1.22 mol). After 2 h, the gel, with a pH between 8-9, was introduced into a Teflon cup (125 mL capacity) of an autoclave (Anton Paar 4748) and heated in an oven for 72 h at 240 °C. After hydrothermal treatment, the product was filtered, washed with hot ultrapure water up to neutral pH and dried in an oven overnight at 100 °C.

The so-produced material called SAP (6.59 g of white powder) was submitted to cation-exchange procedure (in order to ensure a chemical uniformity of the exchange sites): 2.50 g of SAP were dispersed in 250 mL of saturated sodium chloride (NaCl) solution for 36 h at RT to replace all possible cations present (*i.e.* Al³⁺, Mg²⁺, H⁺) with Na⁺ ions in the interlayer space. Then, the final solid material (named Na-SAP) was filtered, washed with hot ultrapure water until the complete elimination of chlorides (confirmed by silver nitrate, AgNO₃, spot test) and dried in an oven overnight at 100 °C.

4.2.2 Gd³⁺/Y³⁺-complexes

- **Synthesis of GdL0 and YL0 chelates:** The synthesis of the novel TETA monoamide ligand bearing a 2-aminoethylacetamide pendant arm (TETAMA, named **L0**), used for the preparation of relative Gd³⁺ and Y³⁺ chelates (Gd**L0** and Y**L0**, respectively), was carried out starting from the TETA macrocycle.^{29,30}

In the first step, the bromoacetamide pendant arm (1) was synthesized following an optimized procedure reported in the literature.²⁶ In detail, N-Boc-ethylenediamine (0.400 g, 2.496 mmol), dissolved in 4 mL of dichloromethane (CH₂Cl₂/DCM), was added to a 1 M NaOH solution (8.00 mL, 7.489 mmol) and slowly stirred at 0 °C for 15 min. Afterwards, a solution of 2-bromoacetyl bromide (620 µL, 3.745 mmol) in 15 mL of DCM was added dropwise to the reaction mixture, under nitrogen flow and at 0 °C. The mixture was then slowly stirred at RT for 20 h. After that, several purification treatments were performed in order to obtain the pure bromoacetamide pendant arm (1). In detail, 15 mL of water were added to the mixture, followed by concentration *in vacuo*; the residue/organic phase was extracted in DCM (3 x 15 mL), dried with sodium sulphate (Na₂SO₄), filtered and evaporated *in vacuo* until a whitish powder was obtained. The desired product was isolated through purification in chromatographic column (DCM:methanol/MeOH 90:10) and the fraction in DCM was finally concentrated *in vacuo* (bromoacetamide pendant arm (1), 0.300 g, 1.067 mmol, 38% yield).

TE3A(*t*-BuO)₃ (2) was prepared by reacting the TETA macrocycle with *tert*-butyl 2-bromoacetate. In detail, TETA (0.500 g, 2.496 mmol) was dissolved in 25 mL of anhydrous acetonitrile (ACN), under nitrogen flow and at RT, and slowly stirred at 0 °C for 10 min. Sodium hydrogen carbonate (NaHCO₃, 0.315 g, 3.749 mmol) was added and the mixture was slowly stirred at 0 °C for 30 min. Next, *tert*-butyl 2-bromoacetate (1.100 mL, 7.510 mmol) was added dropwise at 0 °C and the reaction mixture was slowly stirred at RT for 48 h. After that, the solution was concentrated *in vacuo* until a yellowish oil-like compound was

recovered. The desired product was isolated through purification in chromatographic column (DCM:MeOH 95:5) and the fraction in DCM was finally concentrated *in vacuo* until a whitish powder was obtained (TE3A(*t*-BuO)₃ (2), 0.735 g, 1.354 mmol, 55% yield).

Subsequently, TE3A(*t*-BuO)₃ (2) (0.200 g, 0.368 mmol) and potassium carbonate (K₂CO₃, 0.150 mg, 1.085 mmol) were dissolved in 20 mL of ACN at RT; then, a solution of bromoacetamide pendant arm (1) (0.137 g, 0.487 mmol) in 10 mL of ACN was added dropwise at RT and the reaction mixture was slowly stirred at 60 °C for 48 h. After that, the mixture was filtered and finally concentrated *in vacuo* until a yellowish powder was obtained (TE3A(*t*-BuO)₃-monoacetamide-Boc (3), 0.299 g, 0.402 mmol, 98% yield).

The simultaneous deprotection of *tert*-butyl ester and Boc groups was accomplished by reacting the intermediate TE3A(*t*-BuO)₃-monoacetamide-Boc (3) (0.299 g, 0.402 mmol) with a 1:1 mixture solution of 13 mL of DCM and 13 mL of trifluoroacetic acid (TFA) at 0 °C, then slowly stirred at RT for 48 h. After that, several purification treatments were performed in order to obtain the TETAMA ligand (**L0**). In detail, 10 mL of diethyl ether were added to the mixture, followed by filtration and concentration *in vacuo* of the filtered solution; 15 mL of ultrapure water were added to the yellowish oil-like compound, the residue/aqueous phase was washed it thoroughly with DCM (3 x 15 mL) and finally evaporated *in vacuo* until a yellowish oil-like compound was obtained (TETAMA (**L0**), 0.146 g, mmol, 76% yield).

Finally, TETAMA (**L0**), 0.146 g, 0.307 mmol) and gadolinium chloride hexahydrate (GdCl₃·6H₂O; 0.135 g, 0.363 mmol) were dissolved at room temperature (RT) in 15 mL of ultrapure water and then the pH of the solution was brought to 6.5 with a NaOH solution. The reaction mixture was then stirred at RT overnight. After that, the pH was again corrected from 6.5 to 10 with to precipitate unchelated Gd³⁺ ions as hydroxide (Gd(OH)₃), which was eliminated by centrifugation (10000 rpm for 5 min) and filtration through 0.2 μm filters. The

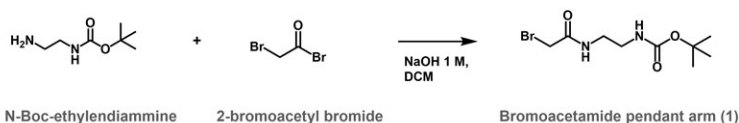
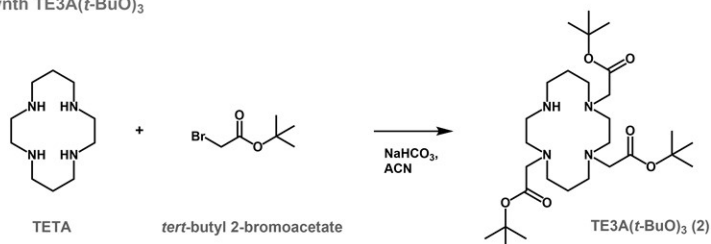
pH of the complex solution was finally adjusted to 7 with a hydrochloric acid (HCl) solution and lyophilized overnight until a whitish solid was obtained (GdL0, 0.233 g, 0.370 mmol, 99% yield) (Scheme 3).

For YL0, a slightly different complexation procedure than the one described above was used: L0 (0.192 mg, 0.404 mmol), yttrium chloride hexahydrate ($\text{YCl}_3 \cdot 6\text{H}_2\text{O}$; 0.147 g, 0.485 mmol), 15 mL of ultrapure water, reaction mixture stirred for 5 days at 50 °C. 313 mg (0.557 mmol, 99% yield) of the final chelate were prepared (Scheme 3).

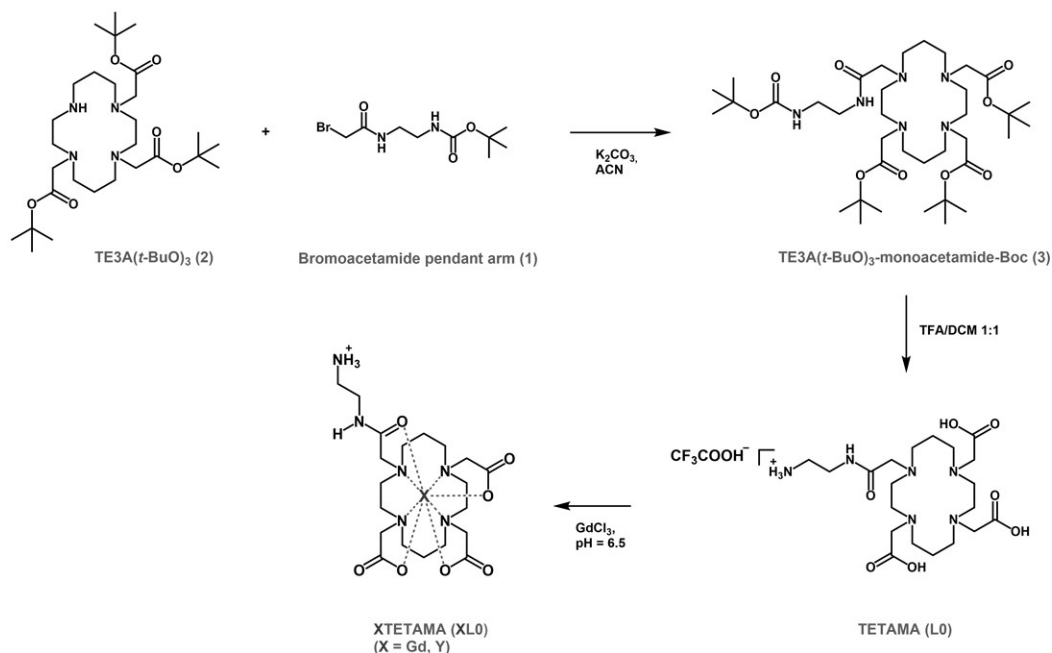
- Bromoacetamide pendant arm (1):
 - HPLC-MS ESI⁺ (m/Z) = 281.25 [(M + H)⁺]; calculated $\text{C}_9\text{H}_{17}\text{BrN}_2\text{O}_3$ = 281.15.
 - ¹H-NMR (CDCl_3) 500 MHz, δ [ppm] = 3.95 (s, 2H, BrCH_2), 3.48 (t, 2H, NHCH_2), 3.40 (t, 2H, CH_2NH), 1.54 (s, 9H, CH_3).
 - ¹³C-NMR (CDCl_3) 100 MHz, δ [ppm] = 171.6 ($\text{C}=\text{ONH}$), 166.3 ($\text{NHC}=\text{OO}$), 77.3 ($\text{C}(\text{CH}_3)_3$), 41.5 (CH_2NH), 39.8 (NHCH_2), 29.4 (CH_3), 28.7 (BrCH_2).
- TE3A(*t*-BuO)₃ (2):
 - HPLC-MS ESI⁺ (m/Z) = 543.70 [(M + H)⁺]; calculated $\text{C}_{28}\text{H}_{54}\text{N}_4\text{O}_6$ = 542.76.
 - ¹H-NMR ($\text{ACN-}d$) 500 MHz, δ [ppm] = 3.29 (s, 6H, $\text{CH}_2\text{C}=\text{O}$), 2.80-2.65 (t, 16H, other CH_2 aromatic ring), 1.68 (m, 4H, apical CH_2 aromatic ring), 1.50 (s, 27H, CH_3).
 - ¹³C-NMR ($\text{ACD-}d$) 100 MHz, δ [ppm] = 170.8 ($\text{C}=\text{O}$), 82.5 (quaternary $\text{C}(\text{CH}_3)_3$), 57.8 ($\text{CH}_2\text{C}=\text{O}$), 65.0-40.0 (other CH_2 aromatic ring), 31.7 and 30.8 (apical CH_2 aromatic ring), 28.8 (CH_3).
- TE3A(*t*-BuO)₃-monoacetamide-Boc (3):
 - HPLC-MS ESI⁺ (m/Z) = 744.05 [(M + H)⁺]; calculated $\text{C}_{37}\text{H}_{70}\text{N}_6\text{O}_9$ = 743.00.

- $^1\text{H-NMR}$ (CDCl_3) 500 MHz, δ [ppm] = 3.39 (t, 2H, NHCH_2 pendant arm), 3.30 (t, 2H, CH_2NH pendant arm), 3.21 (s, 2H, NHC=OCH_2 pendant arm), 3.05 (s, 6H, $\text{CH}_2\text{C=O}$), 2.75 and 2.63 (t, 16H, other CH_2 aromatic ring), 1.62 (m, 4H, apical CH_2 aromatic ring), 1.51 (s, 36H, CH_3).
- $^{13}\text{C-NMR}$ (CDCl_3) 100 MHz, δ [ppm] = 173.5 (NHC=O pendant arm), 170.7 (C=O), 157.6 (OC=ONH pendant arm), 82.8 (quaternary $\text{C}(\text{CH}_3)_3$), 79.3 (quaternary $\text{C}(\text{CH}_3)_3$ pendant arm), 59.3 (NHC=OCH_2 pendant arm), 58.2 ($\text{CH}_2\text{C=OO}$), 55.0-50.0 (other CH_2 aromatic ring), , 41.2 (CH_2NH pendant arm), 38.1 (NHCH_2 pendant arm), 29.8 and 29.3 (apical CH_2 aromatic ring), 28.1 (CH_3).
- **TETAMA (L0):**
 - HPLC-MS ESI⁺ (m/Z) = 475.65 [(M + H)⁺]; calculated $\text{C}_{19}\text{H}_{39}\text{N}_6\text{O}_7 = 474.56$.
 - $^1\text{H-NMR}$ (D_2O) 500 MHz, δ [ppm] = 3.38 (t, 4H, $^+\text{H}_3\text{NCH}_2\text{CH}_2\text{NH}$ pendant arm), 3.21 (s, 2H, NHC=OCH_2 pendant arm), 3.18 (s, 2H, $\text{CH}_2\text{C=O}$), 2.71 and 2.58 (t, 16H, other CH_2 aromatic ring), 1.70 (m, 4H, apical CH_2 aromatic ring).
 - $^{13}\text{C-NMR}$ (D_2O) 100 MHz, δ [ppm] = 172.9 (C=O), 168.6 (NHC=O pendant arm), 60.0-50.0 (CH_2), 38.9 ($^+\text{H}_3\text{NCH}_2$ pendant arm), 37.2 (CH_2NH pendant arm), 22.5 (apical CH_2 aromatic ring),
- **GdL0:** HPLC-MS ESI⁺ (m/Z) = 629.89 {[(M + H)]⁺}; calculated $\text{C}_{19}\text{H}_{36}\text{GdN}_6\text{O}_7 = 628.79$ (100.0 %) (isotopic distributions consistent with Gd^{3+}).
- **YL0:** HPLC-MS ESI⁺ (m/Z) = 585.84 {[(M + Na)]⁺}; calculated $\text{C}_{19}\text{H}_{36}\text{YN}_6\text{O}_7 = 560.44$.

1) Synth Bromoacetamide pendant arm

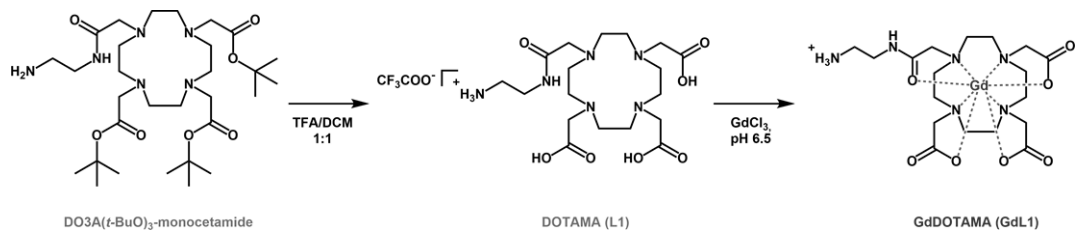
2) Synth TE3A(*t*-BuO)₃

3) Synth GdL0 and YL0 Chelates



Scheme 1. Synthetic pathway for the preparation of **L0**, **GdL0** and **YL0**.

- **Synthesis of GdL1 chelate:** Cationic GdDOTA monoamide chelate bearing a 2-aminoethylacetamide pendant arm (GdDOTAMA, named **GdL1**) was synthesized using a procedure optimized in the literature by Barge *et al.* (Scheme 2).^{26,27}



Scheme 2. Synthetic pathway for the preparation of **L1** and **GdL1**.

- **Synthesis of GdL2 chelate:** The synthesis of cationic GdAAZTA-Ph-DETA chelate (named **GdL2**) was carried out starting from the tetra *tert*-butyl ester protected AAZTA derivative bearing a phenyl isothiocyanate group (AAZTA(*t*-BuO)₄-Ph-NCS), previously described by Gugliotta *et al.*²⁸

In the first step, the *N,N*-diBoc-diethylenetriamine (**1**) was synthesized following the procedure reported in the literature.³¹ In details, *tert*-butanol (0.640 mL, 6.67 mmol), potassium hydroxide (KOH, 9.9 g, 0.17 mmol) and 1,1-carbonyldiimidazole (CDI, 1.08 g, 6.67 mmol) were dissolved under nitrogen flow in 25 mL of anhydrous toluene and slowly stirred at 60 °C for 3 h. After 3 h, diethylenetriamine (DETA, 0.340 mL, 3.34 mmol) was added dropwise to the reaction mixture, which was then stirred for further 3 h. After that, the ‘cold’ solution was concentrated *in vacuo* and the residue/organic phase was extracted with DCM (3 x 20 mL), washing it with water (3 x 20 mL). The organic phase was then dried with Na₂SO₄ and evaporated *in vacuo* until a transparent dense gel was obtained (*N,N*-diBoc-diethylenetriamine (**1**), 0.086 g, 0.28 mmol, 8.4% yield).

AAZTA(*t*-BuO)₄-Ph-NCS (0.163 g, 0.21 mmol) was reacted with the free secondary amine of the diBoc-protected diethylenetriamine: the compound, dissolved in 2 mL of DCM, was added to a solution of *N,N*-diBoc-diethylenetriamine (**1**) (0.750 mL, 0.21 mmol) and 35 μL of *N,N*-diisopropylethylamine (DiPEA, 0.20 mmol) in DCM (5 mL), slowly stirred at RT overnight. The solution was concentrated *in vacuo* and the product was then recovered by washing it thoroughly with water with 2-3 drops of a concentrated

HCl solution to aid the removal of DiPEA (3 x 20 mL). The organic phase was then dried with Na₂SO₄ and evaporated *in vacuo* until a yellowish solid was obtained (AAZTA(*t*-BuO)₄-Ph-DETA-Boc₂ (2), 0.182 g, 0.168 mmol, 80% yield).

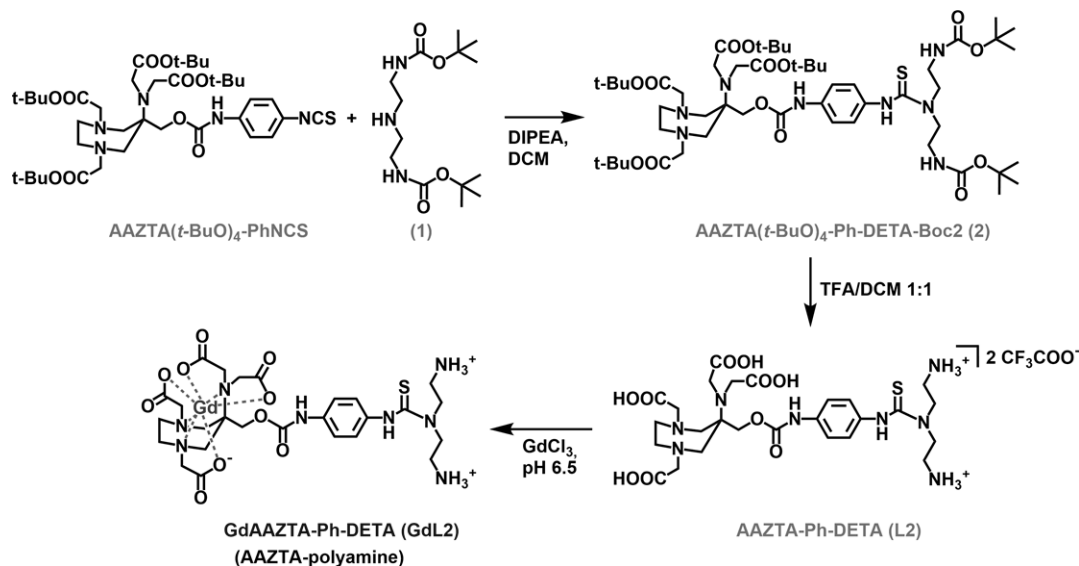
The simultaneous deprotection of *tert*-butyl ester and Boc groups was accomplished by reacting the intermediate AAZTA(*t*-BuO)₄-Ph-DETA-Boc₂ (2) (0.182 g, 0.168 mmol) with a 1:1 mixture solution of 15 mL of DCM and 15 mL of TFA at 0 °C, then slowly stirred at RT overnight. The solution was concentrated *in vacuo* and the product (AAZTA-Ph-DETA, **L2**) was then recovered by washing it thoroughly with diethyl ether (3 x 10 mL) and then dried *in vacuo* until a yellowish solid was obtained in a quantitative yield.

Finally, AAZTA-Ph-DETA (**L2**) (0.140 g, 0.22 mmol) and GdCl₃·6H₂O (0.047 g, 0.22 mmol) were dissolved at RT in 16.5 mL of ultrapure water and then the pH of the solution was brought to 6.5 with a NaOH solution. The reaction mixture was then stirred at RT overnight. After that, the pH was again corrected from 6.5 to 10 to precipitate unchelated Gd³⁺ ions as Gd(OH)₃, which was eliminated by centrifugation (10000 rpm for 5 min) and filtration through 0.2 μm filters. The pH of the complex solution was finally adjusted to 7 with a HCl solution and lyophilized overnight until a yellowish solid (Gd**L2**) was obtained (Scheme 3).

➤ *N,N*-diBoc-diethylenetriamine (1):

- HPLC-MS ESI⁺ (*m/z*) = 304.52 [(M + H)⁺]; calculated C₁₄H₂₉N₃O₄ = 303.40.
- ¹H-NMR (CDCl₃) 500 MHz, δ [ppm] = 7.69 (s, 1H, NHCHN imidazole by-product), 7.10 (s, 2H, NHCHCHN imidazole by-product), 3.20 (m, 2H, NHCH₂), 2.70 (m, 2H, CH₂NH), 1.44 (s, 18H, CH₃).
- ¹³C-NMR (CDCl₃) 100 MHz, δ [ppm] = 156.2 (C=O), 135.0 (NHCHN imidazole by-product), 122.1 (NHCHCHN imidazole by-product), 89.4 (C(CH₃)₃), 48.8-40.1 (CH₂), 28.4 (CH₃).

- AAZTA(*t*-BuO)₄-Ph-DETA-Boc₂ (2):
- HPLC-MS ESI⁺ (*m/z*) = 1081.8 [(M + H)⁺]; calculated C₅₂H₈₈N₈O₁₄S = 1081.4.
 - ¹H-NMR (CDCl₃) 500 MHz, δ [ppm] = 11.40 and 9.30 and 7.30 (s, 4H, NH), 8.01-7.52 (s, 4H, CH aromatic ring), 2.50-4.50 (m, 26H, CH₂), 1.51 (s, 54H, CH₃).
 - ¹³C-NMR (CDCl₃) 100 MHz, δ [ppm] = 182.2 (C=S), 172.8 and 170.8 and 153.3 (C=O), 135.7 (quaternary C aromatic ring), 126.5 and 118.3 (CH aromatic ring), 80 (quaternary C(CH₃)₃), 68.3 (quaternary C-N), 68.0-38.0 (67.7, 62.2, 58.9, 51.5, 38.9) (CH₂), 29.1 (CH₃).
- AAZTA-Ph-DETA (L2):
- HPLC-MS ESI⁺ (*m/z*) = 657.5 [(M + H)⁺]; calculated C₂₆H₄₀N₈O₁₀S = 656.7.
 - ¹H-NMR (D₂O) 500 MHz, δ [ppm] = 7.41 and 7.28 (s, 4H, CH aromatic ring), 4.52-3.00 (m, 26H, CH₂), 1.20 (s, 2H, NH₂).
 - ¹³C-NMR (D₂O) 100 MHz, δ [ppm] = 182.7 (C=S), 176.8 and 171.4 and 154.6 (C=O), 136.2 (quaternary C aromatic ring), 120.6 and 118.3 (CH aromatic ring), 58.9 (quaternary C-N), 62.0-35.0 (61.6, 58.0, 53.1, 51.7, 47.9, 36.6) (CH₂).
- GdL2: HPLC-MS ESI⁻ (*m/z*) = 746.0 and 608.5 {fragments of [(M + K - 2H)]⁻}; calculated C₂₄H₃₆GdN₈O₁₀S = 809.9 (100.0 %) (isotopic distributions consistent with Gd³⁺).



Scheme 3. Synthetic pathway for the preparation of **L2** and **GdL2**. (Adapted from: "S. Marchesi et al., Dalton Trans., 2018, 47, 7896")

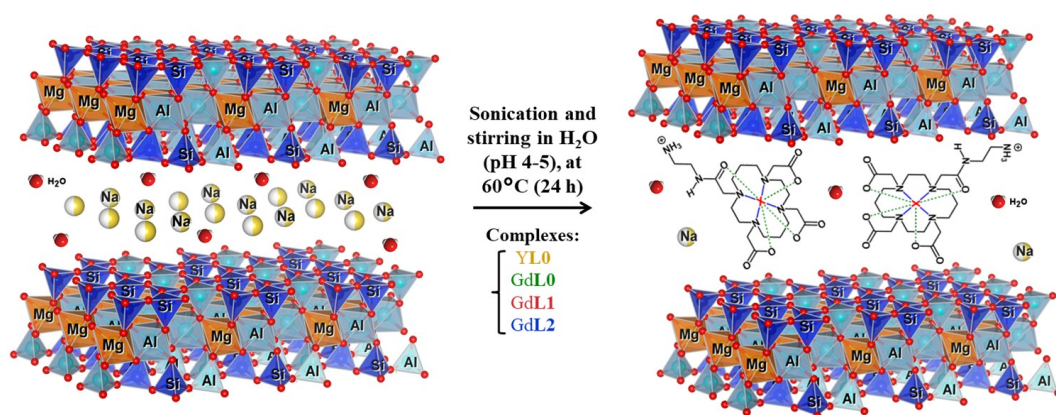
4.2.3 Intercalated materials

The hybrid organic-inorganic intercalated saponite clays were prepared by ionic exchange of a fraction of Na^+ ions located in the interlayer space of a sodium-exchanged synthetic nanosized saponite (Na-SAP) with the relative metal chelates.

- Preparation of paramagnetic GdLn/SAP clays:** The intercalation procedures of **GdL0**, **GdL1** and **GdL2** chelates in the interlayer of synthetic sodium-saponite Na-SAP were optimized following procedures reported in the literature for similar systems (Scheme 4).⁹ The Gd^{3+} -complexes were added in a molar quantity equal to the CEC of the saponite (37.3 ± 1.8 meq/100 g). In details, 0.300 g of Na-SAP were dispersed in 35 mL of ultrapure water in a round-bottom glass flask, which was placed in a crystallizer with water. The dispersion was then subjected to the following treatment: 1 h of sonication (introducing the tip of the sonicator in the water bath), 2 h of magnetic stirring with Teflon rod (placed inside the flask) and a mechanical stirrer and the last hour of sonication. During the 3th h, a specific amount of each chelate (**GdL0**: 0.071 g, 0.113 mmol;

GdL1: 0.090 g, 0.150 mmol; GdL2: 0.173 g, 0.214 mmol) was dissolved each in 10 mL of ultrapure water and the pH was brought to 4-5 with a 0.1 M HCl solution. At the end of the last hour, the sonication was stopped and the aqueous solution of the selected chelate was transferred into the flask, controlling the pH (it needed to be between 4-5). The reaction mixture was then stirred at 60 °C for 20 h. After this time, the product was filtered, washed with hot ultrapure water up to neutral pH and dried in an oven overnight at 100 °C. The so-produced materials, called GdL0/SAP, GdL1/SAP and GdL2/SAP respectively, were finally obtained.

- **Preparation of diamagnetic YL0/SAP clay:** The intercalation of YL0 in the Na-SAP was carried out with same procedure applied for GdLn/SAP, with the YL0 added in a molar quantity equal to the CEC of saponite (37.3 ± 1.8 meq/100 g): Na-SAP (0.300 g), ultrapure water (40 mL for the dispersion of Na-SAP and 10 mL for YL0), YL0 (0.267 g, 0.476 mmol); the final material, named YL0/SAP, was finally obtained (Scheme 4).



Scheme 4. Schematic view of the preparation of intercalated paramagnetic and diamagnetic saponite clays. In the scheme is reported the synthesis of XL0/SAP ($X = Y^{3+}$ or Gd^{3+}).

4.3 Results and Discussion

4.3.1 Characterization of GdL1/SAP and GdL2/SAP materials

The Gd³⁺ content, determined by inductively coupled plasma mass spectrometry (ICP-MS) after mineralization of the solids in acidic media, is comparable for the paramagnetic GdLn/SAP materials, and assumes the values of 0.05 mmol/g for GdL1/SAP and of 0.06 mmol/g for GdL2/SAP. It is important to note that the amounts of intercalated Gd³⁺-complexes correspond to *ca.* 15% of the CEC of saponite, estimated to be 37.3 ± 1.8 meq/100 g.¹

The structure and morphology of GdLn/SAP samples were analysed by X-ray powder diffraction (XRPD) (Figure 2) and high-resolution transmission electron microscopy (HRTEM) (Figure 3). XRPD analyses were performed to evaluate the structural order of the clay before and after intercalation and the confinement degree of the Gd³⁺-complexes in the saponite. First, these data clearly indicate that the structure is preserved after intercalation of the metal chelates, as shown by the presence in the XRPD patterns of the reflections assigned to (001), (110)-(020), (004), (130)-(201), (311) and (060) planes, typical of the pristine Na-SAP (Figure 2A, *a*).¹ In addition, a slight shift of the basal plane (001) from $8.23^\circ 2\theta$ (*d*-spacing of 1.07 nm) to $7.80^\circ 2\theta$ (1.13 nm) and $7.50^\circ 2\theta$ (1.18 nm) is evident in the case of GdL1/SAP and GdL2/SAP, respectively (see inset in Figure 2A, *b-c*). This effect can be attributed to the confinement of Gd³⁺-chelates in the saponite gallery.

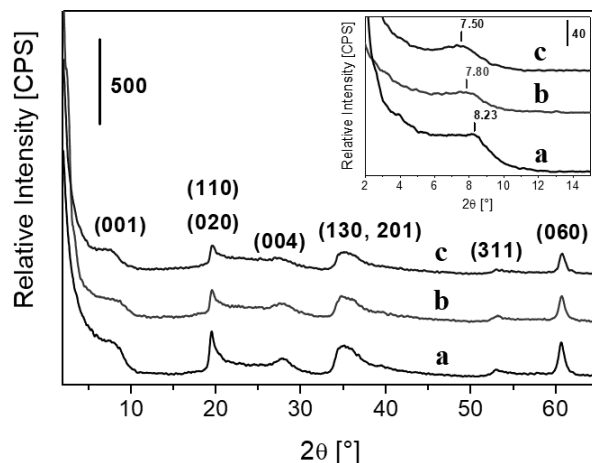


Figure 2. X-ray powder diffraction profiles of Na-SAP (a), GdL1/SAP (b) and GdL2/SAP (c). Diffractograms collected at low angles (2° - 15° 2θ) are reported in the insets. (Adapted from: "S. Marchesi et al., Dalton Trans., 2018, 47, 7896")

HRTEM images of GdL1/SAP, GdL2/SAP and Na-SAP (Figure 3A-C) samples show different levels of spatial organization of the lamellae: single structures with sheet-like morphology tend to aggregate with formation of tactoids of different dimensions. Lamellae present a range of lengths of a few tens of nanometres and show a tendency to stack on top of each other. By analysing HRTEM micrographs at high magnifications (Figure 3D-F) is possible to evaluate the d -spacing distribution of lamellae and to have more insights on the intercalation degree for the hybrid materials. The distribution of the d -spacing values (obtained by counting more than 100 particles) for GdL1/SAP and GdL2/SAP (Figure 3G-I) show quite comparable $d(001)$ broad distributions centred around 1.1-1.2 nm along with a fraction of lamellae with $d(001)$ values up to 1.9 nm, significantly larger than those of Na-SAP (Figure 3I), associated with the presence of Gd^{3+} -chelates confined in the interlayer gallery. In fact, Na-SAP exhibits a narrow distribution centred at 1.1 nm. This result represents a clear indication that the intercalation has occurred.³² Moreover, the simultaneous presence of lamellae with d -spacing typical of pure Na-SAP might be related to the low amount of intercalated GdL complexes.

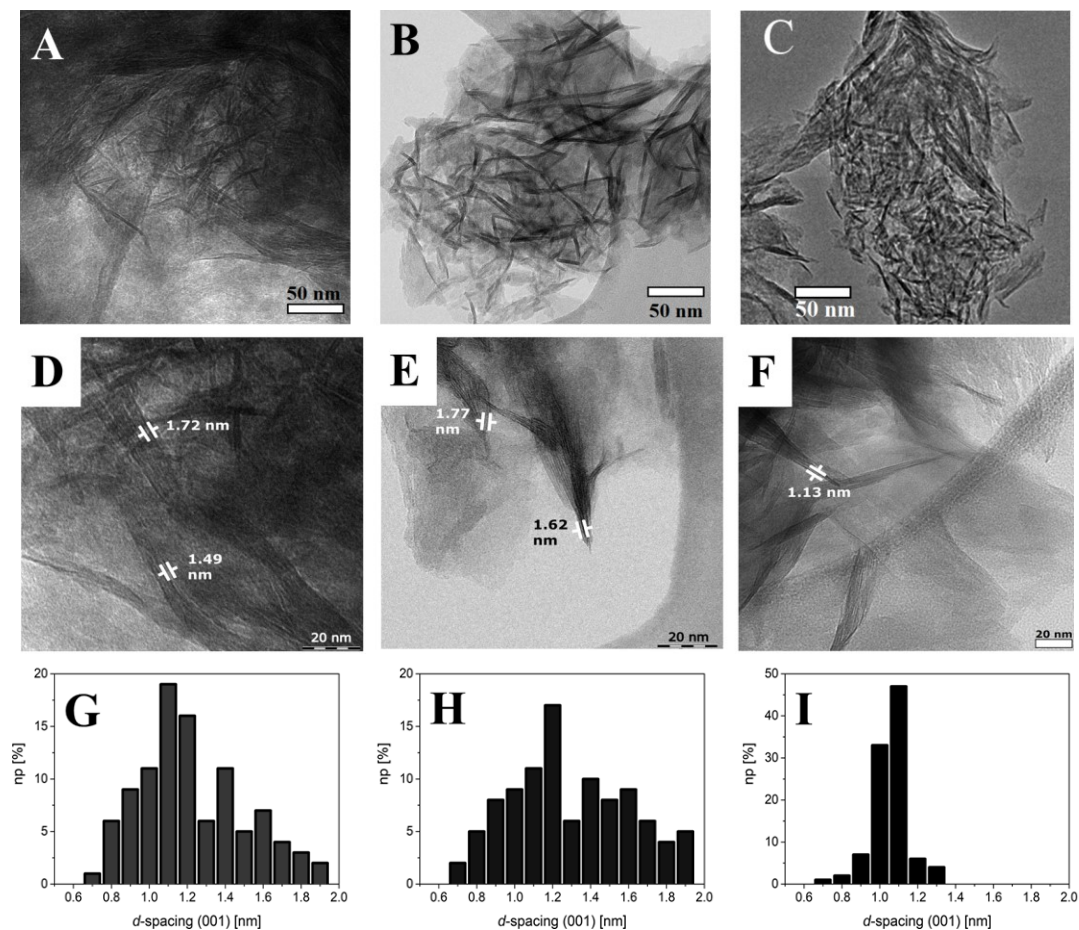


Figure 3. HRTEM images of GdL1/SAP (A), GdL2/SAP (B) and Na-SAP (C). HRTEM magnification are reported in D, E and F, while the relative distributions of the $d_{(001)}$ -spacing values are shown in G, H and I. (*Adapted from: "S. Marchesi et al., Dalton Trans., 2018, 47, 7896"*)

Thermogravimetric analyses (TGA) were performed to confirm the presence of the Gd^{3+} complexes inside the interlayer of the saponite and to evaluate their thermal stability in the intercalated materials. The TGA and the derivative profile (DTG) of Na-SAP collected under oxygen flow (Figure 4) shows two main weight losses: the first one, occurring between 50-150 °C (3.73 wt.%), is associated to water adsorbed on external surface, while the second one, between 150-750 °C (4.48 wt.%), is a consequence of the gradual release of interlamellar water and of the initial dehydroxylation of the layered structure.

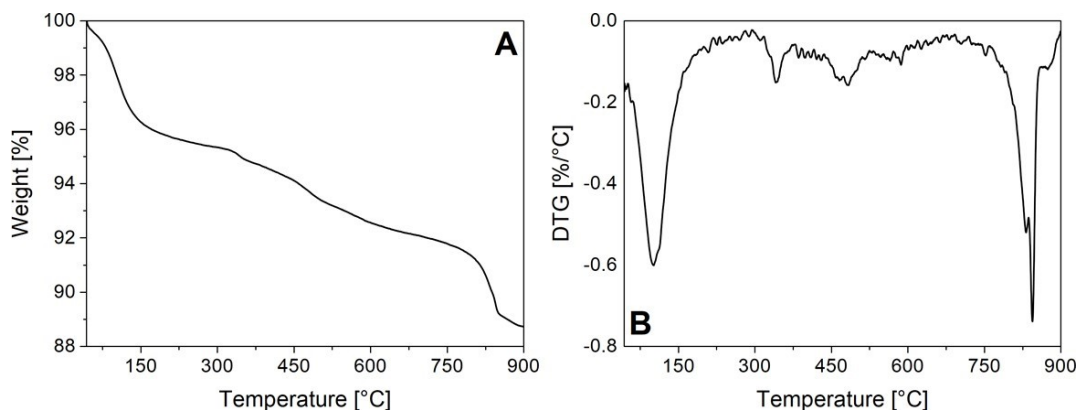


Figure 4. TG (A) and DTG (B) profiles of Na-SAP. The analysis was carried out under oxygen flow. (Adapted from: "S. Marchesi et al., Dalton Trans., 2018, 47, 7896")

The TGA and DTG profiles of GdL1/SAP and GdL2/SAP, collected under oxygen flow (Figure 5), show a first weight loss at 100°C (ca. 4.5 wt.%) related to the physisorbed water. In addition, the thermal profiles of both samples are characterized by a second degradation peak centred at about 340 °C with a weight loss calculated in the 330-750°C range of 7.53 wt.% and 9.69 wt.%, respectively, attributed to the decomposition of the organic fraction and to the release of interlamellar water. The maximum of degradation of the organic fraction in the intercalated saponite shifts of *ca.* 100 °C and 40 °C, if compared to what observed for pure GdL1 and GdL2, respectively. Indeed, DTG profiles of pure GdL1 and GdL2 show a main weight loss at 255 °C and 300 °C, respectively (Figure 5C and D). The delay of the degradation of the organic fraction in the hybrid materials represents a clear and further confirmation that the Gd³⁺-chelates are mainly confined in the interlayer space of the clay (with, probably, a negligible fraction adsorbed on the surface) and then thermally stabilized.

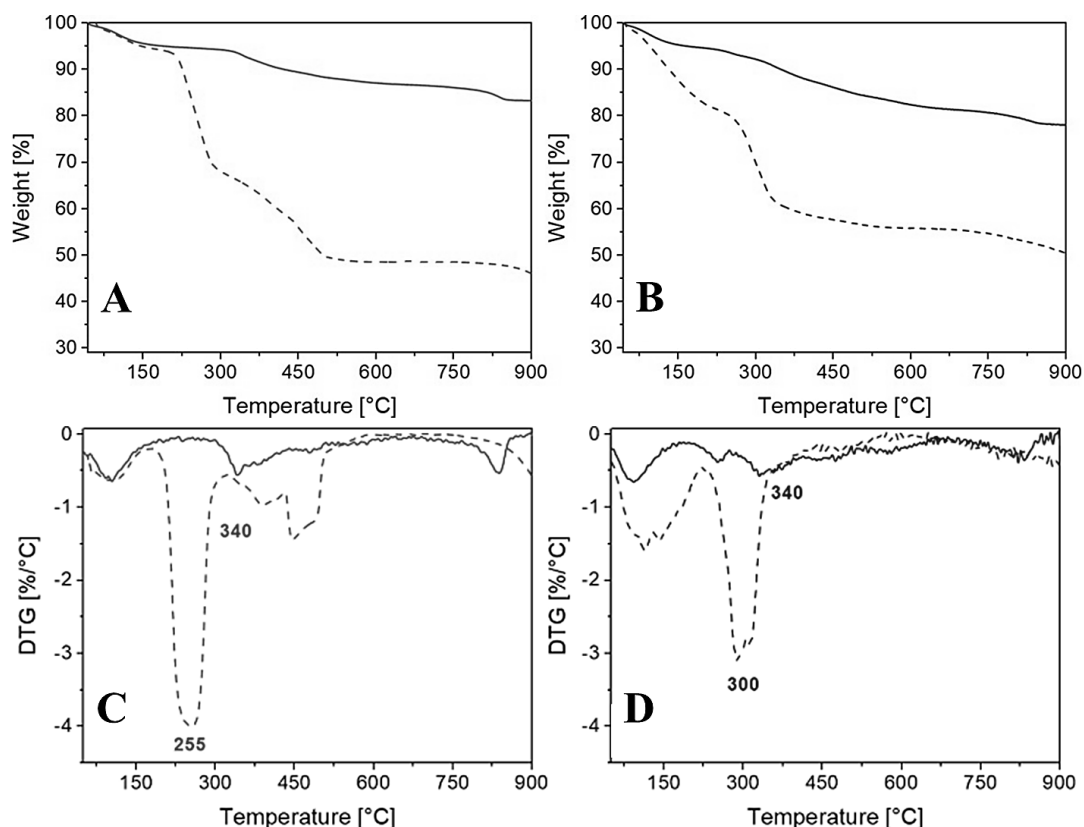


Figure 5. TG profiles of GdL1 (A, *dash*), GdL1/SAP (A, *solid*), GdL2 (B, *dash*) and GdL2/SAP (B, *solid*). DTG profiles of GdL1 (C, *dash*), GdL1/SAP (C, *solid*), GdL2 (D, *dash*) and GdL2/SAP (D, *solid*). The analyses were carried out under oxygen flow. (Adapted from: "S. Marchesi *et al.*, *Dalton Trans.*, 2018, 47, 7896")

Infrared spectroscopy (FTIR) further confirm the presence of the complexes in the paramagnetic clays. Indeed, FTIR spectra of GdL1/SAP and GdL2/SAP samples, collected under vacuum at room temperature showed, besides the typical IR bands of the saponite,¹ additional bands assigned to the vibrational modes of the functional groups (C=C and C=O bonds) of the Gd³⁺ chelates.

Particular attention was addressed to investigate the solvent water-Gd³⁺ interactions that govern the nuclear magnetic relaxometric properties of the free complexes and of the hybrid clays. The best way to carry out the study is through the measurement of the longitudinal relaxivity (r_1) of the water protons of aqueous

solutions/suspensions of GdLn and GdLn/SAP samples by $^1\text{H-NMR}$ relaxometric technique. The parameter r_1 defines the efficiency of a paramagnetic system and is associated with the enhancement of the water proton relaxation rates ($R_1 = 1/T_1$) normalized to the concentration (mM) of the paramagnetic ion, as described in Eq. (1).³⁴

$$r_1 = \frac{\left(\frac{1}{T_1}\right)_{obs} - \left(\frac{1}{T_1}\right)_d}{[Gd]} \quad (1)$$

Prior to the relaxometric analysis, the intercalated clays were dispersed in ultrapure water containing 0.1 wt.% of xanthan gum. The latter is often used to stabilize NPs suspensions by hampering aggregation and sedimentation of particles over time.^{16,33} The hydrodynamic size values of both hybrid clays in aqueous solution, measured by dynamic light scattering (DLS) at 25 °C, were found to be under 100 nm (Figure 6). The suspensions remain also stable and homogeneous for several hours.

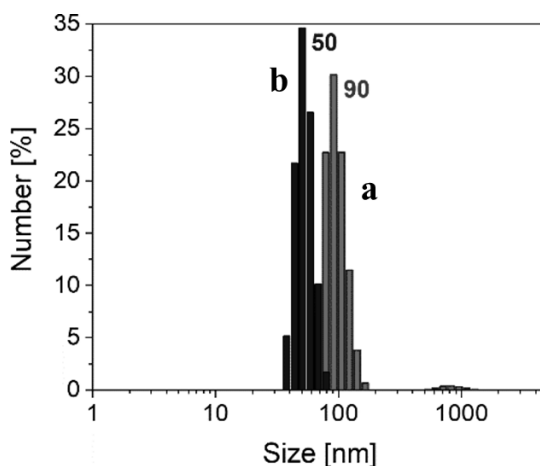


Figure 6. DLS analysis at 25 °C of GdL1/SAP (a) and GdL2/SAP (b) aqueous suspensions containing 0.1 wt.% of xanthan gum. (*Adapted from: "S. Marchesi et al., Dalton Trans., 2018, 47, 7896"*)

Relaxivity is influenced by a number of experimental and molecular parameters, among which the most important are: the applied magnetic field strength B_0 ,

temperature, number q of water molecules in the inner coordination sphere of the paramagnetic ion, the rotational correlation time τ_R of the Gd-O_w vector (O_w is the oxygen nucleus of the bound water molecule), the residence lifetime (or mean residence time) of the bound water molecule(s) $\tau_M (= 1/k_{ex})$, the hydration parameter q/r^6 that describes the number and distance of water molecules in each hydration sphere, the Gd-H_w distance r_{Gd-H} and the parameters describing the electronic relaxation (Δ^2 and τ_v) times (Figure 7).³⁴

Some of the parameters can be directly determined by analysing the magnetic field dependency of r_1 over an extended range of values. The experimental data, collected at a given temperature and pH, are typically reported under the form of an NMRD (Nuclear Magnetic Relaxation Dispersion) profile, which represents the frequency dependence of the longitudinal relaxivity of water protons (r_1). The NMRD profiles of GdL1, GdL2 and of the intercalated materials, measured in the frequency range 0.01-70 MHz and at 37 °C, are reported in Figure 9.

GdL1 and GdL2 show NMRD profiles (Figure 8, *a-b*) characterized by a very similar shape and different amplitude, reflecting their different state of hydration. Relaxivity is constant up to *ca.* 1 MHz, then decreases with a dispersion about 6-8 MHz to finally reach a new plateau at frequencies above 20 MHz. This behaviour is quite typical of low-molecular weight paramagnetic chelates undergoing fast tumbling motion (short τ_R).³⁴ Under these conditions, at high fields (≥ 20 MHz) r_1 is determined essentially by q and τ_R . In fact, the water exchange lifetime τ_M does limit relaxivity of the complexes since they are under the fast exchange condition, as evidenced by the increase of r_1 as the temperature decreases for both complexes (Figure 9).²⁷ Therefore, the higher q value of GdL2 accounts for the greater amplitude of its NMRD profile.

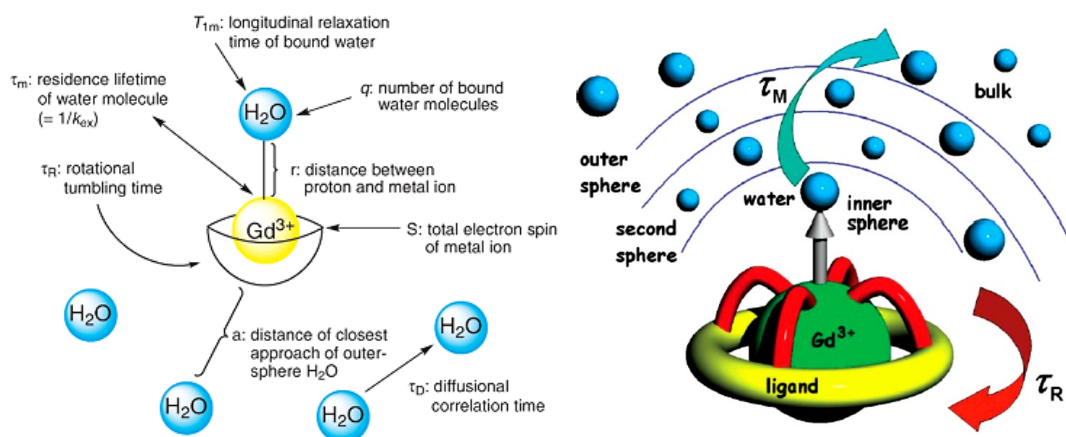


Figure 7. Most of the parameters that governs the r_1 for paramagnetic probes.^{35,36}

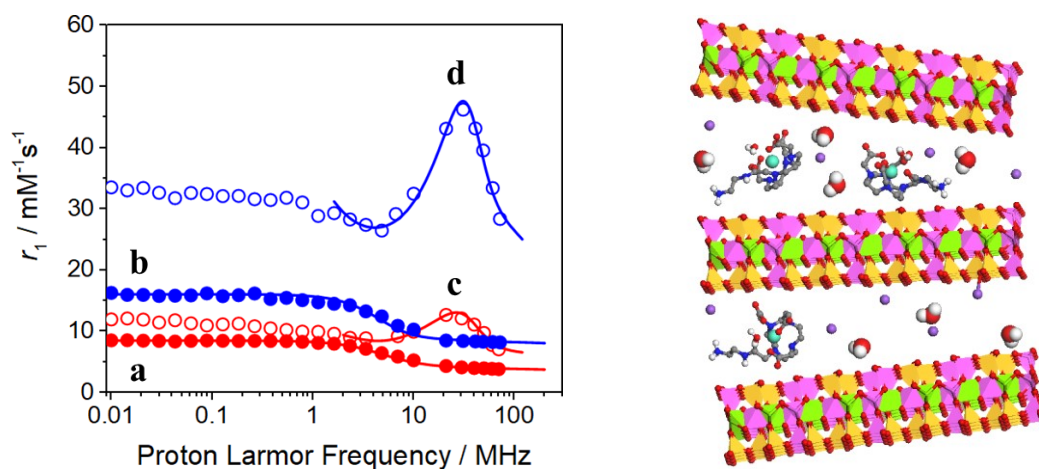


Figure 8. $1/T_1$ ^1H -NMRD profiles of GdL1 (a), GdL2 (b), GdL1/SAP (c) and GdL2/SAP (d) at 37 °C, over the frequency range 0.01-70 MHz and neutral pH. The best-fit curves (solid lines) are calculated using the parameters of Table 1. (Adapted from: "S. Marchesi et al., Dalton Trans., 2018, 47, 7896")

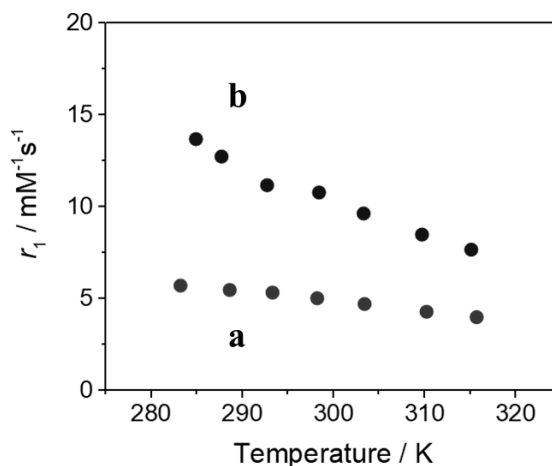


Figure 9. Variable-temperature dependence of r_1 for GdL1 (a) and GdL2 (b), at 20 MHz. (Adapted from: "S. Marchesi et al., Dalton Trans., 2018, 47, 7896")

The ^1H -NMRD profiles of GdL1 and GdL2 (Figure 8, *a-b*) were analysed by fitting the data to the Solomon-Bloembergen-Morgan (SBM) and Freed equations for the inner- (IS) and outer-sphere (OS) proton relaxation mechanisms, respectively.^{37,38} Given the large number of parameters, it is customary to fix some of these at known or reasonable values. In the fitting procedure the distance $r_{\text{Gd-H}}$ was set to 3.0 Å, the distance of closest approach of the outer-sphere solvent molecules to Gd^{3+} , a , was fixed to 4.0 Å and for the water-solute relative diffusion coefficient, D , the value of $3.1 \times 10^{-5} \text{ cm}^2 \text{ s}^{-1}$ (37 °C) was used. In the case of GdL1, the number q of coordinated water molecules was fixed to 1 with lifetime τ_{M} value of 0.7 μs in line with data previously obtained from ^{17}O NMR data.²⁷ For GdL2, q was set to 2 whereas for τ_{M} we used the value calculated for a strictly similar derivative (0.07 μs).³⁹ A good fit of the data was obtained with the rotational correlation times listed in Table 1. In addition to q , the parameter τ_{R} is the most relevant to determine the relaxivity of the complexes.

Data analysis (Table 1) clearly indicates that the increased relaxivity of GdL2 is due not only to the higher hydration state but also to the longer τ_{R} value reflecting its greater molecular size. The values of the electronic relaxation parameters are fully

comparable with those already reported or found in the case of structurally similar complexes.⁴⁰ The actual value of k_{ex} is not relevant because the correlation time is dominated by molecular tumbling.

On the other hand, when the complexes are intercalated in the saponite, their NMRD profiles (Figure 8, *c-d*) change significantly in both form and amplitude. We note that the first inflection point is shifted to lower frequencies (about 2-4 MHz) and is followed by a peak centred around 30 MHz, broad and of modest amplitude for GdL1 and instead narrow and intense for GdL2. At higher fields, r_1 decreases sharply and, at 70 MHz, assumes values like those in the ultra-low field range. Such behaviour is quite characteristic of Gd-based nanometric systems wherein the molecular tumbling is considerably slowed down (long τ_R).⁴¹ Remarkably, at 20 MHz the r_1 of GdL2 is *ca.* 97% higher than that of GdL1 (8.5 vs 4.3 mM⁻¹s⁻¹). After intercalation in the saponite clay, the r_1 of GdL2/SAP peaks at 30 MHz with a value of 46.2 mM⁻¹s⁻¹, which is *ca.* 280% higher than that of GdL1/SAP (12.1 mM⁻¹s⁻¹). Such marked difference between the r_1 values of the two intercalated complexes, along the whole frequency range explored, cannot be attributed only to the different number of water molecules in the inner coordination sphere of the complexes. Rather, it suggests a limiting effect of the exchange lifetime τ_M on relaxivity. This hypothesis is well supported by the temperature dependency of the relaxivity. Unlike GdL1 and GdL2, both GdL1/SAP and GdL2/SAP have r_1 values that increase with increasing temperature (Figure 10). Therefore, the intercalated paramagnetic complexes are in conditions of slow exchange and this has a particularly significant effect on the relaxometric properties of GdL1.

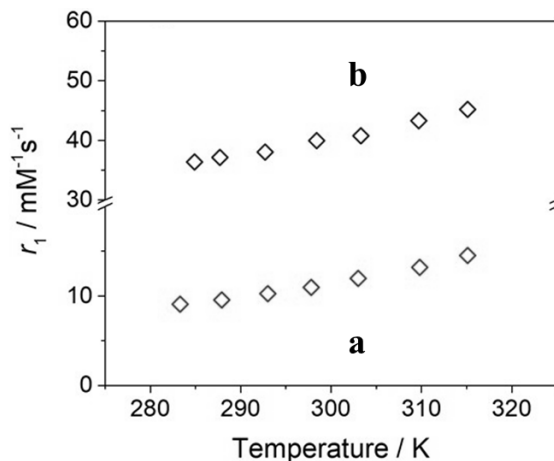


Figure 10. Variable-temperature dependence of r_1 for GdL1/SAP (a) and GdL2/SAP (b) at 20 MHz. (Adapted from: "S. Marchesi et al., Dalton Trans., 2018, 47, 7896")

The NMRD curves of GdL1/SAP and GdL2/SAP (Figure 8, *c-d*) were fitted according to the Lipari-Szabo model-free approach that describes the rotational dynamics in terms of a local (τ_{RL}) and a global (τ_{RG}) rotational correlation times related by the order parameter S^2 . If the motion of the Gd^{3+} complex is independent of the nanoparticle, then $S^2 = 0$; if the complex is completely immobilized in the interlamellar space, then $S^2 = 1$.^{42,43} The global correlation time was fixed to 1 μs , based on earlier findings in the case of Gd-functionalised mesoporous silicas,^{44,45} whereas the local correlation time τ_{RL} for each Gd chelate was left to vary along with the parameters S^2 and τ_{M} . The a , D , r , q parameters were fixed to the same values adopted for the free complexes. The high-fields regions of the NMRD curves are well reproduced and the resultant fitted parameters are given in Table 1 (the full list of parameters is provided in Table S1, *Chapter 8*). The intercalated complexes show a marked difference between global and local correlation times, although the order parameter S^2 is very similar for the two systems. In the interlamellar space, GdL2 seems to have a more restricted rotational motion as evidenced by the value of τ_{RL} about two times longer than that of GdL1. Likely, the delocalization of the positive charge favours a stronger interaction of GdL2 with the negatively charged

lamella. These results are a clear proof that the Gd^{3+} -chelates are intercalated in the saponite gallery, thus confirming TGA, FTIR and HRTEM results.

For both the hybrid clays, we observe a marked increase of the exchange lifetime τ_M , as anticipated by the qualitative analysis of the NMRD profiles. The increase is particularly pronounced for GdL2 but the limiting effect on r_1 is more marked for GdL1, for which τ_M exceeds the value of 1 μs . The decrease in the exchange rate of the coordinated water molecules may be due to the confinement of the complexes in the interlayer space, where the electrostatic interactions between complexes and lamellae also involve the water of the second hydration sphere.⁴⁶ However, it is likely that a limited diffusion of solvent molecules through the interlamellar space may play a non-negligible contribution as also observed for microporous zeolite-based materials.⁴⁷ Hence, these calculated values of τ_M should only be considered as "effective" values that reflect a complex dynamic process of exchange between bulk water, water that diffuses into the interlamellar space and water interacting with the metal ions in the first and second coordination spheres.

Table 1. Selected best-fit parameters obtained from the analysis of $1/T_1$ ^1H -NMRD profiles (37 °C) for GdL1, GdL2, GdL1/SAP and GdL2/SAP samples. A table with all the parameters used in the fit analysis is reported in Table S1 in *Chapter 8*. ^aFixed during the best fit procedure. (*Adapted from: "S. Marchesi et al., Dalton Trans., 2018, 47, 7896"*)

	$^{20}r_1$ [mM ⁻¹ s ⁻¹]	τ_{RL} [ns]	τ_{RG} [ps]	τ_M [μs]	S^2
GdL1	4.3	/	74±2	0.7 ^a	/
GdL2	8.5	/	92±3	0.07 ^a	/
GdL1/SAP	12.4	0.28±0.04	1 μs^a	1.08±0.10	0.26±0.07
GdL2/SAP	43.1	0.60±0.03	1 μs^a	0.30±0.06	0.24±0.02

Finally, through relaxometric methods we tested the stability of the hybrid nanoparticles in several aqueous suspensions of varying complexity: ultrapure water, PBS 0.01 M (phosphate buffer saline), HSA (human serum albumin) and

reconstituted Human Serum (SeronomTM). The r_1 of paramagnetic clays was monitored as a function of time at the proton Larmor frequency of 20 MHz and at 25 °C and 37 °C. In water medium at 25 °C, the r_1 undergoes only a slight decrease during the first hour, and then stabilizes up to 24 h. This behaviour seems related to process of aggregation of particles rather than to a partial release of the intercalated complex: therefore, this underlines a good stability of the hybrid materials. In the other matrixes at 37 °C, after 1 h the r_1 values of the GdL1/SAP and GdL2/SAP in PBS do not show any appreciable variation, while in HSA a slight decrease was observed (Figure 11). Furthermore, in SeronomTM we measured a small decrease of r_1 of *ca.* 20% for both GdL1/SAP and GdL2/SAP. However, this decrease occurs only initially and r_1 reaches a plateau value that remains constant over at least 24 h. Even in this case, this phenomenon is not clearly due to a release of the complexes from the hybrid material. On the contrary, it seems plausible that it is the result of a perturbation of the dynamics of water exchange by some of the constituents of this complex matrix.

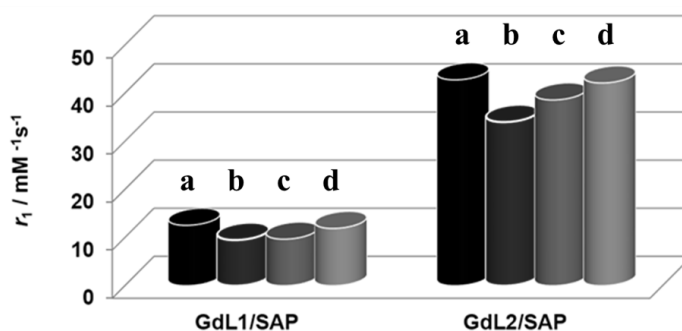


Figure 11. Plot of r_1 at 20 MHz and 37 °C of GdL1/SAP and GdL2/SAP in ultrapure water (a), Human Serum (SeronomTM, b), HSA (human serum albumin, c) and PBS 0.01 M (d) matrices after 1h of suspension stabilization. (Adapted from: "S. Marchesi et al., Dalton Trans., 2018, 47, 7896")

4.3.2 Characterization of GdL0/SAP and YL0/SAP materials

The Gd^{3+} and Y^{3+} loading in the intercalated materials, determined by ICP-MS after mineralization of the solids in acidic media, were found to be 0.05 mmol/g for GdL0/SAP and 0.03 mmol/g for YL0/SAP, corresponding to an intercalated amount of *ca.* 10-15 % of the CEC of saponite (37.3 ± 1.8 meq/100 g).

XRPD analyses were carried out on GdL0/SAP sample in order to evaluate the structural order of the paramagnetic material after the intercalation process (Figure 12). After intercalation of GdL0 in Na-SAP solid, the basic structure of the clay is preserved as observed from the presence in the XRPD pattern of the typical signals of the pristine saponite. The basal plane (001) shifts from 8.23° 2θ (d -spacing of 1.07 nm) to 7.60° 2θ (1.16 nm) (see inset in Figure 12, *b*). This indicates the success on the confinement of the GdL0 in the interlayer space of saponite, as already observed for the previous intercalated materials (Figure 2).⁴⁸

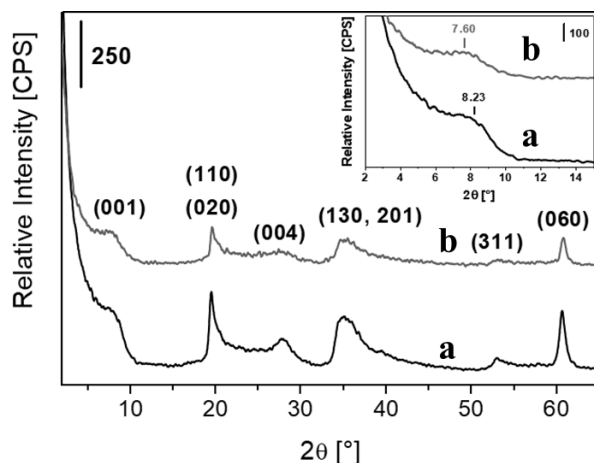


Figure 12. X-ray powder diffraction profiles of Na-SAP (*a*) and GdL0/SAP (*b*). Diffractograms collected at low angles (2° - 15° 2θ) are reported in the insets.

The FTIR spectra of GdL0/SAP sample, collected under vacuum at room temperature, was compared with that of Na-SAP (Figure 13A and B). The typical IR bands of the saponite remain nearly unchanged in the paramagnetic sample, with just minor differences in their intensities. Furthermore, the spectrum of GdL0/SAP

shows the additional bands of the vibrational mode of the functional groups of the Gd^{3+} chelate (Figure 13A, *b*), in particular a large band centred at 1630 cm^{-1} assigned to the C=O stretching of carboxylates groups, with a shoulder at 1650 cm^{-1} attributed to the C=O stretching of the amide group.

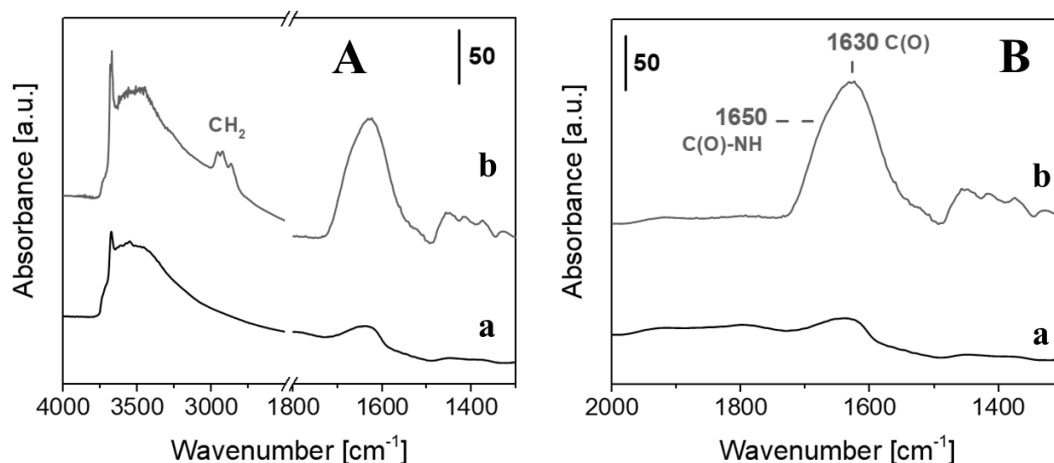


Figure 13. A) Normalized FTIR spectra in vacuum of Na-SAP (*a*) and GdL0/SAP (*b*). In B is reported the magnification of the $2000\text{--}1300\text{ cm}^{-1}$ range of spectra in Frame A.

DLS analyses were performed prior the relaxometric experiments on the paramagnetic clay. The hybrid clay was dispersed in ultrapure water containing 0.1 wt.% of xanthan gum^{16,33} and the measurement was carried out at $25\text{ }^{\circ}\text{C}$. The stable and homogeneous suspension of GdL0/SAP showed a hydrodynamic size of 105 nm, like the value observed for GdL1/SAP (Figure 6, *a*).⁴⁸

A detailed ^1H -NMR relaxometric study on GdL0 and GdL0/SAP aqueous solution/suspension, carried out by analysing the relaxivity r_1 as a function of applied magnetic fields, temperature and over time, was then performed in order to investigate in more detail the molecular dynamics of water molecules into the interlayer space.

The overall r_1 is composed by three distinct contributions: outer-sphere (r_1^{OS}), second-sphere (r_1^{SS}) and inner-sphere (r_1^{IS}), as described in Eq. (2).⁴⁹

$$r_1 = r_1^{OS} + r_1^{SS} + r_1^{IS} \quad (2)$$

These three parameters provide a descriptive model to understand changes in relaxivity in different systems. In particular, the outer-sphere (OS) contribution arises from diffusion of solvent/water molecules past the paramagnetic entity (Figure 8), and it is mainly governed by the solute-water mutual translation diffusion coefficient (D). The GdTETA chelate studied in literature by K. M. Payne *et al.*,⁵⁰ which serves as reference for the amino-functionalized GdTETA synthesized in this study (GdL0), it's an "outer-sphere complex", with no inner-sphere water bound to Gd^{3+} ($q = 0$) and therefore no inner-sphere relaxivity (r_1^{IS}). Indeed, the r_1 is mainly controlled by the OS contribution and generally influenced by the parameters describing the electronic relaxation (Δ^2 and τ_v) times.³⁴

With the purpose of study the parameters that governs the water molecular dynamics in the interlayer of saponite clay, we first collected the $1/T_1$ 1H -NMRD profile of GdL0 in the frequency range 0.01-70 MHz at 25 °C and neutral pH (Figure 14, *b*), and we compared it with that of GdTETA⁵⁰ in the same experimental conditions (Figure 14, *a*). Both GdTETA and GdL0 show very similar NMRD profiles typical of low-molecular weight paramagnetic chelates: r_1 is higher at lower fields and constant up to *ca.* 1 MHz, then decreases as the field increases with a dispersion from 6-10 MHz, and finally reach a new plateau at frequencies above 20 MHz. The presence of the amino-functionalized pendant arm in the GdL0 structure leads to an increase at all fields of the r_1 value compared to GdTETA, and this behaviour is due to a non-negligible effect of second-sphere (SS) contribution to the relaxivity. In general, r_1^{SS} is favoured by increasing either *i*) the second hydration sphere (q^{SS}), *ii*) their proximity to Gd^{3+} centres (r_{Gd-H}^{SS}), *iii*) the residence lifetime of the water close to the chelate and/or *iv*) rotational correlation time of SS (τ_R^{SS}).⁵¹ The values of the electronic relaxation parameters are fully comparable with those of GdTETA.⁵⁰

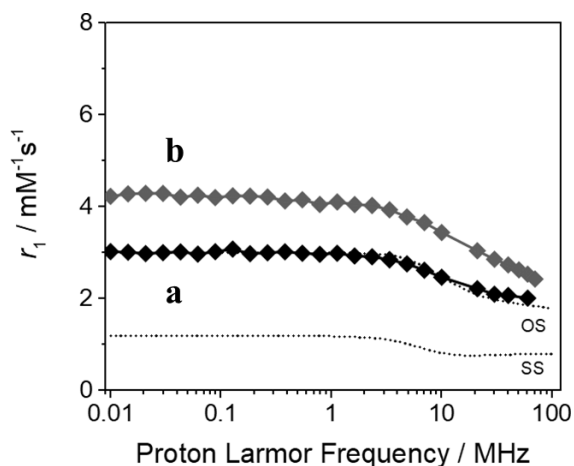


Figure 14. $1/T_1$ ^1H -NMRD profiles of GdTETA (a)⁵⁰ and GdL0 (b) at 25 °C, over the frequency range 0.01-70 MHz and neutral pH. The best-fit curves (solid lines) are calculated using the parameters of Table 2.

The NMRD profile of the intercalated GdL0/SAP (Figure 15, b) changes significantly in both form and amplitude, as previously observed for Gd^{3+} -chelates based on amino-derived DOTA and AAZTA ligands.⁴⁸ The first inflection point is shifted to lower frequencies (about 2-4 MHz) and is followed by a peak centred around 40 MHz, broad and of intense amplitude; at higher fields, r_1 decreases gradually, while maintaining values higher than those at low field range. This behaviour is characteristic of Gd-based nanometric systems wherein the molecular tumbling is considerably slowed down (long τ_R).⁴¹ Remarkably, at 20 MHz the r_1 of GdL0/SAP is *ca.* 217% higher than that of GdL0 (9.68 vs 3.05 $\text{mM}^{-1} \text{s}^{-1}$).

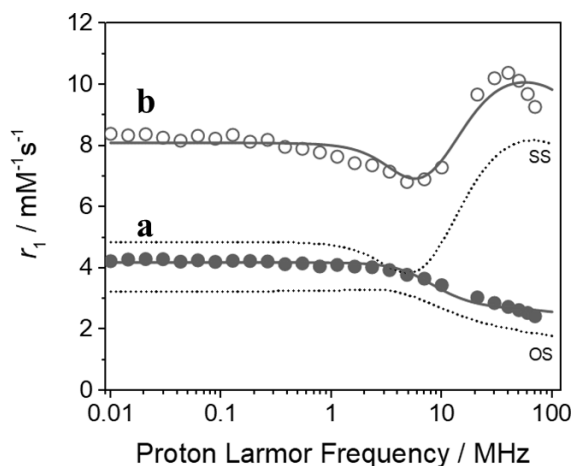


Figure 15. $1/T_1$ ^1H -NMRD profiles of GdL0 (a) and GdL0/SAP (b) at 25 °C, over the frequency range 0.01-70 MHz and neutral pH. The best-fit curves (solid lines) are calculated using the parameters of Table 2.

The marked difference between the r_1 values before and after the intercalation, along the whole frequency range explored, is attributed to the reduced tumbling motion of SS water molecules inside the interlayer space of saponite (τ_R^{SS}). Moreover, the temperature dependency analyses of the r_1 at 20 MHz for GdL0/SAP (Figure 16, b), compared to GdL0 (Figure 16, a), suggests a limiting effect of the water diffusion on relaxivity, due to its increase with the temperature in the 280-315 K range. The interlayer-bulk water exchange is largely controlled and limited by water diffusion mechanisms in the interlamellar region of saponite, also observed for microporous zeolite-based materials,⁴⁷ and these slow down the overall magnetization transfer process (dipolar interactions) from the paramagnetic Gd^{3+} entities to the bulk water.

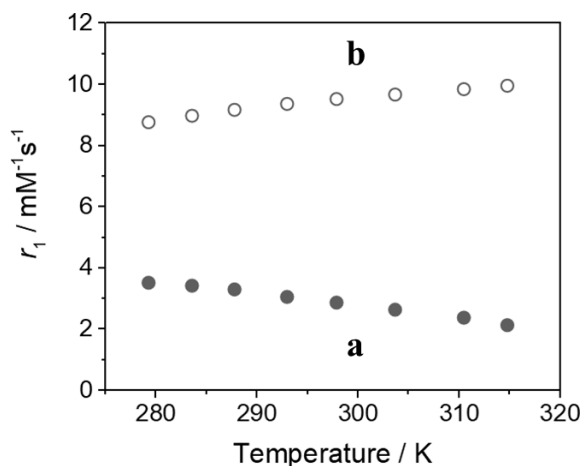


Figure 16. Variable-temperature dependence of r_1 for GdL0 (a) and GdL0/SAP (b), at 20 MHz.

The ^1H -NMRD profiles of GdL0 and GdL0/SAP, compared to GdTETA,⁵⁰ were analysed by fitting the data according to the Solomon-Bloembergen-Morgan (SBM), which includes the second-sphere (SS) parameters, and Freed equations for the outer-sphere (OS) proton relaxation mechanisms.^{37,38} Given the large number of parameters, it is customary to fix some of these at known or reasonable values. In the fitting procedure. The distance of closest approach of OS solvent molecules to Gd^{3+} (a) was fixed to 4.0 Å and for the water-solute relative diffusion coefficient (D) the value of $2.24 \times 10^{-5} \text{ cm}^2 \text{ s}^{-1}$ (25 °C) was used. The NMRD curves are well reproduced and the resultant fitted parameters are given in Table 2; the full list of parameters is provided in Table S2, *Chapter 8*.

While the NMRD profile of GdTETA is reasonably well modelled by a purely OS contribution,⁵⁰ the data of GdL0 and GdL0/SAP were well fitted considering the contribution of the SS parameters. A good fit of the data for GdL0/SAP was obtained with the SS rotational correlation time τ_R^{SS} of 375 ps, almost five times longer than the value obtained for GdL0 (76 ps), an indication of a more restricted rotational motion of the water molecules in the interlayer space of the clay. Additionally, the number of water molecules in the SS increase from 0.52 for the free complex to 1.06 after intercalation, with comparable $r_{\text{Gd-H}}^{\text{SS}}$. These changes, coupled with complex

dynamic process of exchange between bulk water, water that diffuses into the interlamellar space and water interacting with the metal ions in the second coordination sphere, greatly influencing the relaxometric properties of the intercalated **GdL0**.

The results obtained for the paramagnetic clay are also a clear proof of the confinement of **GdL0** in the interlayer of saponite, where the electrostatic interactions between the complex and lamellae also involve the water of the second hydration sphere, as already observed for similar intercalated paramagnetic clays.⁴⁸

Table 2. Selected best-fit parameters obtained from the analysis of $1/T_1$ ^1H -NMRD profiles (25 °C) for GdTETA⁵⁰, **GdL0** and **GdL0/SAP** samples. A table with all the parameters used in the fit analysis is reported in Table S2 in *Chapter 8*.

	$^{20}r_1$ [mM ⁻¹ s ⁻¹]	q^{SS}	r_{Gd-H}^{SS} [Å]	τ_R^{SS} [ps]
GdTETA ⁵⁰	2.2	/	/	/
GdL0	3.1	0.52±0.03	3.34	76±12
GdL0/SAP	9.7	1.06±0.02	3.30	375±11

The stability of the suspension of **GdL0/SAP** both in ultrapure water and in reconstituted Human Serum (SeronormTM) was tested by relaxometric technique by monitoring the r_1 as a function of time over a period of 24 h, at the proton Larmor frequency of 20 MHz. In aqueous medium at 25 °C, the r_1 of the solid remains stable over time, thus underlines a good stability of paramagnetic clay material as observed for previous hybrid clays with GdDOTA and GdAAZTA derivatives.⁴⁸ In SeronormTM matrix at 37 °C, instead, we measured an initial decrease of r_1 of *ca.* 3% compared to the value in aqueous medium, with a final reduction after 24 h of *ca.* 13%. This behaviour is associated to a perturbation of the dynamics of water exchange by some of the constituents of the complex matrix.⁴⁸

Finally, NMR experiments were employed to *i)* assign the proton and carbon resonances of the cationic **YL0** chelate, *ii)* characterize the structure of the clay (in

terms of speciation of Si, Al and H sites), *iii*) determine whether intercalation between the interlayer has occurred and *iv*) probe the molecular interactions between the small molecule and the saponite lamellae. Atomic-level insights into the interaction between organic compounds intercalated into inorganic frameworks are particularly difficult to obtain because of the small crystallite sizes of the saponites, the morphological and structural heterogeneity of the intercalated material, and the complexity of the layer structure. In this sense, ssNMR represents a powerful tool to study such clays since it can access nuclei belonging to both the inorganic layers (^{29}Si , ^{27}Al , ^1H) and the inter-lamellar spaces (^{23}Na , ^1H , ^{13}C), thus providing structural information on the interactions between the complex and the lamellae.¹⁻³ An NMR characterization of **YL0** was first performed in solution by means of homo- and hetero-nuclear correlation spectroscopy (2D ^1H - ^1H COSY, ^1H - ^1H TOCSY and ^1H - ^{13}C HSQC), which allows the unambiguous assignment of the majority of proton and carbon resonances of the chelate. Both ^1H and ^{13}C resonance assignment were easily transferred to spectra of crystalline **YL0** acquired by ssNMR (Figure 17).

Interestingly, the ^1H 1D spectrum acquired on the crystalline **YL0** showed narrow ^1H lines (< 100 Hz), suggesting that the complex undergoes fast molecular motions. In addition, Cross-Polarization (CP) based experiments performed on the crystalline complex resulted unfeasible, also indicating that the complex experiences high degrees of motions in solids, as confirmed by measurements of proton transverse and longitudinal relaxation times. Once **YL0** is intercalated in the interlayer space of the saponite clay, ^1H - ^{13}C CP experiments acquired on **YL0/SAP** became feasible, thus suggesting a reduction of mobility of the complex because of its confinement into the host material gallery.⁵²

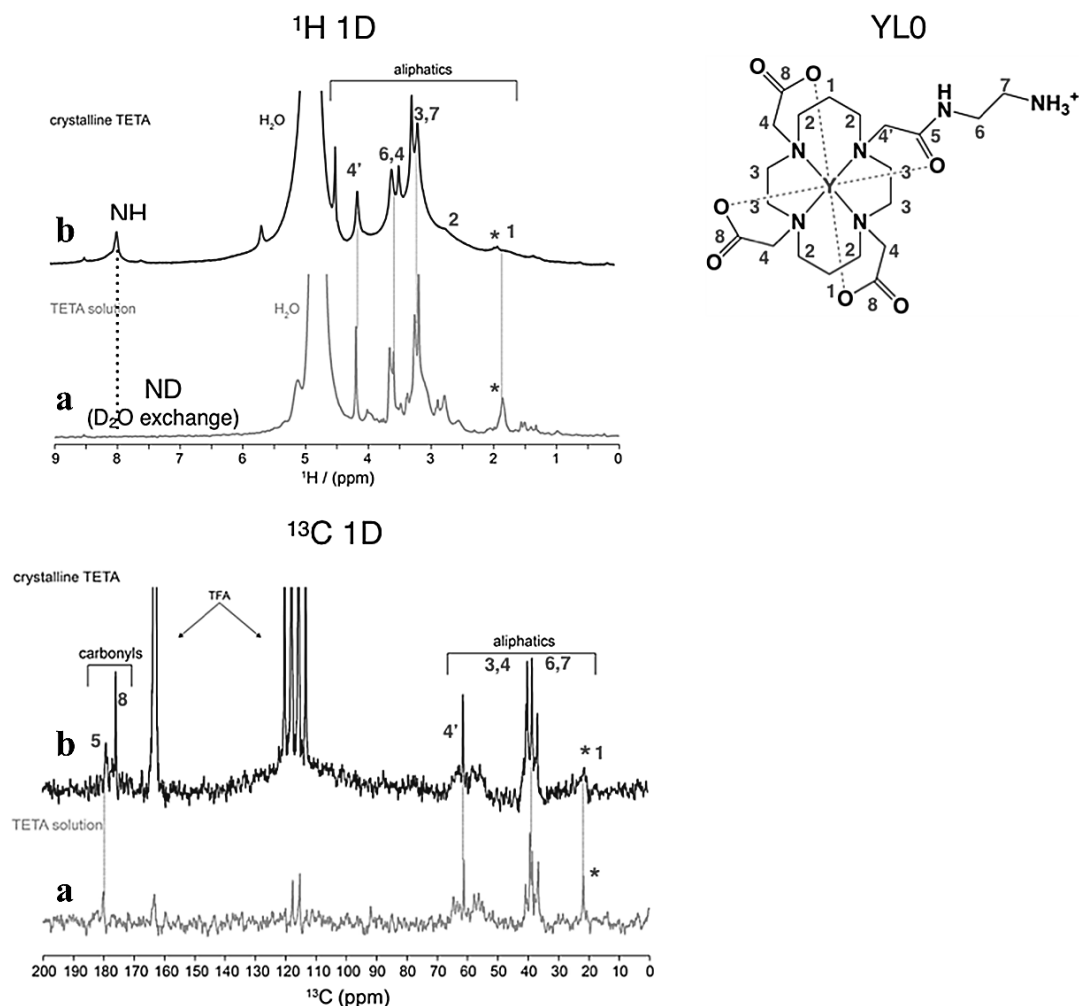


Figure 17. 1D ¹H and ¹³C spectra acquired on YL0 in solution (a) and in solid (b).

²³Na ssNMR studies were carried out to indirectly monitor the occurrence of cation-exchange in the saponite clay. A *ca.* 50% reduction of the interlamellar Na⁺ content following the incorporation of YL0 in the Na-SAP suggests that the complex intercalates between the interlayer spaces of saponite, after displacing Na⁺, to ensure the charge balance (Figure 18).

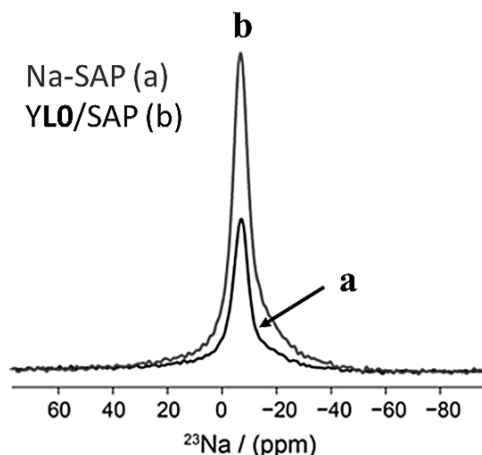


Figure 18. 1D ^{23}Na ssNMR spectra acquired on the Na-SAP (a) and YL0/SAP (b).

^1H MAS ssNMR studies provided particularly useful information on variations of the structure, chemical environment, hydrogen bonds and acidity that may occur upon intercalation of the complex into the saponite clay. In particular, 1D ^1H ssNMR spectra acquired on the Na-SAP and YL0/SAP showed a hydroxyl signal with the same intensity and chemical shift (0.6 ppm)⁵³ and an interlayered water band with *ca.* 20% increased intensity for the YL0/SAP, centred at lower fields (4.2 ppm) with respect to the Na-SAP (3.9 ppm) (Figure 19). The increasing water content in the interlayer spacing of the saponite after intercalation, is due to a higher hydration sphere of the YL0 complex with respect to the Na^+ ion, as well as to an increase of the interlamellar space. Variations of the water chemical shift values reflect the presence of different cations in the clay that may affect the proton acidity. While the retention of the structural hydroxyl group content and chemical shift suggests no modification of the tetrahedral layer structure and demonstrates that OH-groups are not affected by the presence of different type of interlayer cations.

Two-dimensional heteronuclear correlation spectroscopy (^1H - ^{29}Si and ^1H - ^{27}Al HETCOR) were applied to elucidate the molecular interactions between the organic cation and the positively charged lamellae (Figure 23). The incorporation of YL0 in the saponite clay leads to the disappearance of the hydrogen bonded silanols resonances in the 2D ^1H - ^{29}Si HETCOR spectrum, and to the appearance of a new

signal at a ^1H frequency of *ca.* 2 ppm ascribed to the methylene group (1 CH_2) of the organo-complex, which is in close proximity to the $[\text{Q}^3\text{Si}(\text{OAl})]$ sites of the tetrahedral sheet (Figure 20A). This indicates the occurrence of a molecular interaction between **YLO** within the interlamellar space of the saponite clay. On this line, the comparison of ^1H - ^{27}Al HETCOR spectra of the samples with different interlayer cations shows the retention of the same set of resonances, and the appearance of additional correlation peak at *ca.* 2 ppm of ^1H frequency (Figure 20B). This suggests that the tetrahedral/octahedral structural organization and ordering is preserved regardless of the identity of the interlayer cations, and confirms the presence of host-guest interactions, in which the complex is near the tetrahedral layers of the saponite.

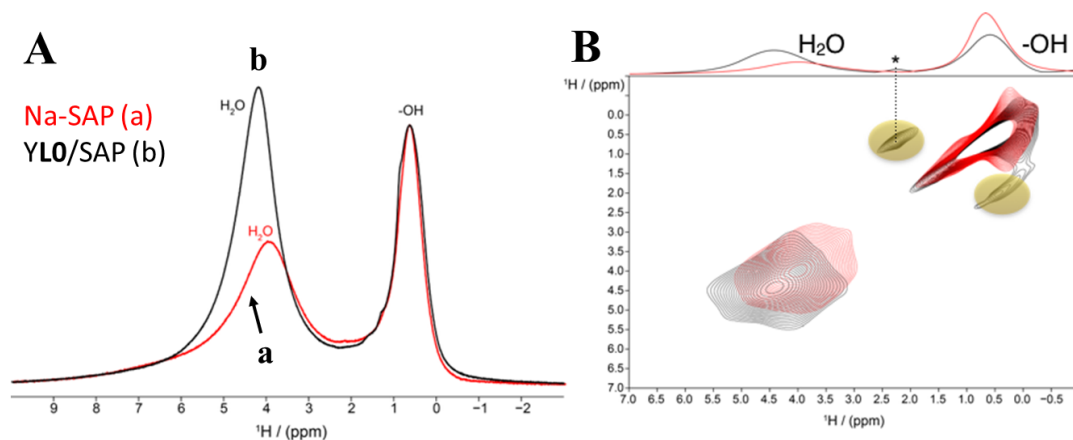


Figure 19. 1D ^1H (A) and 2D ^1H - ^1H Spin Diffusion (B) ssNMR spectra acquired on the Na-SAP (a, red trace) and YL0/SAP (b, black trace).

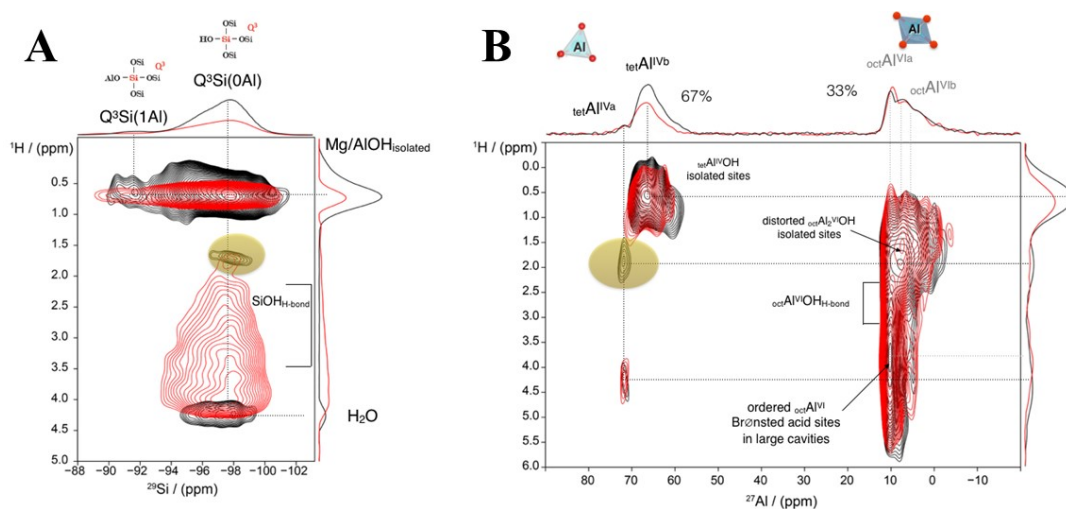


Figure 20. A) 2D ^1H - ^{29}Si HETCOR ssNMR spectrum acquired on Na-SAP (red trace) and YL0/SAP (black trace). B) 2D ^1H - ^{27}Al HETCOR ssNMR spectrum acquired on Na-SAP (red trace) and YL0/SAP (black trace).

4.4 Conclusions

Three stable paramagnetic cationic Gd^{3+} -chelates based on TETA-monoamide (GdL0), DOTA-monoamide (GdL1) and AAZTA-polyamine (GdL2) ligands, and one diamagnetic cationic Y^{3+} -chelate based on the same functionalized TETA ligand (YL0), were successfully confined in the interlayer space of a nanosized synthetic saponite clay. To limit the platelets size at *ca.* 50 nm, the saponite (named Na-SAP) was synthesized through hydrothermal method using a well-defined H_2O/Si molar ratio (110). The cation-exchange procedure was optimized to ensure the intercalation of Gd^{3+} -chelates (*ca.* 15% of the cationic exchange capacity of saponite) and Y^{3+} -chelate (*ca.* 10% of CEC) in the interlamellar region of the layered host. Structural and morphological analyses indicate that the chelates are firmly confined in the interlayer space of the hybrid GdL0/SAP, GdL1/SAP, GdL2/SAP and YL0/SAP materials.

1H -NMR relaxometric investigations of the intercalated clays with Gd^{3+} -complexes in aqueous media, as a function of applied magnetic field strength, temperature and over time, provided insight on the chemical nature and the accessibility of exchange sites of these novel paramagnetic materials, especially on the mechanisms responsible of the magnetic interaction with water and the role of key molecular parameters in the relaxivity enhancement observed. Moreover, additional information of the molecular dynamics of water molecules inside the interlayer space of saponite were also extrapolated by relaxometric analyses on the material intercalated with the Gd^{3+} -chelate without inner-sphere water. Once confined in the interlayer space, the complexes are characterized by an anisotropic and markedly slowed molecular motion. This reduction of the local mobility of the confined complexes is the main factor responsible for improving the longitudinal relaxivity at high magnetic fields as compared to the free Gd^{3+} complexes. However, even the effective exchange rate of the water molecule bound or interacting to Gd^{3+} ions slows down and this partly attenuates the relaxivity enhancement, also

established a decrease of water diffusion through the interlamellar space. Such behaviour clearly indicates the occurrence of strong interactions between the cationic complexes/water molecules and the layered inorganic framework; this also explains the remarkable stability observed in aqueous solutions of varying complexity (water, human serum...). The difference in relaxivity arises from their different hydration state, rate of water exchange and degree of local rotational flexibility.

A more accurate overview of the structural and chemical interaction between the complex/water and the inorganic framework has been carried out by solid-state NMR analyses on a diamagnetic analogue intercalated clay with Y^{3+} -TETA monoamide. Once intercalated, the chelate showed a reduction of its mobility due to the confinement into the host saponite gallery. The reduction of the interlamellar sodium content is a further indication of the incorporation of the Y^{3+} -complex in the interlayer region. Moreover, after intercalation there is an increase of the amount of water in the interlayer due to a higher hydration sphere of the complex respect to the sodium ion. 2D 1H - ^{29}Si and 1H - ^{27}Al measurements suggests that the saponite structural organization is preserved regardless of the identity of the interlayer cations. The data also confirms the presence of host-guest interactions in which the complex is near the tetrahedral layers of the saponite: indeed, the chelate shows a parallel organization to the saponite lamellae.

These features are promising for the development of new materials for potential applications in several fields, as in diagnostic (MRI), in theranostics, for the development of more efficient paramagnetic probes (thanks to the high relaxivity performance \rightarrow better contrast in MR images), for sensor and light-harvesting systems, as catch-and-release systems for the purification of surface waters and for the study of the diffusion phenomena of liquids inside layered systems, in order to increase the knowledge of the physico-chemical properties of other intercalated materials based on lanthanide compounds.

4.5 Notes and References

- 1 D. Costenaro, G. Gatti, F. Carniato, G. Paul, C. Bisio and L. Marchese, *Microp. Mesop. Mater.*, 2012, **162**, 159-167.
- 2 C. Bisio, G. Gatti, E. Boccaleri, G. Superti, H. Pastore and M. Thommes, *Microp. Mesop. Mater.*, 2008, **107**, 90-101.
- 3 C. Bisio, G. Gatti, E. Boccaleri, L. Marchese, L. Bertinetti and S. Coluccia, *Langmuir*, 2008, **24**, 2808-2819.
- 4 M.I. Boyanov, D.E. Latta, M.M. Scherer, E.J. O'Loughlin and K.M. Kemner, *Chemical Geology*, 2017, **464**, 110-117.
- 5 M. Mokhtar, *Materials*, 2017, **10**, 760-772.
- 6 M. Guidotti, R. Psaro, N. Ravasio, M. Sgobba, F. Carniato, C. Bisio, G. Gatti and L. Marchese, *Green Chem.*, 2009, **11**, 1173-1178.
- 7 F. Carniato, C. Bisio, R. Psaro, L. Marchese and M. Guidotti, *Angew. Chem. Int. Ed.*, 2014, **53**, 10095-10098.
- 8 L.A. Utracki, M. Sepehr and E. Boccaleri, *Polym. Adv. Technol.*, 2007, **18**, 1-37.
- 9 F. Carniato, C. Bisio, G. Gatti, E. Boccaleri, L. Bertinetti, S. Coluccia, O. Monticelli and L. Marchese, *Angew. Chem. Int. Ed.*, 2009, **48**, 6059-6061.
- 10 Y.-C. Lee, T.-H. Lee, H.-K. Han, W. J. Go, J.-W. Yang and H.-J. Shin, *Photochem. Photobiol.*, 2010, **86**, 520-527.
- 11 K. V. Rao, K. K. R. Datta, M. Eswaramoorthy and S. J. George, *Angew. Chem. Int. Ed.*, 2011, **123**, 1211-1216.
- 12 F. Olivero, F. Carniato, C. Bisio and L. Marchese, *J. Mater. Chem.*, 2012, **22**, 25254-25261.
- 13 K. J. Balkus Jr. and J. Shi, *Langmuir*, 1996, **12**, 6277-6281.
- 14 X. Chen, Y. Xu, H. Li and B. Liu, *Sens. Actuators B*, 2017, **246**, 344-351.
- 15 M. Jin, D.E.M. Spillane, C. F. G. C. Geraldles, G. R. Williams and S. W. A. Bligh, *Dalton Trans.*, 2015, **44**, 20728-20734.
- 16 A. Sanchez, Y. Echeverria, C.M.S. Torres, G. Gonzalez, E. Benavente, *Materials Research Bulletin*, 2006, **41**, 1185-1191.
- 17 D. Talarico de Araujo, K. J. Ciuffi, E. J. Nassar, M. A. Vicente, R. Trujillano, P. S. Calefi, V. Rives and E. H. de Faria, *J. Phys. Chem. C*, 2017, **121**, 5081-5088.
- 18 S.-J. Ryu, A. Kim, M. D. Kim, S. W. Hong, S. S. Min, J.-K. Lee, H. Jung and J.-H. Lee, *Appl. Clay Sci.*, 2014, **101**, 52-59.
- 19 X. Chen, Y. Wang, R. Chai, Y. Xu, H. Li and B. Liu, *ACS Appl. Mater. Interfaces*, 2017, **9**, 13554-13563.
- 20 D. Yang, Y. Wang, Y. Wang and H. Li, *Sensors and Actuators B*, 2016, **235**, 206-212.
- 21 J. A. Peters and K. Djanashvili, *Eur. J. Inorg. Chem.*, 2012, **2012**, 1961-1974.
- 22 K. J. Balkus Jr. and I. Bresinska, *J. Alloys Compd.* 1994, **207/208**, 25-28.

- 23 S. K. Sur, J. F. Heinsbergen and R.G. Bryant, *J. Magn. Reson. Ser. A*, 1993, **103**, 27-33.
- 24 P. Caravan, J.J. Ellison, T.J. McMurry and R.B. Lauffer, *Chem. Rev.*, 1999, **99**, 2293-2352.
- 25 S.H. Koenig and R.D. Brown III, *Prog. NMR Spectr.*, 1990, **22**, 487-567.
- 26 A. Barge, L. Tei, D. Upadhyaya, F. Fedeli, L. Beltrami, R. Stefania, S. Aime and G. Cravotto, *Org. Biomol. Chem.*, 2008, **6**, 1176-1184.
- 27 L. Tei, G. Gugliotta, Z. Baranyai and M. Botta, *Dalton Trans.*, 2009, **21**, 9712-9714.
- 28 G. Gugliotta, M. Botta and L. Tei, *Org. Biomol. Chem.*, 2010, **8**, 4569-4574.
- 29 M. Rami, A. Cecchi, J.-L. Montero, A. Innocenti, D. Vullo, A. Scozzafava, J.-Y. Winum, and C. T. Supuran, *ChemMedChem*, 2008, **3**, 1780-1788.
- 30 S. Singh, A. K. Tiwari, R. Varshney, R. Mathur, P. P. Hazari, B. Singh and A. K. Mishra, *RSC Adv.*, 2015, **5**, 41977-41984.
- 31 S. P. Rannard and N. J. Davis, *Org. Lett.*, 2000, **2**, 2117-2120.
- 32 C. Bisio, F. Carniato, G. Paul, G. Gatti, E. Boccaleri and L. Marchese, *Langmuir*, 2011, **27**, 7250-7257.
- 33 J. L. Zatz and C. Yarus, *Pharmaceutical Research*, 1986, **3(2)**, 118-121.
- 34 S. Aime, M. Botta and E. Terreno, *Adv. Inorg. Chem.*, 2005, **57**, 173-237.
- 35 P. Hermann, J. Kotek, Kubicek and I. Lukes, *Dalton Trans.*, 2008, **21**, 3027-3047.
- 36 E. Boros, E. M. Galea and P. Caravan, *Dalton Trans.*, 2015, **44**, 4804.
- 37 L. P. Hwang and J. H. Freed, *J. Chem. Phys.*, 1975, **63**, 4017-4025.
- 38 J. H. Freed, *J. Chem. Phys.*, 1978, **69**, 4034-4037.
- 39 G. Gugliotta, G. Gambino, M. Fekete and M. Botta, *Isr. J. Chem.*, 2017, **57**, 887-895.
- 40 G. Gambino, S. De Pinto, L. Tei, C. Cassino, F. Arena, E. Gianolio and M. Botta, *J. Biol. Inorg. Chem.*, 2014, **19**, 133-143.
- 41 A) M. Botta and L. Tei, *Eur. J. Inorg. Chem.*, 2012, **12**, 1945-1960; B) E. Cittadino, M. Botta, L. Tei, F. Kielar, R. Stefania, E. Chiavazza, S. Aime and E. Terreno, *ChemPlusChem*, 2013, **78**, 712-722.
- 42 G. Lipari and S. Szabo, *J. Am. Chem. Soc.*, 1982, **104**, 4546-4559.
- 43 G. Lipari and S. Szabo, *J. Am. Chem. Soc.*, 1982, **104**, 4559-4570.
- 44 F. Carniato, L. Tei, W. Dastru, L. Marchese and M. Botta, *Chem. Commun.*, 2009, **10**, 1246-1248.
- 45 F. Carniato, L. Tei, M. Cossi, L. Marchese and M. Botta, *Chem. Eur. J.*, 2010, **16**, 10727-10734.
- 46 X. D. S. Zhou, R. Marzke, Z. Peng, I. Szilágyi and S. K. Dey, *Inorg. Chem.*, 2019, **58**, 12112-12121.
- 47 C. Platas-Iglesias, L. Vander Elst, W. Zhou, R. N. Muller, C. F. G. C. Geraldes, T. Maschmeyer and J. A. Peters, *Chem. Eur. J.*, 2002, **8**, 5121-5131.

- 48** S. Marchesi, F. Carniato, C. Bisio, L. Tei, L. Marchese and M. Botta, *Dalton Trans.*, 2018, **47**, 7896-7904.
- 49** A. Beeby, I. M. Clarkson, R. S. Dickins, S. Faulkner, D. Parker, L. Royle, A. S. de Sousa, J. A. G. Williams and M. Woods, *J. Chem. Soc., Perkin Trans.*, 1999, **2**, 493-504.
- 50** K. M. Payne, J. M. Wilds, F. Carniato, M. Botta and M. Woods, *Israel Journal of Chemistry*, 2017, **57**, 880-886.
- 51** M. Botta, *Eur. J. Inorg. Chem.*, 2000, **3**, 399-407.
- 52** G. Gonzalez, *Mol. Cryst. Liq. Cryst.*, 2010, **521**, 93-103.
- 53** M. D. Alba, A. I. Becerro, M. A. Castro and A. C. Perdigón, *Chem. Comm.*, 2000, **1**, 37-38.

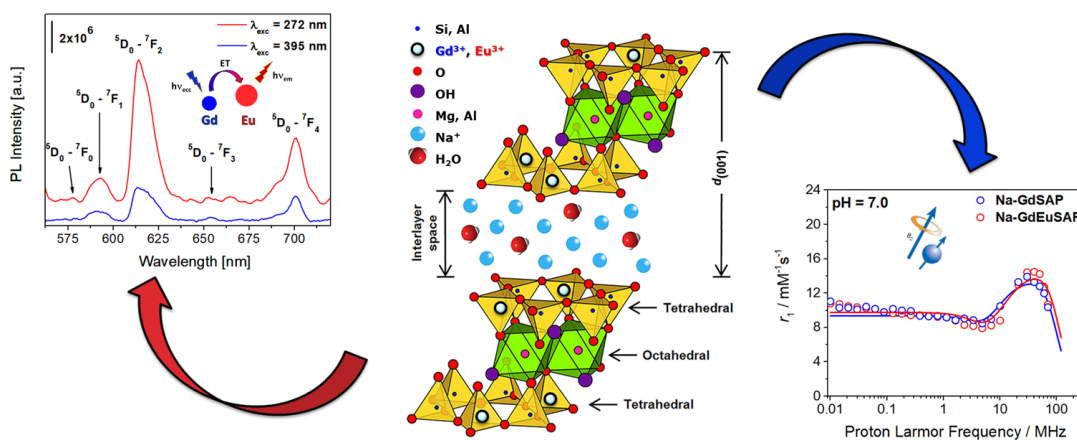
5

“Inclusion of Paramagnetic and Luminescent Lanthanide Ions in the Framework of Synthetic Saponite Clays”

In this chapter, the introduction of two different lanthanides, Gd^{3+} and Eu^{3+} , in form of ions in the tetrahedral in-framework positions of synthetic saponite clays was accomplished by an innovative one-pot (single-step) hydrothermal approach.

The novel materials showed paramagnetic and luminescent properties (see Figure below). The materials were thoroughly characterized by a multi-technique approach aiming to assess their physico-chemical properties.

Information on the local chemical environment surrounding the lanthanides, and their interaction with the water molecules inside the interlayer gallery, were extrapolated from a combined solid-state/relaxometric NMR and photoluminescence study, which also provided interesting insights on the final magnetic and light-emitting features. The stability of the solids in different aqueous solutions was also evaluated by relaxometric techniques.



5.1 Introduction

Synthetic saponite clays, of the family of smectites, have stimulated particular interest over the past few decades for application in plentiful scientific and technological fields,¹⁻¹⁵ due to their interesting properties in terms of more controlled chemical composition than natural minerals, high thermal stability, high specific surface area and acidity, low costs and, especially, excellent chemical versatility.¹⁻³ Because of the latter, their physico-chemical properties can be easily fine-tuned by modifying three main domain levels: 1) the particles size and morphology,² 2) the chemical composition of the interlayer space⁴ and 3) the lamellae framework.^{5,6} These modifications can be achieved both *i*) during the synthesis (by an appropriate choice of reactants) and *ii*) with post-synthesis treatments (*i.e.* intercalation of functionalized organometallic compounds or modulation of the surface features). This indicates the possibility to design novel advanced clays with innovative features through the proper selection of guest species (*i.e.* metal ions, dyes...).

In particular, the introduction of one or more *f*-block elements (*i.e.* gadolinium/ Gd^{3+} , europium/ Eu^{3+} , terbium/ Tb^{3+} ...), as ions or complexes,¹³⁻²⁰ in the clay structure allows to develop novel metal-functionalized layered systems with interesting properties, especially with higher thermal stability and mechanical strength than isolated ions or complexes. The resulting materials can assume magnetic properties or exhibit light-emitting features, for example, depending on the nature of the lanthanide selected for their preparation.

Recently, we reported the intercalation of different Gd^{3+} -complexes inside synthetic saponite clays through a cation-exchange process of the interlayer Na^+ ions with the cationic chelates (see also *Chapter 4* for more details).⁴ ^1H -NMR relaxometric study on the paramagnetic clays give important information on the molecular characteristics of the confined chelates and on the water molecular dynamics inside the interlayer space of the saponite, which is largely influenced by diffusional factors.⁴

However, the preparation of this new class of intercalated clay materials has two main limitations: 1) the relatively high costs of the Gd^{3+} -chelates, whose synthesis normally require several steps, quite amount of different reactants and numerous purification procedures; 2) the long preparation times to obtain the a single paramagnetic clay (see *Chapter 4* for more details).

Starting from these knowledges and to overcome the limitations of the previous intercalated clays described above, in the first part of this chapter we explored the possibility to introduce lanthanide elements, in form of simple ions, directly in the inorganic framework of saponite clays in one single-step of synthesis. Besides, in this way the interlayer space remains open to further functionalization (i.e. introduction of functionalized compounds...).

In detail, two different lanthanide ions, Gd^{3+} and Eu^{3+} , were inserted in the tetrahedral in-framework (*T*-layers) of a synthetic saponite clay by means of an innovative *one-pot* solvothermal procedure, followed by sodium-exchange process.²⁴⁻²⁶ The resulting material, hereafter Na-GdEuSAP, showed both paramagnetic and optical/luminescent properties, conferred by gadolinium and europium respectively. Clays with only Gd^{3+} or Eu^{3+} were also prepared as references (named Na-GdSAP and Na-EuSAP, respectively). These properties can be exploited synergistically for *i*) several applications in optoelectronic and diagnostic fields and *ii*) in order to have a more comprehensive view of the chemical environment surrounding the lanthanides itself. Besides the paramagnetic features of Gd^{3+} , well explored in *Chapter 4*, the Eu^{3+} was chosen because 1) it shares similar physico-chemical properties with gadolinium (i.e. trivalent state, ionic radius and coordination chemistry), 2) its luminescent features are sensible to changes in the local surroundings, thus information on chemical nature and geometrical aspects of the environment surrounding the metal sites (i.e. hydration state...) can be extrapolated from photoluminescence analyses.¹³⁻¹⁷

Besides, the presence of Gd^{3+} in the same T-layers with Eu^{3+} also give rise to a $Gd^{3+} \rightarrow Eu^{3+}$ metal-to-metal energy transfer (MMET) process, which led to an

increase of the emission of the europium upon excitation of the gadolinium. In order to further improve the luminescence properties of Eu^{3+} ions in the bifunctional Na-GdEuSAP clay, an “antenna system” (1,10-phenantroline, Phen) was intercalated, in the interlayer space of the sample, at different loadings, obtaining the final composite materials hereafter collectively called Phen-GdEuSAP. Na^+ -exchanged saponites (Na-SAP, see *Chapter 3*) intercalated with Phen were also prepared as references (named Phen-SAP). Phen is able coordinate to the metal centres,²⁸ harvesting and transferring energy to the nearby emitting sites of Eu^{3+} through Förster resonance energy transfer (FRET), thus (photo)sensitizing the luminescence of Eu^{3+} sites.²⁷ This non radiative ligand-to-metal energy transfer (LMET) mechanism is based on a phonon-mediated coulombic (dipolar-dipolar) interaction between Phen and Eu^{3+} .

A detailed physico-chemical characterization was performed on all the materials prepared, and attention was devoted to the investigation of their final photophysical and relaxometric properties.

5.2 Experimental Approach

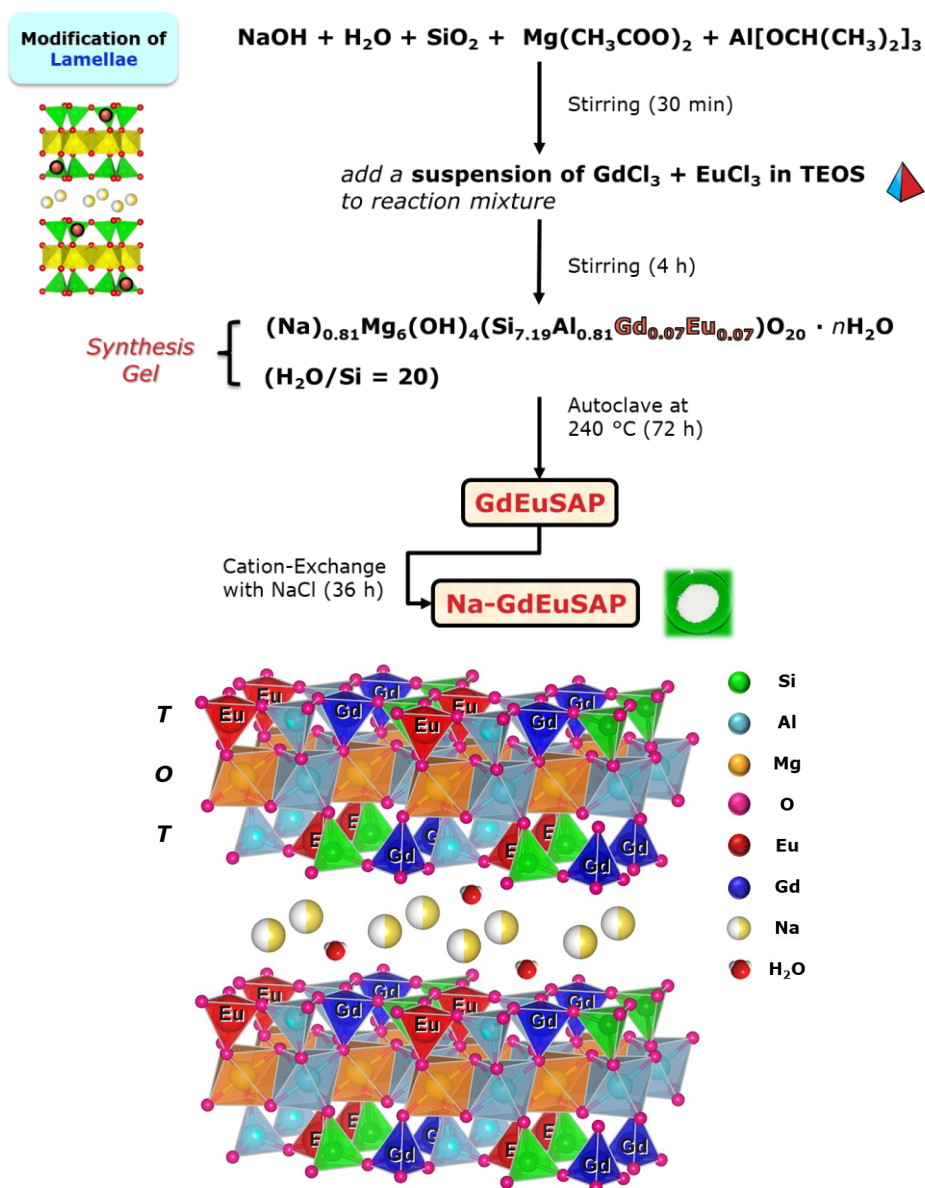
5.2.1 Materials

- **Synthesis of Na-GdEuSAP clays:** synthetic saponite containing Gd^{3+} and Eu^{3+} ions, was synthesized by a modified *one-pot* hydrothermal procedure, adapted from the literature (Scheme 1).²⁴⁻²⁶ A gel with the molar composition of $[\text{SiO}_2:\text{MgO}:\text{Al}_2\text{O}_3:\text{Na}_2\text{O}:\text{GdCl}_3:\text{EuCl}_3:\text{H}_2\text{O}]$ 1:0.835:0.056:0.056:0.01:0.01:20 and $\text{H}_2\text{O}/\text{Si}$ molar ratio of 20 was prepared. In detail, 6.68 g (0.10 mol) of amorphous silica (SiO_2 fumed, 99.8%) were gradually dispersed in a solution prepared by dissolving 0.63 g (0.01 mol) of sodium hydroxide (NaOH) in 45.00 g (2.50 mol) of ultrapure water (equal to 5/6 of the total water content). The obtained gel was then mixed accurately. After 30 min, 24.86 g (0.09 mol) of magnesium acetate tetrahydrate ($\text{Mg}(\text{CH}_3\text{COO})_2 \cdot 4\text{H}_2\text{O}$, 99%) and 3.20 g (0.01 mol) of aluminium isopropoxide ($\text{Al}[\text{OCH}(\text{CH}_3)_2]_3$, $\geq 98\%$) were added to the

reaction mixture. Simultaneously, suspension with 1:1 molar ratio of anhydrous gadolinium chloride (GdCl_3 ; 0.373 g, 0.001 mol) and europium chloride (EuCl_3 ; 0.353 g, 0.001 mol) in tetraethyl orthosilicate (TEOS; 6.03 mL, 0.03 mol) was prepared, the pH was then corrected between 2-3 with 1-2 drops of concentrated sulphuric acid (H_2SO_4) solution and the mixture was left in agitation at RT for 5 min. After this, 0.50 g (0.03 mol) of ultrapure water were added to the suspension, stirred for another 5 min and, finally, introduced into the clay synthesis gel. The remaining ultrapure water (5.00 g, 0.28 mol) was then added to the reaction mixture. After 4 h, the gel, with a pH between 8-9, was introduced into a Teflon cup (125 mL capacity) of an autoclave (Anton Paar 4748) and heated in an oven for 72 h at 240 °C. After hydrothermal treatment, the product was filtered, washed with hot ultrapure water up to neutral pH and dried in an oven overnight at 100 °C.

The so-produced material called GdEuSAP (was submitted to cation-exchange procedure in order to ensure a chemical uniformity of the exchange sites: 2.50 g of GdEuSAP were dispersed in in 250 mL of saturated sodium chloride (NaCl) solution for 36 h at RT to replace all possible cations present (*i.e.* Al^{3+} , Mg^{2+} , H^+) with Na^+ ions in the interlayer space. Then, the final solid (a-GdSAP) was filtered, washed with hot ultrapure water until the complete elimination of chlorides (confirmed by silver nitrate, AgNO_3 , spot test) and dried in an oven overnight at 100 °C (Scheme 1).

- **Synthesis of Na-GdSAP and Na-EuSAP clays:** The preparation of nanosized Na-GdSAP and Na-EuSAP samples followed the same procedure described above.

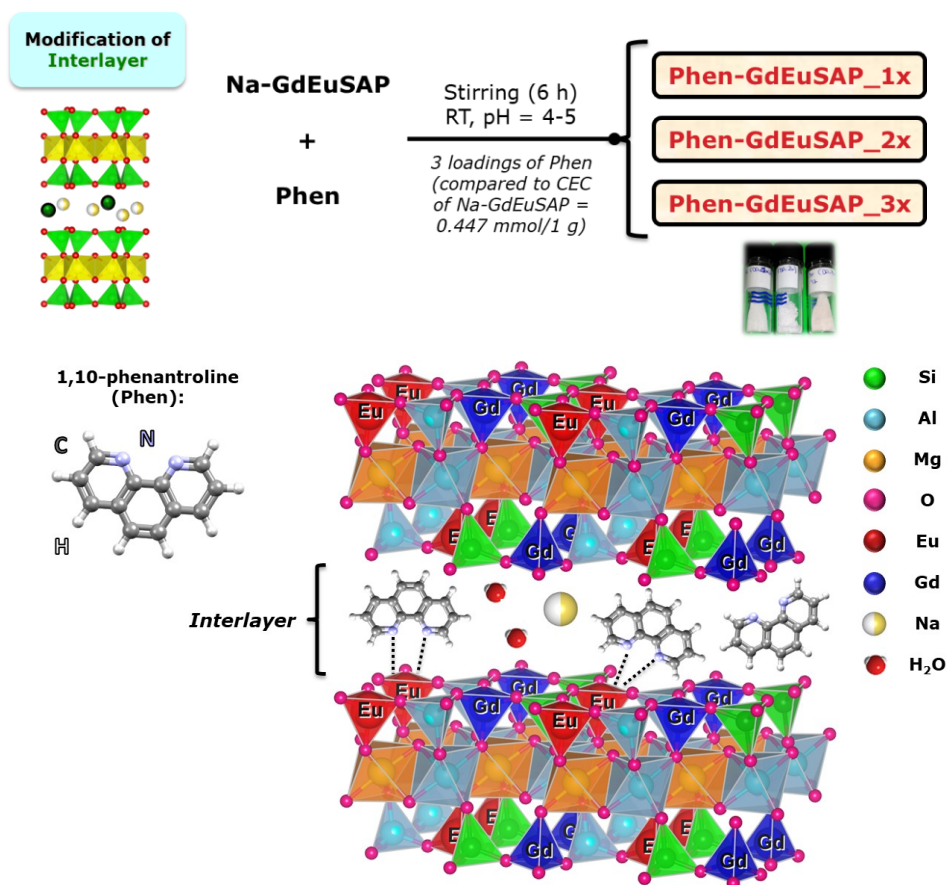


Scheme 1. Schematic view of the preparation of the bifunctional magnetic and optical Na-GdEuSAP clay and related structure.

- **Intercalation of 1,10-phenantroline in Na-GdEuSAP:** Phen-GdEuSAP_{*n*} (*n* = 1x, 2x, 3x) samples were prepared through intercalation of 1,10-phenantroline (Phen) in molar quantities of 1-2-3 times the cation-exchange capacity (CEC) of Na-GdEuSAP clay (estimated to be 44.7 ± 0.9 meq/100 g) (Scheme 2). In detail, an appropriate amount of Phen was dissolved in 35 mL of ultrapure water at pH

between 4-5, then 0.350 g of Na-GdEuSAP were added and the mixture was stirred at RT for 6 h. After that, the suspension was centrifuged (8000 rpm for 5 min) and the solid was washed first with ethanol (EtOH, 5x50 mL) and then with hot ultrapure water (5x50 mL). The solid was finally dried in an oven overnight at 100 °C.

Reference materials were obtained by intercalation of Phen molecules in pristine Na⁺-exchanged synthetic saponite clays prepared with the same H₂O/Si molar ratio and with a CEC of 87.9 ± 2.3 meq/100 g (Na-SAP-20, see *Chapter 3*), following the same procedure described above. The samples were named Phen-SAP_*n*, where *n* = 1x, 2x, 3x.



Scheme 2. Schematic view of the intercalation of Phen molecules in the Na-GdEuSAP clay and related structure.

5.3 Results and Discussion

5.3.1 Characterization of GdEuSAP material

The Gd³⁺ and Eu³⁺ loadings in the bifunctional GdEuSAP clay, determined by inductively coupled plasma mass spectrometry (ICP-MS) after mineralization of the solid in acidic media, were found to be equal to 0.03 mmol/g and no concentration reduction was detected after the Na⁺-exchange process, thus suggesting that both metals are mainly located in the framework positions. The same results were observed for the reference GdSAP and EuSAP clays.

The introduction of both ions in the structure of the final bifunctional clay did not alter the crystalline 2:1 *T-O-T* tri-octahedral layered structure of saponite,²⁴⁻²⁶ as observed by X-ray powder diffraction (XRPD) analyses (Figure 1A). The X-ray pattern of GdEuSAP (Figure 1, *b*) showed the presence of the typical reflections assigned to (001), (110)-(020), (004), (130)-(201), (311) and (060) planes of smectite clay (Figure 1A, *a*).^{1,29} After ion-exchange, a shift of the basal plane (001), from 6.44° 2θ (d -spacing of 1.37 nm) to 7.27° 2θ (1.21 nm) was observed (see inset in Figure 1A, *b-c*). Similar results were obtained for GdSAP, EuSAP and Na⁺-exchanged derivatives.

The morphological features of the bifunctional clay were evaluated by scanning (SEM) and high-resolution transmission (HRTEM) electron microscopies (Figure 1B and 1C, respectively). Na-GdEuSAP showed different levels of spatial organization of lamellae particles, from single structures with sheet-like morphology to aggregate with formation of tactoids of different size, with a tendency to stack on top of each other (Figure 1C). The introduction of Gd³⁺ and Eu³⁺ ions in the saponite structure greatly affects the size of lamellae, which show a range of lengths of a few tens of nanometres (Figure 1B), rather similar to saponites prepared with higher dilution of the synthesis gel^{1,2,4} and for Nb⁵⁺ and V³⁺-containing saponites obtained with the same H₂O/Si = 20.²⁴⁻²⁶ The distribution of the $d_{(001)}$ -spacing values, obtained by counting more than 100 particles, was found to be broad, heterogenous and

centred around 1.2-1.3 nm (Figure 1D). Similar results were also observed for reference monofunctionalized clays.

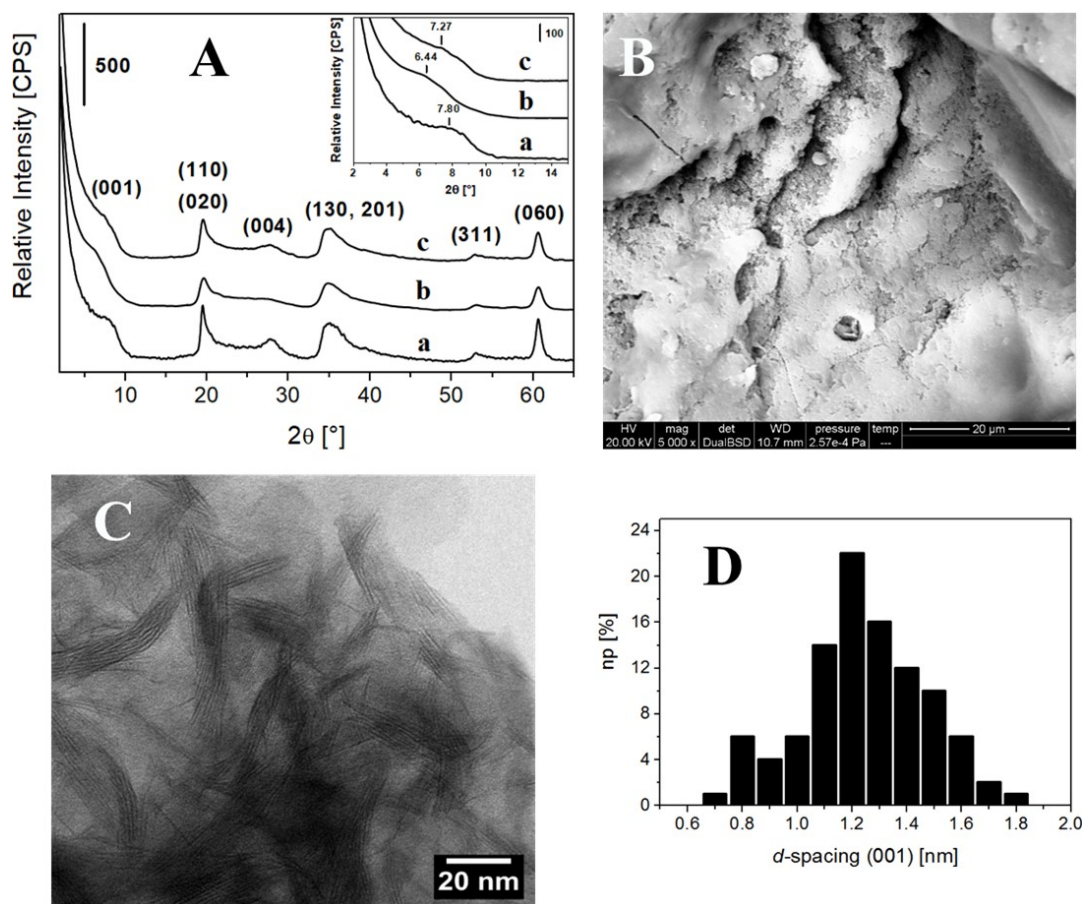


Figure 1. A) X-ray powder diffraction profiles of Na-SAP (a), GdEuSAP (b) and Na-GdEuSAP (c); diffractograms collected at low angles (2° - 15° 2θ) are reported in the insets. B) SEM micrograph of Na-GdEuSAP. C) HRTEM image of Na-GdEuSAP; the distribution of the $d_{(001)}$ -spacing is shown in D.

The inclusion of Gd^{3+} and Eu^{3+} ions in the framework of the saponite was further investigated by one-dimensional ^{27}Al high-power decoupling with magic angle spinning solid-state NMR (1D ^{27}Al HPDEC/MAS ssNMR) analyses, carried out on Na-GdSAP (Figure 2, b), employed as ‘model’ for these kind of systems, and on a parent Na-SAP (Figure 2, a). The data showed two resolved contributions at *ca.* 66-67 and 6-9 ppm, in both spectra, associated to tetrahedrally (Al^{IV}) and octahedrally

(Al^{VI}) coordinated aluminium, respectively (Table 1).^{1,29} The integration of the respective peaks showed a difference in the relative concentration of tetrahedral and octahedral species. The Al^{IV}/Al^{VI} ratio decrease from 1.71 to 1.15 passing from Na-SAP (*a*) to Na-GdSAP (*b*) (Table 1), suggesting that gadolinium tends to be preferentially incorporated in the tetrahedral sites of saponite. Consequently, the lanthanides are more exposed and accessible to the surrounding water molecules in the interlayer region.

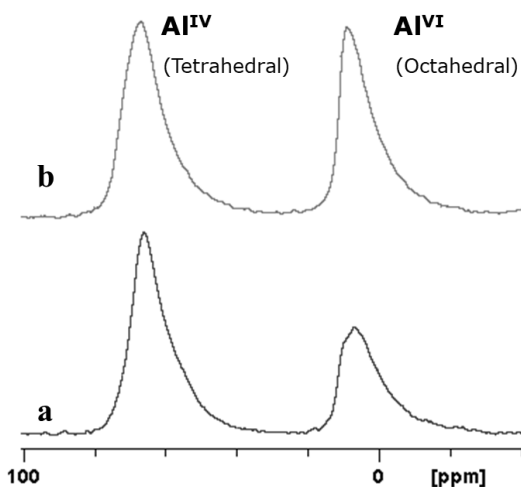


Figure 2. 1D ²⁷Al HPDEC/MAS ssNMR spectra of Na-SAP (*a*) and Na-GdSAP (*b*).

Table 1. Isotropic chemical shifts, δ_{iso} , and concentration of tetrahedral (Al^{IV}) and octahedral (Al^{VI}) ²⁷Al sites in saponite samples.

Sample		Al ^{IV} [<i>T</i> -layers]	Al ^{VI} [<i>O</i> -layers]	Al ^{IV} /Al ^{VI}
Na-SAP	δ_{iso} [ppm]	66.0	6.9	1.71
	Area	53.78	31.37	
Na-GdSAP	δ_{iso} [ppm]	67.2	9.2	1.16
	Area	43.35	37.51	

The CEC values, evaluated through the classical ultraviolet-visible-near infrared (UV-Vis-NIR) method reported in literature,^{30,31} are comparable for the three functionalized clays and they were estimated to be 44.7 ± 0.9 meq/100 g, 45.1 ± 0.5

meq/100 g and 43.0 ± 0.7 meq/100 g for Na-GdEuSAP, Na-EuSAP and Na-GdSAP, respectively.

Dynamic light scattering (DLS) analyses were carried out prior the photophysical and relaxometric experiments on the lanthanide clays. The samples were dispersed in ultrapure water containing 0.1 wt.% of xanthan gum^{16,32} and measurements were performed at 25 °C. The stable and homogeneous suspensions showed hydrodynamic size values of 45-60 nm, before and after the ion-exchange process.

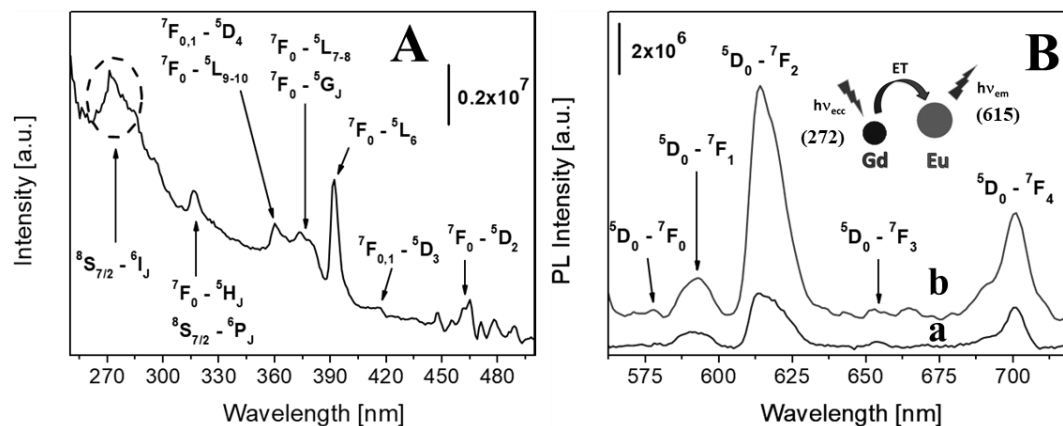
The photophysical properties of the bifunctional Na-GdEuSAP clay, both at solid state and in aqueous suspension (with 0.1 wt.% of xanthan gum),^{16,32} were studied in detail by photoluminescence (PL) spectroscopy, obtaining important information on the chemical nature and geometrical aspects of the environment surrounding the Eu³⁺ sites. Na-EuSAP was used as reference for a more comprehensive overview of the optical features of the bifunctional clay.

The excitation spectrum at solid state of Na-GdEuSAP (Figure 3A), recorded at the most intense emission line of Eu³⁺ at 615 nm, presented the narrow peaks due to the characteristic intra-4*f*⁶ electronic transitions of Eu³⁺ (⁷F₀-⁵H_{*J*}, ⁵D_{*J*}, ⁵L_{*J*}) with a λ_{\max} at 395 nm ascribed to ⁷F₀-⁵L₆,³³ while additional ⁸S_{7/2}-⁶I_{*J*} ($\lambda_{\max} = 272$ nm) and ⁸S_{7/2}-⁶P_{*J*} electronic transitions were associated to Gd³⁺.³⁴ The presence of the latter is a good proof of a Gd³⁺ → Eu³⁺ energy transfer process: this effect is related to the partial overlapping of their energy levels of the two metals, as indicated in the Jablonski energy diagrams reported in Figure 3D. The MMET mechanism can be exploited to enhance the optical emission of the Eu³⁺ sites.³⁵ The same transitions were observed in the spectrum in aqueous suspension.

The emission spectra at solid state of Na-GdEuSAP, collected under irradiation at both 272 nm (λ_{\max} of Gd³⁺) and 395 nm (λ_{\max} of Eu³⁺) (Figure 3B), showed the characteristics emission peaks of the intra-4*f*⁶ electronic levels of Eu³⁺ (⁵D₀-⁷F_{*J*}, *J* = 0-4).³³ An enlargement magnification of the 564-583 nm range (Figure 3C) indicates the presence of two weak bands at 572 and 578 nm related to the ⁵D₀-⁷F₀ transition, under both excitation wavelength. The multiplicity of this band is associated with

the heterogeneity of the Eu^{3+} , since both the initial and final states are non-degenerate. Two chemically distinct environments or coordinated sites of Eu^{3+} may be present.³⁶ Most importantly, upon excitation of Gd^{3+} there is an increase in the intensity of the hypersensitive ${}^5\text{D}_0$ - ${}^7\text{F}_2$ transition at 615 nm of Eu^{3+} compared to the direct excitation of the latter of *ca.* 240%, thus suggesting the occurrence of $\text{Gd}^{3+} \rightarrow \text{Eu}^{3+}$ ET phenomenon.³⁵ Similar results were obtained in aqueous suspension, with a major intensification of the emission of europium of *ca.* 550%.

The integrated intensity ratio of the electric dipole/ED ${}^5\text{D}_0 \rightarrow {}^7\text{F}_2$ at 615 nm on the magnetic dipole/MD ${}^5\text{D}_0 \rightarrow {}^7\text{F}_1$ at 592 nm, called asymmetry factor (R), gives information on the site geometrical/coordination aspects of Eu^{3+} centres.³⁷⁻⁴⁰ R can be close to 0 when the excited Eu^{3+} are located in a symmetric environment, whereas it assumes higher values when the ions are characterized by lower degree of symmetry.⁴⁰ First, the presence of the very intense peak at 615 nm (Figure 3B) suggests that symmetry of Eu^{3+} sites are low.⁴¹ Furthermore, R factors for Na-GdEuSAP, calculated at solid state for both excitation wavelengths, are between 3-5, thus indicating a highly asymmetrical local environment surrounding Eu^{3+} sites; comparable results were found in aqueous suspension (Table S3, Chapter 8).



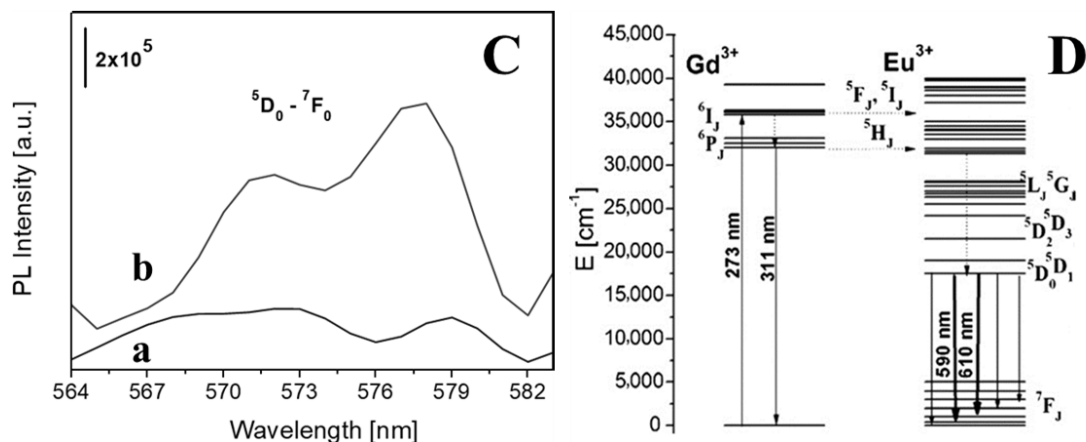


Figure 3. A) Excitation spectrum at solid state of Na-GdEuSAP, collected at 615 nm. B) Emission spectra at solid state of Na-GdEuSAP, under excitation at 395 (λ_{\max} Eu^{3+} , *a*) and 272 nm (λ_{\max} Gd^{3+} , *b*). The enlarged section of emission spectra on the 564-583 range is shown in C. D) Jablonski energy diagram of $\text{Gd}^{3+} \rightarrow \text{Eu}^{3+}$ energy transfer mechanism.³⁵

The average hydration of the Eu^{3+} (q) was estimated from the radiative lifetimes (τ) measured in H_2O and D_2O (Figure 4A, *a-b*). The decay curves of the $^5\text{D}_0$ excited state, obtained by monitoring the luminescence intensity of $^5\text{D}_0 \rightarrow ^7\text{F}_2$ at 615 nm under excitation at 370 nm, were fitted with a bi-exponential function, obtaining two distinct lifetimes from which an average value was calculated, thus indicating the presence of two kinds of Eu^{3+} as previously noted. A value of *ca.* 4 coordinated water molecules, calculated through Eq. (1),^{37,38,41} was found for Na-GdEuSAP; the same hydration state was also found for the reference Na-EuSAP sample (Table S3, Chapter 8).

$$q^{\text{Eu}} = 1.2 \cdot \left(\frac{1}{\tau_{\text{H}_2\text{O}}} - \frac{1}{\tau_{\text{D}_2\text{O}}} - 0.25 \right) \quad (1)$$

The $^5\text{D}_0$ intrinsic quantum efficiency of Eu^{3+} ($\Phi^{\text{Eu}}_{\text{Eu}}$) for Na-GdEuSAP was then estimated taking into account the emission spectrum in aqueous suspension at 395 nm (Figure 4B), the $^5\text{D}_0$ lifetime value in H_2O (Figure 4A, *a*) and by using the Eq. (2),^{37,42} where τ and τ_0 are the measured and radiative lifetimes of the Eu^{3+} emission,

respectively. The τ_0 for Eu^{3+} can be calculated from the corrected emission spectrum, without the intervention of the Judd-Ofelt Theory, using the Eq. (3),^{37,43} where $A_{\text{MD},0}$ is the spontaneous emission probability of the MD ${}^5\text{D}_0$ - ${}^7\text{F}_1$ transition *in vacuo* (14.65 s^{-1}), n is the refractive index of the solvent (1.333 for H_2O) and $I_{\text{tot}}/I_{\text{MD}}$ is the total area of the corrected emission spectrum on the ${}^5\text{D}_0$ - ${}^7\text{F}_1$ area.

$$\Phi_{\text{Eu}}^{\text{Eu}} = \tau / \tau_0 \quad (2)$$

$$1/\tau_0 = A_{\text{MD},0} \cdot n^3 \cdot (I_{\text{tot}}/I_{\text{MD}}) \quad (3)$$

The values of $\Phi_{\text{Eu}}^{\text{Eu}}$ for Na-GdEuSAP was established to be 4.29%, higher than the one calculated for Na-EuSAP (3.25%) (Table S3, Chapter 8).

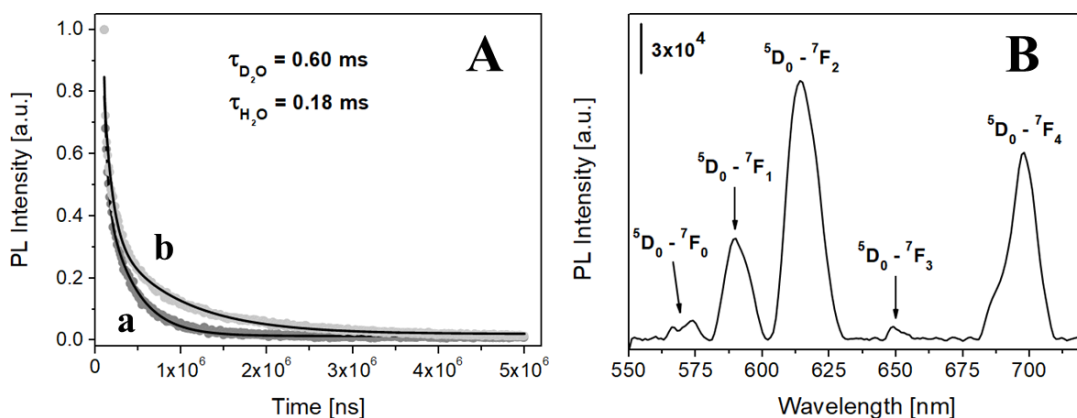


Figure 4. A) PL ${}^5\text{D}_0$ - ${}^7\text{F}_2$ (615 nm) intensity decay over time of Na-GdEuSAP dispersed in H_2O (a) and D_2O (b), under irradiation at 370 nm. The curves fitting was performed with a bi-exponential function (black lines). C) Emission spectrum in aqueous suspension of Na-GdEuSAP under excitation at 395 nm ($\lambda_{\text{max}} \text{Eu}^{3+}$).

Photobleaching tests were performed under continuous irradiation both at 395 (a) and 272 (b) nm for 1 h, monitoring the emission at 615 nm. In general, Na-GdEuSAP showed good photostability in solid form (Figure 5A) and in water (Figure 5B); the same behaviour was found for Na-EuSAP.

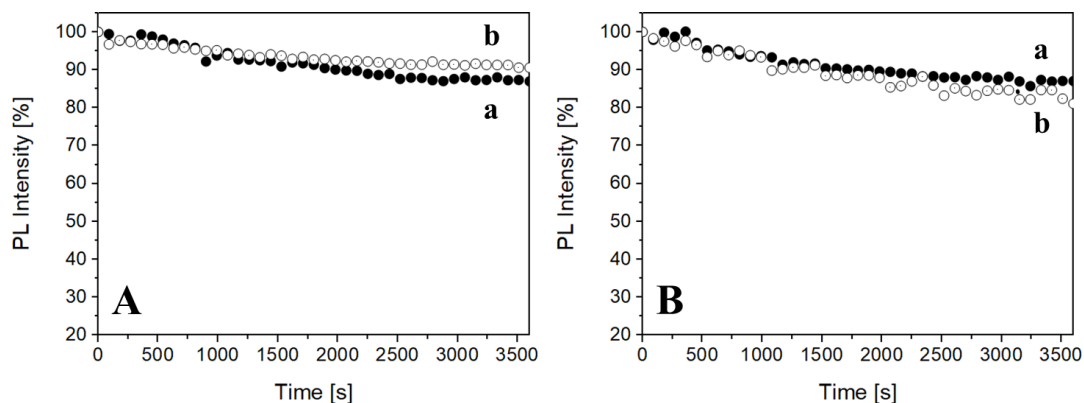


Figure 5. Photobleaching tests of Na-GdEuSAP at solid state (A) and in aqueous suspension (B), under irradiation at 395 (a, -●-) and 272 (b, -○-) nm. The intensity of $^5\text{D}_0$ - $^7\text{F}_2$ (615 nm) was monitored for 1 h.

A complete ^1H NMR relaxometric study on the Na-GdEuSAP aqueous suspension, carried out by analysing the relaxivity parameter (r_1)^{4,44-46} was performed with the aim to investigate the inclusion of paramagnetic ions into the framework of a clay material and to gather additional data on the water dynamics in the interlayer space.⁴ The Na-GdSAP was used as reference.

^1H $1/T_1$ nuclear magnetic relaxation dispersion (NMRD) profiles of both Na-GdEuSAP and Na-GdSAP, collected in the frequency range 0.01-120 MHz at 37 °C and neutral pH (Figure 6A), show the typical shape of slowly tumbling systems⁵¹ characterized by a broad and intense hump centred at 30-40 MHz; at higher fields, r_1 decreases gradually while maintaining values higher than those at low field range. Both materials showed improved relaxometric performances at high magnetic fields compared to the commercially available Gd^{3+} -chelates,⁴ while being analogous at 20 MHz to the GdL1/SAP clay (Figure 7), previously studied in *Chapter 4*,⁴ and to some Gd^{3+} -doped microporous zeolites.⁴⁷ At 60 MHz, the r_1 of lanthanide clays is even higher than GdL1/SAP. (Figure 7). The r_1 is also greatly influenced by water diffusion phenomena through the interlamellar region, as suggested by the increase of r_1 with temperature (Figure 6C). The four Gd^{3+} inner-sphere water molecules (A), whose number was obtained from PL analyses (Table S3, *Chapter 8*), exchange

quickly with the intra-interlayer water molecules (B, not coordinated to Gd^{3+}), then diffuse through the saponite gallery and slowly exchange with the bulk water (C) outside the lamellae (Figure 6B). Therefore, the diffusion is the rate-limiting step of the whole relaxation effect, as previously observed in clays (*Chapter 4*)⁴ and zeolite-based systems.⁴⁷

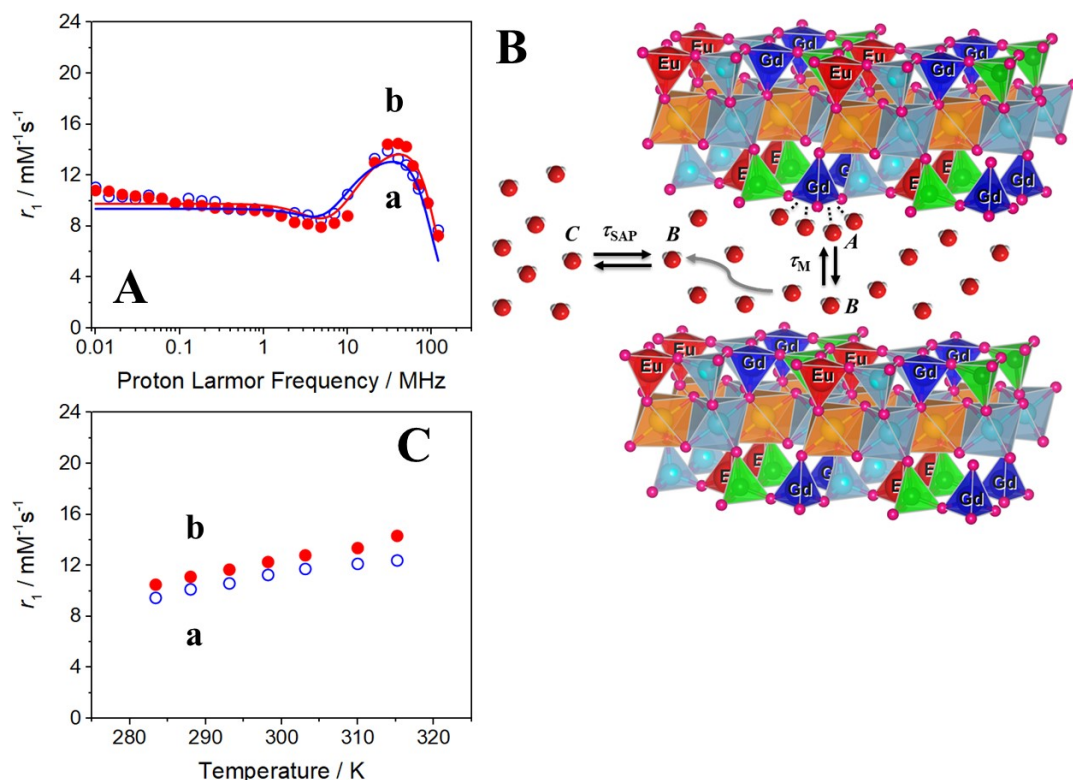


Figure 6. A) $1/T_1$ ^1H -NMRD profiles of Na-GdSAP (a, \circ -) and Na-GdEuSAP (b, \bullet -) at 37 °C, over the frequency range 0.01-120 MHz and neutral pH. B) Schematic representation of the “two-step” model to account the relaxation effect in the lanthanide clays. C) Variable-temperature dependence of r_1 for Na-GdSAP (a) and Na-GdEuSAP (b), at 20 MHz.

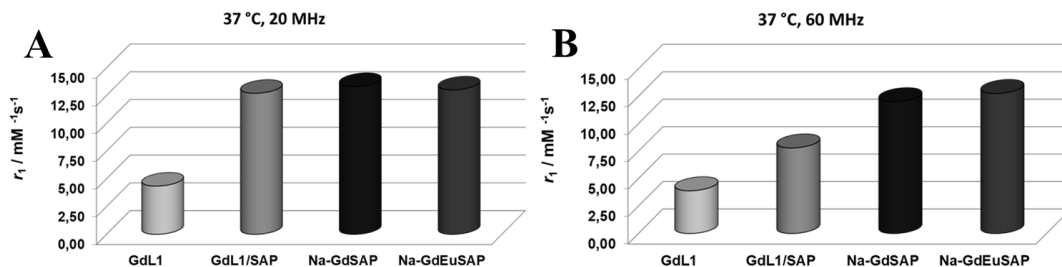


Figure 7. Comparison of r_1 at 20 (A) and 60 (B) MHz for GdL1,⁴ GdL1/SAP,⁴ Na-GdSAP and Na-GdEuSAP, at 25 °C and neutral pH.

The ¹H-NMRD profiles of Na-GdEuSAP and Na-GdSAP (Figure 6A, *a-b*) were analysed by fitting the data to a “two-step” model^{47,48} based on a heavily modified version of the Solomon-Bloembergen-Morgan (SBM) and Freed equations, which considers only the inner-sphere (IS) contribution to the proton relaxation mechanisms.^{49,50} This model considers two separate water exchange processes, one 1) between the Gd³⁺ bound water (A) and the water inside the interlayer space and the other 2) between the water inside with that outside the clay. New diffusional parameters were evaluated during the best-fit procedure.^{47,48} In particular: *a*) c is the number of free water molecules inside the saponite per Gd³⁺ ion, *b*) $1/T_{1\text{ SAP}}$ is the relaxation rate of water protons inside the saponite and *c*) τ_{SAP} is the mean residence time of the water protons inside the saponite (Table 2). In the fitting procedure, τ_{R} was fixed to 0.08 μs , while the number of Gd³⁺ inner-sphere water (q) was fixed to 4 as determined by PL analyses (Table S3, Chapter 8). The NMRD curves are well reproduced and the resultant fitted parameters are given in Table 2 (full list in Table S4, Chapter 8). A good fit of the data for both solids was obtained with τ_{M} of 0.4-05 μs , a number of intra-interlayer water molecules c between 34-36 and τ_{SAP} values between 43-48 μs , two times longer than τ_{M} , indicative of the slow exchange process between the water inside the lamellae channel and the bulk water.

Table 2. Selected best-fit parameters obtained from the analysis of $1/T_1$ ^1H -NMRD profiles (37 °C) for Na-GdSAP and Na-GdEuSAP samples. A table with all the parameters used in the fit analysis is reported in Table S4 in *Chapter 8*. ^aData from PL Analyses (Table S3, *Chapter 8*).

	$^{20}r_1$ [mM ⁻¹ s ⁻¹]	q	c	τ_M [μs]	τ_{SAP} [μs]
Na-GdEuSAP	13.00	4 ^a	34.81	0.48	43.89
Na-GdSAP	13.31	4 ^a	36.00	0.56	47.41

To evaluate the chemical integrity of the functional materials and the stability of the suspensions, the r_1 value of Na-GdEuSAP sample was evaluated over time in different aqueous media. The r_1 remains constant in water at 20 MHz and 25 °C up to 24 h. The sample was then treated with an increasing amount of ethylenediaminetetraacetic acid (EDTA) ligand (Figure 8). No release of paramagnetic Gd^{3+} ions in solution was observed in the presence of high EDTA concentrations, even over time at the highest [EDTA]/[Gd] molar ratio.⁵³ The changes in r_1 values are mainly due to perturbation of the water exchange dynamics and aggregation of nanoparticles. The data confirmed the high chemical stability of the systems.

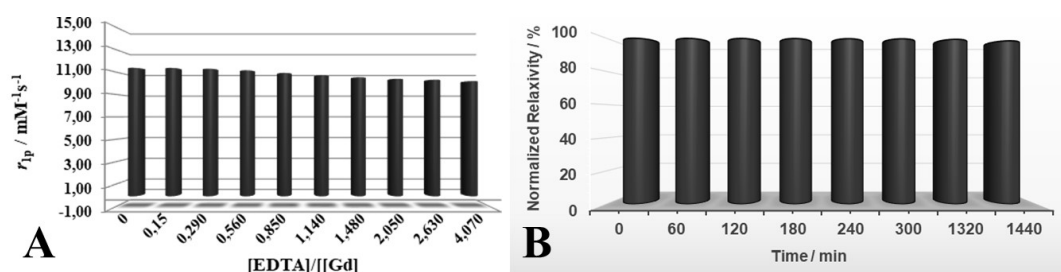


Figure 8. Histograms of r_1 at 20 MHz and 25 °C of Na-GdEuSAP treated with an increase amount of EDTA (A) and over time (with [EDTA]/[Gd] = 4.070) (B).

5.3.2 Luminescence enhancement of GdEuSAP by intercalation of Phen

A detailed multi-technique study was then carried out on the final Phen-GdEuSAP and Phen-SAP materials, with attention on the nature of the energy transfer from the excited triplet state (T_1) of Phen ligand to the nearby emitting states of Eu^{3+} .

The XRPD analyses, carried out on the bifunctional composite materials, confirmed the intercalation of the Phen in the Na-GdEuSAP clay (Figure 9A), as indicated by the marked shift of basal plane (001) reflections in the Phen-GdEuSAP samples (*b-d*) compared to the starting bifunctional clay (*a*) (see inset in Figure 9B), from 7.27° 2θ (1.21 nm) to 6.40° - 6.45° 2θ (1.34-1.38 nm). Similar behaviour was also noted for the reference Phen-SAP solids.

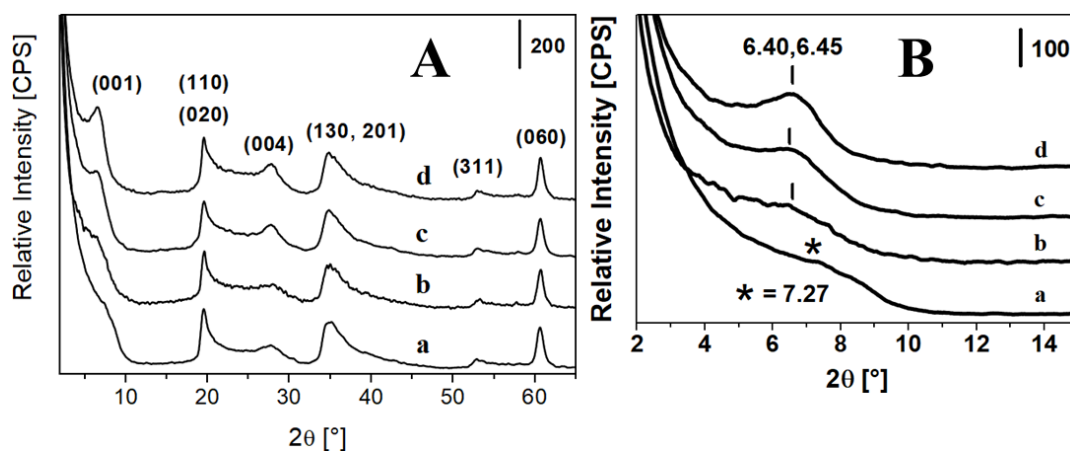


Figure 9. A) X-ray powder diffraction profiles of Na-GdEuSAP (*a*), Phen-GdEuSAP_1x (*b*), Phen-GdEuSAP_2x (*c*) and Phen-GdEuSAP_3x (*d*). Diffractograms collected at low angles (2° - 15° 2θ) are reported in B.

Thermogravimetric analyses (TGA) were performed to *i*) further confirm the presence of the Phen inside the interlayer of the Na-GdEuSAP, *ii*) to evaluate their thermal stability in the intercalated materials and *iii*) to quantify the amount of intercalated Phen. The TGA profiles of Phen-GdEuSAP samples, collected under oxygen flow (Figure 10A), show the classical weight loss of the clay at 100°C

(physisorbed water) and in the range of 150-750 °C (gradual release of interlamellar water/initial dehydroxylation of the layered structure). The decomposition peak of the organic Phen shifts from to 355 °C (Figure 10A) to 570-630 °C (Figure 10B.), as observed in the DTG profiles. The increase of the thermal stability of Phen confirms its presence in the interlayer space.⁴ Similar results were obtained for reference Phen-SAP solids. The amount of intercalated ligand, expressed as mmol of Phen per one gram of saponite, was then extrapolated from the TGA curves and the results are reported in Table 3. The intercalated amount of Phen in the reference Na-SAP samples seems to have a non-linear correlation with the starting loading (x), contrary to what is observed for Na-GdEuSAP materials: this could be attributed so several reason, for which a more comprehensive study is needed in the future.

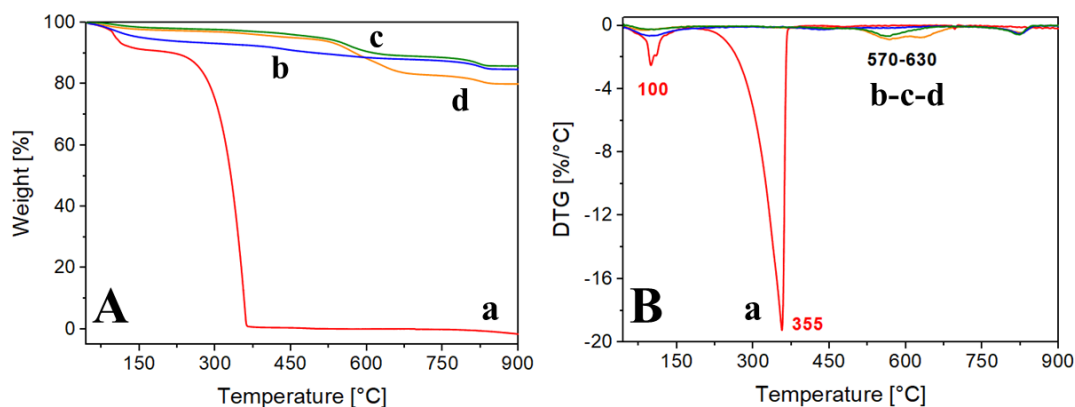


Figure 10. TGA (A) and DTG (B) profiles of Phen (a), Phen-GdEuSAP_1x (b, blue), Phen-GdEuSAP_2x (b, green) and Phen-GdEuSAP_3x (d, orange). The analyses were carried out under oxygen flow.

Table 3. Phen loading in Phen-GdEuSAP_{*n*} and Phen-SAP_{*n*} ($n = 1x, 2x, 3x$) samples.

Sample	Phen content [mmol/g]
Phen-SAP_1x	0.568
Phen-SAP_2x	0.665
Phen-SAP_3x	0.783

Phen-GdEuSAP_1x	0.283
Phen-GdEuSAP_2x	0.565
Phen-GdEuSAP_3x	0.960

UV-Vis-NIR spectra of all the composite materials were collected in aqueous suspensions (with 0.1 wt.% of xanthan gum^{16,32}) to obtain the λ_{\max} of absorption of the intercalated Phen, which was found to be at 275 nm ($S_0 \rightarrow S_1$: $\pi \rightarrow \pi^*$ electronic transition)^(*), in accordance with the literature.⁵⁴

The photophysical properties of Phen-GdEuSAP and Phen-SAP, were thoroughly investigated by PL spectroscopy, at the solid state and in aqueous suspensions containing 0.1 wt.% of xanthan gum^{16,32}, in order to obtain information on the dependence of the energy transfer on the Phen loadings and to evaluate the parameters that control the FRET/LMET process from Phen to Eu^{3+} .²⁷ The Phen acted as an energy donor species (donator, D) to the metal ion (acceptor, A), leading to the formation of an “D-A system” that greatly enhance the luminescence of Eu^{3+} . Preliminary analyses were made on the crystalline Phen to derive the position of the main excitation ($\lambda_{\text{exc}} = 275 \text{ nm}$, S_0-S_1)^(*) and emission bands ($\lambda_{\text{em}} = 415 \text{ nm}$, T_1-S_0).⁵⁴

The excitation spectrum of Phen-GdEuSAP_2x collected at solid state at 615 nm (Figure 11A), used as a ‘sample model’ to illustrate the properties of the bifunctional composite materials prepared, presented the narrow peaks of the characteristic intra- $4f^6$ electronic transitions of Eu^{3+} ($^5D_0-^7F_J$, $J = 0-4$; $\lambda_{\max} = 395 \text{ nm}$, $^7F_0-^5L_6$)³³ and Gd^{3+} ($^8S_{7/2}-^6I_J$, $\lambda_{\max} = 272 \text{ nm}$; $^8S_{7/2}-^6P_J$)³⁴, as previously observed in the Na-GdEuSAP (Figure 3A), and the S_0-S_1 electronic transition of Phen located at 275 nm.⁵⁴ The emission spectra of the Phen-GdEuSAP_2x, measured at solid state under irradiation at both 275 (λ_{exc} Phen) and 395 nm (λ_{exc} Eu^{3+}) (Figure 11B), showed that upon excitation of organic moieties there is a marked increase in the intensity of the hypersensitive $^5D_0-^7F_2$ transition at 615 nm of Eu^{3+} compared to the direct excitation of the metal, thus suggesting the occurrence of the FRET process from Phen \rightarrow Eu^{3+} (Figure 11C). The best optical improvement was observed with the Phen-

GdEuSAP_2x sample ($\uparrow I_{615} = ca. 2050\%$), while at the highest loading the luminescence is in part quenched ($\uparrow I_{615} = ca. 1070\%$), probably by aggregation of Phen molecules. The sample with the lowest Phen loading presents only an improvement of *ca.* 450%; however, the value is higher than the one previously found for Na-GdEuSAP by considering the Gd^{3+} - Eu^{3+} energy transfer (*ca.* +250%, Figure 3B). The energy transfer through an antenna system, even at the lowest loading, proved to be the most efficient way to enhance the luminescence of Eu^{3+} centres alone in the clay, compared to the MMET mechanism.

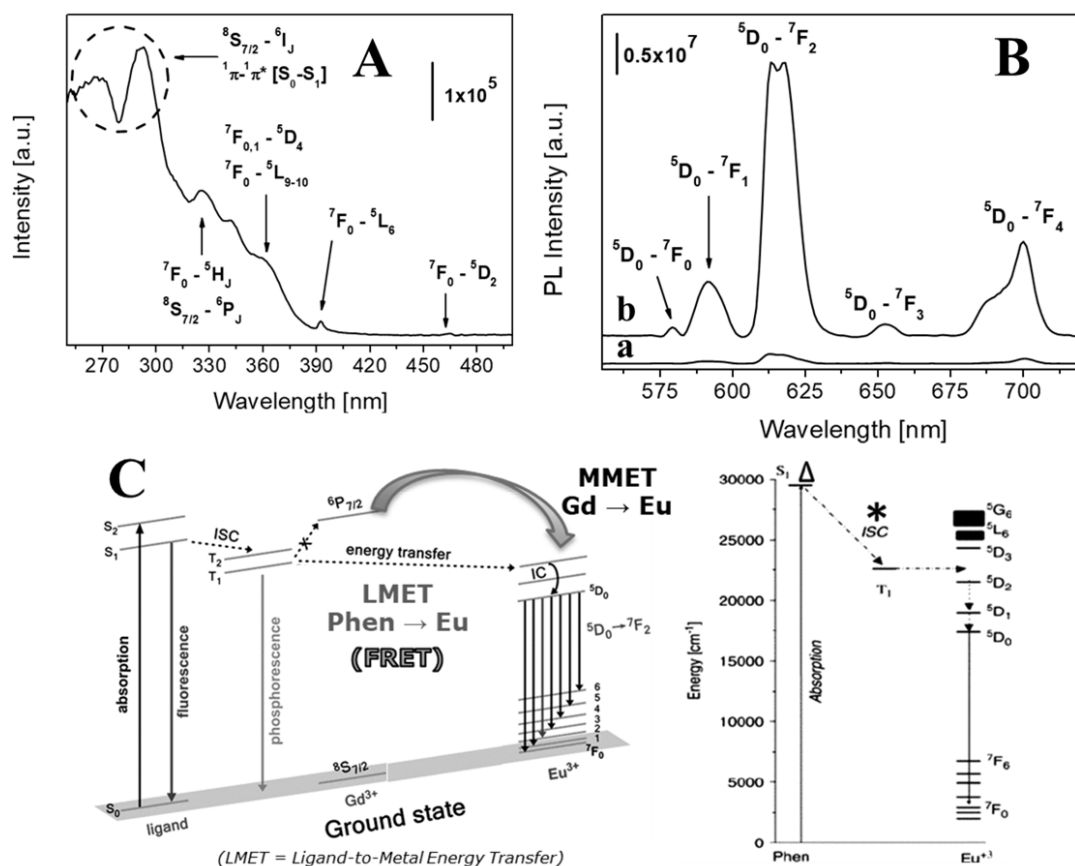


Figure 11. A) Excitation spectrum at solid state of Phen-GdEuSAP_2x, collected at 615 nm. B) Emission spectra at solid state of Phen-GdEuSAP_2x, under excitation at 392 (λ_{max} Eu^{3+} , *a*) and 275 nm (λ_{max} Phen, *b*). C) Schematic view of the Phen \rightarrow Eu^{3+} FRET process.²⁷

The results observed were further confirmed by a more deeply analyses of the parameters that describe the efficiency (E_{EnT} or η_{sens}), the constant rate (k_{EnT}) and the overall quantum yield ($\Phi^{Phen_{Eu}}$) of the FRET process (see Eq. (4-5-6), respectively).⁵⁵⁻⁵⁷ The parameters were derived from the analyses of the radiative lifetime of D-only (τ_D , Phen-SAP) and D-A (τ_{DA} , Phen-GdEuSAP) systems collecting the decay curves of the S_0 excited state of Phen donor group at 415 nm, under excitation at 295 nm in solid form and in suspensions (Table 4). The Phen-GdEuSAP_2x, whose results are reported in Table 4, proved to be the best material in terms of enhancement of emission properties of Eu^{3+} . A full list of the parameters analysed for all the composite materials is reported in Table S5 in *Chapter 8*.

$$E_{EnT} (o \eta_{sens}) [\%] = \left(1 - \frac{\tau_{DA}}{\tau_D}\right) \cdot 100 \quad (4)$$

$$k_{EnT} [s^{-1}] = \left(\frac{1}{\tau_{DA}} - \frac{1}{\tau_D}\right) \quad (5)$$

$$\Phi_{Eu}^{Phen} [\%] = [\eta_{sens} \cdot \Phi_{Eu}^{Eu}] \cdot 100 \quad (6)$$

Table 4. Radiative lifetime (τ) of Phen-SAP_2x (D) and Phen-GdEuSAP_2x (DA) samples at solid state (SS) and in aqueous suspensions (H_2O), under excitation at 295 nm, and efficiency (E_{EnT}), constant rate (k_{EnT}) and overall quantum yield ($\Phi^{Phen_{Eu}}$) parameters of the FRET mechanism. ^a Φ_{Eu}^{Eu} Na-GdEuSAP (in H_2O), used in Eq. (6) = 4.29% (Table S3, *Chapter 8*).

	SS	H_2O
τ_D [ns]	4.28	4.41
τ_{DA} [ns]	3.37	3.82
k_{EnT} [s^{-1}]	6.31E+07	6.83E+07
E_{EnT} [%]	21.26	24.71
Φ_{Eu}^{Phen} [%] ^[a]	/	1.06

The average hydration of the Eu^{3+} (q) was also estimated after the intercalation of the Phen molecules from the τ values measured in H_2O and D_2O , by monitoring the 615 nm emission and using the Eq. (2).^{37,38,41} The decay curves of the $^5\text{D}_0$ excited state of Eu^{3+} , fitted with a bi-exponential function, show a reduction of the number of inner-sphere water of luminescent metal (and of Gd^{3+}) from *ca.* 4 of Na-GdEuSAP to an average of *ca.* 1 (near 0 for 2x and 3x samples) for Phen-GdEuSAP (Table S6, Chapter 8), thus confirming the coordination of Phen molecules to the metal centres.

An evaluation of the colorimetric performance of Phen-SAP and Phen-GdEuSAP materials was also carried out, obtaining the chromaticity coordinates (xy) and related parameters according to CIE 1931 colour spaces,⁵⁸ as reported in Figure 12 (see also Table S7 in Chapter 8). The LMET process led to emissions in the blueish-violet visible region of the electromagnetic spectrum for Phen-GdEuSAP samples, compared to the pure red emission of the direct excitation of Eu^{3+} sites.

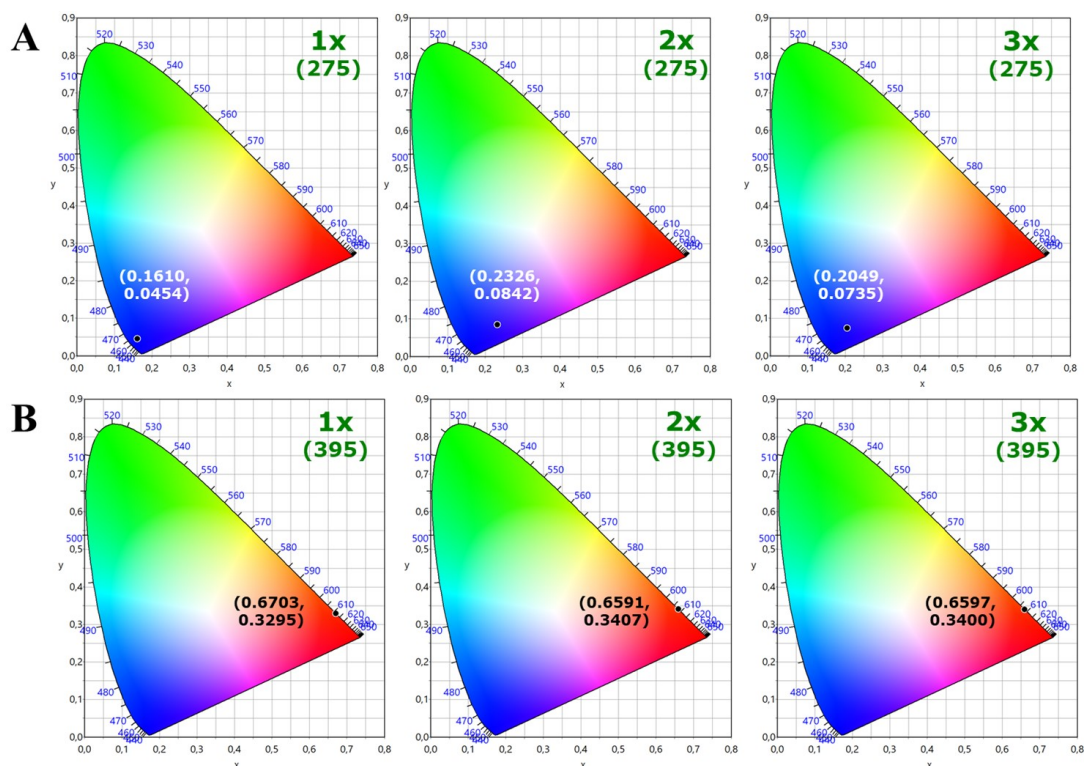


Figure 12. CIE 1931 xy chromaticity diagrams of Phen-GdEuSAP_{*n*} ($n = 1, 2, 3x$), at $\lambda_{\text{exc}} = 275$ (A) and 395 nm (B).

Finally, the aqueous suspension of Phen-GdEuSAP_2x sample was submitted to preliminary ^1H -NMR relaxometric analysis, measuring the $1/T_1$ ^1H NMRD profile at $37\text{ }^\circ\text{C}$ (Figure 13). The profile of Phen-GdEuSAP_2x (*b*), compared to the one of Na-GdEuSAP sample (*a*), showed lower r_1 values at high magnetic fields (20-90 MHz), with a narrower hump centred at 30 MHz. This effect could be partially attributed to the reduction of the inner-sphere water of Gd^{3+} , as derived from PL analyses (Table S3, Chapter 8). A more comprehensive study will be performed in the future to get additional information of the relaxometric properties of the Phen-GdEuSAP materials.

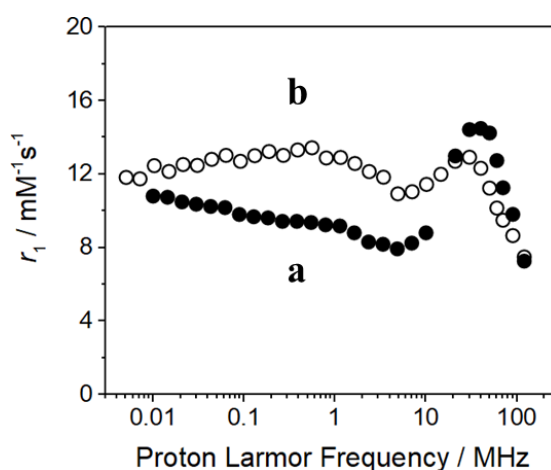


Figure 13. Comparison of $1/T_1$ ^1H -NMRD profiles of Na-GdEuSAP (*a*) and Phen-GdEuSAP_2x (*b*) at $37\text{ }^\circ\text{C}$, over the frequency range 0.01-120 MHz and neutral pH.

5.4 Conclusions

Two different lanthanide ions, gadolinium and europium, were directly inserted in the tetrahedral positions of the framework of a synthetic saponite clay, taking advantage of a novel *one-pot* hydrothermal synthetic procedure using a $\text{H}_2\text{O}/\text{Si}$ molar ratio of 20 and a 1:1 molar ratio between the metals. The solid so prepared was submitted to a sodium-exchange process, obtaining the final novel bifunctional

layered material (named Na-GdEuSAP) which presents both paramagnetic and luminescent properties. Materials with only gadolinium (GdSAP) or europium (EuSAP) were also prepared as references. A detailed physico-chemical characterization was performed on the materials, and attention was devoted to the investigation of the final photophysical and relaxometric properties.

Structural and morphological analyses indicate that the inclusion of the lanthanides in the structure of the final bifunctional clay did not alter the basic layered features of the saponite. The presence of gadolinium and europium in the tetrahedral sheets was further confirmed by ^{27}Al solid state NMR experiments. The decrease of the molar ratio of tetrahedral on octahedral coordinated aluminium species suggests that lanthanides tends to be preferentially incorporated in the tetrahedral units of the clay. Consequently, the ions are more exposed and accessible to the surrounding water molecules in the interlayer region.

The photophysical properties of the bifunctional Na-GdEuSAP clay were deeply investigated both at solid state and in aqueous suspensions, obtaining important information on the chemical nature and geometrical aspects of the environment surrounding the europium sites. The presence of both gadolinium and europium in the same layers give rise to an energy transfer from Gd^{3+} to Eu^{3+} , which increased the luminescence of europium. The chemical environment around the luminescence metal resulted to be highly asymmetric, with Eu^{3+} ions coordinated to four inner-sphere water molecules.

The luminescence performance of the Na-GdEuSAP sample were further improved by intercalation into interlayer space of 1,10-phenantroline, at different loadings, which acted as an “antenna system”. Indeed, phenanthroline molecules harvest and transfer energy to the nearby emitting states of europium by Förster resonance energy transfer process, thus photosensitizing the emission from the europium centres. The energy transfer with the antenna system, even at low loadings (especially true for the Phen-GdEuSAP_2x sample), proved to be the most efficient

way to enhance the luminescence of europium alone, especially compared to the metal-to-metal energy transfer observed in the starting bifunctional clay.

Finally, ^1H -NMR relaxometric investigations of the paramagnetic clays were carried out in aqueous media, as a function of applied magnetic field strength, temperature, in order to obtain more insights on the chemical nature and the accessibility of exchange sites and the molecular dynamics of water molecules inside the interlayer space of saponite. The NMRD profiles were analysed by fitting the data with a “two-step” model that considers two separate water exchange processes, one between the gadolinium inner-sphere water and the water in the interlayer space, and the other between the latter and the bulk water (outside the lamellae). The data extrapolated from the analyses indicated that the inner-sphere water coordinated to Gd^{3+} exchange quickly with the intra-interlayer water molecules (not coordinated to the ion), then diffuse through the lamellae channel and slowly exchange with the bulk water outside the lamellae. Therefore, the diffusion is the rate-limiting step of the whole relaxation effect, as also indicated by the increase of relaxivity as a function of temperature. The suspensions remain stable in water over time and in the presence of EDTA ligand no release of paramagnetic ions was observed in solution, demonstrating the high chemical stability of these materials.

These features are quite promising for the development of a novel class of lanthanide-*based* multifunctional clay nanomaterials, which can be prepared in relatively short time and low cost, for potential applications in several scientific and technological sectors, for example for optical/optoelectronic devices and luminescent sensors (*i.e.* detection of hazardous compounds), in magnetic and/or optical diagnostic (*i.e.* new markers for bio-imaging) and to expand the knowledge of the physico-chemical properties of layered clay solids.

5.5 Notes and References

- 1 D. Costenaro, G. Gatti, F. Carniato, G. Paul, C. Bisio and L. Marchese, *Microp. Mesop. Mater.*, 2012, **162**, 159-167.
- 2 C. Bisio, G. Gatti, E. Boccaleri, G. Superti, H. Pastore and M. Thommes, *Microp. Mesop. Mater.*, 2008, **107**, 90-101.
- 3 C. Bisio, G. Gatti, E. Boccaleri, L. Marchese, L. Bertinetti and S. Coluccia, *Langmuir*, 2008, **24**, 2808-2819.
- 4 S. Marchesi, F. Carniato, C. Bisio, L. Tei, L. Marchese and M. Botta, *Dalton Trans.*, 2018, **47**, 7896-7904.
- 5 G. Paul, C. Bisio, I. Braschi, M. Cossi, G. Gatti, E. Gianotti and L. Marchese, *Chem. Soc. Rev.*, 2018, **47**, 5684-5739.
- 6 M. X. Reinholdt, J. Brendlé, M.-H. Tuilier, S. Kaliaguine and E. Ambrose, *Nanomaterials*, 2013, **3**, 48-69.
- 7 M. I. Boyanov, D. E. Latta, M. M. Scherer, E. J. O'Loughlin and K. M. Kemner, *Chemical Geology*, 2017, **464**, 110-117.
- 8 M. Mokhtar, *Materials*, 2017, **10**, 760-772.
- 9 M. Guidotti, R. Psaro, N. Ravasio, M. Sgobba, F. Carniato, C. Bisio, G. Gatti and L. Marchese, *Green Chem.*, 2009, **11**, 1173-1178.
- 10 G. Mata, R. Trujillano, M. A. Vicente, C. Belver, M. Fernández-García, S. A. Korili and A. Gil, *Appl. Catal. A-Gen.*, 2007, **327**, 1-12.
- 11 L. A. Utracki, M. Sepehr and E. Boccaleri, *Polym. Adv. Technol.*, 2007, **18**, 1-37.
- 12 F. Carniato, C. Bisio, G. Gatti, E. Boccaleri, L. Bertinetti, S. Coluccia, O. Monticelli and L. Marchese, *Angew. Chem. Int. Ed.*, 2009, **48**, 6059-6061.
- 13 Y.-C. Lee, T.-H. Lee, H.-K. Han, W. J. Go, J.-W. Yang and H.-J. Shin, *Photochem. Photobiol.*, 2010, **86**, 520-527.
- 14 K. V. Rao, K. K. R. Datta, M. Eswaramoorthy and S. J. George, *Angew. Chem. Int. Ed.*, 2011, **123**, 1211-1216.
- 15 F. Olivero, F. Carniato, C. Bisio and L. Marchese, *J. Mater. Chem.*, 2012, **22**, 25254-25261.
- 16 K. J. Balkus Jr. and J. Shi, *Langmuir*, 1996, **12**, 6277-6281.
- 17 X. Chen, Y. Xu, H. Li and B. Liu, *Sens. Actuators B*, 2017, **246**, 344-351.
- 18 M. Jin, D. E. M. Spillane, C. F. G. C. Geraldles, G. R. Williams and S. W. A. Bligh, *Dalton Trans.*, 2015, **44**, 20728-20734.
- 19 A. Sanchez, Y. Echeverria, C.M.S. Torres, G. Gonzalez and E. Benavente, *Materials Research Bulletin*, 2006, **41**, 1185-1191.
- 20 A) D. Talarico de Araujo, K. J. Ciuffi, E. J. Nassar, M. A. Vicente, R. Trujillano, P. S. Calefi, V. Rives, E. H. de Faria, *J. Phys. Chem. C*, 2017, **121**, 5081-5088;
B) H. Li, M. Li, Y. Wang and W. Zhang, *Chem. Eur. J.*, 2014, **20**, 10392-10396;

- C) Y. Wang, P. Li, S. Wang and H. Li, *Journal of Rare Earths*, 2019, **37**, 451-467.
- 21 S.-J. Ryu, A. Kim, M. D. Kim, S. W. Hong, S. S. Min, J.-K. Lee, H. Jung and J.-H. Lee, *Applied Clay Science*, 2014, **101**, 52-59.
- 22 X. Chen, Y. Wang, R. Chai, Y. Xu, H. Li and B. Liu, *ACS Appl. Mater. Interfaces*, 2017, **9**, 13554-13563.
- 23 D. Yang, Y. Wang, Y. Wang and H. Li, *Sensors and Actuators B*, 2016, **235**, 206-212.
- 24 F. Carniato, C. Bisio, G. Gatti, S. Roncoroni, S. Recchia and L. Marchese, *Catal. Lett.*, 2009, **131**, 42-48.
- 25 F. Carniato, C. Bisio, R. Psaro, L. Marchese and M. Guidotti, *Angew. Chem. Int. Ed.*, 2014, **53**, 10095-10098.
- 26 D. Costenaro, C. Bisio, F. Carniato, S. L. Safronyuk, T. V. Kramar, M. V. Taran, M. F. Starodub, A. M. Katsev and M. Guidotti, *Chemistry Select*, 2017, **2**, 1812-1819.
- 27 D. L. Andrews, *Canad. J. Chem.*, 2008, **86**, 855-870.
- 28 X. Guo, *New J. Chem.*, 2005, **29**, 1351-1358
- 29 C. Bisio, F. Carniato, G. Paul, G. Gatti, E. Boccaleri and L. Marchese, *Langmuir*, 2011, **27**, 7250-7257.
- 30 O. Prieto, M. A. Vincente and M. A. Banares-Munoz, *J. Porous Mater.*, 1999, **6**, 335-344.
- 31 J. C. Dabrowiak, *Metals in Medicine (2nd Ed)*, 2017, John Wiley & Sons Ltd, ISBN: 978-1-119-19130-8.
- 32 J. L. Zatz and C. Yarus, *Pharmaceutical Research*, 1986, **3**, 118-121.
- 33 Y. Wang and N. Lin, *Photochem. Photobiol. Sci.*, 2011, **10**, 42-47.
- 34 A) R. T. Wegh and A. Meijerink, *Acta Physica Polonica A*, 1996, **90**, 333-337;
B) H. Suzuki, T. A. Tombrello, C. L. Melcher, C. A. Peterson and J. S. Schweitzer, *Nucl. Instr. and Meth. in Phys. Res. A*, 1994, **349**, 510-521.
- 35 B. Szpikowska-Sroka, M. Żądło, E. Czoik, L. Żur and W. A. Pisarski, *Journal of Luminescence*, 2014, **154**, 290-293.
- 36 K. Binnemans and C. Gorller-Walrand, *J. Rare Earths*, 1996, **14**, 173-180.
- 37 S. Marchesi, F. Carniato and E. Boccaleri, *New J. Chem.*, 2014, **38**, 2480-2485.
- 38 S. Marchesi, F. Carniato and E. Boccaleri, *ChemPlusChem*, 2015, **80**, 915-918.
- 39 R. Reisfeld, *Struct. Bonding (Berlin)*, 1973, **13**, 53-98.
- 40 S. F. Tang, A. Babai and A. V. Mudring, *Angew. Chem. Int. Ed.*, 2008, **47**, 7631-7638.
- 41 P. Zhang, Y. Wang, H. Liu and Y. Chen, *J. Mater. Chem.*, 2011, **21**, 18462-18466.
- 42 S. I. Klink, G. A. Hebbink, L. Grave, P. G. B. Oude Alink, F. C. J. M. van Veggel and M. H. V. Werts, *J. Phys. Chem. A*, 2002, **106**, 3681.
- 43 M. H. V. Werts, *Luminescent Lanthanide Complexes, Visible Light Sensitised Red and Near-Infrared Luminescence*, PhD thesis, The Netherlands, 2000.

- 44** S. Aime, M. Botta and E. Terreno. *Adv. Inorg. Chem.*, 2005, **57**, 173-237.
- 45** P. Hermann, J. Kotek, Kubíček and I. Lukes, *Dalton Trans.*, 2008, **21**, 3027-3047.
- 46** A. Beeby, I. M. Clarkson, R. S. Dickins, S. Faulkner, D. Parker, L. Royle, A. S. de Sousa, J. A. G. Williams and M. Woods, *J. Chem. Soc., Perkin Trans.*, 1999, **2**, 493-504.
- 47** C. Platas-Iglesias, L. Vander Elst, W. Zhou, R. N. Muller, C. F. G. C. Geraldes, T. Maschmeyer and P. A. Joop, *Chem. Eur. J.*, 2002, **8**, 5121-5131.
- 48** F. Mayer, W. Zhang, T. Brichart, Olivier Tillement, C.S. Bonnet, É. Tóth, J.A. Peters and K. Djanashvili, *Chem. Eur. J.*, 2014, **20**, 3358.
- 49** L. P. Hwang and J. H. Freed, *J. Chem. Phys.*, 1975, **63**, 4017-4025.
- 50** J. H. Freed, *J. Chem. Phys.*, 1978, **69**, 4034-4037.
- 51** M. Botta and L. Tei, *Eur. J. Inorg. Chem.*, 2012, **12**, 1945-1960.
- 52** V. C. Pierre and M. J. Allen, "*Contrast Agents for MRI: Experimental Methods (New Developments in NMR)*", 2017, Royal Society of Chemistry, **ISBN: 978-1-78262-447-9**.
- 53** S. Aime, M. Botta and G. Ermondi, *J. Mag. Reson.*, 1991, **92**, 572-580.
- 54** G. Accorsi, A. Listorti, K. Yoosaf, and N. Armaroli, *Chem. Soc. Rev.*, 2009, **38**, 1690-1700.
- 55** F. Cucinotta, F. Carniato, A. Devaux, L. De Cola and L. Marchese, *Chem. Eur. J.*, 2012, **18**, 15310-15315.
- 56** K. Binnemans, *Coord. Chem. Rev.*, 2015, **295**, 1-45.
- 57** F. Olivero, F. Carniato, C. Bisio and L. Marchese, *Chem. Asian J.*, 2013, **9**, 158-165.
- 58** I. P. Sahu, D. P. Bisen, R. K. Tamrakar, K. V. R. Murthy and M. Mohapatra, *Journal of Science: Advanced Materials and Devices*, 2017, **2**, 59-68.

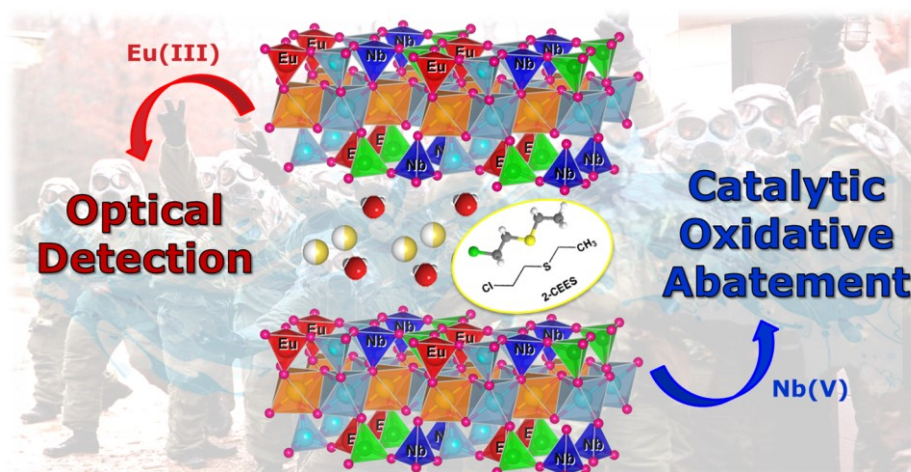
6

“Bifunctional Eu^(III) and Nb^(V)-containing Saponites for Optical Detection and Catalytic Abatement of Chemical Warfare Agents”

In this chapter, europium and niobium elements were combined with synthetic saponite clays obtaining novel layered materials with luminescent and catalytic properties, exploited for the optical detection and catalytic oxidative abatement of blistering chemical warfare agents (see Figure below).

The materials were prepared through two different synthetic strategies: i) intercalation of europium ions into a niobium-saponite sample and ii) one-pot hydrothermal procedure, in which both metals were introduced in the in-framework positions of the clay.

The samples were tested in simple conditions (in water at neutral pH, room temperature, atmospheric pressure and with a mild oxidizing agent) against a simulant of mustard gas called (2-chloroethyl)ethyl sulphide, employing a combination of UV-Vis-NIR, liquid NMR and Photoluminescence techniques.



6.1 Introduction

Among the weapons of mass destruction, the Chemical Warfare Agents (CWAs), commonly defined as “*chemical substances (solid, liquid or gas) intended for use in military operation to kill, seriously injure or incapacitate humans or animals or plants through their highly toxicological effects*”,¹ have been recognized one of the deadliest weapons that humankind have ever invented. Compared to nuclear weapons, for example, they are relatively easy to access and deploy and for this reason they represent a greater threat to national and global security.

The First World War (WWI) is considered as the dawn of the ‘modern chemical warfare’ in the history of human race, in which more than 50 different chloride-based CWA (*i.e.* tear gases, chlorine, phosphagen and diphosgene, mustard gas or yperite...) were massively deployed on several battlefields, causing approximately 1.3 million of non-fatal casualties and 90.000-100.000 fatalities.²⁻⁵ In the following years, several organophosphate-based nerve agents were discovered and some of these were later developed for military purposes, though never been ‘official’ used in warfare.²⁻⁵ Unfortunately, still nowadays the CWA represent a great safety threat towards the global community, due to their illegal employment in current war scenarios (even against civilians) and in terrorist attacks,⁶ against the international rules dictated by the “Chemical Weapons Convention” (CWC) administered by the Organisation for the Prohibition of Chemical Weapons (OPCW).⁷

Based on their effects on humans, the CWAs have been generally categorized in: blistering or vesicants chemicals (which cause severe skin, eye and mucosal pain as the infamous mustard gas), incapacitating agents (*i.e.* fentanyl) and nerve gas (*i.e.* Sarin, which mortally affects the nervous system) (Figure 1).^{8,9}

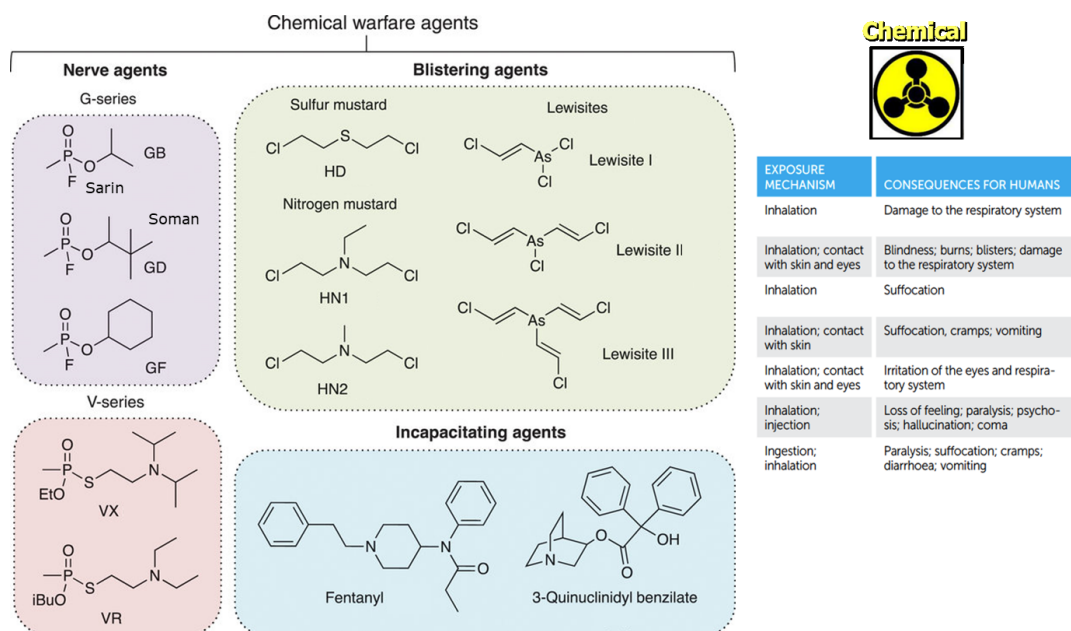


Figure 1. Categories of CWAs based on their toxicological effects on human beings.

Because of their high toxicity and dangerousness to human beings and the environment, over the years the development of suitable procedures for the safe destruction and abatement of stockpiled CWA has been always an active area of research in the scientific community.^{10,11} On this topic, several protection methods have been developed.

The conventional degradation methodologies are commonly relying on *i*) physical removal (*i.e.* adsorption on solid materials such as clays, deposition, dissolution with organic solvents/petrol/paraffin...), *ii*) thermal removal (*i.e.* high temperature, combustion...), *iii*) use of advanced techniques (*i.e.* microwaves, plasma...) and *iv*) over-stoichiometric oxidation reaction with active chlorine-based oxidants (*i.e.* basic solutions, detergents, chlorinated lime, *decon* solution with sodium and calcium hypochlorite, NaOCl and Ca(ClO)₂ respectively, or dichloroisocyanurate ...).¹²⁻¹⁵ However, even though they proved to be effective and safe for technical operators and personnel, all these techniques need huge amounts of reactants and energy and this poses several non-negligible problems in terms of safety, environmental and economical sustainability, costs and disposal of the detoxified by-products.^{10,11,16}

To overcome these drawbacks, in the last years the research has focused on the development of more effective, cheap and reliable heterogeneous and nanostructured solid catalysts for the selective oxidation of CWAs into partially or fully oxidized nontoxic products.¹⁷⁻²¹ Several materials were explored in the literature, from supported transition metals (V, Mo and Fe) polyoxometalates (POMs),^{22,23} porous oxides with catalytically metal sites (activated by light or with mild oxidizing agents),^{16,24,25} metal-containing silica and zeolite-based nanostructured solids, metal organic frameworks (MOFs) and modified activated carbons.^{19,20,26-29}

Recently, layered inorganic materials such as phyllosilicate clays, in particular Fe-bentonites³² and synthetic smectite saponites,^{30,31} have been used effectively in the decontamination of hazardous CWAs, due to their advantages such as high robustness, high chemical versatility, enhanced adsorption capabilities and very low production costs.³³⁻³⁵ Above all, saponite clays with relatively high surface acidity bearing in-framework Nb⁵⁺ sites were successfully employed in the selective oxidization of the organosulphur (2-chloroethyl)ethyl sulphide (CEES or 2-CEES), a simulant of the sulphur mustard CWA (blister HD agent) with comparable chemical architecture and reactivity but remarkably reduced toxicity, into nonnoxious products (*i.e.* sulfoxides) under mild conditions (in organic solvents with aqueous hydrogen peroxide, H₂O₂).^{30,31}

Another important aspect relating to the control of highly toxic CWAs concerns their detection, both before (as a form of prevention) and after their ‘deployment’: indeed, during hazardous materials (“hazmat”) incidents, the rapid recognition and identification of CWAs is vital to the protection of first responders and emergency medical personnel at local medical facilities as well as to the effective treatment of casualties.^{3,4,12,36,37} Besides standard equipment which rely on conventional handheld detectors, commonly adopted by several military forces around the world,¹ an important and growing area of the research is the development of more sensitive and selective analytical systems in form of molecular or material bio/chemosensors, particularly to “sense” sulphuric and organophosphorus CWAs.³⁹⁻⁴³ On this regard,

compounds containing luminescent lanthanides as europium (Eu^{3+}), generally as complexes with/without organic antenna groups or combined with other metals as iridium,⁴⁴⁻⁴⁶ have been recently proposed as ideal candidates for the design of novel optical chemosensors (*i.e.* ratiometric, colorimetric..), by exploiting their luminescent properties.⁴⁷ The trivalent europium ion shows unique spectroscopic characteristics, including long fluorescence lifetime, high quantum efficiency, large Stoke shift (with excitation in the ultraviolet region and emission in the UV-Visible range) and narrow and intense emission bands highly sensible to slightly changes in the chemical surroundings. Moreover, it is relatively non-toxic.⁴⁸ The sensing capacity of Eu^{3+} rely upon modulation of its luminescence emission in the presence of the target CWA, made possible by a high coordinative affinity for phosphoryl/phosphonyl bonds ($\text{P}=\text{O}$) and sulphur groups, which can occur via multiple pathways: *i*) competitive binding (static quenching), *ii*) chemical reactivity and *iii*) subsequent binding of degradation products, *iv*) hydrolysis or *v*) alteration of the local chemical environment in close proximity to the metal.^{47,49-52}

To the best of our knowledge, the combination of both detection and catalytic degradation capabilities of CWAs into a single nanostructured material, and the application of these properties in real life-*like* (*i.e.* in water) experimental conditions, have not been fully explored yet in the literature. Thus, for the first time in this study we aimed at designing multifunctional solids with both optical recognition and decontamination abilities, with the purpose to test them in a water environment. Thanks to knowledge acquired in previous chapters, related to the inclusion of lanthanides in the interlamellar space or in the framework of synthetic saponite clays, in this work Eu^{3+} centres were incorporated into NbSAP clays (whose abatement performance has been well studied)^{30,31} in different ways by properly modifying the synthetic protocol. Eu^{3+} species were inserted, together with Nb^{5+} ions, directly in the saponite framework through a *one-pot* (single-step) procedure (material hereafter named NbEuSAP), or introduced in the interlamellar region by post-synthesis cation-exchange process on a NbSAP clay^{30,31} (sample named Eu-NbSAP) (Figure 2). A

solid containing only Nb^{5+} species was prepared as reference (called NbSAP) using a synthetic procedure established in literature by Costenaro *et al.*^{30,31} EuSAP and SAP-20 clays, prepared in *Chapter 5* and *5* respectively, were also used as references in some measurements. All functionalized materials were submitted to a complete characterization from the physico-chemical point of view. Particular attention was devoted to the optical detection and catalytic oxidative tests against the CEES simulant, which were performed in ‘practical’ or more simple experimental conditions, especially if compared to previous studies executed in organic phase (*n*-heptane):^{30,31} in aqueous medium at neutral pH, at room temperature (RT, 25 °C) and atmospheric pressure (1 atm) and with a mild oxidizing agent (30 wt.% aqueous H_2O_2).

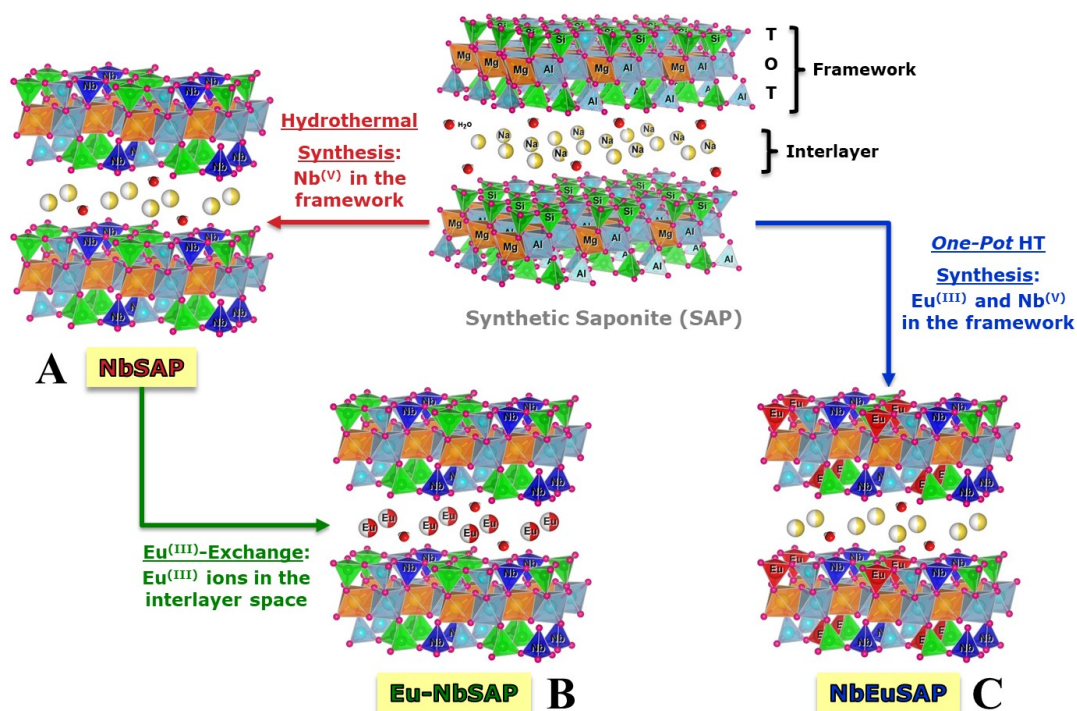


Figure 2. Different synthetic pathways adopted for the preparation of NbSAP (A), Eu-NbSAP (B) and *one-pot* NbEuSAP (C) clays.

6.2 Experimental Approach

6.2.1 Materials

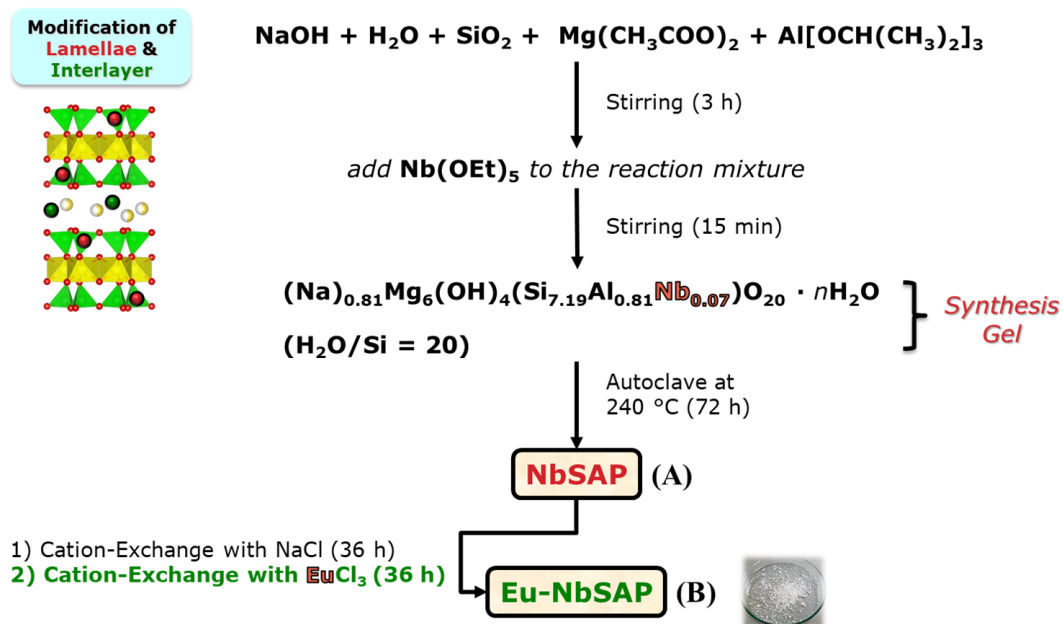
- **Synthesis of NbSAP clay:** Nanosized synthetic saponite containing Nb⁵⁺, positioned in the tetrahedral positions of the framework, was synthesized following the hydrothermal procedure adopted in the literature by Carniato *et al.* (Scheme 1, A).^{30,31} A gel with the molar composition of [SiO₂:MgO:Al₂O₃:Na₂O:Nb(OEt)₅:H₂O] 1:0.835:0.056:0.056:0.01:20 and H₂O/Si molar ratio of 20 was prepared. In detail, 8.50 g (0.13 mol) of amorphous silica (SiO₂ fumed, 99.8%) were gradually dispersed in a solution prepared by dissolving 0.63 g (0.01 mol) of sodium hydroxide (NaOH) in 50.00 g (2.78 mol) of ultrapure water. The obtained gel was then mixed accurately. After 1 h, 24.86 g (0.09 mol) of magnesium acetate tetrahydrate (Mg(CH₃COO)₂·4H₂O, 99%) and 3.20 g (0.01 mol) of aluminium isopropoxide (Al[OCH(CH₃)₂]₃, ≥ 98 %) were added to the reaction mixture and stirred for 2 h. After that, 347 μL (0.001 mol) of niobium ethoxide (Nb(OEt)₅, 99.95%) were added and the gel was left to stir for 15 min. After this, the gel, with a pH between 8-9, was introduced into a Teflon cup (125 mL capacity) of an autoclave (Anton Paar 4748) and heated in an oven for 72 h at 240 °C. After hydrothermal treatment, the product was filtered, washed with hot ultrapure water up to neutral pH and dried in an oven overnight at 100 °C.

The so-produced material called NbSAP (12.85 g of white powder) was submitted to cation-exchange procedure (in order to ensure a chemical uniformity of the exchange sites): 2.50 g of NbSAP were dispersed in 250 mL of saturated sodium chloride (NaCl) solution for 36 h at RT to replace all possible cations present (*i.e.* Al³⁺, Mg²⁺, H⁺) with Na⁺ ions in the interlayer space. Then, the solid material (named Na-NbSAP) was filtered, washed with hot ultrapure water until the complete elimination of chlorides (confirmed by silver nitrate, AgNO₃, spot test) and dried in an oven overnight at 100 °C.

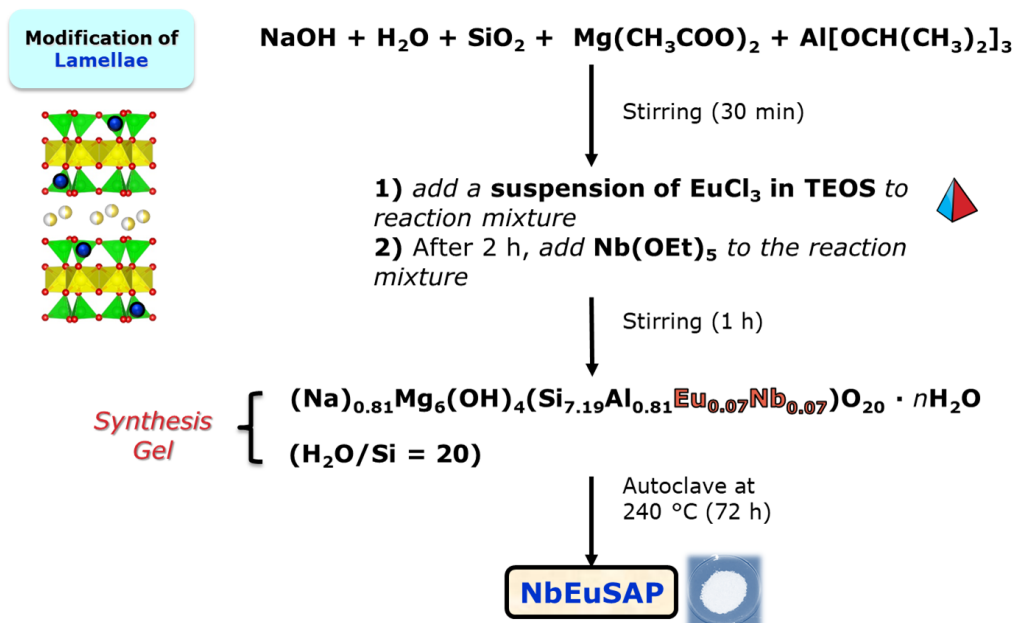
- **Preparation of Eu-NbSAP clay via Eu^{3+} -exchange of Na-NbSAP:** The introduction of Eu^{3+} ions in the interlamellar region of Na-NbSAP clay was achieved by classical cation-exchange procedure (Scheme 1, B).⁵³ The europium chloride precursor was added in a molar quantity equal to the CEC of Na-NbSAP (estimated to be 45.4 ± 1.3 meq/100 g). In details, 1.00 of NbSAP was dispersed in 125 mL of ultrapure water containing 0.117 g of anhydrous europium chloride (EuCl_3 ; $4.53\text{E-}4$ mol) and stirred for 36 h at RT. After that, the final material (named Eu-NbSAP) was filtered, washed with hot ultrapure water and dried in an oven overnight at 100 °C.
- **Synthesis of NbEuSAP clay via *one-pot* procedure:** Nanosized synthetic saponite containing both Eu^{3+} and Nb^{5+} in the tetrahedral layers of clay structure was synthesized by a modified *one-pot* hydrothermal procedure, adapted from the literature^{30,31} and from *Chapter 5* (Scheme 2). A gel with the molar composition of $[\text{SiO}_2:\text{MgO}:\text{Al}_2\text{O}_3:\text{Na}_2\text{O}:\text{Nb}(\text{OEt})_5:\text{EuCl}_3:\text{H}_2\text{O}]$ 1:0.835:0.056:0.056:0.01:0.01: 20 and $\text{H}_2\text{O}/\text{Si}$ molar ratio of 20 was prepared. In detail, 3.51 g (0.053 mol) of SiO_2 fumed (99.8%) were gradually dispersed in a solution prepared by dissolving 0.30 g (0.005 mol) of NaOH in 22.50 g (1.25 mol) of ultrapure water. The obtained gel was then mixed accurately. After 30 min, 24.86 g (0.09 mol) of $\text{Mg}(\text{CH}_3\text{COO})_2 \cdot 4\text{H}_2\text{O}$ (99%) and 3.20 g (0.01 mol) of $\text{Al}[\text{OCH}(\text{CH}_3)_2]_3$ ($\geq 98\%$) were added to the reaction mixture. Simultaneously, a suspension with of anhydrous EuCl_3 (0.177 g, $6.85\text{E-}4$ mol) in tetraethyl orthosilicate (TEOS; 3.02 mL, 0.015 mol) was prepared, the pH was then corrected between 2-3 with 1-2 drops of concentrated sulphuric acid (H_2SO_4) solution and the mixture was left in agitation at RT for 5 min. After this, 0.25 g (0.015 mol) of ultrapure water were added to the whitish suspension, stirred for another 5 min and, finally, introduced into the clay synthesis gel. The remaining ultrapure water (2.50 g, 0.14 mol) was then added to the reaction mixture. After 2 h, 167 μL ($6.65\text{E-}4$ mol) of $\text{Nb}(\text{OEt})_5$ (99.95%) were added and the gel was left to stir for another hour. After this, the gel, with a pH between 8-9, was

introduced into a Teflon cup (125 mL capacity) of an autoclave (Anton Paar 4748) and heated in an oven for 72 h at 240 °C. After hydrothermal treatment, the product was filtered, washed with hot ultrapure water up to neutral pH and dried in an oven overnight at 100 °C.

The so-produced material called NbEuSAP (7.80 g of white powder) was submitted to cation-exchange procedure (in order to ensure a chemical uniformity of the exchange sites): 2.50 g of NbEuSAP were dispersed in 250 mL of saturated NaCl solution for 36 h at RT to replace all possible cations present (*i.e.* Al³⁺, Mg²⁺, H⁺) with Na⁺ ions in the interlayer space. Then, the solid material (named Na-NbEuSAP) was filtered, washed with hot ultrapure water until the complete elimination of chlorides (confirmed by AgNO₃ spot test) and dried in an oven overnight at 100 °C.



Scheme 1. Schematic view of the preparation of NbSAP^{30,31} (A) and Eu-NbSAP (B) clays.



Scheme 2. Schematic view of the preparation of NbEuSAP clay.

6.3 Results and Discussion

6.3.1 Characterization of Eu^(III)/Nb^(V)-containing saponite materials

The Nb⁵⁺ and Eu³⁺ content in the prepared samples were determined by inductively coupled plasma mass spectrometry (ICP-MS) after mineralization of the solids in acidic media, and the results are reported in Table 1. The Eu-NbSAP sample showed an amount of structural Nb⁵⁺ and intercalated Eu³⁺ equal to 0.18 and 0.30 mmol/g, respectively. The Nb⁵⁺ content remained unchanged after europium-exchange. The *one-pot* sample NbEuSAP, instead, presented a lower content of both metals compared to the Eu-NbSAP. This can be attributed to a competition effect between the Nb⁵⁺ and Eu³⁺ ions during the formation of the tetrahedral units in the synthetic gel.

Table 1. Amount of Nb⁵⁺ and Eu³⁺ ions obtained from elemental analyses on EuSAP, NbSAP, Eu-NbSAP and NbEuSAP. ^aData from *Chapter 5*.

Sample	Nb ⁵⁺ [mmol/g]	Eu ³⁺ [mmol/g]
EuSAP ^[a]	/	0.03 ± 1.00E-3
NbSAP	0.19 ± 1.98E-3	/
Eu-NbSAP	0.18 ± 1.70E-3	0.30 ± 2.05E-3
NbEuSAP	0.02 ± 1.57E-3	0.03 ± 1.65E-3

The CEC values, evaluated through the classical UV-Vis-NIR method reported in literature,^{58,59} were estimated to be 45.5 ± 1.3 meq/100 g and 59.9 ± 1.1 meq/100 g for NbSAP and NbEuSAP, respectively. The values are similar of those reported for nanosized Nb⁵⁺-saponites^{30,31} and Ln³⁺-SAP clays from *Chapter 5*.

The structural properties of prepared solids were evaluated by X-ray powder diffraction (XRPD) analyses (Figure 3A and B). The addition of niobium and europium did not change the basic structure of the clay,^{30,31,55} as observed by the presence and relative positions of the (001), (110)-(020), (004), (130)-(201), (311) and (060) reflections (Figure 3A).³³⁻³⁵ The shift of the basal plane (001) from 6.70°

2θ (d -spacing of 1.32 nm) in NbSAP (*b*) to 6.10° 2θ (1.45 nm) in Eu-NbSAP (*c*) (Figure 3B) confirms the introduction of Eu^{3+} ions in the interlayer space of the sample. This effect can also be partially attributed to the hydration sphere of the intercalated Eu^{3+} ions, bigger than that of Na^+ ions. The NbEuSAP sample showed a negligible shift of the basal plane if compared to NbSAP clay, with a value of 6.40° 2θ (1.38 nm) (Figure 3B, *d*). This value is in line with those of paramagnetic/luminescent saponite clays with structural Gd^{3+} and Eu^{3+} (Ln^{3+} -SAP) described in *Chapter 5*.

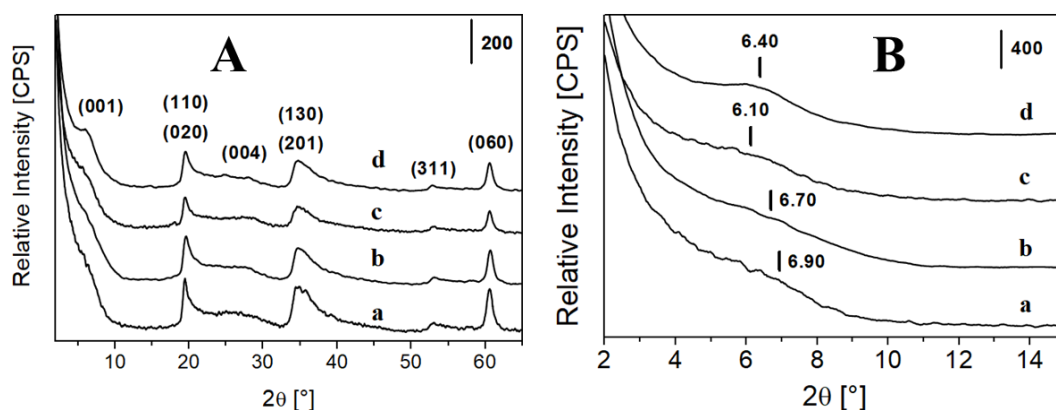


Figure 3. A) X-ray powder diffraction profiles of SAP-20 (*a*), NbSAP (*b*), Eu-NbSAP (*c*) and NbEuSAP (*d*); diffractograms collected at low angles (2° - 15° 2θ) are reported in Frame B.

The stability of the aqueous suspensions of the prepared materials was evaluated by dynamic light scattering (DLS) analyses (Figure 4). The samples were dispersed in ultrapure water containing 0.1 wt.% of xanthan gum^{60,61} and measurements were performed at 25°C . The homogenous suspensions remained stable for several hours, showing general hydrodynamic size values in the nanometric range of 45-70 nm (Figure 4), in agreement with results on Nb^{5+} -saponites from literature.^{30,31}

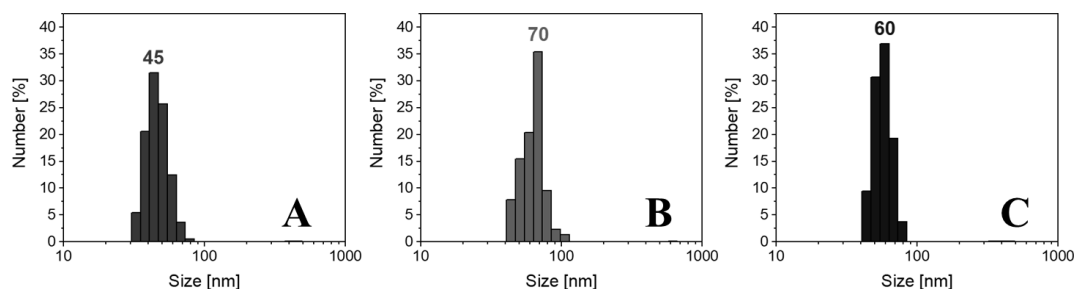
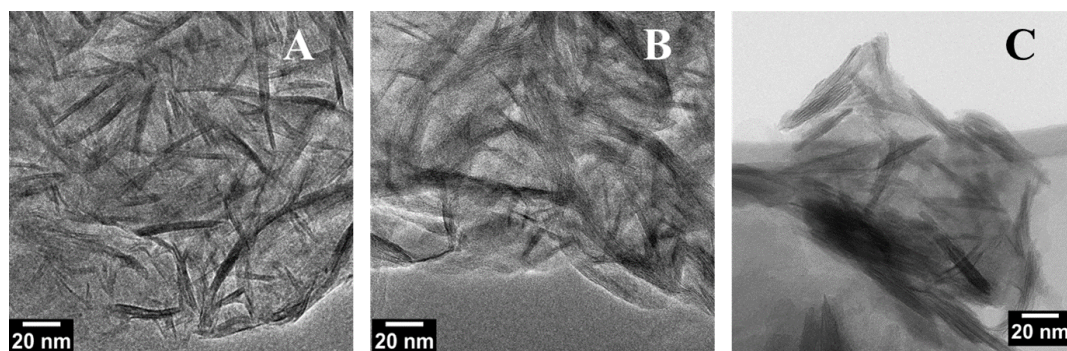


Figure 4. DLS analysis at 25 °C of NbSAP (a), Eu-NbSAP (b) and NbEuSAP (c) aqueous suspensions containing 0.1 wt.% of xanthan gum.

The morphological features of NbSAP, Eu-NbSAP and NbEuSAP samples were evaluated by high-resolution transmission electron microscopy (HRTEM) (Figure 5A-C). The materials showed different levels of spatial organization of lamellae particles (*i.e.* from sheet-like single structures to tactoids of different size), with a range of lengths of a few tens of nanometres, analogous to previous Nb⁵⁺-saponites^{30,31} and Ln³⁺-SAP clays (Chapter 5) prepared with a H₂O/Si of 20. The distribution of the $d_{(001)}$ -spacing values, acquired by counting more than 100 particles, was found to be slightly broad, heterogenous and centred around 1.3-1.5 nm (Figure 5D-F). For Eu-NbSAP sample (E) the $d_{(001)}$ was estimated to be 1.44 nm, from 1.30 nm of NbSAP (D), further established the success of the intercalation of Eu³⁺ ions. Accordingly, a schematic view³ of the structures of NbSAP, Eu-NbSAP and NbEuSAP is reported in the G, H and I frames, respectively.



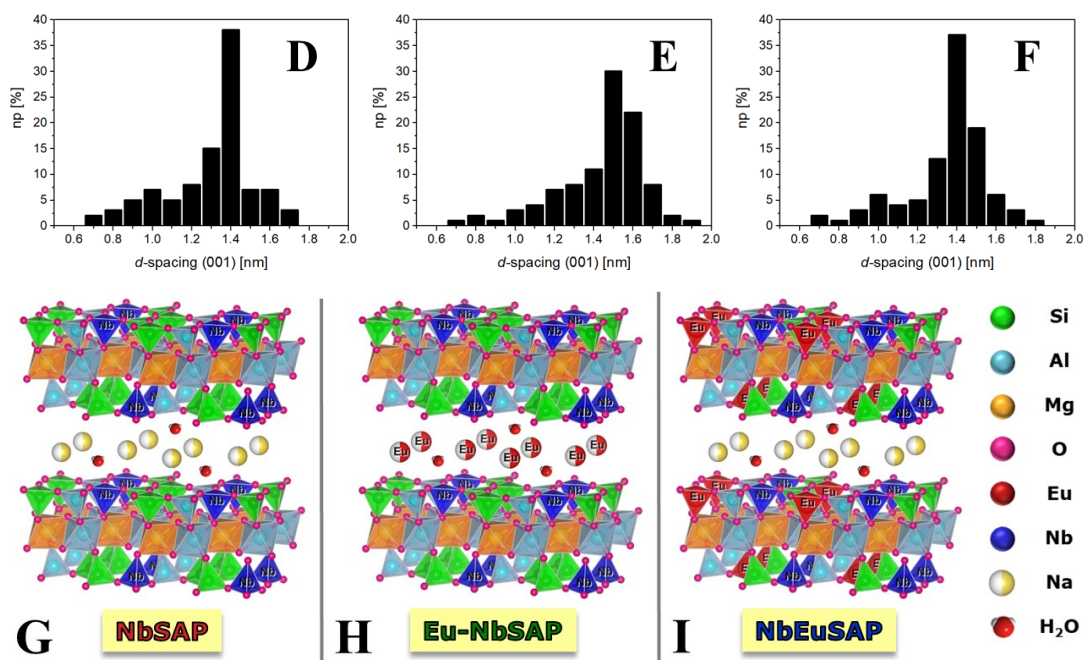


Figure 5. HRTEM micrographs of NbSAP (A), Eu-NbSAP (B) and NbEuSAP (C).

The distribution of the $d_{(001)}$ -spacing are shown in D, E, F respectively. Schematic illustrations of NbSAP (G), Eu-NbSAP (H) and NbEuSAP (I) structures.

The coordination state of the Nb⁵⁺ species in NbSAP, Eu-NbSAP and NbEuSAP samples was investigated by diffuse reflectance ultraviolet-visible-near infrared (DR UV-Vis-NIR) spectroscopy (Figure 6), by diluting the solid samples in barium sulphate matrix (at 20 wt.%). The DR UV-Vis-NIR spectra of the samples showed two main absorptions: the most intense at 235/250 nm is assigned to charge transfer transitions between oxygen atoms and Nb⁵⁺ centres in tetrahedral coordination (“Td”) in the tetrahedral layers, while the second one at 270 nm is related to structural octahedral coordinated Nb⁵⁺ species (“Oh”) in defective zones of lamellae, due to expansion of the metal geometry promoted by water coordination.^{30,31,21,56} The less intense shoulder at 320 nm is commonly associated to the presence of niobium oligomers. The band is near absent in NbEuSAP sample (Figure 6, c) and this is attributed to the lower Nb⁵⁺ loading compared to the other two materials, NbSAP and Eu-NbSAP. In all spectra, in general, no absorption bands were detected above

400 nm, thus suggesting the absence of large extra-phase niobium oxide (*i.e.* Nb₂O₅) domains.

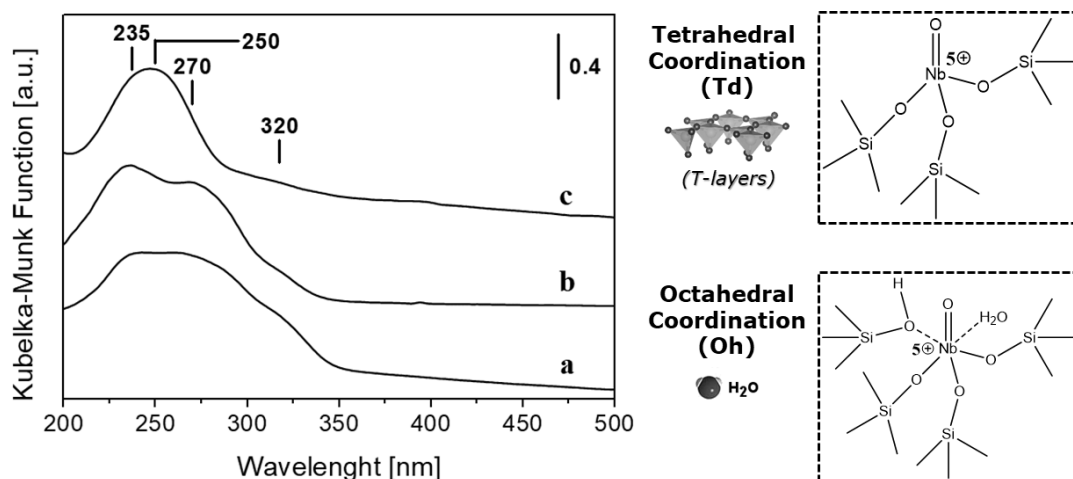


Figure 6. Normalized DR UV-Vis-NR spectra of NbSAP (a), Eu-NbSAP (b) and NbEuSAP (c), diluted in BaSO₄ matrix (20 wt.%), in air and at RT.

The quantification of acid sites in the samples was performed by using FTIR spectroscopy of adsorbed gaseous ammonia (NH₃).⁵⁷ Figure 7 showed the infrared (FTIR) spectra collected after admission of 95 mbar of NH₃ on the three samples (previously outgassed at 300 °C) and subsequent evacuation at RT for 90 min. The spectra of all samples show different bands centred at 1445, 1505, 1575, 1620 and 1680 cm⁻¹. The bands at 1445 and 1505 cm⁻¹ are due to the asymmetric bending modes of ammonium ions (δ_{as} NH₄⁺) formed by interaction of basic NH₃ with Brønsted acid sites (*i.e.* Si-O(H)-Al, Al-OH on surface).³⁵ The band at 1620 cm⁻¹ is due to δ of NH₃ adsorbed on Lewis acid sites (*i.e.* Na⁺ at exchange sites) and/or silanols (Si-OH) at the surface of saponite materials. The signal located at 1575 cm⁻¹, instead, is due to Si-NH₂ species formed by interaction of NH₄⁺ with distorted siloxane bridges (Si-O-Si) by condensation of vicinal Si-OH during the thermal activation of the sample.³⁵ Finally, the signal at 1680 cm⁻¹ is due symmetric δ_s NH₄⁺. The concentration of Brønsted acid sites ([H⁺]) was then calculated by considering the FTIR bands of adsorbed NH₃ at RT using the Eq. (1), where A is the integrated

intensity of the band at 1445 cm^{-1} ($\delta_{\text{as}}\text{NH}_4^+$ ions), ρ is the pellet density (g/cm^2) and $\varepsilon_{\text{N-H}}$ is the molar extinction coefficient of the N-H bond ($13\text{ cm}/\mu\text{mol}$).^{31,33-35}

$$[\text{H}^+] = A / (\rho \cdot \varepsilon) \quad (1)$$

The total concentration of Brønsted acid sites is comparable between the samples, with values of 0.08, 0.09 and 0.11 mmol/g for NbSAP, Eu-NbSAP and NbEuSAP, respectively.

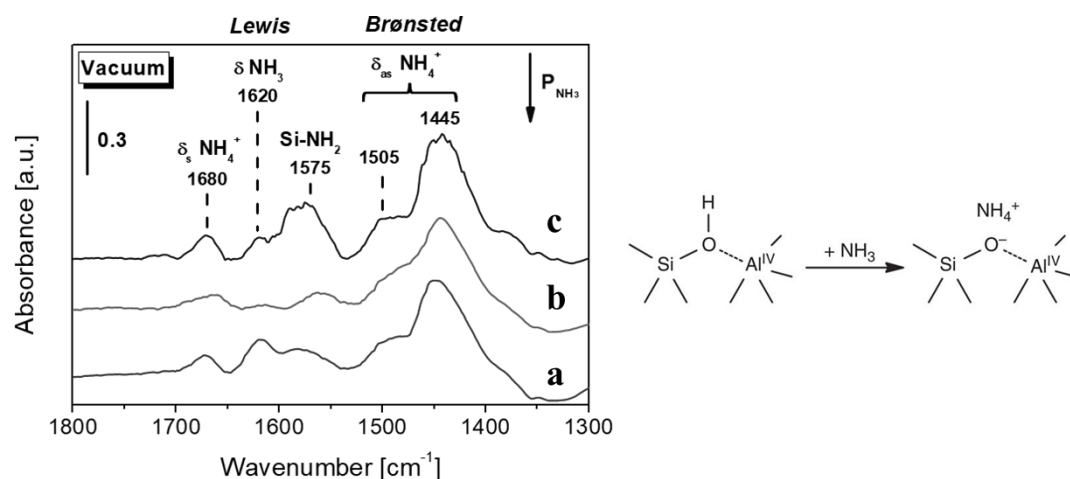


Figure 7. FTIR spectra, in the $1800\text{-}1300\text{ cm}^{-1}$ region, of NH_3 (95 mbar) adsorbed and then evacuated a RT on NbSAP (a), Eu-NbSAP (b) and NbEuSAP (c), outgassed at $300\text{ }^\circ\text{C}$. Spectra are reported after subtraction of the relative spectrum before ammonia adsorption.

The photophysical properties of Eu-NbSAP and NbEuSAP clays were studied by photoluminescence (PL) spectroscopy, both at solid state and in aqueous suspensions (with 0.1 wt.% of xanthan gum),^{60,61} in order to obtain information on the chemical nature/geometrical aspects of the environment around Eu^{3+} sites. The EuSAP sample was used as reference. The excitation spectrum in suspension of NbEuSAP (Figure 8A), recorded at the most intense emission line of Eu^{3+} at 615 nm, presented the narrow peaks due to the characteristic intra- $4f^6$ electronic transitions of Eu^{3+} (${}^7\text{F}_0\text{-}{}^5\text{H}_J, {}^5\text{D}_J, {}^5\text{L}_J$) with a λ_{max} at 395 nm ascribed to ${}^7\text{F}_0\text{-}{}^5\text{L}_6$.⁴⁸ The same transitions were

found for the Eu-NbSAP sample. The emission spectra of both luminescent clays was then collected under irradiation at 395 nm (λ_{\max} of Eu^{3+}) and showed the typical emission peaks of the intra- $4f^6$ electronic levels of Eu^{3+} ($^5\text{D}_0$ - $^7\text{F}_J$, $J = 0-4$) (Figure 8B).⁴⁸ Similar results were obtained at solid state. Additional photophysical information, both in suspension and at solid state, on the heterogeneity of Eu^{3+} sites,⁶² geometrical/coordination aspects of Eu^{3+} centres (asymmetry/symmetry of the local environment),⁶³⁻⁶⁷ hydration state,^{63,64,67} quantum efficiencies^{63,68,69} and photostability of the samples were also thoroughly studied (in the same way as it was did for the luminescent clays in *Chapter 5*), and the final results are shown in Table S8 in *Chapter 8*. For both materials the local environments surrounding the luminescent centres were found to be highly asymmetric, with *ca.* three water molecules coordinated to Eu^{3+} for NbEuSAP and *ca.* four for Eu-NbSAP.

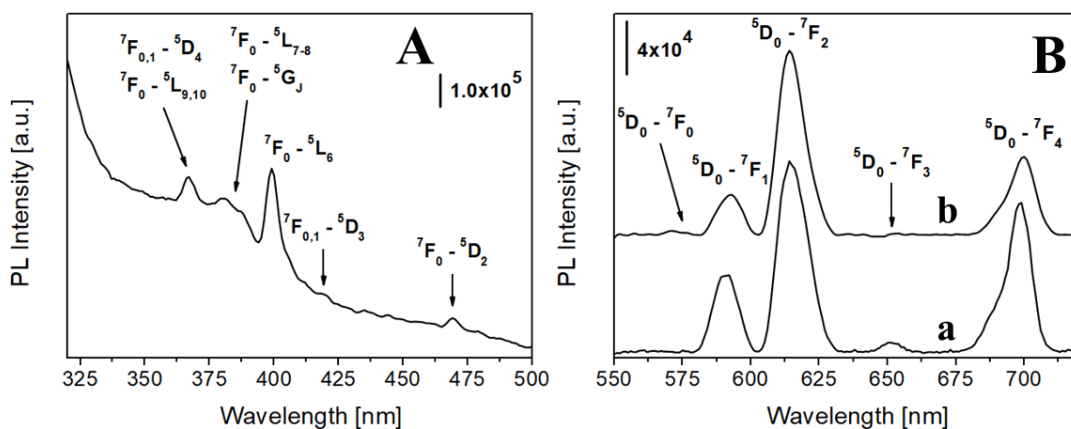


Figure 8. A) Excitation spectrum of NbEuSAP, collected at 615 nm. B) Emission spectra of Eu-NbSAP (*a*) and NbEuSAP (*b*), under excitation at 395 (λ_{\max} Eu^{3+}). The spectra were collected in aqueous suspension (with 0.1 wt.% of xanthan gum).^{60,61}

6.3.2 Catalytic oxidative abatement tests

The catalytic oxidative abatement tests of the blistering agent simulant CEES (98%) were performed on NbSAP, Eu-NbSAP and NbEuSAP clays, in 50 mL single neck reaction flasks. The experiments were carried out in aqueous medium at neutral

pH, at RT and atmospheric pressure. In detail, 33 μL of CEES (14 mM) were mixed in 20 mL of phosphate buffer solution (PBS, 10 mM, pH = 7.0) and stirred until complete dissolution; 20 mg of solid clay catalyst follows by 143 μL of 30 wt.% aqueous H_2O_2 (70 mM) were then added to the mixture and the dispersion was stirred continuously throughout the test. Samples of the reaction mixture were withdrawn at regular intervals (0, 30', 1-2-3-4-5-6-7-24 h) and filtered to remove any suspended clay particles. An experiment without catalyst (*blank*) was performed as well, also to assess the stability of CEES in water. SAP-20 clay (see *Chapter 3*) was also tested with CEES to evaluate the catalytic behaviour in water of a pristine saponite.

The gradual consumption of CEES by the active solid catalysts over time was followed by UV-Vis-NIR spectroscopy (Figure 9) in absorption mode, by monitoring the intensity of the characteristic maximum absorption of CEES in water at $\lambda_{\text{max}} = 200 \text{ nm}$ (associated to the $n \rightarrow \sigma^*$ / $\sigma \rightarrow \sigma^*$ electronic transitions of the C-S bond), derived from spectroscopic analyses carried out on the CWA simulant alone prior the catalytic tests. For measurements, 75 μL of each filtered sample was diluted to a total of 3040 μL with 2965 μL of PBS, in a 3.0 mL quartz cuvette.

The UV-Vis-NIR spectra of NbEuSAP sample (used as example) collected at different contact times with CEES are reported in Figure 9A. The same behaviour was found for the reference NbSAP and the Eu-NbSAP. In Figure 9B, instead, are reported the CEES abatement kinetics profiles in water for NbSAP (*a*), Eu-NbSAP (*b*), NbEuSAP (*c*) and SAP-20 (*d*) samples and without catalyst (*blank*, *e*), obtained by extrapolating the CEES concentration remained in solution over time from the UV-Vis-NIR spectra in Figure 9A.

The *blank* experiment, performed in absence of any catalyst (Figure 9B, *e*), showed a negligible CEES self-decomposition trend in aqueous medium (*ca.* 2 % after 24 h), probably promoted by a marginal oxidant activity of the H_2O_2 . Using a Nb^{5+} -free saponite sample as a catalyst (SAP-20; Figure 9B, *d*), a 26% of CEES abatement is observed in 24h, thus proving that the clay itself does possess limited sulphide degradation and physical adsorption capabilities in water and cannot

account for a complete removal of CWA simulant.^{30,31} as previously observed in organic phase (*n*-heptane).

On the contrary, an astonishing degradation capability in water was observed over all the Nb⁵⁺-containing saponite clays (Figure 9B). As noted in previous studies,^{30,31} the synergic effect between Nb⁵⁺ centres and acid sites affect the catalytic activity of Nb⁵⁺-containing saponites. The Nb⁵⁺ centres confer oxidizing properties, while the presence of protonic/H⁺ sites helps to increase the abatement activity via acid-promoted degradation. Also, H⁺ sites can take part in the formation of niobium hydroperoxo species, in which the selective heterolytic O₂ transfer from H₂O₂ to CEES takes place.^{70,71} NbSAP (*a*) and Eu-NbSAP (*b*) samples presented the best catalytic performances, with more than 85-90 % of CEES decomposed after 24 h, while the NbEuSAP (*c*) sample showed a slightly lower catalytic activity (70 %). The absence of significant niobium oligomeric sites, as seen in UV-Vis-NIR analyses (Figure 6A), allows to exclude any effect of these species on the final catalytic behaviour of the solids.⁷² Moreover, all the materials showed comparable acid sites concentrations, as noted from the FTIR study (Figure 7). Furthermore, for all samples the active Nb⁵⁺ sites are evenly dispersed in the tetrahedral in-framework positions (*T*-layers). Therefore, the divergence in CEES degradation activity observed in the abatement profiles of the three functionalized saponites (Figure 9B) should be mainly correlated to their different Nb⁵⁺ concentration. Indeed, NbSAP and Eu-NbSAP samples, which have similar Nb⁵⁺ content (Table 1) and surface acidity (Figure 7) showed almost the same catalytic oxidative abatement properties. The NbEuSAP sample showed a relative lower catalytic performance than NbSAP and Eu-NbSAP solids, which is mainly attributed to the lower concentration of Nb⁵⁺ species compared to those of previous samples (Table 1). Considering that this material can be synthesized in one single-step (Scheme 2), it is possible to conclude that, in any case, the NbEuSAP clay showed quite remarkable CEE abatement performance in water.

Besides, the addition of Eu^{3+} , into the interlayer or in the structure of the clay, does not seem to influence the final catalytic activities of the prepared materials.

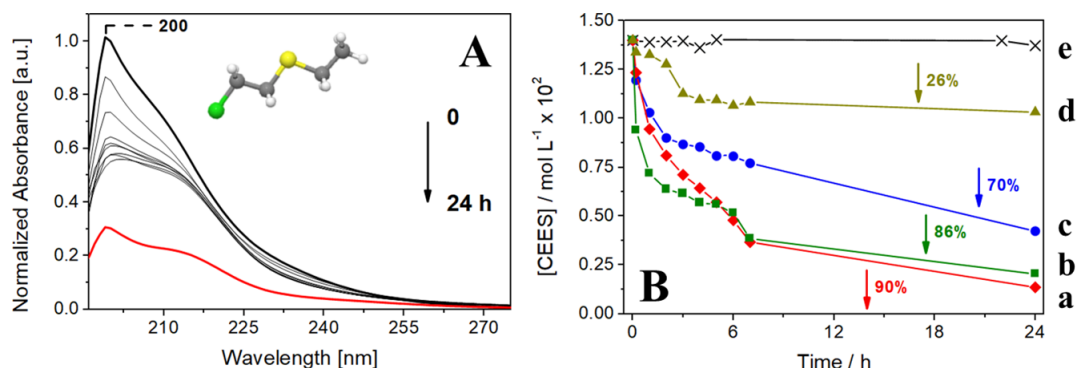


Figure 9. A) UV-Vis-NIR spectra of the reaction mixture in the presence of NbEuSAP catalyst, from 0-24 h. B) Oxidative abatement of CEES in NbSAP (a, -◆-), Eu-NbSAP (b, -■-), NbEuSAP (c, -●-), SAP-20 (d, -▲-) and without catalyst (e, -X-). Reaction conditions: 14 mM CEES, 70 mM 30 % aq. H_2O_2 , PBS solution at neutral pH, 20 mg of catalyst and 25 °C.

In order to monitor the CEES decomposition process over time and to determine the structure of the produced chemical species, liquid ^1H -NMR experiments were performed on the reaction mixture at different contact times (up to 24 h), after their extraction in deuterated chloroform (CDCl_3) (Figure 10). Because of the adopted extraction procedure, only a qualitative evaluation of the degradation products can be effectively obtained from the NMR analyses. The experiments were carried out as follows: 600 μL of each filtered sample of the reaction mixture in PBS, withdrawn at regular intervals (0, 5-15', 1-5-24 h), was extracted in 600 μL of CDCl_3 and placed in 5 mm NMR tube. The evolution of the ^1H signals of CEES, and related main by-products was monitored in the chemical shift (δ) range of 1.00-4.00 ppm.^{22,54} The NMR spectra over time of CEES without catalyst (*blank*) were also recorded.

In Figure 10A are reported the NMR spectrum of CEES alone, while in Figure 10B are reported the NMR spectra CEES (a) and of NbSAP (b), Eu-NbSAP (c) and NbEuSAP (d) catalysts after 5 h of contact time.

The NMR spectrum of CEES alone (Figure 10A) showed the four characteristic ^1H signals of the CWA simulant at chemical shift (δ [ppm]) 1.30 (triplet/ t , $-\text{CH}_3$, area: 3.00), 2.58 (quartet/ q , $\text{S}-\text{CH}_2$ area: 1.90), 2.77 (t , CH_2-S area: 1.67) and 3.75 (t , $\text{Cl}-\text{CH}_2$ area: 1.80).²² Without any catalyst, the CEES is stable in water under the experimental conditions, showing no modification of the position, relative intensity and multiplicity of its resonances after 5 h, further confirming the UV-Vis-NIR data (*vide supra*, Figure 9B).

With the addition of Nb^{5+} , Eu^{3+} -containing catalysts and after 5 h of reaction in aqueous phase (Figure 10B), both metal sites additionally led to the hydrolysis of the chlorine-containing moiety and to the formation of hydroxy-organosulfur by-products.^{73,74} The NbSAP (*b*) solid showed an almost complete erosion of the signals of CEES, which are no longer visible in the spectrum (Figure 10B, *b*); this could be also partly due to the low amount of CEES remained in solution and after extraction in CDCl_3 . The Eu-NbSAP (*c*) and NbEuSAP (*d*) samples, instead, presented only two weak signals assigned to the CH_2 groups around the central sulphur atom in the CEES structure. The $-\text{CH}_3$ and $\text{OH}-\text{CH}_2$ resonance peaks are not clearly visible and in their place two new set of ^1H signals with distinct multiplicity are present, labelled with *. From the NMR spectra of CEES treated with NbSAP (*b*), Eu-NbSAP (*c*) and NbEuSAP (*d*) clays, it is possible to observe the formation of at least two main decomposition products, the (2-chloroethyl)ethyl sulfoxide (CEESO) and (2-chloroethyl)ethyl sulfone (CEESO₂) derivatives, in chlorinated or hydrolysed forms, as shown by the ^1H structural assignment reported in Figure 10B.²²

The results obtained from the NMR study are consistent with the abatement kinetics trends reported in Figure 9B. Parallel assessments were made for additional contact times, up to 24 h. More information on the CEES decomposition mechanism are expected in future studies.

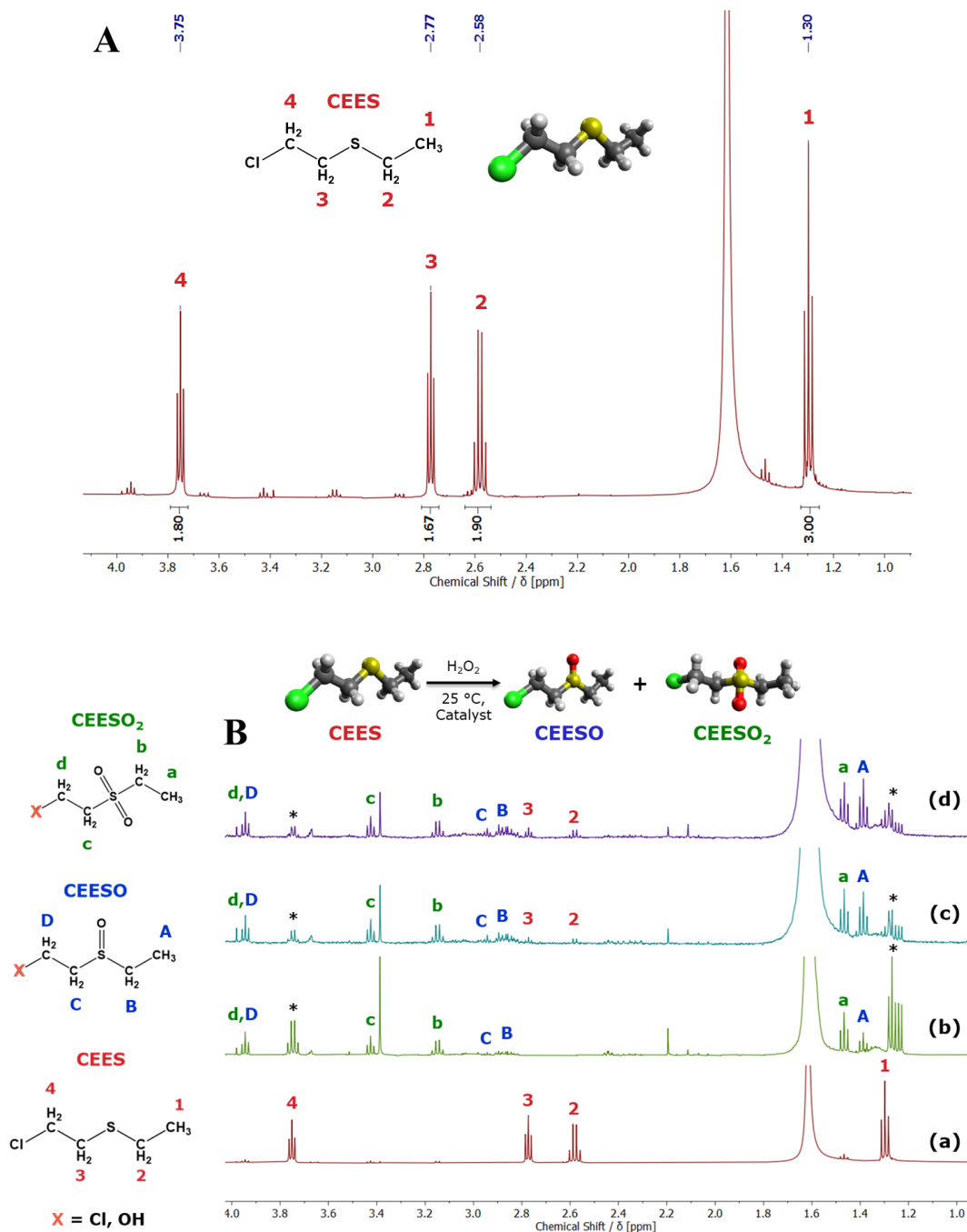


Figure 10. A) ^1H -NMR spectrum in CDCl_3 of CEES. B) ^1H -NMR spectra in CDCl_3 of CEES alone (a), NbSAP (b), Eu-NbSAP (c) and NbEuSAP (d), after 5 h of reaction. The peaks of CEES, CEESO and CEESO₂ are labelled in each spectrum based on their relative structure.

6.3.3 Optical detection tests:

Finally, preliminary studies on the optical detection of CEES by the Eu^{3+} -containing clays (Eu-NbSAP and NbEuSAP samples) were evaluated by PL analyses in aqueous suspensions, under continuous stirring and excitation at 395 nm, by monitoring the evolution of the main emission band of Eu^{3+} at 615 nm over time,⁴⁷ from *ca.* 10 sec up to 3 h. The tests were carried out as follows: 20 mg of clay was dispersed in 3 mL of PBS solution, and the mixture was sonicated for 10 min. The dispersion was transferred in a 3.0 mL quartz cuvette, placed in the spectrofluorometer and stirred continuously throughout the test. The emission spectrum of each clay, under excitation at 395 nm ($\lambda_{\text{max}} \text{Eu}^{3+}$),⁴⁷ was recorded before contact with the CWA simulant; after that, 100 μL of CEES (286 mM) were added to the dispersion and emission spectra were collected over time at regular intervals (0, 2-4-6-8-10-15-20-25-30-60-90-120-150-180'). An experiment on EuSAP without CEES (*blank*) was performed to evaluate the general stability of the clay suspension throughout the experiment time. The EuSAP sample was also tested with CEES, in the same conditions described above, with the purpose to validate the optical detection method and optimizing the measurement parameters.

In Figure 11A are reported the emission spectra of NbEuSAP sample (used as example) collected at different contact times with CEES. The same behaviour was found for Eu-NbSAP. In Figure 11B, instead, are reported the normalized intensity curves of the 615 nm band over time for Eu-NbSAP (*a*) and NbEuSAP (*b*).

Before adding the CWA simulant (Figure 11A, black curve), the emission spectra of the Eu^{3+} -saponites showed the characteristic intra- $4f^6$ electronic levels of Eu^{3+} ($^5\text{D}_0$ - $^7\text{F}_J$, $J = 0-4$),^{48,63,64} as previously assigned in Figure 8B for the NbEuSAP sample. After addition of 100 μL of CEES, a marked reduction of the intensity of the 615 nm band over time can be clearly observed. This signal is related to the $^5\text{D}_0$ - $^7\text{F}_2$ electronic transition of europium and it is highly sensitive to changes in local chemical environment around the luminescent sites, associated in this case to coordination of CEES molecules to Eu^{3+} . This interaction lead to a drastic decrease

of the intensity of the band, which translate to the luminescence recognition for the sulphur-based blistering agent simulant by both bifunctional materials.⁴⁴⁻⁴⁷ Indeed, both solids were able to quickly detect the CEES, as shown by a *ca.* 20 % decrease of the normalized intensity of the 615 band after few seconds of contact time (Figure 11B, red spectrum in Figure 11A) if compared to the initial intensity in the absence of the CWA simulant (Figure 11B, black spectrum in Figure 11A). Furthermore, in the following minutes the NbEuSAP sample was capable of detect the CEES more rapidly than Eu-NbSAP, as shown by an intensity reduction of 35 % for NbEuSAP versus a 23 % only for Eu-NbSAP after 2 min, until convergence of both curves at 30 min.

The behaviour observed should be related to a higher accessibility of the Eu^{3+} sites in the *one-pot* NbEuSAP material compared to the exchanged Eu-NbSAP material (Figure 12B and A, respectively): because of this, the CEES may coordinates to Eu^{3+} both on the lamellae surface and in the interlayer space, while in the Eu-NbSAP the simulant molecules needs to diffuse first in the interlamellar region and then interact with the Eu^{3+} ions located there.

These preliminary results demonstrated good detection capabilities for both Eu-NbSAP and NbEuSAP clays. In particular, the NbEuSAP, with the lowest Eu^{3+} concentration and the best overall luminescence performance, resulted to be the best *sensor-like* materials for the rapid detection of sulphur-based blistering CWAs. More information on the CEES interaction with Eu^{3+} and optimization of the luminescence recognition performances of these materials are expected in future studies.

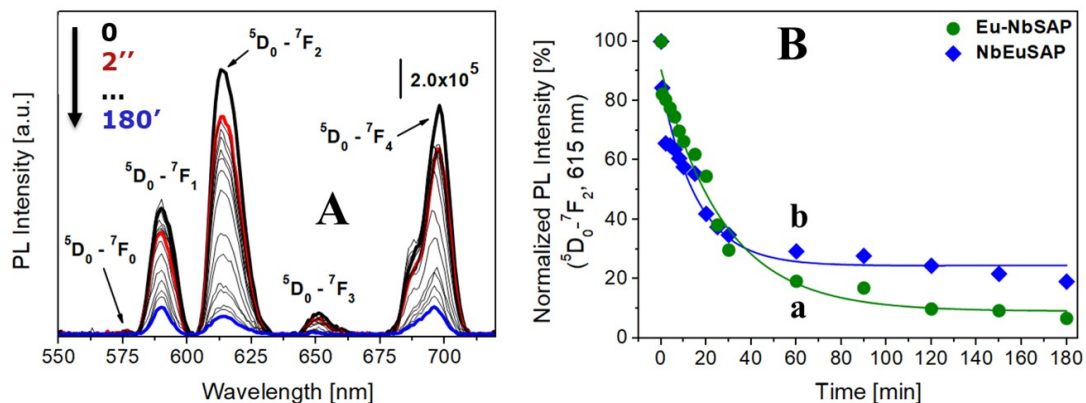


Figure 11. A) Emission spectra of NbEuSAP, under excitation at 395 (λ_{\max} Eu^{3+}), before (black curve) and after addition of CEES (red curve = 10 s, blue curve = 3 h). The spectra of samples were collected in aqueous suspensions, under continuous stirring. B) Normalized PL intensity of 615 nm band over time for Eu-NbSAP (a, \bullet -) and NbEuSAP (b, \blacklozenge -).

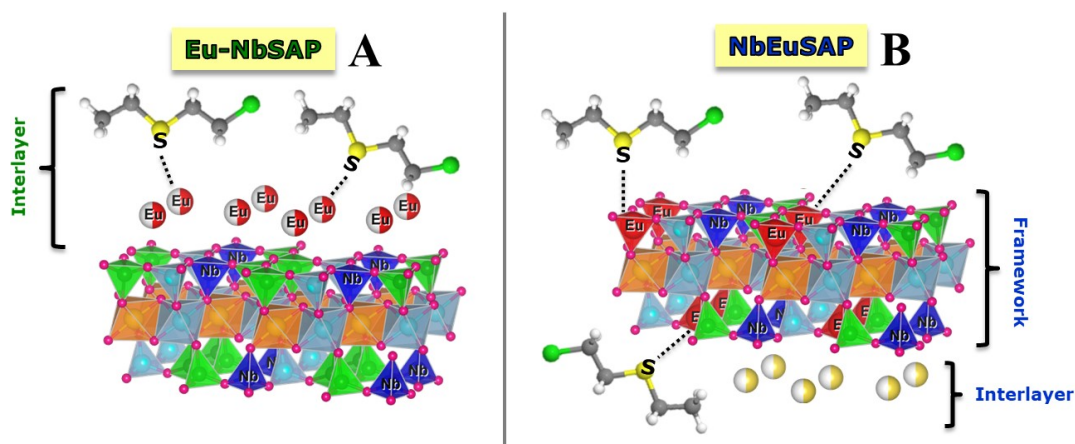


Figure 12. A schematic view of chemical interactions between CEES molecules and Eu^{3+} sites is reported in frame A and B.

6.4 Conclusions

In this work, we successfully designed two novel bifunctional saponite samples containing both europium and niobium in the same material. The europium was introduced *i)* in the tetrahedral structural positions together with niobium by a *one-pot* hydrothermal procedure (NbEuSAP) and *ii)* in the interlayer space of a NbSAP clay through intercalation of a europium precursor. All the functionalized materials were submitted to a complete physico chemical characterization, in order to assess their properties (*i.e.* coordination of niobium centres, local environment around the europium sites...). Particular attention was devoted to the optical detection and catalytic oxidative abatement studies performed against the blistering agent simulant CEES. The tests were carried out in aqueous medium maintained at neutral pH, at room temperature, atmospheric pressure and in the presence of aqueous hydrogen peroxide, as mild oxidizing agent.

The CEES abatement performance was tested for the Nb⁵⁺-containing saponites in liquid-phase under batch conditions, followed by UV-Vis-NIR and ¹H-NMR analyses. It was shown that framework Nb⁵⁺ centres and the surface acidity of clays are the key factors for the oxidative degradation of CEES by the Nb⁵⁺-loaded saponites. The Eu-NbSAP sample, for example, was able to decompose more than 80% of CEES in 6 h. The presence of Eu³⁺ in exchange positions did not significantly inhibit the catalytic performance, whereas sample with in-framework Eu³⁺ species (NbEuSAP) decomposed *ca.* 70% of CEES after 24 h. This difference is probably due to the lower content of Nb⁵⁺ species in the sample. In aqueous phase, both metal sites additionally led to the hydrolysis of the chlorine-containing moiety, with the formation of hydroxy-organosulfur by-products, as observed from NMR experiments.

The Eu³⁺-containing saponite clays were able to rapidly and effectively detect the presence of CEES in aqueous medium even after few seconds of contact time, as suggested by the decrease of the intensity of the emission band of Eu³⁺ at 615 nm,

which is greatly sensitive to the coordination to CEES. The Eu^{3+} sites in the NbEuSAP material resulted more accessible to CEES molecules, thus leading to a more efficient detection of the CWA simulant compared to Eu-NbSAP .

The materials were thus identified as reliable catalysts for the chlorine-free oxidative abatement of organosulphur blistering chemical warfare agents with hydrogen peroxide under mild conditions. Both bifunctional solids proved to be potential candidate as sensor-like systems for sulphur-based chemical warfare agents. Further studies, aiming to optimize the catalytic and luminescence performances of these metal-functionalized clay systems, will be performed in the future.

6.5 Notes and References

- 1 K. Ganesan, S. K. Raza and R. Vijayaraghavan, *J. Pharm. Bioallied. Sci.*, 2010, **2**, 166-178.
- 2 G. J. Fitzgerald, *Am. J. Public Health.*, 2008, **98**, 1158.
- 3 A. Richardt, *CBRN Protection: Managing the Threat of Chemical, Biological, Radioactive and Nuclear Weapons*, 2012, Wiley-VCH, **ISBN**: 978-3-527-32413-2.
- 4 R. C. Gupta, *Handbook of Toxicology of Chemical Warfare Agents*, 2015, Elsevier Inc., **ISBN**: 978-0-12-800159-2.
- 5 A) A. Brunning, *Chemical & Engineering News*, 2015; B) www.compoundchem.com.
- 6 A) D. R. Coats, *Statement for the Record: 2018 Worldwide Threat Assessment of the US Intelligence Community*, 2019; B) T. Schneider and T. Lütkefend, *Nowhere to Hide: The Logic of Chemical Weapons Use in Syria*, Global Pulic Policy Institute, 17 February 2019.
- 7 *Convention on the Prohibition of the Development, Production, Stockpiling and Use of Chemical Weapons and on their Destruction*, United Nations Treaty Collection, retrieved on February 2020.
- 8 C. A. Valdez, R. N. Leif, S. Hok and B. R. Hart, *Reviews in Analytical Chemistry*, 2017, **37**, 1-26.
- 9 www.opcw.org/about-chemical-weapons/what-is-a-chemical-weapon/, retrieved on February 2020.
- 10 F. M. Raushel, *Nature*, 2011, **469**, 310-311.
- 11 R. D. Gall, C. L. Hill and J. E. Walker, *Chem. Mater.*, 1996, **8**, 2523-2527.

- 12 A) G. W. Wagner, L. R. Procell, D. C. Sorrick, G. E. Lawson, C. M. Wells, C. M. Reynolds, D. B. Ringelberg, K. L. Foley, G. J. Lumetta, D. L. Blanchard Jr., *Ind. Eng. Chem. Res.*, 2010, **49**, 3099-3105; B) K. Kim, O. G. Tsay, D. A. Atwood, D. G. Churchill, *Chem. Rev.*, 2011, **111**, 5345-5403.
- 13 R. D. Albright, *Cleanup of Chemical and Explosive Munitions*, William Andrew, Norwich, 2008.
- 14 S. Polat, M. Gunata and J. Parlakpinar, *Annals of Medical Research*, 2018, **25**, 776-782.
- 15 E. T. Dickinson and J. S. Love, *J. Emerg. Med. Serv.*, 2017, **2**.
- 16 G. K. Prasad, P. V. R. K. Ramacharyulu, B. Singh, K. Batra, A. R. Srivastava, K. Ganesan and R. Vijayaraghavan., *J. Mol. Catal. A: Chemical*, 2011, **349**, 55-62.
- 17 Y. C. Yang, J. A. Baker and J. R. Ward, *Chem. Rev.*, 1992, **92**, 1729-1743.
- 18 G. W. Wagner, *Ind. Eng. Chem. Res.*, 2011, **50**, 12285-12287.
- 19 N. S. Bobbitt, M. L. Mendonca, A. J. Howarth, T. Islamoglu, J. T. Hupp, O. K. Farha and R. Q. Snurr, *Chem. Soc. Rev.*, 2017, **46**, 3357-3385.
- 20 K. Kibong, G. T. Olga, A. A. David, G. C. David, *Chem. Rev.*, 2011, **111**, 5345-5403.
- 21 C. Tiozzo, C. Bisio, F. Carniato and M. Guidotti, *Catalysis Today*, 2014, **235**, 49-57.
- 22 Y. Hou, H. An, S. Chang and J. Zhanga, *Catal. Sci. Technol.*, 2019, **9**, 2445-2455.
- 23 N. M. Okun, T. M. Anderson and C. L. Hill, *J. Mol. Catal. A*, 2003, **197**, 283-290.
- 24 Ş. Neaţu, B. Cojocaru, V. I. Pârvulescu, V. Şomoghi, M. Alvaro and H. Garcia, *J. Mater. Chem.*, 2010, **20**, 4040-4050.
- 25 S. R. Livingston and C. C. Landry, *J. Am. Chem. Soc.*, 2008, **130**, 13214-13215.
- 26 Y. Y. Liu, S. Y. Moom, J. T. Hupp and O. K. Farha, *ACS. Nano.*, 2015, **9**, 12358-12364.
- 27 I. Timur, A. O. Manuel, P. Emmanuel, J. H. Ashlee, A. V. Nicolaas, A. Ahmet, M. A. Abdullah, J. C. Christopher and K. F. Omar, *Angew. Chem. Int. Ed.*, 2018, **57**, 1-6.
- 28 D. T. Lee, J. J. Zhao, G. W. Peterson and G. N. Parsons, *Chem. Mater.*, 2017, **29**, 4894-4903.
- 29 Y. Q. Li, Q. Gao, Y. S. Zhou, L. L. Zhang, Y. X. Zhong, Y. Ying, C. Zhang, Y. Q. Liu, Y. A. Wang. *J. Hazard. Mater.* 2018, **358**, 113-121.
- 30 F. Carniato, C. Bisio, R. Psaro, L. Marchese and M. Guidotti, *Angew. Chem. Int. Ed.*, 2014, **53**, 10095-10098.
- 31 D. Costenaro, C. Bisio, F. Carniato, S. L. Safronyuk, T. V. Kramar, M. V. Taran, M. F. Starodub, A. M. Katsev and M. Guidotti, *Chemistry Select*, 2017, **2**, 1812-1819.
- 32 F. Carniato, C. Bisio, C. Evangelisti, R. Psaro, V. Dal Santo, D. Costenaro, L. Marchese and M. Guidotti, *Dalton Trans.*, 2018, **47**, 2939-2948.

- 33 D. Costenaro, G. Gatti, F. Carniato, G. Paul, C. Bisio and L. Marchese, *Microp. Mesop. Mater.*, 2012, **162**, 159-167.
- 34 C. Bisio, G. Gatti, E. Boccaleri, G. Superti, H. Pastore and M. Thommes, *Microp. Mesop. Mater.*, 2008, **107**, 90-101.
- 35 C. Bisio, G. Gatti, E. Boccaleri, L. Marchese, L. Bertinetti and S. Coluccia, *Langmuir*, 2008, **24**, 2808-2819.
- 36 M. Burnworth, S. J. Rowan and C. Weder, *Chemistry*, 2007, **13**, 7828-7836.
- 37 *Chemical and Biological Terrorism: Research and Development to Improve Civilian Medical Response*, Institute of Medicine (US) Committee on R&D Needs for Improving Civilian Medical Response to Chemical and Biological Terrorism Incidents, Washington (DC): National Academies Press (US), 1999.
- 38 R. Sferopoulos, *A Review of Chemical Warfare Agent (CWA) Detector Technologies and Commercial-Off-The Shelf Items*, Human Protection and Performance Division DSTO Defence Science and Technology Organisation, 506 Lorimer St Fishermans Bend, Victoria 3207 Australia, 2008.
- 39 E. Dolgin, *Nat. Med.*, 2013, **19**, 1194-1195.
- 40 A. Gulland, *Br. Med. J.*, 2013, **347**.
- 41 A. Papalardo, M. E. Amato, F. P. Ballistreri, V. L. P. Fragola, G. A. Tomaselli, R. M. Toscano and J. T. Sfrazzetto, *J. Chem. Sci.*, 2013, **125**, 869-873.
- 42 E. J. Pacsial-Ong and Z. P. Aguilar, *Frontiers in bioscience (Scholar edition)*, 2013, **S5**, 516-543.
- 43 C. M. Whitaker, E. E. Derouin, M. B. O'Connor, C. K. Whitaker, J. A. Whitaker and J. J. Snyder, *J. Macromol. Sci. A*, 2016, **54**, 40-46.
- 44 A. J. Metherell, C. Curty, A. Zaugg, S. T. Saad, G. H. Dennison and M. D. Ward, *J. Mater. Chem. C*, 2016, **4**, 9664-9668.
- 45 G. H. Dennison, C. Curty, A. J. Metherell, E. Micich, A. Zaugg and M. D. Ward, *RSC Advances*, 2019, **9**, 7615-7619.
- 46 G. N. Dennison, C. G. Bochet, C. Curty, J. Ducry, D. J. Nielsen, M. R. Sambrook, A. Zaugg and M. R. Johnston, *Eur. J. Inorg. Chem.* 2016, **9**, 1348-1358.
- 47 G. H. Dennison and M. R. Johnston, *Chem. Eur. J.*, 2015, **21**, 6328-6338.
- 48 Y. Wang and N. Lin, *Photochem. Photobiol. Sci.*, 2011, **10**, 42-47.
- 49 D. Knapton, M. Burnworth, S. J. Rowan and C. Weder, *Angew. Chem. Int. Ed.*, 2006, **118**, 5957-5961.
- 50 S. Sarkar, A. Mondal, A. K. Tiwari and R. Shunmugam, *Chem. Commun.*, 2012, **48**, 4223-4225.
- 51 E. R. Menzel, L. W. Menzel and J. R. Schwierking, *Talanta*, 2005, **67**, 383-387.
- 52 J. H. Kim, J. Ryu and C. B. Park, *Small*, 2011, **7**, 718-722.
- 53 S. Marchesi, F. Carniato, C. Bisio, L. Tei, L. Marchese and M. Botta, *Dalton Trans.*, 2018, **47**, 7896-7904.
- 54 X. Shi, W. Ma, H. Ou, X. Han, C. Lu, Y. Chen and J. Wei, *J. Braz. Chem. Soc.*, 2012, **23**, 1536-1542.

- 55 F. Carniato, C. Bisio, G. Gatti, S. Roncoroni, S. Recchia and L. Marchese, *Catal. Lett.*, 2009, **131**, 42-48.
- 56 L. Ostinelli, S. Recchia, C. Bisio, F. Carniato, M. Guidotti, L. Marchese and R. Psaro, *Chem. Asian J.*, 2012, **7**, 2394-2402.
- 57 M. Guidotti, R. Psaro, N. Ravasio, M. Sgobba, F. Carniato, C. Bisio, G. Gatti and L. Marchese, *Green Chem.*, 2009, **11**, 1173-1178.
- 58 O. Prieto, M. A. Vincente and M. A. Banares-Munoz, *J. Porous Mater.*, 1999, **6**, 335-344.
- 59 J. C. Dabrowiak, *Metals in Medicine (2nd Ed)*, 2017, John Wiley & Sons Ltd, **ISBN: 978-1-119-19130-8**.
- 60 K. J. Balkus Jr. and J. Shi, *Langmuir*, 1996, **12**, 6277-6281.
- 61 J. L. Zatz and C. Yarus, *Pharmaceutical Research*, 1986, **3**, 118-121.
- 62 K. Binnemans and C. Gorller-Walrand, *J. Rare Earths*, 1996, **14**, 173-180.
- 63 S. Marchesi, F. Carniato and E. Boccaleri, *New J. Chem.*, 2014, **38**, 2480-2485.
- 64 S. Marchesi, F. Carniato and E. Boccaleri, *ChemPlusChem*, 2015, **80**, 915-918.
- 65 R. Reisfeld, *Struct. Bonding (Berlin)*, 1973, **13**, 53-98.
- 66 S. F. Tang, A. Babai and A. V. Mudring, *Angew. Chem. Int. Ed.*, 2008, **47**, 7631-7638.
- 67 P. Zhang, Y. Wang, H. Liu and Y. Chen, *J. Mater. Chem.*, 2011, **21**, 18462-18466.
- 68 S. I. Klink, G. A. Hebbink, L. Grave, P. G. B. Oude Alink, F. C. J. M. van Veggel and M. H. V. Werts, *J. Phys. Chem. A*, 2002, **106**, 3681.
- 69 M. H. V. Werts, *Luminescent Lanthanide Complexes, Visible Light Sensitised Red and Near-Infrared Luminescence*, PhD Thesis, The Netherlands, 2000.
- 70 M. Trejda, B. Pokora and M. Ziolk, *Catal. Today*. 2015, **254**, 104-110.
- 71 A. Gallo, C. Tiozzo, R. Psaro, F. Carniato and M. Guidotti, *J. Catal.*, 2013, **298**, 77-83.
- 72 M. Ziolk, I. Sobczak, P. Decyk, K. Sobanska, P. Pietrzyk and Z. Sojka, *Appl. Catal. B: Env.*, 2015, **164**, 288-296.
- 73 J. E. Mondloch, M. J. Katz, W. C. Isley, P. Ghosh, P. Liao, W. Bury, G. W. Wagner, M. G. Hall, J. B. DeCoste, G. W. Peterson, R. Q. Snurr, C. J. Cramer, J. T. Hupp and O. K. Farha, *Nat. Mater.*, 2015, **14**, 512-516.
- 74 P. Asha, M. Sinha and S. Mandal, *RSC Adv.*, 2017, **7**, 6691-6696.

7

Conclusions

The main object of this Ph.D. thesis was the development of novel nanostructured multifunctional layered materials obtained by the combination of different lanthanides ions and transition metal centres with synthetic saponites clays. These innovative metal-containing 2D materials were designed to be applied in different scientific and technological fields, from environmental to biomedical, light harvesting systems and heterogeneous catalysis. All the materials designed in this work were prepared by applying or modifying existing hydrothermal procedures or through establishment of brand-new synthetic protocols. The synthetic saponite clays are incredible versatile materials, and through the chemical functionalization and modulation of their structure at three different domain levels (morphology and particle size, interlayer/interlamellar space and inorganic lattice) it was possible to easily obtain in this study several interesting novel advanced layered materials. The knowledge acquired in each chapter were applied to all the subjects explored in the thesis, from synthesis to physico-chemical analyses, thus connecting all the novel functionalized saponite clays produced. The materials were fully characterized through a multi-technique approach aiming to determine their physico-chemical properties in light of their potential applications.

In the *Chapter 1*, a general overview was given on the characteristics and applications of clay materials, a class of hydrated aluminosilicates with 2D-nature

and interesting physico-chemical features (*i.e.* large availability and low costs, high structural and thermal stability...), clarifying the differences between natural and synthetic ones and showing the strengths of the latter, especially with reference to a specific kind of synthetic clays called saponites. The saponites are being part of the large family of 2:1 *T-O-T* (tetrahedral-octahedral-tetrahedral) trioctahedral-type layered smectites. The literature data demonstrate the growing interest in the synthetic saponites, due to their peculiar physico-chemical properties such as high surface area, surface acid properties and very high chemical versatility. Saponites present more controlled chemical composition and particles size, aggregation and textural features than natural counterpart minerals. Moreover, their properties can be easily and efficiently tune through modification of the lamellae structure and/or interlamellar region composition (*i.e.* by adding different metals), in order to introduce specific functionalities that could make these systems suitable for a wide range of applications, from biomedical to sensors and for the development of new nanomaterials. For these reasons, synthetic saponites proved to be excellent versatile materials and they have been the subject of several recent studies on clays.

In the **Chapter 3**, two different synthetic saponite clays were employed for the extraction of lanthanides ions with different ionic radius (lanthanum, gadolinium and lutetium) from different aqueous solutions with varying complexity (pure water and simulated freshwater and seawater solutions). The sodium-exchanged saponite samples named Na-SAP-20 and Na-SAP-110, prepared by a classical hydrothermal approach using two different H₂O/Si molar ratio (20 and 110), differs on the basis of their cation exchange capacity (87.9 ± 2.3 meq/100 g for Na-SAP-20 and 37.3 ± 1.8 meq/100 g for Na-SAP-110), particles size (sub-micrometric for Na-SAP-20 and nanometric for Na-SAP-110) and textural properties. The uptake tests of lanthanides, performed in pure water and simulated freshwater and seawater solutions and at different concentrations of metal ions, demonstrated that clays have good sorption capacity with high lanthanides ions capture after few hours of contact. The metal

extraction performance of both clays was found to be comparable to several natural clays and significantly higher than traditional liquid-liquid methods used in the industry.

The extraction process exploited by the two saponites is mainly correlated to their cation-exchange capacity. For this reason, the saponite with higher ion extraction capabilities (Na-SAP-20) was able to remove a larger amounts of lanthanide ions (45-55 mg/g versus 18-24 mg/g for Na-SAP-110). A promising performance was also obtained in the uptake of Gd^{3+} in simulated freshwater and seawater solutions. Additionally, both solid samples showed a marked selectivity for lanthanides ions with lower ionic radius, such as lutetium, both in pure water and simulated freshwater solutions. Preliminary study concerning the recovery of metal ions from the layered solid sorbents were also explored, testing the saponite samples (after uptake of gadolinium ions) in a saturated sodium chloride solution. The experiments showed promising results for both clays, especially for the Na-SAP-110 sample.

In the light of these results and considering the simplicity and low costs associated to the preparation of these clays, synthetic saponites can be considered an attracting alternative to the solids reported in the literature for the removal of lanthanide ions from different aqueous solutions.

In the *Chapter 4*, novel paramagnetic and diamagnetic synthetic saponite clays, bearing in the interlayer space positively charged gadolinium/yttrium complexes, based on TETA-monoamide, DOTA-monoamide and AAZTA-polyamine ligands, were prepared by classical hydrothermal procedure followed by cation-exchange process. The saponite clay (named Na-SAP) was obtained using a well-defined H_2O/Si molar ratio (110), showing particle size of *ca.* 50 nm. The cation-exchange procedure or intercalation was optimized to ensure the confinement of a fixed amount of metal chelates (*ca.* 10-15 % of the cation-exchange capacity of the clay) in the interlayer space of the saponite. Structural and morphological analyses

indicated that the metal complexes are firmly confined in the interlayer space of the hybrid materials, named GdL0/SAP, GdL1/SAP, GdL2/SAP and YL0/SAP.

A combined ^1H -NMR relaxometric study in aqueous solution and mono- and bidimensional solid-state NMR experiments were performed on the intercalated materials, obtaining relevant information on the chemical nature and the accessibility of exchange sites to water molecules, on the mechanisms responsible of the magnetic interaction with water, on the role of the key molecular parameters responsible of the relaxivity enhancement data and on the molecular organization of the chelates in the saponite interlayer space. The materials intercalated with gadolinium chelates showed improved longitudinal relaxivity values at high magnetic field as compared to the free gadolinium complexes. This effect is due to the reduction of the local rotational mobility of the confined organometallic compounds, as suggested by both relaxometric and solid-state NMR experiments, the latter conducted on the diamagnetic YL0 and YL0/SAP samples. The relaxometric measurements also suggests that the diffusion process of the water molecules though the interlayer gallery limited the relaxivity enhancement, as indicated by the increase of relaxivity as a function of temperature. The combination of these effects indicates the occurrence of strong interactions between the cationic complexes/water molecules with the lamellae structure. The chelates are in proximity (and in a parallel organization) to the tetrahedral layers of the saponite.

These features are promising for the design of novel intercalated layered materials for potential applications in diagnostic (MRI) and theranostics, as catch-and-release systems for the purification of surface waters and for the study of the diffusion phenomena of liquids inside layered systems.

In the *Chapter 5*, starting from the knowledges learned in *Chapter 4* and to overcome the limitations of the previous intercalated clays (*i.e.* long preparation times and relatively high costs of the complexes), we explored the possibility to introduce the lanthanides, in form of simple ions, directly in the inorganic framework

of the saponite in one single-step of synthesis; besides, in this way the interlayer space remains open to further functionalization. More specifically, two different lanthanide ions (gadolinium and europium) were successfully inserted together in the tetrahedral in-framework positions of a synthetic saponite clay. The presence of both gadolinium and europium confer to the final material both paramagnetic and luminescent properties, which can be exploited synergistically for *i*) several applications in optoelectronic and diagnostic fields and *ii*) in order to have a more comprehensive view of the chemical environment surrounding the lanthanides itself. The preparation of the bifunctional sample, named GdEuSAP, was accomplished by an innovative *one-pot* hydrothermal synthetic approach, using a H₂O/Si molar ratio of 20 and a 1:1 molar ratio between the two lanthanides. Solids with only gadolinium (GdSAP) or europium (EuSAP) were also prepared as references. A post-synthesis cation-exchange process was performed to ensure a homogeneity in the chemical composition of the interlayer space of the materials.

Structural and morphological analyses indicate that the introduction of lanthanides in structural positions did not alter the layered features of the saponite. ²⁷Al solid state NMR experiments suggested that lanthanides tend to be preferentially incorporated in the tetrahedral units of the clay. The ions are thus more accessible to surrounding water molecules in the interlayer region. The materials showed lamellae lengths of a few tens of nanometres and particle hydrodynamic sizes of 40-60 nm, with overall cation exchange capacity of *ca.* 40 meq/100 g.

The photophysical properties were deeply investigated both at solid state and in aqueous suspensions, extrapolating relevant data on the chemical nature and geometrical aspects of the surroundings of europium sites. The presence of both lanthanides in the same layers led to an energy transfer from gadolinium to europium, which increased the final luminescence properties of europium. The chemical environment around metal centres resulted to be highly asymmetric, with four coordinate water molecules in the inner sphere in agreement with the presence of europium in the tetrahedral position of the saponite framework.

The luminescence performance of the bifunctional GdEuSAP clay was further improved by intercalation of an “antenna” ligand (1,10-phenanthroline), with different loadings, which can transfer energy to the nearby emitting states of europium through Förster resonance energy transfer.

$^1\text{H-NMR}$ relaxometric studies were carried out in aqueous solution, obtaining more insights on the chemical nature and the accessibility of exchange sites and on the molecular dynamics of water inside the interlayer space of saponite. The data extrapolated from nuclear magnetic dispersion profiles indicated that the inner-sphere water molecules exchange quickly with the intra-interlayer water molecules, then diffuse through the lamellae channel and slowly exchange with the bulk water outside the lamellae. Therefore, the diffusion is the rate-limiting step of the overall relaxation effect, as also indicated by the increase of relaxivity as a function of temperature. The structure of materials proved to be robust even in harsh conditions (*i.e.* in EDTA solution), as observed by relaxometric analyses.

These features are quite promising for the development of a novel class of nanosized multifunctional lanthanide clays, which can be obtained in relatively short time and low cost. Potential applications as luminescent devices and sensors or in diagnostic can be expected in the future.

In the final **Chapter 6**, starting from a previous work concerning the application of niobium-containing saponites for the decontamination of chemical warfare agents and with the knowledges gathered in the studies from the prior chapters, two novel bifunctional inorganic layered solids based on the combination of two different metal elements, europium and niobium (in form of ions), with synthetic saponite clays were successfully designed. The luminescent and catalytic properties exhibited by the final materials, conferred by the europium and niobium respectively, were exploited for the optical detection and oxidative abatement of a simulant of the blistering chemical warfare agent mustard gas, called 2-chloroethyl)ethyl sulphide (CEES). The tests were carried out in simple experimental conditions, particularly in aqueous

solution at neutral pH, at room temperature and atmospheric pressure and in the presence of a mild oxidant agent (aq. hydrogen peroxide) for the degradation reaction.

The samples were prepared through two different synthetic routes: 1) ion-exchange of a fraction of sodium ions in the interlayer space of a niobium-saponite, previously obtained by adopting a hydrothermal procedure optimized in literature in which the niobium is located in the clay structure, with europium ions (sample named Eu-NbSAP); 2) *one-pot* hydrothermal synthesis in which both europium and niobium were directly inserted in the tetrahedral in-framework positions of the saponite (sample named NbEuSAP). Sample with only niobium (NbSAP) and europium (EuSAP) elements, located in the inorganic framework, were also used as references.

The chemical warfare agent abatement capability of the samples was thoroughly tested in liquid-phase under batch conditions, followed by UV-Vis-NIR and $^1\text{H-NMR}$ analyses. The combination of the niobium centres located in the framework and a marked surface acidity is essential to promote an efficient oxidative degradation of CEES. The materials were able to decompose from 70 to 90% of CEES after 24 h. The presence of europium in the structure did not inhibit the catalytic performance of the catalysts.

In optical detection experiments, the functionalized materials were able to rapidly and effectively detect the presence of CEES in water after few seconds, as confirmed by the decrease of the intensity of the main emission band of the europium, sensible to the interaction with the simulant.

The nanosized bifunctional materials were thus identified as promising solids for the catalytic oxidative abatement and optical recognition of organosulphur-based blistering chemical warfare agents. Particularly, the solid prepared through *one-pot* synthetic procedure (NbEuSAP) represents the best *trade-off* in terms of catalytic and detection properties. Further studies, aiming to optimize the performances of these metal-functionalized clay systems, will be carried out in the future.

8

Experimental Techniques

8.1 Analytical Methods

- The elemental analyses were performed on an Ametek Spectro Genesis EOP Inductively Coupled Plasma Atomic Emission Spectrometer equipped with a cross-flow nebulizer (ICP-AES), with simultaneous spectrum capture in the 175-770 nm wavelength range. Furthermore, the elemental analyses were also performed on a Thermo Fisher Scientific X5 Series Inductively Coupled Plasma Mass Spectrometer (ICP-MS; Waltham, MA, USA). Prior to the analysis, the solid samples were mineralized by treatment with a mixture of nitric acid (HNO₃; 5 mL) and hydrofluoric acid (HF; 5 mL) at 100 °C for 8 h, in order to opportunely dilute them in aqueous HNO₃ solution (1 wt.%).
- The chromatographic analyses, performed during the synthesis of GdL0-1-2 and YL0 chelates, were carried out with a Waters System based on a High-Performance Liquid Chromatography-Mass Spectrometry equipped with an Electrospray Ion Source (HPLC-MS ESI^{+/-}), a Waters 1525 Binary HPLC Pump, a Water 2489 UV-Vis Detector and a Water SQD 3100 Mass Detector. The mass spectra, obtained through the MS-ESI^{+/-} technique, were recorded using the Waters SQD 3100 Mass Detector.
- X-ray powder (XRPD) diffractograms were collected on unoriented ground powders with a ThermoARL X'TRA-048 Powder Diffractometer with a Cu-K_{α1} ($\lambda = 1.54062 \text{ \AA}$) monochromatic radiation. Diffractograms were recorded at

room temperature (RT) in the 2° - 65° 2θ range with a step size of 0.02° and a rate of $1.0^{\circ}/\text{min}$. The X-ray profiles at low angles (2 - 15° 2θ) were collected with narrower slits and rate of $0.25^{\circ}/\text{min}$.

- Scanning electron microscope (SEM) images were collected on a Philips/FEI Quanta 200 Environmental SEM (ESEM) using a tungsten (W) filament as electron source (200 keV) and the back-scattering detector, operating at low vacuum. A conductive coating of gold (Au, sputtering thickness of 10 nm) by low-pressure plasma was deposited on samples, previously placed on carbon grids, to avoid the presence of electronically charged insulating particles under the electron beam.
- High-resolution transmission electron microscopy (HRTEM) micrographs were collected on a Zeiss Libra200 FE3010 High Resolution Transmission Electron Microscope operating at 200 kV. Specimens were prepared by depositing the samples on carbon-coated grids.
- The one-dimensional (1D) ^1H and ^{13}C Nuclear Magnetic Resonance (NMR) spectra of Gd**L0-1-2** complexes in solution were recorded at 27°C with a Bruker Advance III Spectrometer equipped with a wide bore 11.7 Tesla magnet. The samples were dissolved in deuterated chloroform (CDCl_3) or water (D_2O) for analyses. The spectrometer is equipped with a 5 mm double resonance Z-gradient broad band probe, with the inner coil optimized for observation of nuclei between ^{31}P and ^{15}N and for ^{19}F (BBFO), and Bruker BVT-3000 unit for temperature control. A set of 1D and two-dimensional (2D) NMR experiments was acquired on Y**L0**, dissolved in a solution of 1:1 molar ratio of $\text{H}_2\text{O}:\text{D}_2\text{O}$ (130.85 mM), at 27°C : 1D ^1H and ^{13}C , plus 2D ^1H - ^1H Correlation Spectroscopy (COSY), ^1H - ^1H Total Correlation Spectroscopy (TOCSY) and ^1H - ^{13}C Heteronuclear Single-Quantum Correlation Spectroscopy (HSQC) spectra for resonance assignment. The 2D COSY spectrum was collected using a standard phase-insensitive COSY sequence with gradient coherence selection, with 2048 acquired data points in F2, 256 time increments in F1, 16 scans, a 2 s recycle

delay and a spectral window (both F2 and F1) of 10 ppm. The 2D TOCSY using the mlev sequence for mixing,³ with 2048 acquired data points in F2, 200 time increments in F1, 24 scans, a 2 s recycle delay and a spectral window (both F2 and F1) of 10 ppm. The ¹H-¹³C HSQC spectrum was collected by standard gradient selected pulse sequence.⁴⁻⁶ The spectrum was acquired with 2048 data points in F2 and 256 data points in F1, 64 scans, a 2 s recycle delay, an F2 (¹H) spectral width of 10 ppm (carrier frequency at 4.7 ppm), and an F1 (¹³C) spectral width of 60 ppm (carrier frequency at 45 ppm). The catalytic experiments with NbSAP, Eu-NbSAP and NbEuSAP samples were carried out as follows: 600 μL of each filtered sample of the reaction mixture in PBS, withdrawn at regular intervals (0, 5-15', 1-5-24 h), was extracted in 600 μL of deuterated chloroform (CDCl₃) and placed in 5 mm NMR tube for analyses. The NMR spectra over time of CEES without catalyst (*blank*) were also recorded. All chemical shifts are reported using δ [ppm] scale and are externally referenced to tetramethylsilane (TMS) at 0 ppm.

- Solid-state NMR (ssNMR) spectra were acquired on a Bruker Avance III 500 Spectrometer equipped with a wide bore 11.7 Tesla and a 4 mm triple resonance probe. Solid samples (YL0 and YL0/SAP) were packed on a zirconia rotor and spun at a Magic Angle Spinning (MAS) rate of 12 kHz, at RT. A set of 1D and 2D NMR experiments was recorded, including: 1D MAS-NMR (¹H, ²⁹Si, ²³Na and ²⁷Al), ¹³C Cross Polarization (CP)-MAS-NMR, 2D ¹H-¹H Spin Diffusion, ¹H-²⁹Si and ¹H-²⁷Al Heteronuclear Correlation (HETCOR) spectroscopy with Frequency Switched Lee Goldberg (FSLG) Heteronuclear decoupling. The magnitudes of radio frequency (RF) pulses were 100, 42, 36, and 31 kHz for ¹H, ²⁹Si, ²³Na and ²⁷Al, respectively. The relaxation delay, d1, between accumulations was 2s for ¹H, ²⁹Si, ²³Na and ²⁷Al. ²⁷Al 1D MAS spectra have been acquired on large sweep width with small pulse angle ($\pi/12$) to ensure quantitative interpretation. The ¹H-²⁹Si CP was performed using a constant RF frequency applied to ²⁹Si of 37 kHz and a pulse linearly ramped from 50% to

100% of a maximum RF frequency of 22 kHz on ^1H . The ^1H - ^{27}Al cross polarization (CP) was performed using a constant RF frequency applied to ^{27}Al of 3 kHz and a pulse linearly ramped from 50% to 100% of a maximum RF frequency of 31 kHz on ^1H with a contact time of 500 μs . High power Two Pulse Phase Modulation (TPPM)⁹ decoupling of 100 kHz was applied for heteronuclear decoupling. The spectrum ^1H - ^{27}Al FSLG HETCOR spectra were acquired with an acquisition time of 10 ms in F2 and 2 ms in F1, 64 scans and 2 s recycle delay. The spectrum ^1H - ^{29}Si FSLG HETCOR spectra were acquired with an acquisition time of 10 ms in F2 and 2.4 ms in F1, 128 scans and 2 s recycle delay. 1D ^{27}Al High-Power Decoupling (HPDEC)/MAS ssNMR spectra were collected on Na-SAP and Na-GdSAP samples (operational frequency of 130.33 MHz for Al, MAS rate of 5 kHz and d1 of 1 s). All chemical shifts are reported using δ [ppm] scale and are externally referenced to TMS at 0 ppm.

- The cationic exchange capacity (CEC) was determined by ultraviolet-visible-near infrared (UV-Vis-NIR) method, as reported in the literature.¹ In details, 0.300 g of Na-SAP were exchanged with 10 mL of a 0.02 M solution of $[\text{Co}(\text{NH}_3)_6]^{3+}$ at RT for 60 h. After separation by centrifugation (5000 rpm for 5 min, two times), the solution was analysed by UV-Vis-NIR spectroscopy. UV-Vis-NIR spectra were recorded at RT in the range 300-600 nm with a resolution of 1 nm, using a double-beam Perkin Elmer Lambda 900 Spectrophotometer. The absorbance of the band at 475 nm ($^1\text{A}_{1g} \rightarrow ^1\text{T}_{1g}$),² relative to a $d-d$ spin-allowed Laporte-forbidden transition of Co^{3+} , was evaluated in order to quantify the amount of Co^{3+} ions remained in solution.
- UV-Vis-NIR spectra were analysed by UV-Vis-NIR spectroscopy. Phen-SAP and Phen-GdEuSAP samples were dispersed in ultrapure (5 mg/mL) with 0.1 wt.% of xanthan gum, at pH of 5.5. The spectra were recorded at RT in the range 200-400 nm with a resolution of 1 nm. NbSAP, Eu-NbSAP and NbEuSAP samples were dispersed in barium sulphate (BaSO_4) at 20 wt.%. The spectra were recorded in air at RT in the range 200-500 nm with a resolution of 1 nm. For

catalytic oxidative abatement tests with NbSAP, Eu-NbSAP and NbEuSAP samples, the spectra of liquid samples were recorded at RT in the range 200-500 nm with a resolution of 1 nm. All the spectra were recorded using a double-beam Perkin Elmer Lambda 900 Spectrophotometer.

- Infrared (FTIR) spectra of Na-SAP sample were collected on a Bruker Equinox 55 Spectrometer in the range 4000-400 cm^{-1} with a resolution of 4 cm^{-1} . Self-supporting pellets were placed into an IR cell with potassium bromide (KBr) windows permanently connected to vacuum line (residual pressure lower than 10^{-4} mbar). Before measurements, the Na-SAP sample was outgassed at 350 °C with a heating ramp of 10 °C/min for 3 h, using a special oil-free apparatus and grease-free vacuum line in order to remove adsorbed water from the surface, while the intercalated samples were outgassed at 100 °C with a heating ramp of 10 °C/min for 1 h. FTIR spectra of NbSAP, Eu-NbSAP and NbEuSAP samples were collected on a Thermo Electron Corporation FT Nicolet 5700 Spectrometer in the range 4000-400 cm^{-1} with a resolution of 4 cm^{-1} . Self-supporting pellets were placed into an IR cell with KBr windows permanently connected to vacuum line (residual pressure lower than 10^{-4} mbar), by which all treatments and ammonia ($\text{NH}_{3(\text{g})}$) adsorption-desorption experiments have been carried out in situ. Before gas adsorption tests, the samples were outgassed at 300 °C with a heating ramp of 10 °C/min for 3 h, using a special oil-free apparatus and grease-free vacuum line in order to remove adsorbed water from the surface. All samples were cooled down to RT prior to the collection of spectra upon NH_3 adsorption. The spectra of the various samples were normalized taking as a reference the intensity of the overtones and combination modes of the saponite framework (bands in the 2200-1600 cm^{-1} range). In this way, differences in the intensity of the bands across different samples related to intrinsic oscillators of the materials (*i.e.* hydroxyl groups, -OH) can be associated to actual differences in the amount of such species in the samples. Because of the normalization, the absorbance values are reported as arbitrary unit [a.u.].

- Nitrogen (N₂) physisorption measurements were carried out at liquid nitrogen temperature in the relative pressure from 1×10^{-6} to 1 P/P₀ by using a Quantachrome Autosorb 1MP/TCD instrument. Prior to the analysis, the samples were outgassed with the following procedure: 60 °C for 2h, 100 °C for 2 h, 150 °C for 2 h, 200 °C for 2 h and finally at 250 °C for 4 h (the residual pressure lower was than 10^{-6} Torr). Specific surface areas were determined using the BET (Brunauer-Emmett-Teller) equation, in the relative pressure range from 0.01 to 0.1 P/P₀. Pore-size distributions were obtained by applying Non-Localized Density Functional Theory (NLDFT) method (N₂ silica kernel based on a cylindrical pore model applied to the desorption branch).
- Thermogravimetric analyses (TGA) were carried out with a Setaram SETSYS Evolution Thermobalance. The data were collected in the range 50-1100 °C with scan rate of 10 °C/min under oxygen (O₂) flow (100 mL/min).
- Dynamic light scattering (DLS) experiments were carried out at 25 °C by using a Malvern Zetasizer NanoZS operating in a particle size range from 0.6 nm to 6 mm and equipped with a He-Ne laser with $\lambda = 633$ nm. The samples were dispersed in ultrapure water (5 mg in 3 mL) in the presence of xanthan gum (0.1 wt.%) to improve particle dispersion. Before measurements, the suspensions were sonicated for 10 min. The particles dispersed in water tend to form large aggregates. In the solution stabilized with xanthan gum this effect is strongly limited and no precipitation is observed after hours. The pH of suspensions was 7.0.
- The water proton longitudinal relaxation rates (T_1) were measured by using an HTS-110 3T Metrology Cryogen-free Superconducting Magnet combined with a Stellar Spinmaster Spectrometer (Mede, Italy), operating in the overall range of proton Larmor frequencies of 20-120 MHz (0.47-3.00 T). The measurements were performed using the standard inversion recovery sequence (20 experiments, 2 scans) with a typical 90° pulse width of 3.5 μ s and the reproducibility of the data was within $\pm 0.5\%$. The temperature was controlled with a Stellar VTC-91

heater airflow equipped with a copper-constantan thermocouple (uncertainty of ± 0.1 °C). The $1/T_1$ ^1H Nuclear Magnetic Relaxation Dispersion (NMRD) profiles were measured on a Fast-Field Cycling (FFC) Stelar SmarTracer Relaxometer over a continuum of magnetic field strengths from 0.00024 to 0.25 T (corresponding to 0.01-10 MHz proton Larmor Frequencies). The relaxometer operates under computer control with an absolute uncertainty in $1/T_1$ of $\pm 1\%$. Additional data points in the range 20-120 MHz were obtained on the HTS-110 3T Metrology Magnet coupled with Stelar Spinmaster Spectrometer. GdL0-1-2 chelates (1 mg) were dissolved in 1 mL of ultrapure water, while GdL0-1-2/SAP (10 mg) were dispersed in 1.5 mL of ultrapure water in the presence of xanthan gum (0.1 wt.%) to improve particle dispersion. Before measurements, the intercalated suspensions were sonicated for 10 min. The pH of solutions/suspensions was 7.0. The concentration of Gd^{3+} for each complex was estimated by ^1H -NMR (500 MHz) measurements using Evans's method.⁷ Na-GdEuSAP, Na-GdSAP and Phen-GdEuSAP_2x solids (10 mg) were dispersed in 1.5 mL of ultrapure water in the presence of xanthan gum (0.1 wt.%) to improve particle dispersion. Before measurements, the suspensions were sonicated for 30 min. The pH of suspensions was 7.0.

- Photoexcitation and photoluminescence (PL) emission spectra were recorded on a Horiba Jobin-Yvon Model IBH FL-322 Fluorolog 3 Spectrometer equipped with a 450 W xenon arc lamp, double grating excitation and emission monochromators ($2.1 \text{ nm}\cdot\text{mm}^{-1}$ dispersion; 1200 grooves per mm), and a Hamamatsu Model R928 photomultiplier tube. For Na-EuSAP and Na-GdEuSAP samples, excitation spectra were monitored at 615 nm, while emission spectra were recorded under irradiation at 272 and 395 nm. For Phen-SAP samples, excitation spectra were monitored at 415 nm, while emission spectra were recorded under irradiation at 275. For Phen-GdEuSAP samples, excitation spectra were monitored at 615 nm, while emission spectra were recorded under irradiation at 275 and 395 nm. For Eu-NbSAP and NbEuSAP samples, excitation

spectra were monitored at 615 nm, while emission spectra were recorded under irradiation at 395 nm. In general, all samples analysed were characterized both at solid state and in aqueous suspension (5 mg/mL, in the presence of 0.1 wt.% of xanthan gum). Time-resolved measurements were performed by using the time-correlated single-photon counting (TCSPC) option. A 370 nm spectralLED laser was used to excite Na-EuSAP, Na-GdEuSAP, Eu-NbSAP and NbEuSAP samples. A 295 nm nanoLED laser was used to excite Phen-SAP and Phen-GdEuSAP samples. Signals were collected using an IBH DataStation Hub photon counting module. Data analysis was performed using the commercially available DAS6 software (HORIBA Jobin Yvon IBH).

8.2 Tables

Table S1. Best-fit parameters obtained from the analysis of $1/T_1$ $^1\text{H-NMRD}$ profiles (37 °C) for GdL1, GdL2, GdL1/SAP and GdL2/SAP samples. (*Adapted from: "S. Marchesi et al., Dalton Trans., 2018, 47, 7896"*)

	GdL1	GdL2	GdL1/SAP	GdL2/SAP
$^{20}r_1$ [$\text{mM}^{-1}\text{s}^{-1}$]	4.3	8.5	12.4	43.1
Δ^2 [10^{19} s^{-2}]	3.70 ± 0.22	2.82 ± 0.77	1.82 ± 0.11	1.36 ± 0.07
τ_V [ps]	12.3 ± 0.2	23.8 ± 4.1	27.2 ± 4.0	11.7 ± 0.7
τ_{RL} [ns]	/	/	0.28 ± 0.04	0.60 ± 0.03
τ_{RG}	74 ± 2 ps	92 ± 3 ps	$1\ \mu\text{s}^{[a]}$	$1\ \mu\text{s}^{[a]}$
τ_M [μs]	0.7	0.07	1.08 ± 0.10	0.30 ± 0.06
S^2	/	/	0.26 ± 0.07	0.24 ± 0.02
$r_{\text{Gd-H}}$ [\AA] ^[a]	3.0	3.0	3.0	3.0
q ^[a]	1	2	1	2
a [\AA] ^[a]	4.0	4.0	4.0	4.0
D^{310} [$10^{-5}\text{ cm}^2\text{ s}^{-1}$] ^[a]	3.1	3.1	3.1	3.1

[a] Fixed during the best fit procedure

Table S2. Best-fit parameters obtained from the analysis of $1/T_1$ ^1H -NMRD profiles (25 °C) for GdTETA,⁸ GdL0 and GdL0/SAP samples.

	GdTETA ⁸	GdL0	GdL0/SAP
$^{20}r_1$ [$\text{mM}^{-1}\text{s}^{-1}$]	2.22	3.05	9.68
Δ^2 [10^{19}s^{-2}]	7.20 ^[a]	7.20 ^[a]	3.50±0.04
τ_V [ps]	19.0 ^[a]	19.0 ^[a]	31.0±0.03
a [Å] ^[a]	4.0	4.0	4.0
D^{298} [$10^{-5}\text{cm}^2\text{s}^{-1}$] ^[a]	2.24	2.24	2.24
q^{SS}	/	0.52±0.03	1.06±0.02
$r_{\text{Gd-H}}^{\text{SS}}$ [Å] ^[a]	/	3.34	3.30
τ_R^{SS} [ps]	/	76±12	375±11

[a] Fixed during the best fit procedure.

Table S3. Summary table of the photophysical parameters of Na-GdEuSAP and Na-EuSAP, as solid state (SS) and in aqueous suspensions (H_2O). $\lambda_{\text{exc}} = 272$ and 395 nm for Na-GdEuSAP sample

	Na-EuSAP	Na-GdEuSAP
Asymmetry Factor (R)	SS: 3.10 H_2O : 2.76	SS: 4.29 (272), 3.10 (395) H_2O : 2.74 (272), 11.02 (395)
τ_{SS} [ms]	0.04	0.05
$\tau_{\text{H}_2\text{O}}$ [ms]	0.19	0.18
$\tau_{\text{D}_2\text{O}}$ [ms]	0.60	0.60
τ_0 [ms]	5.84	4.19
q^{Eu}	4.02	4.37
$\Phi_{\text{Eu}}^{\text{Eu}}$ [%]	3.25	4.29

Table S4. Best-fit parameters obtained from the analysis of $1/T_1$ ^1H -NMRD profiles (37 °C) for Na-GdSAP and Na-GdEuSAP samples.

	Na-GdEuSAP	Na-GdSAP
$^{20}r_1$ [$\text{mM}^{-1}\text{s}^{-1}$]	13.00	13.31
Δ^2 [10^{19} s^{-2}]	5.12±0.07	3.87±0.04
τ_V [ps]	22.82±0.20	30.48±0.35
τ_R [μs] ^[a]	0.08	0.08
τ_{SAP} [μs]	43.89±0.52	47.41±0.45
τ_M [μs]	0.48±0.01	0.56±0.02
r [Å] ^[a]	3.1	3.1
q ^[b]	4	4
c	34.81±0.23	36.00±0.29

[a] Fixed during the best fit procedure.

[b] Data from PL Analyses (Table S3).

Table S5. Radiative lifetime (τ) of Phen-SAP (D) and Phen-GdEuSAP (DA) samples at solid state (SS) and in aqueous suspensions (H_2O), under excitation at 295 nm, and efficiency (E_{EnT}), constant rate (k_{EnT}) and overall quantum yield ($\Phi^{\text{Phen}_{\text{Eu}}}$) parameters of the FRET mechanism. ^a $\Phi^{\text{Eu}_{\text{Eu}}}$ Na-GdEuSAP (in water), used in Eq. (6) = 4.29% (Table S3)

	SS	1x	2x	3x
τ_D [ns]		3.82	4.28	4.81
τ_{DA} [ns]		3.41	3.37	4.36
k_{EnT} [s^{-1}]		3.15E+07	6.31E+07	2.15E+07
E_{EnT} [%]		10.73	21.26	9.36

	H_2O	1x	2x	3x
τ_D [ns]		4.49	4.41	4.89
τ_{DA} [ns]		3.82	3.82	4.69
k_{EnT} [s^{-1}]		3.91E+07	6.83E+07	8.72E+05

$E_{\text{EnT}} [\%]$	14.92	24.71	4.09
$\Phi_{\text{Eu}}^{\text{Phen}} [\%]^{\text{[a]}}$	0.64	1.06	0.18

Table S6. Summary table of the other photophysical parameters of Phen-GdEuSAP samples. $\lambda_{\text{exc}} = 275$ and 395 nm for Phen-GdEuSAP samples.

	1x	2x	3x
Asymmetry Factor (R)	5.19 (275)	6.96 (275)	4.70 (275)
[at solid state (SS)]	6.15 (395)	5.05 (395)	5.73 (395)
$\tau_{\text{SS}} [\text{ms}]$	0.11	0.28	0.31
$\tau_{\text{H}_2\text{O}} [\text{ms}]$	0.18	0.26	0.33
$\tau_{\text{D}_2\text{O}} [\text{ms}]$	0.23	0.22	0.23
q_{Eu}	1.03	< 0	< 0

Table S7. Photometric data, in accordance to CIE 1931 colour spaces, for Phen-SAP (D) and Phen-GdEuSAP (DA) samples.






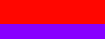




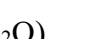
SAMPLE	$\lambda_{\text{exc}} [\text{nm}]$	x	y	R	G	B	Hex	Color	Color Purity [%]
Phen-SAP_1x (D)	275	0,1642	0,0814	58	52	254	3A34FE		85,7%
Phen-SAP_2x (D)	275	0,1688	0,1040	53	81	255	3551FF		80,7%
Phen-SAP_3x (D)	275	0,1712	0,1089	57	85	254	3955FE		80,0%
Na-GdEuSAP [A]	272	0,6566	0,3431	255	22	0	FF160		100,0%
Na-GdEuSAP [A]	392	0,6438	0,3559	255	50	0	FF320		100,0%
Phen-GdEuSAP_1x (DA)	275	0,1610	0,0454	74	0	255	4A0FF		93,3%
Phen-GdEuSAP_1x (DA)	392	0,6703	0,3295	255	0	0	FF00		100,0%
Phen-GdEuSAP_2x (DA)	275	0,2326	0,0842	167	0	254	A70FE		87,7%
Phen-GdEuSAP_2x (DA)	392	0,6591	0,3407	255	6	0	FF60		100,0%
Phen-GdEuSAP_3x (DA)	275	0,2049	0,0735	136	0	255	880FF		79,2%
Phen-GdEuSAP_3x (DA)	392	0,6597	0,3400	255	0	0	FF00		100,0%

Table S8. Summary table of the photophysical parameters of Eu-NbSAP and NbEuSAP, at solid state (SS) and in aqueous suspensions (H_2O).

	Eu-NbSAP	NbEuSAP
Asymmetry Factor (R)	SS: 2.75 H_2O : 2.53	SS: 4.88 H_2O : 4.60
$\tau_{\text{SS}} [\text{ms}]$	0.12	0.09
$\tau_{\text{H}_2\text{O}} [\text{ms}]$	0.15	0.19

$\tau_{\text{D}_2\text{O}}$ [ms]	0.37	0.43
τ_0 [ms]	4.60	3.33
q^{Eu}	4 (4.46)	3 (3.23)
$\Phi_{\text{Eu}}^{\text{Eu}}$ [%]	3.26	5.71

8.3 Notes and References

- 1 C. Bisio, G. Gatti, E. Boccaleri, G. Superti, H. Pastore and M. Thommes, *Microporous Mesoporous Mater.*, 2008, **107**, 90-101.
- 2 J. C. Dabrowiak, *Metals in Medicine (2nd Ed)*, 2017, John Wiley & Sons Ltd, ISBN: 978-1-119-19130-8.
- 3 A. Bax and D.G. Davis, *J. Magn. Reson.*, 1985, **65**, 355-360.
- 4 A. G. Palmer III, J. Cavanagh, P. E. Wright and M. Rance, *J. Magn., Reson.*, 1991, **93**, 151-170.
- 5 L. E. Kay, P. Keifer and T. Saarinen, *J. Am. Chem. Soc.*, 1992, **114**, 10663-10665
- 6 J. Schleucher, M. Schwendinger, M. Sattler, P. Schmidt, O. Schedletsky, S. J. Glaser, O. W. Sorensen and C. Griesinger, *J. Biomol. NMR*, 1994, **4**, 301-306.
- 7 A) D. F. Evans, *J. Chem. Soc.*, 1959, 2003-2005; B) D. F. Evans, G. V. Fazakerley and R. F. Phillips, *J. Chem. Soc. (A)*, 1971, 1931-1934.
- 8 K. M. Payne, J. M. Wilds, F. Carniato, M. Botta and M. Woods, *Israel Journal of Chemistry*, 2017, **57**, 880-886.
- 9 A. E. Bennett, C. M. Rienstra, M. Auger, K. V. Lakshmi and R. G. Griffin, *J. Chem. Phys.*, 1995, **103**, 6951-6958.

Curriculum Vitae et Studiorum & List of Publications of:

Stefano Marchesi



Stefano Marchesi (S.M.) was born in Voghera (Pavia) on 23.08.1990. He graduated in Materials Science-Chemistry (108/110) at the University of Piemonte Orientale in Alessandria (2013). He obtained a Master in Materials for Energy and Environment with top mark (110/110 with laude) at the University of Piemonte Orientale in Alessandria in collaboration with the Consorzio Università ed Impresa Vercelli (Univer) (2014). He graduated in Chemical Science at the University of Piemonte Orientale in 2016 (110/110).

Currently, S.M. has a position as PhD student in “Chemistry & Biology” (XXXII cycle) at the University of Piemonte Orientale in Alessandria (2016-*in progress*).

Since 2013, S.M. has focused his studies on the synthesis of molecular organosilica compounds (POSS) and layered materials (Saponite clay) with

controlled chemical composition and on their structural, morphological, spectroscopic, thermogravimetric and relaxometric characterization. Large attention has been devoted to the functionalization of these materials with different molecular entities following several synthetic methodologies, such ionic exchange reactions for example, in order to obtain multifunctional materials of interest for several applications.

Currently, S.M. is involved in the study of novel advanced hybrid materials with luminescent, paramagnetic and/or catalytic properties, which are suitable for a wide range of technological applications.

➤ **Main Fields of Interest**

- Inorganic-organic hybrid materials
- Paramagnetic and optical nanoparticles
- Coordination chemistry
- Luminescent materials
- Materials (*i.e.* catalyst...) for environmental remediation
- Synthesis and physico-chemical characterization of porous and layered materials, by means of several analytical techniques (*i.e.* x-ray diffraction, IR and UV spectroscopy, spectrofluorimetry, NMR relaxometry...)

➤ **Current Issues of Research**

- Synthesis and characterization of multifunctional inorganic/organic nanoparticles with catalytic, paramagnetic and luminescent properties
- Preparation of advanced layered materials for paramagnetic, optical, catalytic and environmental applications

➤ **Publications and Editorial Activity**

S.M. is author of 4 original publications on international scientific journals, published in *New Journal of Chemistry*, *Dalton Transaction* and *ChemPlusChem*.

S.M. participated to several national and international congresses and schools with 4 oral presentation and 6 posters in the three years of PhD program, with 2 more posters and 3 more oral presentations by Prof.ssa Chiara Bisio and Dr.ssa Daniela Lalli containing material from the XXXII cycle of Ph.D. program in "*Chemistry & Biology*".

➤ **Membership of Professional Societies**

S.M. is a member of the Italian Chemical Society (SCI) and the Italian Discussion Group on Magnetic Resonance (GIDRM). He is affiliated to the COST Action CA15209 "Eurelax" (European Network on NMR relaxometry, Working Groups WG2-Medical applications).

➤ **Scientific Publications of Associated Investigators**

A. Published:

- 1) S. Marchesi, F. Carniato, M. Guidotti, M. Botta, L. Marchese and C. Bisio, "*Synthetic saponite clays as promising solids for lanthanide ions recovery*", *New J. Chem.*, **2020**, Advance Article for NJC Themed Issue "*Sustainability from Intercalation Compounds*" + **Back-Cover**.
- 2) S. Marchesi, C. Bisio, E. Boccaleri and F. Carniato, "*Luminescent Polysilsesquioxane Obtained by Self-Condensation of Anionic Polyhedral Oligomeric Silsesquioxanes (POSS) and Europium(III) Ions*", *ChemPlusChem*, **2020**, 85, 176-182.

- 3) S. Marchesi, F. Carniato, C. Bisio, L. Tei, L. Marchese and M. Botta, "*Novel Paramagnetic Clays obtained through intercalation of Gd³⁺-Complexes*", *Dalton Transaction*, **2018**, 47, 7896-7904 + **Back-Cover**.
- 4) S. Marchesi, F. Carniato, L. Marchese, E. Boccaleri, "*Luminescent Mesoporous Silica Built through Self-Assembly of Polyhedral Oligomeric Silsesquioxane and Europium(III) Ions*", *ChemPlusChem*, Issue 6, **2015**, 80, 915-918.
- 5) S. Marchesi, F. Carniato, L. Palin, E. Boccaleri, "*POSS as building-blocks for the preparation of polysilsesquioxanes through an innovative synthetic approach*", *Dalton Trans.*, Issue 5, **2015**, 44, 2042-2046.
- 6) S. Marchesi, F. Carniato, E. Boccaleri, "*Synthesis and characterisation of a novel europium(III)-containing heptaisobutyl-POSS*", *New J. Chem.*, Issue 6, **2014**, 38, 2480-2485.

B. Work in-progress:

- 1) S. Marchesi, D. Lalli, F. Carniato, C. Bisio, L. Tei, L. Marchese and M. Botta, "*Solution and Solid-State NMR Study of Synthetic Saponite Materials Intercalated with Lanthanide Chelates*", in preparation
- 2) S. Marchesi, F. Carniato, M. Guidotti and C. Bisio, "*Novel Bifunctional Eu^(III) and Nb^(V)-containing Saponites for the Optical Detection and Catalytic Abatement of Chemical Warfare Agents in Aqueous Conditions*", in preparation
- 3) S. Marchesi *et al.*, "*Inclusion of Paramagnetic and Luminescent Lanthanide Ions in the Framework of Synthetic Saponite Clays*", in preparation
- 4) S. Marchesi *et al.*, "*Enhancing the Luminescence Properties of Gd(III) & Eu(III)-containing Saponites through Intercalation of Phenanthroline*", in preparation
- 5) S. Marchesi *et al.*, "*Introduction of Tb(III) & Eu(III) Elements in the Structure of Synthetic Saponite Clays: A Novel Luminescent Sensing Layered Platform*", in preparation

Acknowledgements

Desidero innanzitutto ringraziare dal profondo i supervisor della mia Tesi di Dottorato, la Prof.ssa Chiara Bisio e il Dr. Fabio Carniato, per il loro costante ed instancabile impegno, supporto, interesse ed entusiasmo dimostrato in questi anni nella realizzazione di questo progetto, oltre al fatto che rappresentano per me una fonte di ispirazione sia scientifica che personale. *Grazie!*

Ringrazio inoltre il Prof. Mauro Botta e il Prof. Leonardo Marchese, assieme al Dr. Matteo Guidotti, al Prof. Lorenzo Tei e alla Dr.ssa Daniela Lalli, per la loro professionalità scientifica dimostratami e per il loro imprescindibile apporto nelle tematiche esplorate in questo progetto.

Un ringraziamento speciale va a tutti coloro che mi sono stati vicini durante questi tre anni di dottorato, per tutto l'aiuto e l'affetto (reciproco) che mi hanno saputo dare e per avermi fatto vivere una bella esperienza in un clima di serenità e allegria. In particolare, ringrazio Ivana Miletto, Chiara Vittoni, Valentina Toson, Federico Begni, Mattia Lopresti, Vanessa Miglio, Elena Perin, Francesca Barbato, Marco Coppola, Francesco Volta, Massimo Cesale, Giorgio Carelli, Marco Barbetta, Enrico Luciano Appiani, Martina Ricagno, Simone Nascimbene, Alessandro Nicorelli, Marcello Benzi, Bianca Bolfi, Mina Errahali, Vittoria Sacchetto, Daniele Costenaro, ... le persone dei gruppi di ricerca di chimica-fisica ed inorganica e coloro che non ho citato tra queste poche righe.

Vorrei esprimere un sincero *Grazie* a Chiara Ivaldi, Valeria Lagostina, Selene Ivaldi e Diego Bonzani, tra le persone più importanti che io abbia mai conosciuto nella mia intera carriera universitaria, per la piacevole e divertente compagnia dentro e fuori i laboratori e per il loro incredibile supporto scientifico e morale, soprattutto durante i periodi difficili: senza di voi, non credo che sarei la persona che sono oggi!

Vorrei ringraziare anche Lorenza Schiavonetti, per la sua sensibilità, curiosità e passione ‘scientifica’, oltre che per l’affetto e il sostegno dimostrato (e dimostratogli) sia durante l’esperienza giornaliera di laboratorio che al di fuori di esso. *Grazie*

Un sincero grazie va al Dr. Claudio Cassino, al Prof. Maurizio Aceto, alla Dr.ssa Elena Perin, alla Dr.ssa Elisa Calà e al Dr. Davide Musso (DiSIT - Università del Piemonte Orientale “*Amedeo Avogadro*”, Alessandria), assieme al Dr. Claudio Evangelisti (Centro CNR-ICCOM, Milano), per le analisi NMR, ICP-OES/MS, CHN e HRTEM effettuate.

Un ulteriore ringraziamento va al Prof. Ciro Isidoro e alla Dr.ssa Chiara Vidoni (DiSS - Università del Piemonte Orientale “*Amedeo Avogadro*”, Novara), alla Prof.ssa Danuta Kruk e al Dr. Evrim Umut (University of Warmia and Mazury, Department of Mathematics and Computer Science, Olsztyn, Poland) e ai Dr.i Matteo Guidotti e Rinaldo Psaro (Centro CNR-SCITEC - Istituto di Scienze e Tecnologie Chimiche “*G. Natta*”, Milano) per avermi dato l’opportunità di eseguire missioni scientifiche (nazionali ed estere) presso le loro strutture di ricerca.

Questa ricerca è stata supportata finanziariamente da: 1) COST (European Cooperation in Science and Technology) Action CA15209 "European Network on NMR Relaxometry" (EURELAX), 2) EU Framework Programme "Horizon 2020", 3) Consorzio Interuniversitario di Ricerca in Chimica dei Metalli nei Sistemi Biologici (CIRCMSB), 4) Compagnia di San Paolo (CSP-2014 THERASIL Project, F. C. L. T.), 5) Università del Piemonte Orientale (Ricerca locale FAR2019) e 6) Ministero dell'Istruzione, dell'Università e della Ricerca (MIUR) Italiano.

Vorrei esprimere la mia gratitudine all’Università degli Studi del Piemonte Orientale “*Amedeo Avogadro*” (UPO) e al Dipartimento di Science e Innovazione Tecnologica (DiSIT).

Infine, desidero ringraziare con affetto i miei familiari e amici per il sostegno datomi e per essermi stati vicini durante questi tre anni.

... Grazie anche a tutti quelli che hanno letto questa Tesi di Dottorato ...

“Somewhere, something incredible is waiting to be known.”

- Carl Sagan

“Recognize that the very molecules that make up your body, the atoms that construct the molecules, are traceable to the crucibles that were once the centers of high mass stars that exploded their chemically rich guts into the galaxy, enriching pristine gas clouds with the chemistry of life. So that we are all connected to each other biologically, to the earth chemically and to the rest of the universe atomically. That’s kinda cool! That makes me smile and I actually feel quite large at the end of that. It’s not that we are better than the universe, we are part of the universe. We are in the universe and the universe is in us.”

- Neil deGrasse Tyson